Development of InGaN/GaN Core-Shell Light Emitters

Girgel, Ionut

Award date:
2017

Awarding institution:
University of Bath

Development of InGaN/GaN Core-Shell Light Emitters

submitted by

Ionuţ Gîrgel

for the degree of Doctor of Philosophy

of the

University of Bath

Department of Electronic and Electrical Engineering

September 2016

Abstract

Gallium nitride (GaN) and its related semiconductor alloys are attracting tremendous interest for their wide range of applications in blue and green LEDs, diode lasers, high-temperature and high-power electronics. Nanomaterials such as InGaN/GaN core-shell three-dimensional nanostructures are seen as a breakthrough technology for future solid-state lighting and nano-electronics devices. In a core-shell LED, the active semiconductor layers grown around a GaN core enable control over a wide range of wavelengths and applications.

In this thesis the capability for the heteroepitaxial growth of a proof-of-principle core-shell LED is advanced. A design that can be applied at the wafer scale using metal-organic vapor phase epitaxy (MOVPE) crystal growth on highly uniform GaN nanorod (NR) structures is proposed. This project demonstrates understanding over the growth constraints of active layers and dopant layers. The impact of reactor pressure and temperature on the morphology and on the incorporated InN mole fraction was studied for thick InGaN shells on the different GaN crystal facets. Mg doping and effectiveness of the p-n junction for a core-shell structure was studied by extensive growth experiments and characterization. Sapphire and Si substrates were used, and at all the stages of growth and fabrication. The structures were optimized to achieve geometry homogeneity, high-aspect-ratio, incorporation homogeneity for InN and Mg dopant. The three-dimensional nature of NRs and their light emission provided ample challenges which required adaptation of characterization and fabrication techniques for a core-shell device.

Finally, an electrically contacted core-shell LED is demonstrated and characterized. Achieving a proof-of-principle core-shell device could be the starting point in the development of nanostructure-based devices and new physics, or in solving technical problems in planar LEDs, such as the polarization of emitted light, the quantum-confined Stark effect, efficiency droop, or the green gap.

Acknowledgements

This work was possible with the support of some remarkable people at the University of Bath, as well as from other research groups. In the following, I shall try to acknowledge the most important contributions, although my appreciation extends to colleagues and individuals important in the completion of this work, that I may not get to mention explicitly.

First I would like to thank my supervisor, Dr. Philip A. Shields, for selecting and entrusting me with the advancement of this project, and for being always supportive in our discussions and work. I learned a great deal of professional and life lessons in his group and the extended semiconductors group at the University of Bath. Second, I am grateful to Dr. Duncan Allsopp for the opportunity to work within Lighting the Future project, and for the extensive discussions and reviews before journal submissions.

A special thank you to Dr. Emmanuel Le Boulbar, who instructed me on processing techniques for nanorods and early MOVPE growth, and who was always demanding and available to analyze the next experiment or the next paper submission. Also, I am grateful for the support and discussions on MOVPE with Dr. Pierre-Marie. Coulon and Dr. Quanzhong Jiang.

A lot of the characterization and cleanroom work was possible with the training and fruitful discussions with Dr. J. Mitchells, Dr. S. Sivaraya, and Dr. S. Wedge.

I also enjoyed the collaboration work with groups in the UK and Slovakia. Thank you to Dr. Paul Edwards, doctoral candidate Chris Bryce and Prof. Robert Martin from the University of Strathclyde, who provided hyperspectral CL analysis for the samples in this work. Thank you to Dr. Lata Sahonta for the TEM and EDX analysis. Also, I am grateful for the thorough sample analysis and discussions on CL and EBIC with Prof. Alexander Šatka and Dr. Juraj Priesol from the Slovak University of Technology.

Finally, I would like to thank my parents for they trust and support. And thank you to all the office and non-office mates I got to know closely during the time and work I shall always cherish in Bath.

Declaration

Most of the sample fabrication and characterization unless otherwise specified was carried out by myself. However, several samples were characterized by other contributors.

The small pitch (0.6 μm) samples examined in Chapter 3 for diameter and height uniformity for GaN growth with passivation were fabricated by Dr. E. Le Boulbar. The NR heights data was further processed by Dr. P. Shields with Matlab. The remainder of the samples on 2 μm pitch, electron beam lithography and characterization in Chapter 3 were carried out by myself.

CL analysis was performed in Chapter 4 by Dr. Paul Edwards from the University of Strathclyde. On one sample from the same chapter Dr. Suman-Lata Sahonta at the Cambridge Center for Gallium Nitride carried out TEM and EDX analyses. That sample preparation for TEM was done by Dr. Michael Ward at the University of Leeds and Dr. P-M. Coulon.

Magnesium doped and core-shell LED samples were analyzed by Prof. Alexander Šatka and Dr. Juraj Priesol from the Slovak University of Technology by CL and EBIC in chapters 5 and 6 respectively. Dr. Timothy Batten from Renishaw plc performed a set of Raman spectroscopy measurements on Mg-doped NRs.

In Chapter 6 a set of core-shell LED samples were analyzed by doctoral candidate Chris Bryce from the University of Strathclyde.

Contents

Abbreviations

3D - Three-dimensional
AFM - Atomic Force Microscopy
AlN - Aluminium Nitride
BL - Blue Luminescence (band)
BOE - Buffered Oxide Etchant
CL - Cathodoluminescence
Cp_2Mg - bis(cyclo-penta-dienyl)-magnesium
CRI - Colour Rendering Index
DAP - Donor-Acceptor Pair
e-beam - Electron beam
EBIC - Electron Beam Induced Current
EBL - Electron Beam Lithography
EDX (EDS) - Energy dispersive X-Ray spectroscopy
EL - Electroluminescence
ELO - Epitaxial lateral overgrowth
FIB - Focused ion beam FWHM - Full Width at Half Maximum
GaN - Gallium Nitride
HAADF - High-angular-annular-dark-field
HF - Hydrofluoric acid
HSQ - Hydrogen silsesquioxane
HVPE - Hydride Vapor Phase Epitaxy
ICP - Inductively Coupled Plasma
InGaN -Indium Gallium Nitride
IQE - Internal Quantum Efficiency
LED - Light Emitting Diode
LO - Longitudinal optical (phonon)
MBE - Molecular Beam Epitaxy
MOCVD - Metal-Organic-Chemical-Vapor-Deposition

MOVPE - Metal-Oxide-Vapour-Phase-Epitaxy
MQW - Multiple Quantum Well
NBE - Near Band Edge
NIL - Nanoimprint lithography
NR(s) - Nanorod(s)
NW(s) - Nanowire(s)
PL - Photoluminescence (conventional)
μ PL - Micro Photoluminescence
P(MMA) - Poly-(methyl methacrylate)
QB - Quantum Barrier
QW - Quantum Well
RIE - Reactive-Ion Etching
RT - Room temperature
SAG - Selective Area Growth
SCR - Space charge region
sccm - Standard cubic centimeters per minute
SE - Secondary electron image
SEM - Scanning Electron Microscope
SF - Stacking Fault
SO - Surface optical (phonon)
SOG - Spin-on-glass
SSL - Solid State Lighting
TD - Threading Dislocation
TEM - Transmission Electron Microscope
TMGa - Tri-Methyl-Gallium
TMIn - Tri-Methyl-Indium
TO - Transverse pptical (phonon)
VLS - Vapor-Liquid-Solid
YL - Yellow luminescence (band)

Chapter 1

GaN Nanorod LEDs

1.1 Introduction

Solid state lighting (SSL) is currently replacing incandescent and fluorescent light sources, because of the important energy savings and carbon footprint reduction possible with LEDs [1]. Setbacks in SSL adoption are a high LED bulb unit cost and concerns about how the blue light wavelength, the base of commercial white LEDs, affects the human and animal day-night physiological processes [2]. Both issues are being addressed by constant improvements in crystal growth methods, new phosphor layers to convert the blue light into wider and uniform spectra and high rendering color index, or by advances in packaging to extract and direct light.

Gallium nitride (GaN) is the material of choice for blue and white LEDs because of its characteristic direct wide band gap. A direct band gap and transition provides high recombination efficiency, while part of the blue emission spectra can be down-converted using a phosphor layer to blend blue and yellow wavelengths for white light [3]. Another very important advantage of III-nitrides is that the changing or adding another group III metal (Al, In) to GaN to form a ternary or quaternary alloy provides good control over the band gap, covering a range of $0.8 - 6.2$ eV from InN to AlN [4].

Because a native or common bulk GaN layer does not exist, GaN is obtained by heteroepitaxy on other substrates, mainly on sapphire and Si. Heteroepitaxial growth leads to accumulation of strain and formation of defects, due to the different lattice constants and thermal expansion coefficients between the substrate and the new crystal. Heteroepitaxy is accomplished by metal vapor phase epitaxy (MOVPE) which is the most widespread commercial crystal growth method. Alternatives are hydride

vapor phase epitaxy (HVPE) which provides high growth rates and high-quality GaN at high costs, used mainly as GaN seed layers for MOVPE. Another crystal growth method, molecular beam epitaxy (MBE) is highly versatile but lacks the growth rates necessary for high volume production.

A practical, high-quality and efficient heteroepitaxial blue LED required several scientific contributions and manufacturing innovations: high-quality GaN on an AlN buffer layer was first demonstrated by *Akasaki* and *Amano* [5]. The AlN bufsourcefer layer was used to manage the lattice and thermal mismatch to the sapphire substrate. A p-type GaN layer provides hole carriers and was found to be effective after activation by electron beam irradiation [6], and later by thermal annealing [7]. A GaN buffer layer was achieved by *Nakamura*, using a two gas flow MOVPE reactor [8]. *Nakamura* and *Mukai* proved the first active InGaN layer [9]. Finally, the basic LED design with an InGaN active region, sandwiched between GaN quantum barriers, *n*- and a *p*-type GaN layers, was demonstrated in ref. [10], and is used today by the majority of LED manufacturers. These seminal works were the basis for awarding the 2014 Nobel Prize in Physics to *Nakamura, Amano* and *Akasaki*. Improved heteroepitaxy, enhanced efficiency and light extraction, heat management and integration of multiple devices in a single bulb have been the main development directions and challenges for LEDs recently.

New breakthroughs can originate from advancing novel device designs and growth techniques. A new design moving the active InGaN layer from a continuous horizontal layer to a vertical nanowire LED with a radial core-shell heterostructure layout was proposed by Qian *et al.* [11, 12]. InGaN/GaN laser diode designs on sapphire [13] and on bulk GaN [14] were demonstrated. GaN on GaN growth [15] was achieved from hydride vapor phase epitaxy (HVPE) GaN wafers [16], or by using high-pressure ammonothermal GaN wafers [17].

In this thesis nanorods (NR) were produced by MOVPE to investigate the different growth and fabrication steps necessary for a prototype core-shell LED. Different NR fabrication routes and the current status of the field are discussed in the following sections of this chapter. High-quality MOVPE GaN on sapphire or Si templates were used as the starting point for *top-down* etching and regrowth fabrication of GaN NRs. Concentric layers of GaN, InGaN/GaN quantum wells and barriers (QW/QB), and a *p*-GaN capping shell were grown and thoroughly characterized. A microfabrication route to connect an array of core-shell LEDs into individual devices is proposed.

The novelty and aims of this work were to establish how nanoimprinting and plasma

etching for highly regular arrays of NRs [18] could be applied to achieve uniform morphology and light emission from InGaN/GaN layers grown on the sidewalls of the NRs. The three-dimensional (3D) NRs template provided an excellent opportunity to study InGaN growth on the different crystal facets. No particular wavelength was targeted, the aim was to understand how the growth needs to be controlled to achieve uniform InGaN distribution and emission. Active p-GaN doping levels, dopant distribution and minimal sidewall thickness for magnesium p-doped GaN NRs required more study. Finally achieving a current injected core-shell LED provided a perspective into the effectiveness of the p-GaN layer and valuable knowledge on NR processing and lithography steps for the new structures. The next sections offer a breakdown of the work and a more detailed discussion of the existing scientific literature.

1.2 Outline of the thesis

The remainder of Chapter 1 reviews fundamental topics in planar GaN-based LEDs, opportunities and challenges of three-dimensional LED designs as well as a perspective of the growth processes and current issues in nanorod LED development.

Chapter 2 presents a fabrication overview and a summary of the characterization methods used throughout the work.

Chapter 3 covers a study of nanorod diameter and height uniformity, the influence of fill factor on the MOVPE growth as well as the evolution of strain in the NRs.

Chapter 4 extensively discusses InGaN layer growth and characterization by photoluminescence, cathodoluminescence, transmission electron microscopy, and energy dispersive spectroscopy analyses.

Chapter 5 provides a study and discussion on the effects, efficiency and uniformity of magnesium doping on nanorods.

Chapter 6 discusses the electrically injected prototype core-shell LEDs achieved and provides further comments on device microfabrication. A comparative analysis for the LEDs by optical means (photoluminescence, cathodoluminescence), electrical methods (electron beam induced current and current-voltage characteristics) and finally electroluminescence closes the experimental section of the work.

Finally, Chapter 7 summarizes the main results from this work and provides an outlook on core-shell LEDs development.

1.3 GaN crystal structure

GaN is part of the binary III-nitrides group and displays a hexagonal wurtzite structure at equilibrium, as shown in Figure 1-1 a), with lattice parameters $a = 3.189$Å and $c = 5.185$Å [19]. The proximity of atoms in a periodic crystal leads to the overlap of individual atom wavefunctions and formation of allowed energy bands separated by a band gap. For wurtzite GaN at room temperature an electron energy $\sim E_g = 3.4$ eV [20, 21] can successfully get across the band gap. Furthermore, when the minimum of the conduction band and the maximum of the valence band are in the same reciprocal lattice position $\mathbf{k} = 0$, the center of the Brillouin zone (Γ point), the transitions occur directly, making GaN an excellent material for efficient SSL.

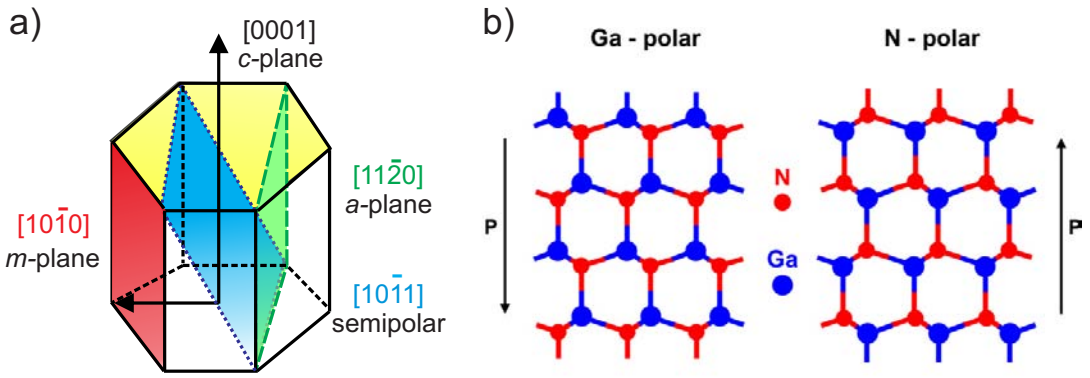

Figure 1-1: a) Polar and nonpolar GaN crystal planes, b) wurtzite structure with ABABAB sequence of atoms and resulting spontaneous dipole moment [22] (republished with permission of Semiconductor Science and Technology).

The succession of Ga and N atoms seen in Figure 1-1 b) follows an ABABAB stacking sequence along the [0 0 0 1] Ga-polar or [0 0 0 $\bar{1}$] N-polar growth directions[1]. The terminating surface layer gives its name to the polarity of the film. Despite using the same sequence of atoms, the orientation of the Ga-N bonds introduce different chemical reactivity and thus the two directions are not analogs to each other [23]. Apart from the wurtzite crystal structure, under certain conditions and with different substrates an ABCABCABC stacking can be obtained for GaN in a cubic phase (zinc-blende) grown along the cubic [1 1 1] direction [24].

[1]Figure 1 (b) republished with permission of Semiconductor Science and Technology, from Keller S. *et al.*, "Recent progress in metal-organic chemical vapor deposition of {0 0 0 $\bar{1}$} nitrides", *Semicond. Sci. Technol. 29*, 113001, (2014), permission conveyed through Copyright Clearance Center, Inc., DOI:10.1088/0268-1242/29/11/113001

1.4 Challenges in planar GaN

1.4.1 Substrates and defects

Recent developments in HVPE [25] and ammonothermal growth [17] can be used to manufacture free-standing homoepitaxial GaN wafers, however at high costs. Thus because of economical necessity, heteroepitaxy on sapphire substrates is the most common source of commercial GaN substrates, even if this growth method introduces quality problems in the form of lattice mismatch and thermal mismatch between the two different materials. However sapphire has its unit cell parallel to the GaN c-axis growth direction in planar layer, and it is also rotated by 30° to the GaN unit cell [26]. The rotation results in a lattice mismatch of only $\sim 12\%$. The thermal mismatch between the substrate and grown material is typically a greater source of threading dislocations into the planar GaN. Significant gains in adoption of Si substrates for which the lattice mismatch is $\sim 20\%$ have been made [27]. For crystal grown directly on foreign substrates, small amounts of strain can be accommodated by very thin pseudomorphic layers. The growth of thicker films leads to accumulated strain in planar InGaN/GaN layers GaN on Si films, resulting in plastic relaxation and the formation of misfit dislocations to relieve the strain and prevent wafer cracking [28]. The dislocations impact the crystal quality, act like carrier traps and reduce the lifetime of a device through heating at the dislocation site. GaN growth on sapphire (or Si) necessitates a GaN (or AlN) buffer layer with a minimum thickness of 3 nm or ($\sim$ 30 nm for Si), while for a thickness of 100 nm (sapphire) the lattice constant becomes identical to bulk GaN [29, 27].

Incremental improvements in heteroepitaxy by buffer layers and patterned dielectric masks through *selective area growth* (SAG) and *epitaxial lateral overgrowth* (ELO) methods have reduced the number of lattice threading dislocations (TD) by ∼four orders of magnitude, from 10^9-10^{11} cm^{-2} to mid 10^6-10^7 cm^{-2} [30]. A commercial GaN-based blue LEDs obtained by the two temperature approach, for a low-temperature GaN buffer layer and high-temperature GaN LED layer, operates having TDs in the range of $\sim 10^9 - 10^8$ cm^{-2}, while laser-diodes require TD values lower than 10^8 cm^{-2} [30]. A SAG process can further reduce the number of dislocations, as during growth it re-directs the TDs to terminate at the edges or interfaces of masked regions, or to locations which are not used for the end-device.

High-quality bulk GaN crystals with TD density of 5×10^3 cm^{-2} are recently available using high-pressure ammonothermal growth [17]. Still, a subject of debate, the large

number of defects relative to other compounds such as GaAs, does not prohibit light emission, possibly because of effects such as carrier localization [31, 32]. Injection of high current density in a LED to achieve high brightness LEDs leads to additional problems related to the nature of GaN and of heteroepitaxy.

1.4.2 Polarization in *c*-axis GaN

The bonds in III-V semiconductors exhibit a polar nature due to the different ionic character of the constituent atoms [33]. The non-overlap of positive and negative atomic charges in the hexagonal (wurtzite) GaN structure prompts spontaneous polarization and an inner electric field GaN along the six-fold symmetry *c*-axis. The polar *c*-axis is the most common GaN growth direction, although more recently the non-polar $[1\,1\,\bar{2}\,0]$ *a*-plane and $[1\,0\,\bar{1}\,0]$ *m*-plane orientations have been studied [26, 34]. In addition, strain-induced polarization or piezoelectric polarization can be introduced if the crystal undergoes pressure or strain from the environment or during crystal growth and cool down. The total polarization from both spontaneous and piezoelectric polarization play an important role in GaN and the efficiency of electron-hole recombinations, and needs to be considered in the design of devices. Figure 1-1 b) shows the orientation of the polarization **P**, opposite to the growth direction in Ga-polar material, and in the growth direction for the N-polar GaN. Due to the inner crystal field, the valence band is separated into three parts for a heavy hole, light hole, and spin-orbit bands. To each band, an exciton transition (A, B, and C) is associated, formed by the coupling of an electron to a hole, both bound to each other by Coulomb interaction. The excitons can be identified in low-temperature PL measurements.

1.4.3 Quantum confined Stark effect

Polarization shifts the LED emission peak position and reduces efficiency as it increases the separation between the electron and hole wavefunctions, a phenomenon known as the *quantum-confined Stark effect* (QCSE) [35]. If an alloy with a different lattice constant (InGaN on GaN or AlGaN on GaN) is grown epitaxially, the surface discontinuities cause a change in the band offsets at the interfaces, because of bound surface charges. The relative alignment of the energy bands at a heterojunction, causing band offsets, are crucial to controlling the degree of confinement of carriers in quantum wells. The band offsets depend on QW/QB thickness, strain states of the two layers in contact, and on the growth order [36]. The offset can reduce or increase the energy barrier for a charge carrier because of the piezoelectric effect through *band-bending*, a design

aspect that needs to be considered for all interfaces, especially for growth in the c-axis direction.

The detrimental effects of QCSE have increased interest towards the non-polar a-plane and m-planes [37] and semipolar planes such as $\{1\,\bar{1}\,0\,1\}$, $\{2\,0\,\bar{2}\,\bar{1}\}$ [38] or $\{1\,1\,\bar{2}\,2\}$ [39] for which the QCSE is null or respectively reduced [40]. An example of the QCSE and its effect on wavefunction overlap is provided by Feezell *et al.*[2] in Figure 1-2.

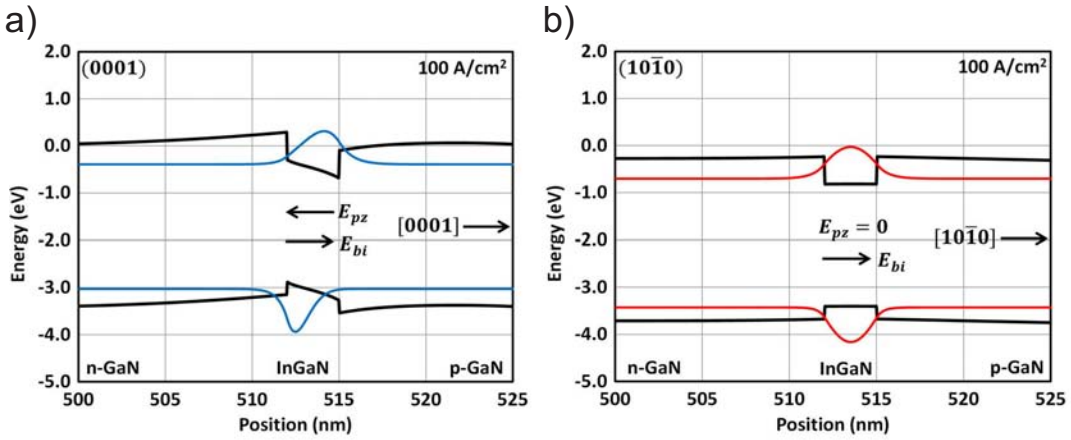

Figure 1-2: Simulated energy band diagrams for a) polar c-axis InGaN/GaN with $\mathbf{E}_{bias} > \mathbf{E}_{pz}$ resulting in a QW with slope opposite to the p-n junction slope, b) non-polar m-plane without polarization and a nearly flat QW (republished with permission of IEEE).

1.4.4 Efficiency droop

The reduction of light emission efficiency or *droop-effect* with forward current observed in planar LEDs could be linked to several causes, such as carrier leakage in the active region [41], increase in non-radiative Auger recombination probability [42, 43], or loss of carrier localization [44, 45].

In the case of carrier leakage, the polarization field in the QW likely pushes the electrons outside of the active region, thus droop can be seen as a recombination taking place outside the active region [41]. The phenomenon was visible in electroluminescence experiments for which the carriers are injected separately from the n- and p- side, while in PL experiments did not manifest droop because no forward bias was driving

[2] Republished with permission of IEEE, from Feezell, Daniel F., Speck, James S., Denbaars, Steven P. Nakamura, Shuji, "Semipolar $\{2\,0\,\bar{2}\,\bar{1}\}$ InGaN/GaN light-emitting diodes for high-efficiency solid-state lighting", *IEEE/OSA J. Disp. Technol. 9*, 190–198 (2013), permission conveyed through Copyright Clearance Center, Inc.

carrier leakage. However, later experiments have shown droop can be identified in PL at the appropriate carrier densities [45].

In the case of Auger recombination the electrons and holes recombine and instead of emitting a photon, the energy is transferred to a third carrier. As the process involves three carriers, the droop gets worse with high carrier densities. Thicker QWs were shown to reduce the impact of droop to less than 5%, albeit on the c-axis GaN the internal quantum efficiency due to wavefunction overlap is also reduced [46]. Figure 1-3 shows the different effects of droop on c- and m-plane due to the internal polarization [3]. The distribution of high current densities over larger volumes has shown to be effective in reducing droop [47, 48].

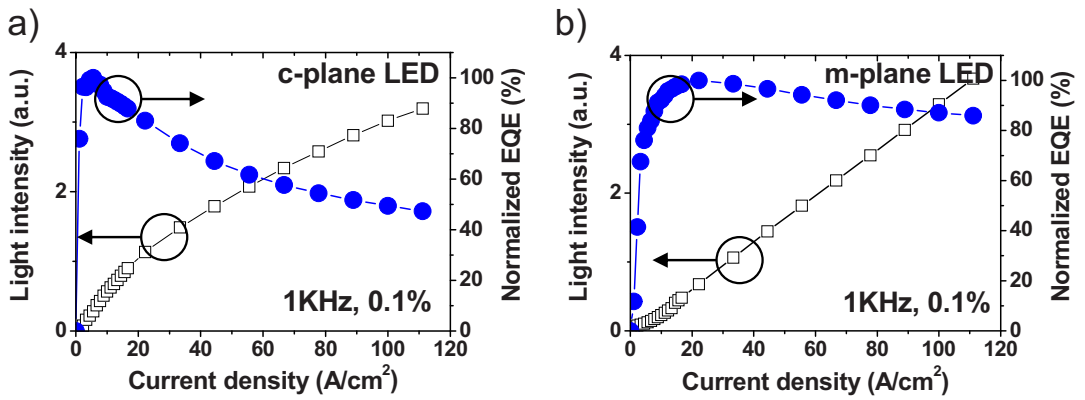

Figure 1-3: Integrated electroluminescence intensity and external quantum efficiency dependence on current desity for c-plane [0 0 0 1] and m-plane [1 0 $\bar{1}$ 0] planar GaN. (Reprinted with the permission of AIP Publishing from ref [49]).

However, discrepancies between theoretical models and experiments indicate the phenomena is not yet fully understood. It was proposed that carrier localization may fail at high current densities and the localized states may become saturated [44, 45]. In all models the droop is expected to increase with carrier density, therefore a design which can reduce the number of carriers per volume could be expected to mitigate the problem of droop.

[3] Ling, Shih-Chun, Lu, Tien-Chang, Chang, Shih-Pang, Chen, Jun-Rong, Kuo, Hao-Chung, Wang, Shing-Chung, "Low efficiency droop in blue-green m-plane InGaN/GaN light emitting diodes", *Appl. Phys. Lett.*, 96, 231101 (2010).

1.4.5 The green gap

A high InN fraction is necessary to achieve green light emission from polar *c*-plane GaN. Achieving higher indium content is possible through longer growth time at lower temperatures, to obtain wider/deeper QWs. This also results in the increase of the separation between electrons and holes because of the existing internal electric field in the [0 0 0 1] direction, reducing the recombination efficiency [50, 51]. A higher InN fraction can increase the strain or the plastic relaxation of strain, which corresponds to an increase in non-radiative recombination [52].

Another cause of loss of recombination efficiency is the incorporation of point defects, which occurs for higher InN fractions [53]. The growth of QWs at higher temperatures is beneficial to the reduction of point defects [51], but also reduces the amount of InN that can be grown.

An option for efficient green emitters is to use a different crystal facet than the *c*-plane. The polarization field can be avoided on non-polar $\{1\,0\,\bar{1}\,0\}$ *m*-planes. The slow growing stability of the $\{1\,\bar{1}\,0\,1\}$ semi-polar facets could also provide a good basis for InGaN growth, as it experiences reduced QCSE.

A very attractive approach has been the use of nanowires (NWs) or nanorods (NRs) as a means to obtain the *m*-planes as the support layer for growth on non-polar GaN. The NR geometry has several other advantages which are presented in the following section.

1.5 Opportunities for nanorod structures

1.5.1 Less dependency on the substrate quality

The growth of NRs without a GaN seed layer as a starting base was achieved in MBE, as NRs were obtained under nitrogen-rich conditions by spontaneous 3D growth on Si(111) [54], AlN [55] or even glass substrates [56]. Similar to *self-organized growth* in MOVPE, the NRs have a wide range of diameters, tilt, and morphologies. Consonni *et al.* suggested that GaN atoms adsorb onto the AlN buffer layer and nucleate into metastable 2D GaN nuclei, which may condensate into more stable strained 3D nuclei [55]. This is followed by a growth stage which aims to minimize free-surface energy and release strain by the formation of 3D nanostructures in the shape of NWs and NRs. These results suggest that GaN NRs could be grown without a particular substrate. In

the case of MOVPE growth, nucleation has only been observed on GaN seed layers.

1.5.2 Dislocation reduction

As the NRs can be grown on a fraction of a two-dimensional substrate, only a small number of the NRs will be affected by the TDs from the planar GaN seed layer, leading to an effective decrease in the number of defects impacting NR light emission. Furthermore, if lateral growth is favored on 3D structures, the TDs originating from the template will bend and migrate towards the growth front [30] and will likely affect only the lower part of the NR, reducing the dislocation density in the upper NR. Planar GaN layers were achieved in MBE and MOVPE from overgrown NRs with reduced number of threading dislocations [57].

1.5.3 Increased surface area

An immediate advantage of the columnar structure is the increase in the active surface area available for lateral or radial growth, surrounding a GaN core with a sequence of shells on vertical m-plane facets [58]. Theoretically, a much smaller chip size can be manufactured and used to extract the same amount of light relative to planar LEDs. In existing literature, the amount of active nanocolumn surface area depends on the growth method, and ranges from low-fill[4] and low coverage of the planar surface for self-assembled nanowires [59], to high coverage, or high-fill[5] for patterned growth [60] as shown in Figure 1-4. Dimensional control of the nanostructures is important for the control of the resulting wavelength, and for the different growth and processing steps (initial GaN core, QW/QB thickness, p-GaN thickness, current spreading layer, contacts, etc.). In this work the aim is to achieve an array of nanorods, each working as an independent LED, electrically connected through a common n-side, and an individual p-side. Also, for the light to escape from the non-polar sidewalls, the NRs should not come in contact with each other along the sidewalls. In the current work (see sections 3.1 and 3.7) it was found that effective fill factors for NRs were varied between 0.28–0.44. The lower half $(0.28 - 0.35)$ of the range is preferred to maintain InGaN growth uniformity on the sidewall and allow space for an indium tin oxide (ITO) current spreading layer and light extraction. Taking into consideration the active area

[4]Reprinted with permission from Hersee, S. D., Sun, X., Wang, X., "The Controlled Growth of GaN Nanowires", *Nano Lett. 6, 1808–1811*, 2006. Copyright 2006 American Chemical Society.

[5]Sekiguchi, H., Kishino, K., Kikuchi, A., "Ti-mask Selective-Area Growth of GaN by RF-Plasma-Assisted Molecular-Beam Epitaxy for Fabricating Regularly Arranged InGaN/GaN Nanocolumns", *Appl. Phys. Express 1*, 124002, 2008. Copyright 2008 The Japan Society of Applied Physics.

only, an optimized 4 µm tall NR, 400 nm diameter, ∼ 28% fill factor, could provide 12× larger active area (see Chapter 3).

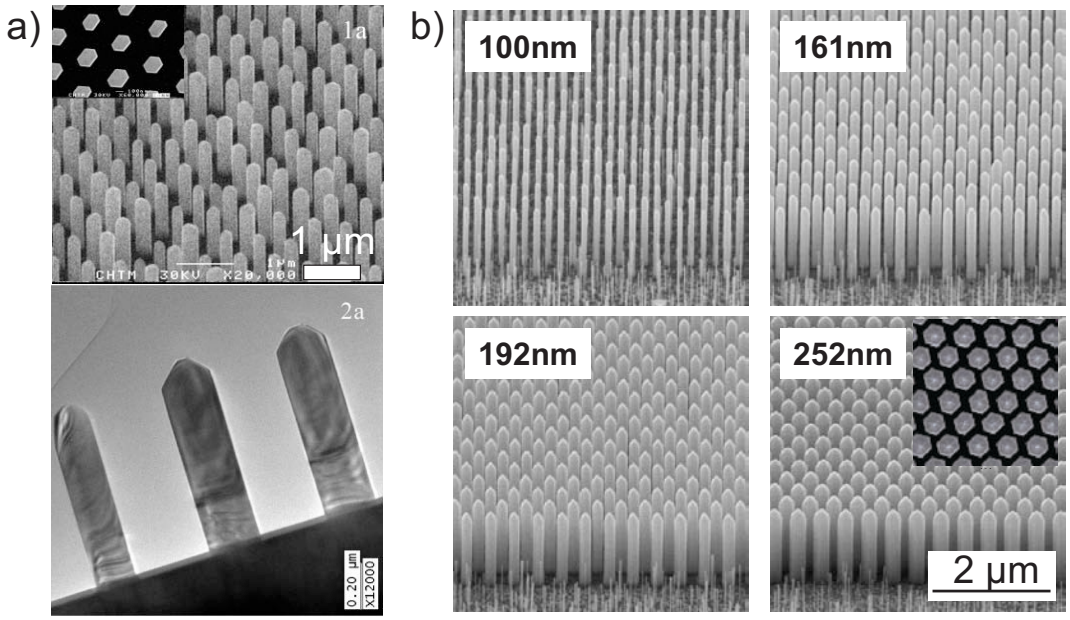

Figure 1-4: NRs grown from an underlying GaN film covered with a SiN_x mask with opening for vertical and lateral growth; the resulting NRs show hexagonal symmetry and vertical sidewalls [61] (Copyright 2006 American Chemical Society), b) Different mask diameters result in different NR diameters with vertical sidewalls and hexagonal facets ([60], Copyright 2008 The Japan Society of Applied Physics).

1.5.4 Strain free growth

Nanorods are free from the biaxial strain exerted in 2D layers if their heights are greater than the NR cross-section diameter [62], which is an advantage in regards to the thermal expansion and formation of cracks likely in strained planar layers. A more stable emission and InN integration are expected if the GaN is grown without strain.

One type of NR structure uses the strain free NR to grow an active section or *quantum disk* between the *n*- and *p*-doped GaN sections, along the *c*-axis [63]. A greater active area can be achieved if the active layers are grown radially on a GaN core, creating a *core-shell* structure. Both types of NR structures obtained by an early Au-catalyst MOVPE growth (vapor-liquid-solid synthesis) are shown in Figure 1-5 a).

1.5.5 Non-polar active layers

Solid state devices on non-polar m-planes could avoid the deleterious effects of charge separation and QCSE due to spontaneous and piezoelectric polarization inherent to c-axis devices. There are few reports on pure $\{1\,0\,\bar{1}\,0\}$ GaN crystal planes obtained from sapphire substrates, because low index planes or faceted defects can appear during growth [64]. Nano-column structures obtained by patterned growth on a GaN seed layer result in uniform $\{1\,0\,\bar{1}\,0\}$ m-plane terminated facets as in Figure 1-4.

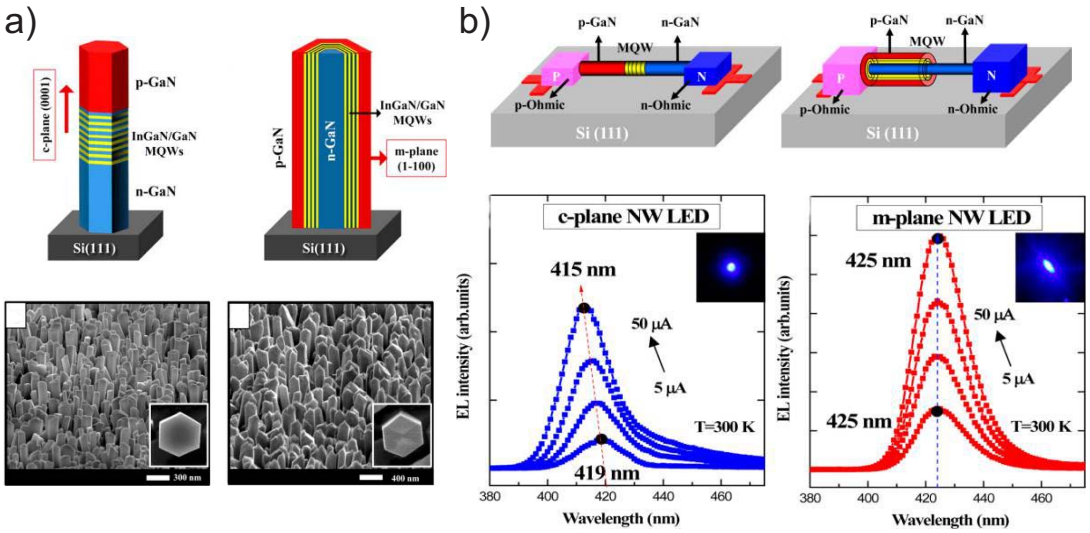

Figure 1-5: a) NRs with quantum disk (left) and core-shell (right) active layers, with corresponding SEM images, b) individual NRs contacted and EL spectra from axial and m-plane QWs (adapted from ref [65], Copyright (2014) American Chemical Society).

The majority of emitted light from core-shell NRs would originate from the large surface m-plane vertical sidewalls, which should experience no piezoelectric fields or blue shift due to the QCSE [65]. Figure 1-5 b) shows electroluminescence (EL) spectra obtained from individual NRs in a catalyst driven MOVPE growth for both quantum disk and core-shell structures[6]. The catalyst method uses the condensation of vapor phase Ga and N atoms at the interface of a metal (Au or Ni) deposited by lithography on the substrate. During the vapor-liquid-solid (VLS) transition, the liquid metal catalyst is pushed to the top of the NR and during cool down it solidifies [66, 11]. Because the complete removal of the metal catalyst and its alloys is near impossible, VLS growth is

[6]Reprinted with permission from Ra, Y.-H., Navamathavan, R., Yoo, H.-I. & Lee, C.-R., "Single nanowire light-emitting diodes using uniaxial and coaxial InGaN/GaN multiple quantum wells synthesized by metalorganic chemical vapor deposition", *Nano Lett. 14*, 1537–1545, (2014), Copyright 2014 American Chemical Society

less common. However, the EL spectra in these structures showed a gradual shift of the emission peak with increasing current, indicating the presence of QCSE or band filling effects. The emission from the NR with active layers on the m-plane showed no shift with current intensity. In other studies involving semi-polar planes [67], or quantum disk structures the emission did record a shift of the main emission peak with current intensity, even if the structures were unstrained [68, 69].

The prior studies on EL from NRs indicate that only the m-plane emission wavelength can remain stable with different current intensities. This is very complicated for spectra obtained in multi-plane faceted NRs as studied in this work. Very recently it was shown that the current path, type, and location of the contact play a very important role in current distribution and main emission peak [70].

1.5.6 Possible route to mitigate droop

The increase in thickness of active area layers was shown to mitigate the efficiency droop in polar devices [47, 48]. For growth on a non-polar m-plane template, a thicker $8 - 16$ nm QW results in a small electroluminescence and efficiency reduction [71]. Other work on m-plane QWs has shown a much smaller efficiency reduction ($\sim 5\%$) than for c-plane ($\sim 25\%$) QWs [72]. NR LEDs with m-plane emission and thicker QWs could provide a LED design with low or zero efficiency loss at high currents.

1.5.7 Diameter dependent wavelength and color mixing

The InGaN/GaN system can be used for different applications by adjusting the InN fraction to obtain light emission from blue to amber wavelengths. This is achieved by controlling the InN fraction during growth, or alternately, by controlling the NR diameters as demonstrated by Sekiguchi *et al.* [73]. Figure 1-6 a) illustrates the effect of PL emission shifting from blue to red with increasing NR diameter[7], in the range of $143 - 270$ nm. CL analysis revealed double peak emission from the $\{1\,0\,\bar{1}\,0\}$ and $\{1\,\bar{1}\,0\,1\}$ facets, which appear as separate data points in Figure 1-6 b). The figure also shows higher InN fraction can be achieved for NRs in close proximity than for NR with a larger pitch, likely because of NRs shadowing each other and reduced Ga incorporation during the QW growth for NRs with larger diameters.

[7]Reprinted from Sekiguchi, H., Kishino, K., and Kikuchi, A., "Emission color control from blue to red with nanocolumn diameter of InGaN/GaN nanocolumn arrays grown on same substrate", *Appl. Phys. Lett. 96*, 231104, 2010, with the permission of AIP Publishing

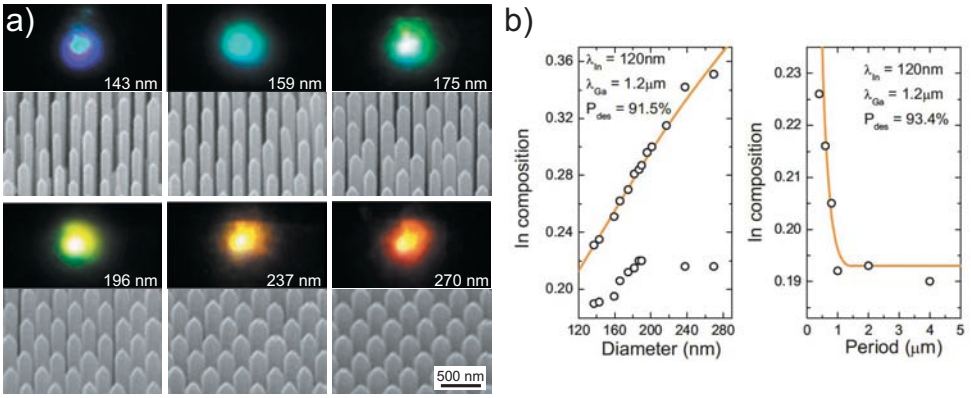

Figure 1-6: a) Near-field PL emission (room temperature) and SEMs of NRs with diameters $143 - 270$ nm in the same growth run, b) Correlation of CL emission peak and InN composition as a dependence of NR diameter and pitch distance or period (Reprinted from [73] with the permission of AIP Publishing).

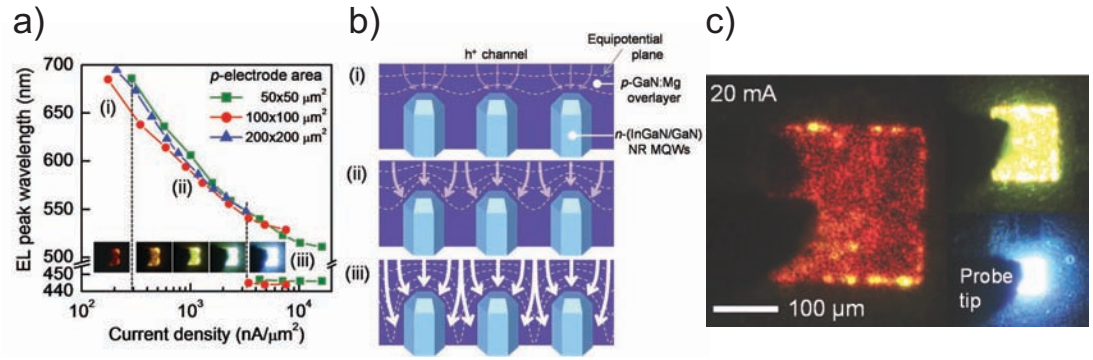

Figure 1-7: a) EL peak emission dependence on current density, b) equipotential planes with increasing forward bias and hole carrier paths in the p-GaN layer covering the NRs, c) for a fixed current density the LED chip area was changed to combine red, yellow and blue wavelengths. (Reprinted by permission of John Wiley & Sons, Inc. [74]).

Another method to obtain color tunability was developed by Hong *et al.* who embedded the NR completely in p-GaN, and changed the emission from red to blue, by increasing the forward bias from $2.65 - 10$ V [74]. The shift in emission was caused by the collection of carriers gradually from the NR tips at low forward bias, to the NR sidewalls, base and between the NRs for very high bias as shown in Figures[8] 1-7 a-b). The same process was applied using a fixed current and and by varying the LED chip size (Figure 1-7 c)), with the current density increasing for smaller LED surfaces, the emission shifted from

[8]Hong, Y. J., Lee, C.-Ho, Yoon, A.,Kim, M., Seong, H.-K.,Chung, H. J., Sone, C., Park, Y. Jo, & Yi, G.-C., "Visible-color-tunable light-emitting diodes", *Adv. Mater. 23*, 3284–3288, 2011. Copyright 2011 by John Wiley & Sons, Inc. Reprinted by permission of John Wiley & Sons, Inc.

red to blue. To better understand the different LED designs covered, growth and processing techniques, an overview of MOVPE and NR growth are given in the next section.

1.6 MOVPE growth

The MOVPE grown GaN crystal require the transport of gas phase organometallic precursors of group III trimethyl-gallium (TMGa) and group V (NH_3) to the reactor chamber where the free Ga and N atoms can react, adsorb, migrate and condensate into nuclei or onto the growing crystal. The different surface processes are shown in Figure 1-8 a). If the temperatures are too high, a large number of atoms will re-evaporate back into the reactor gas, and if the temperature is too low, a large number of defects and electronic trap states may incorporate. Decomposition of NH_3 is the most common source of nitrogen used, and the efficiency of its cracking depends on the reactor temperature. For both MOVPE and MBE, a high partial pressure of NH_3 over TMGa is necessary to obtain high-quality GaN and for NRs in particular.

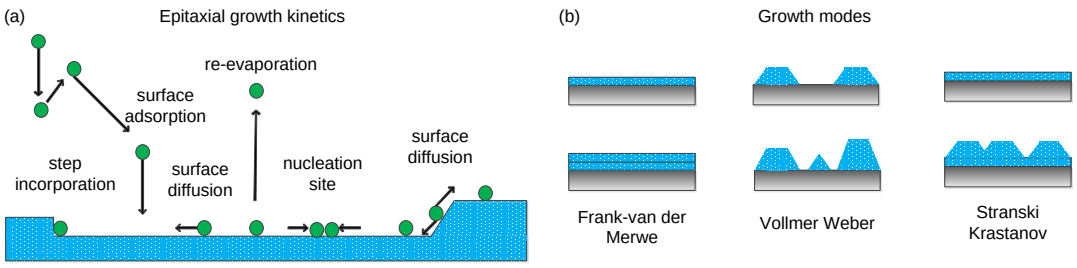

Figure 1-8: a) Surface processes in MOVPE epitaxy, b) Crystal growth models for 2D layers, island growth, and mixed 2D-3D growth.

1.6.1 Growth mechanisms

Heteroepitaxy and the strain build-up occurring cause changes in growth mode, from 2D layers to island nucleation and progression into 3D growth to release accumulated strain. Figure 1-8 b) outlines the three main growth modes. In Frank-van der Merwe (FM) growth nucleation islands form on the substrate surface into a continuous wetting layer. Upon further growth there is no accumulation of strain. This mode is characterized by high diffusion and may give a step flow aspect after each new layer. FM is more common for homoepitaxy and is expected to produce the highest crystalline quality. Volmer-Weber (VW) mode leads to the direct growth of 3D islands, as the atoms bond

more strongly to each other than to the substrate, and their diffusion on the substrate is low. Multiple islands coalesce and form new crystals with increased roughness.

The mixed 2D-3D Stranski-Krastanov (SK) mode occurs for layer thickness larger than the uniformly strained and pseudomorphic layer growth. The strain is released by the formation of isolated islands on top of the continuous film [75, 76]. The islands then undergo a number of successive shape transitions from spherical to truncated pyramids, and full pyramids with $\{1\,\bar{1}\,0\,1\}$ facets [55]. *Elastic relaxation* ensues as a process to release strain by forming new facets with reduced total free energy per unit volume in the new configuration [55]. Further growth causes an increase in the number of dislocations on the NR side facets, indicating a phase of *plastic relaxation*.

1.6.2 MOVPE growth parameters

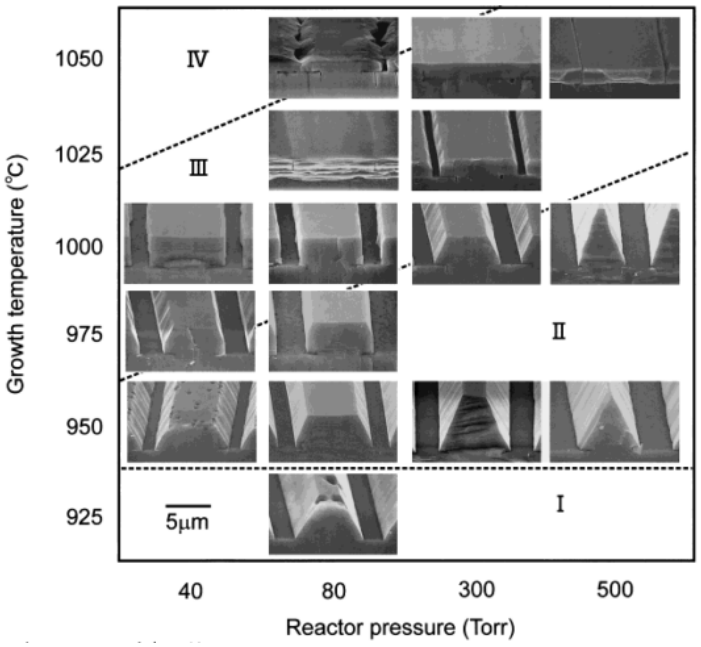

Figure 1-9: Morphological modifications for growth on $[0\,0\,0\,1]$ GaN from $[1\,0\,\bar{1}\,0]$ stripe openings, for different reactor conditions (reprinted from ref. [77], by permission of John Wiley & Sons, Inc.).

The effects of MOVPE reactor parameters on the different GaN crystal planes were studied by Hiramatsu *et al.*, and their findings are shown in Figure[9] 1-9 [77]. Some

[9]Hiramatsu, K. Nishiyama, K., Motogaito, A., Miyake, H., Iyechika, Y., & Maeda, T., "Recent Progress in Selective Area Growth and Epitaxial Lateral Overgrowth of III-Nitrides: Effects of Reactor Pressure in MOVPE Growth",*Phys. Status Solidi 176*, 535–543, 1999, Copyright John Wiley& Sons.

conclusions important to 3D growth can be drawn from the study: the semi-polar $\{1\bar{1}01\}$ plane in both high or low-temperature settings is the most stable and dominant. Medium to high temperatures results in maintaining a smooth c-plane surface (Figure 1-9 region II). The use of very low pressure can improve the ratio of vertical non-polar a-plane to semi-polar planes, shown by the transition from region II to region III. Further insight into relative crystal plane growth rates can be obtained studying Wulff constructs in section 4.2 or references [78, 79, 80].

In addition to GaN growth, the epitaxy of the active InGaN layer introduces new challenges, regarding its lattice mismatch with GaN and the growth temperature range which is different to GaN. A projection of InN fraction integration varies with growth temperature as shown by Figure 1-10 from ref [81].

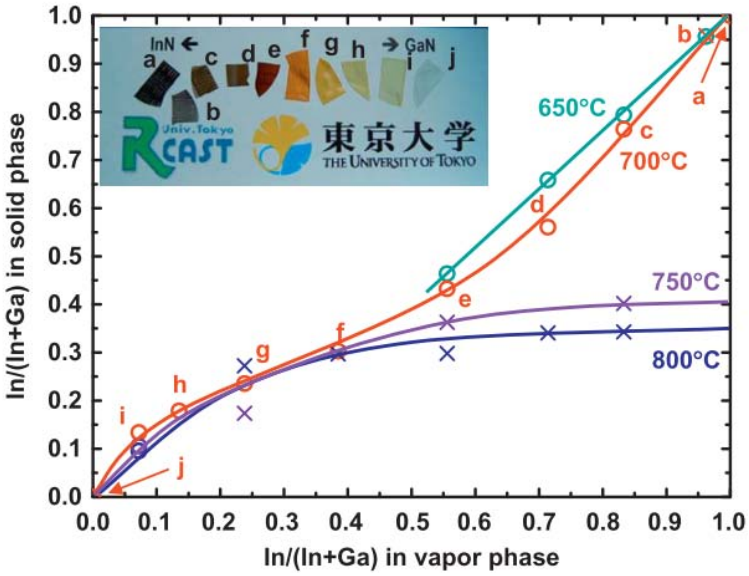

Figure 1-10: Range of temperatures for InGaN growth [81] (reprinted with permission from Elsevier.)

The InN fraction in MOVPE is expected[10] to be in a linear relationship between the indium in vapor phase and incorporated InN in the GaN lattice between $650 - 700$ ℃. Above 700 ℃ the desorption of indium limits the InN fraction to $\sim 0.3 - 0.4$. Using a high V/III ratio was demonstrated to improve InN incorporation [82].

Because of the lattice mismatch between InN and GaN, a high InN fraction may lead to phase separation within the GaN lattice [83, 84].

[10]Reprinted from Shioda, T., Sugiyama, M., Shimogaki, Y., Nakano, Y. "Selective area metal-organic vapor-phase epitaxy of InN, GaN and InGaN covering whole composition range", *J. Cryst. Growth 311*, 2809–2812, (2009), with permission from Elsevier, doi.org/10.1016/j.jcrysgro.2009.01.013

1.7 GaN nanorods via a *bottom-up* growth

A nitrogen rich environment is necessary to encourage 3D or vertical growth while Ga-rich conditions favor planar layers [85]. Bottom-up growth and *self-assembly* of GaN NWs and NRs occurs spontaneously under a high V/III ratio on AlN seed layers [86]. Spontaneous nucleation of NW was demonstrated[11] by Ristić *et al.* to be Volmer-Weber growth driven by lattice mismatch, an issue that also prevents the formation of a continuous wetting layer [87]. Figure 1-11 gives a representation of the growth process:

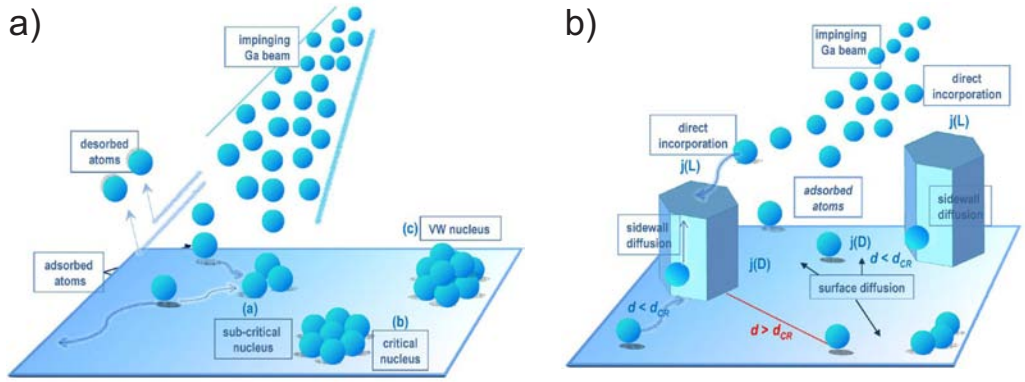

Figure 1-11: Volmer-Weber growth mode is responsible for bottom-up growth by: a) Formation of *critical-size* small islands - nucleation stage, b) Growth of NRs from stable nuclei with contributions from *direct capture* at the top of the rod and from substrate *surface diffussion* [87] (reprinted with permission from Elsevier).

The NRs grow vertically under impinging Ga adatoms onto the *c*-plane and from surface diffusing Ga-N atoms, collected by the nucleation islands or the NR. By diffusion the atoms climb along the sidewalls and incorporate at the NR top [88, 87]. Saturation of the nucleation sites can be achieved if the distance between the islands is larger than twice the mean diffusion length of the Ga adatoms, a characteristic controlled by reactor parameters (temperature, V/III ratio, pressure). An increase in temperature or decrease in reactor pressure results in longer surface diffusion lengths, by supplying more kinetic energy and lowering the number of adatoms collisions respectively in the reactor gas. The excess of nitrogen reduces diffusion length of Ga atoms on the substrate and provides an impetus for vertical growth. In self-assembled growth, the

[11] Reprinted from Ristić, J., Calleja, E., Fernández-Garrido, S., Cerutti, L., Trampert, A., Jahn, U., Ploog, K. H., "On the mechanisms of spontaneous growth of III-nitride nanocolumns by plasma-assisted molecular beam epitaxy", *J. Cryst. Growth 310*, 4035–4045, (2008), with permission from Elsevier, doi.org/10.1016/j.jcrysgro.2008.05.057

reactor conditions and substrate quality control the NR density and diameters. Furthermore, the nucleation does not occur simultaneously all over the substrate, resulting in NRs with different geometry.

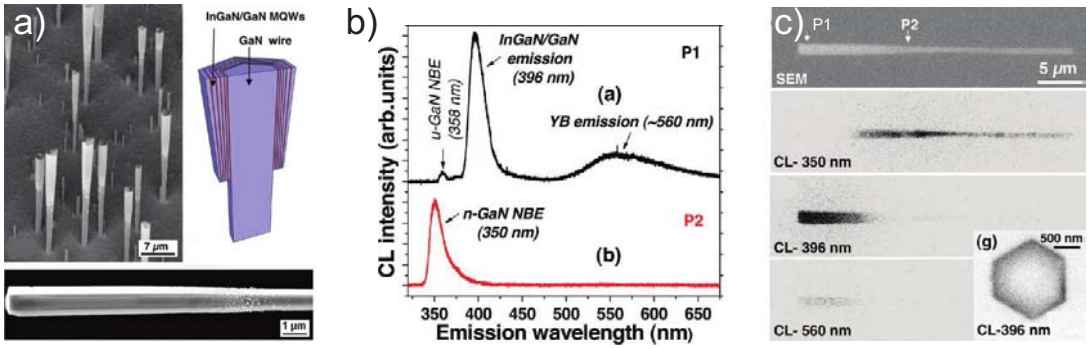

Figure 1-12: a) Self-organized GaN NR growth, b) CL spectra from the middle and top NR parts, c) CL maps indicate source and emission wavelength (Reprinted from reference [89], Copyright 2011 American Chemical Society).

A core-shell LED obtained by bottom-up and self-assembled GaN NRs is shown in Figure 1-12. The optical and electrical properties were measured on a single rod device [89]. A distinct feature of this type of growth is that a few NRs can reach very high aspect ratios, as in Figure 1-12 a), because they capture most of the Ga-N adatoms, while the overall density of NRs on the substrate remains small. Vertical growth is encouraged by doping during the initial NR n-core growth with silane [90]. Once the n-core was obtained, the active layers and then the p-GaN shell were grown radially on the core. The transition between the n-side and the p-side can be seen in the rough area on the sidewalls of the NR in the Figure 1-12 a) inset. The InGaN layer shows a gradient of InN fraction, likely caused by the diffusion of indium atoms toward the upper part of the NR. In Figures[12] 1-12 b)-c) the CL spectra and map indicate the two main emission peaks achieved, with longer wavelengths and higher InN located at the NR upper section. The low density of NRs can be turned into an advantage, as the high aspect NR can be peeled off the substrate, while incorporated in a polymer dielectric and connected to a circuit, as very recently demonstrated by Dai *et al.* [59].

By contrast, nanowires growth using *selective area epitaxy* has the advantage of density and dimensional control of the NRs. A pattern typically obtained by lithography and a SiO_2 film deposition on a GaN *c*-plane film can be used as a mask for GaN NR

[12]Reprinted with permission from Koester, R., Hwang, J.-S., Salomon, D., Chen, X., Bougerol, C., Barnes, J.-P., Dang, D.-S.,Rigutti, L., De Luna-Bugallo, A., Jacopin, G., Tchernycheva, M., Durand, C., Eymery, J., "M-plane core-shell InGaN/GaN multiple-quantum-wells on GaN wires for electroluminescent devices", *Nano Lett. 11*, 4839–4845, (2011). Copyright 2011 American Chemical Society

growth in the openings of the mask. Because typically bottom-up growth results in predominantly pyramid shaped 3D growth, Hersee *et al.* introduced the *pulsed growth* mode by which separate injection and pause, or interruption time, of the precursors result in vertical *c*-axis growth [61]. The interruption of either the Ga or N sources can cause a change in the dominant facets obtained: excess Ga during a lack of NH_3 flow encourages the formation of the semipolar $\{1\,\bar{1}\,0\,1\}$ plane, while excess N during Ga interruption leads to reduced lateral growth rates and predominant $\{1\,0\,\bar{1}\,0\}$ non-polar planes [91]. Figure 1-13 shows the effect of N pause time after 120 cycles of alternate NH_3 and TMGa injection. It was proposed[13] that Ga migrates from the sidewalls to the *c*-plane during the nitrogen interruption and leads to the increase in rod height. The same study showed that vertical growth rate is enhanced at higher reactor temperatures and that during the absence of NH_3 flow, the decomposition of GaN was also observed.

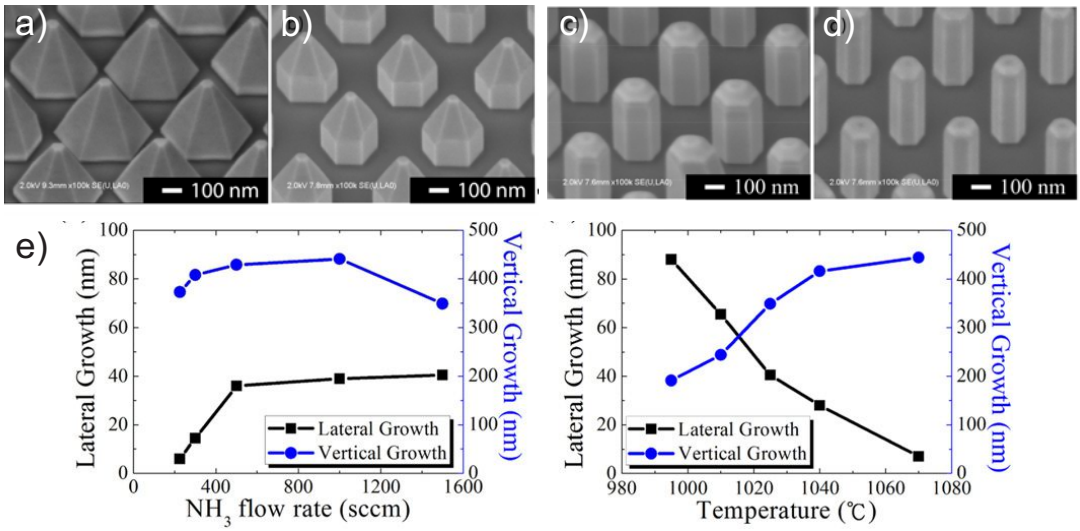

Figure 1-13: Precursors are injected alternatively during pulsed MOVPE growth. The effect of N interruption time in seconds on the lateral/vertical growth for a) 0s b)1s c)2s d)4s e) rod morphology as a function of NH_3 flow and reactor temperature [91] (republished with permission of IOP Publishing).

Bergbauer *et al.* demonstrated that the H concentration in the carrier gas can prevent the formation of the predominant pyramidal $\{1\,\bar{1}\,0\,1\}$ structure. This is caused by the passivation of N-terminated planes with H atoms, i.e. $(0\,0\,0\,1)$ and $\{1\,0\,\bar{1}\,1\}$ in Ga-polar crystals [92]. Thus these planes are more stable and slower growing, determining the

[13]Republished with permission of IOP Publishing from Lin, Y.-T., Yeh, T.-W., Dapkus, P. D.,"Mechanism of selective area growth of GaN nanorods by pulsed mode metalorganic chemical vapor deposition", *Nanotechnology 23*, 465601 (2012), permission conveyed through Copyright Clearance Center, Inc.

eventual crystal shape [93]. A lower V/III ratio is suggested to reduce the effects of passivation [94]. This is potentially the reason why using lower NH_3 precursor flow and high pitch distance for SAG of NRs results in $\{1\,0\,\bar{1}\,0\}$ facets rather than $\{1\,\bar{1}\,0\,1\}$ facets typically obtained during continuous growth [95].

Recently using silane (SiH_4) dopant flows very tall 28 µm tall NRs were obtained [96]. Without silane injection, the height of the NRs achieved a maximum of 3.4 µm. The significant increase in height suggests the presence of silane is increasing the Ga atoms diffusion length. However, with higher silane exposure the surfaces can become passivated and not permit InGaN/GaN QW growth [90].

1.8 Top-down GaN nanorods

Vertical GaN nanowires can be prepared from existing GaN thin films on sapphire or Si $\{1\,1\,1\}$ substrates. Although it requires a GaN film to be grown first, the GaN NRs can provide higher active surfaces than the planar films and excellent design flexibility through highly controllable dimensions. *Top-down* NRs are obtained by a plasma etching process into the 2D GaN, followed by MOVPE regrowth to recover the crystal facets. A metal mask (Ni or Ti) and optimization of plasma etching parameters provide excellent selectivity and high aspect ratio GaN NRs [18].

In this work the top-down nanorod plasma etching and re-growth on GaN cores are used. There are a number of advantages to this method as the underlying GaN defects are isolated to a few nanorods, the patterning resolution with nanoimprinting can be on the order of 25 nm and 70 nm minimum pitch distance [97], it uses practically strain-free GaN, and it can be scaled up for large wafers.

Initial methods for top-down NR fabrication used self-organizing SiO_2 nanospheres as a mask [99, 100]. This type of mask provided better rod uniformity than self-organized growth. The benefits of strain relaxation and increased PL emission due to scattering on the NR sidewalls were observed in those studies.

In Figures 1-14 a) and b) highly uniform NRs arrays were demonstrated using electron beam lithography and a SiO_2 mask. Strain relaxation and 8× more intense PL intensity were observed[14]. Shields *et al.* [18] used a combination of nanoimprint lithography and

[14]Reprinted from Ramesh, V., Kikuchi, A., Kishino, K., Funato, M., Kawakami, Y., "Strain relaxation effect by nanotexturing InGaN/GaN multiple quantum well", *J. Appl. Phys. 107*, (2010), with the permission of AIP Publishing.

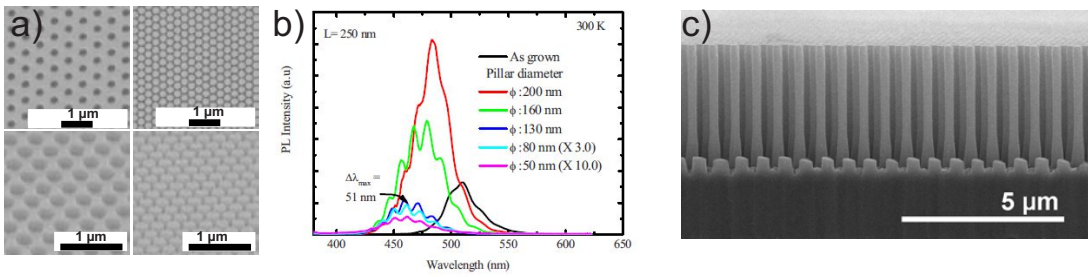

Figure 1-14: a) Nanohole and nanorod arrays with different diameters obtained by selectively etching with a SiO_2 mask, b) PL spectra of as grown and etched NRs indicate a 50 nm emission blue-shift as strain is released from the planar etched GaN, c) array of highly uniform GaN NRs obtained by selectively etching with a metal mask. (Reprinted and adapted with with the permission of AIP Publishing from ref [98], [18]).

metal Ni mask to achieve wafer scale uniform and high aspect ratio NR arrays, as shown[15] in Figure 1-14 c).

Top-down NRs are expected to be affected to a higher degree than bottom-up growth by surface damage due to the plasma process, and to having more dangling bonds and surface states. The surface states may act as traps for carriers at the NW surface and reduce carrier density. The relative constant radiative efficiency for low (12K) and room temperature PL in ref. [18] proves etching does not introduce defects affecting the PL intensity. Further surface treatments by KOH wet etching [101], buffered oxide etch or thermal annealing can further improve the surface. In this work the crystal was repaired by GaN faceting and regrowth [102]. Most of the growth takes place on the non-polar and semi-polar facets, without significant growth in the *c*-axis direction. A new X-ray diffraction study shows high-quality crystal facets are obtained after regrowth [103]. This further confirms that etching and regrowth steps are a compelling path to high-quality GaN-based LEDs.

1.9 Current challenges for NR LEDs

An excellent example of the top-down method is the work by J.-R Chang *et al.*, shown in Figure 1-15, in which a set of six InGaN QWs were grown on the sidewalls of etched GaN cores.

[15]From Shields, Philip, Hugues, Maxime, Zúñiga-Pérez, Jesus, Cooke, Mike, Dineen, Mark, Wang, Wang, Causa, Federica, Allsopp, Duncan, "Fabrication and properties of etched GaN nanorods", *Phys. Status Solidi 9*, 631–634 (2012), Reprinted by permission of John Wiley & Sons, Inc.

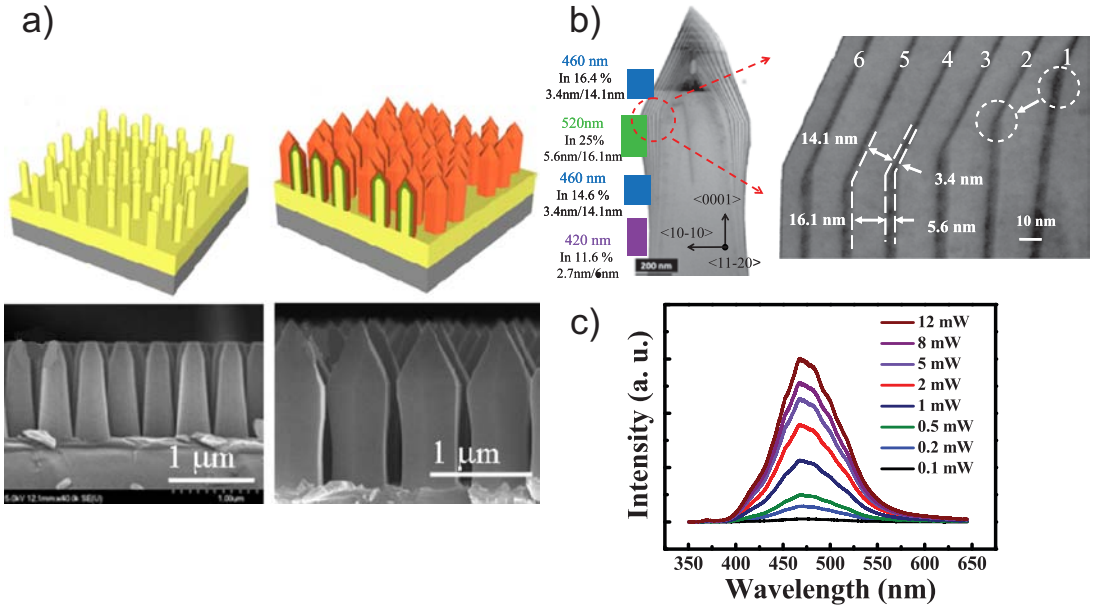

Figure 1-15: a) Schematic and SEM images of top-down core-shell NRs, b)TEM cross-section showing six QWs with varying thickness and InN fraction ($11-16$ %) on the non-polar m-plane and semipolar $\{1\,\bar{1}\,0\,1\}$ plane respectively, c) PL spectra of obtained NRs array show negligible QCSE. (Reprinted from ref. [104] with the permission of AIP Publishing)

CL spectral maps revealed a broad emission from $\sim 420-520$ nm from the bottom to the top of the NRs. The different emission peaks originated from a different InN fraction integration on the $\{1\,0\,\bar{1}\,0\}$ sidewall[16], and from a different growth rate on the $\{1\,\bar{1}\,0\,1\}$ plane, which was suggested to be caused by NR shadowing effects. TEM and EDX analyses reveal in Figure 1-15 b) the relative thicknesses of the QW/QB on the two planes and the corresponding InN fraction incorporated. Similarly, PL emission in Figure 1-15 c) shows the broad emission range from non-polar and semipolar facets has a negligible QCSE related shift with increased carrier excitation.

This work confirmed the preference for the active regions to increase in size toward the top of the NRs, likely due to migration on the sidewall toward the NR tip [63, 87, 89]. A narrower range ~ 50 nm of emitted wavelengths was achieved by Yeh *et al.* using pulsed growth and three QWs [105].

The diameter and InN incorporation uniformity on NRs are crucial topics to solve the

[16]Reprinted from Chang, J.-R., Chang, S.-P., Li, Y.-J., Cheng, Y.-J. Sou, K.-P., Huang, J. -K., Kuo, H. -C., Chang, C.-Y., "Fabrication and luminescent properties of core-shell InGaN/GaN multiple quantum wells on GaN nanopillars", *Appl. Phys. Lett.100*, 261103 (2012), with the permission of AIP Publishing.

control of emitted wavelengths. One target of this work is to obtain uniform growth for the GaN sidewalls and uniform InN incorporation. The facet recovery and active area growth stages impact the range of emitted wavelengths. In Figure 1-15 c) due to the variation of InN fractions ($11-16\%$ InN) along the m-plane, the emission FWHM was $\sim$100 meV. In planar LEDs a FWHM of a couple of tens of nanometers is typical. A more uniform InN fraction integration is likely to obtain a more uniform QW geometry and emission wavelength. A particular wavelength was not targeted, but rather the understanding of how to control growth rates on the different crystal facets and QW uniformity are of primary importance.

Efficient p-doping by magnesium acceptors has been a challenge from the very first planar LED designs and studied intensely, because of a very low active carrier availability [106, 107, 108]. Additional problems of formation of bonds between the Mg atoms to H atoms leading to donor-acceptor-pair transitions or vacancies causing *self-compensation* phenomena and increased electrical resistance compound the problem [109, 110, 111]. In the case of Mg doping of NRs, although some initial electrically pumped devices have been achieved [112], the existing literature can not always be applied to all methods of NR fabrication. As an example, complete coverage in p-GaN [74] may not be applied to high aspect ratio NR. A thorough understanding of the effects of MOVPE growth and integration into the thin p-GaN m-plane shells and studying other approaches for effective p-GaN doped NRs presents high research interest. A related issue to p-type carriers is achieving a uniform p-n junction[17] and electrical transport in NRs as shown in Figure 1-16 a). Indeed this is a current topic of intensive research [113, 114].

The nanorod 3D geometry entails complications in regard to electrical transport and processing. Different techniques have been studied to add electrical contacts, and most work has been done on individual NRs [12, 65, 70]. For NR arrays metal contacts were deposited after a planarization step with a dielectric layer [116, 117, 118]. A continuous transparent Ni/Au layer could serve as a p-contact for bottom-up emission although it likely reduces transparency, or alternatively, a thicker layer could reflect light through a transparent n-contact [119].

Alternatively the planarized NR array could be contacted by a continuous transparent conducting oxide (indium-tin-oxide or ITO) [120] and a metallic contact pad [115] as

[17] M. Tchernycheva, V. Neplokh, H. Zhang, P. Lavenus, L. Rigutti, F. Bayle, F. H. Julien, A. Babichev, G. Jacopin, L. Largeau, R. Ciechonski, G. Vescovi and O. Kryliouk, *Nanoscale*, 7, 11692, 2015, Published by The Royal Society of Chemistry, doi.org/10.1039/C5NR00623F

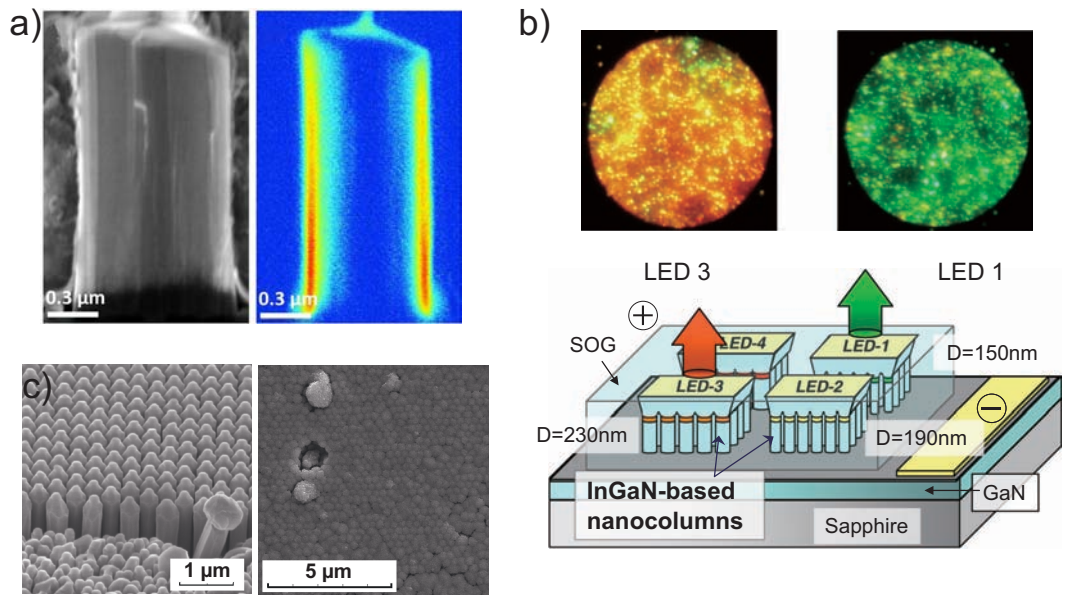

Figure 1-16: a) NR p-n junction with uniform current transport along the sidewalls using a sputtered ITO layer[114] (published (2015) by The Royal Society of Chemistry), b) Device structure with planarizing SOG dielectric and ITO layers c) NRs from Figure 1-16 b), before and after ITO coverage [115] (Copyright 2013 The Japan Society of Applied Physics).

shown in Figures[18] 1-16 b) and c). For closely packed NRs the growth conditions were used to promote coalescence and ultimately a p-GaN planar layer on the top of the NRs [67]. A flexible support PET film or thin metal foil were recently investigated in order to move the NRs to a flexible substrate [121, 59].

A proof of concept electrically driven core-shell LED was targeted for this work. Achieving such a prototype can bring further understanding to the technical issues confronting this design, and it can change and improve the processing and growth stages required. The following chapter will discuss some of the processing techniques and characterization methods used throughout the work to achieve core-shell NR LEDs.

[18]Kishino, K., Nagashima, K., Yamano, K., "Monolithic Integration of InGaN-Based Nanocolumn Light-Emitting Diodes with Different Emission Colors", *Appl. Phys. Express 6*, 12101, (2012), Copyright 2012 The Japan Society of Applied Physics.

Chapter 2

Fabrication and characterization of core-shell nanorods

In the previous chapter, a current literature perspective on GaN and GaN nanowires fabrication for core-shell structures was presented. The present chapter covers a detailed discussion about the terminology, methods and clean-room process used to obtain core-shell structures, as well as a review of the characterization tools used.

In the present work *top-down* fabrication of nanostructures commences from a GaN film grown on [0 0 0 1] direction on a sapphire substrate that was processed by plasma etching to obtain nanorods (NRs). This method was chosen for its reliability and dimensional consistency in achieved NRs. While it may seem counter-intuitive to epitaxially grow a GaN film and to etch it, a high density of NRs with large height-to-diameter aspect ratio leads to an in increased active layer surface [58], relative to the equivalent surface area of planar LED layers. The number of threading dislocations (TD) formed during the epitaxial growth which impact the emitting surfaces are reduced as they are removed by etching or by bending towards the growth front plane [30]. The mask pattern for the *top-down* approach is highly important as it impacts the density of nanorods, the NR diameter and the dimensional uniformity for subsequent growth. It is very important to achieve a narrow emission wavelength because NRs with variable diameter can result in different emission wavelengths [73]. The 'top-down' approach for core-shell LED has advantages in regards to dimensional uniformity, constant crystal quality along the entire NR length, and strain relaxation [62, 102]. The fill factor is defined as the fraction of NR planar [0 0 0 1] surface area relative to the sample's planar area, and a high fill factor corresponds to a tightly packed array of NRs. The control of fill factor is important in the fabrication of photonic crystals, as it directly affects the refractive

index of the equivalent GaN-air crystal [122].

The alternative method of *bottom-up* growth has shown to result in highly variable NR diameters, heights and a long growth time necessary [11, 123, 92]. More recently the use of patterned substrates and pulsed growth have made bottom-up growth more predictable [91]. Strain-relaxed bottom-up grown NRs by MOVPE may use silane doping to obtain high-aspect ratio GaN NRs, which introduces a passivating SiN_x layer on the nanorods, making uniform nucleation difficult for subsequent growth of QWs and increasing the defect density [90]. A key benefit of the top-down approach is the potential high uniformity that can be achieved on the wafer scale.

2.1 Fabrication proceses

The processing used in the present work for top-down nanostructures for LED required patterning of a metal mask on the GaN film, plasma etching of nanorods and GaN regrowth in an MOVPE reactor to recover the hexagonal GaN facets. The further steps of InGaN/GaN QW/QB and p-type GaN cap layer growth are similar for both top-down and bottom-up approaches. Selective growth on the NR sidewalls without growth between the NRs was possible by using a hydrogen silsesquioxane (HSQ) passivation layer. A thicker HSQ layer was also used to planarize the 3D device structure. A conducting indium-tin-oxide (ITO) layer, transparent for visible wavelengths after thermal annealing, improved current spreading in the NR structure. Deposition of metal contacts by electron beam evaporation was necessary to take the structure towards a usable device. Each of the steps is to be discussed in detail in the following sections.

2.1.1 Substrates and templates

GaN on sapphire and GaN on Si{1 1 1} substrates were used. The GaN on sapphire film was thicker (4 µm) than the available GaN on Si (2 µm) and thus provided high-aspect NRs and electrical conduction. Because of its thickness, a continuous layer of 1 µm thick GaN on sapphire was left in place to make an electrical contact to the n-core. Furthermore, the sapphire-based samples were n-type because of Si doping during the planar template growth used by the manufacturer. A further Si substrate set of samples was provided by OSRAM through the EU FP7 SMASH programme, and were used mainly as a proof of principle and for optical studies. The GaN was grown on the Si wafers by using an intermediary AlN buffer layer, which made the lattice match to

the GaN film possible, but electrical conduction could not be achieved on Si substrates, as the AlN band gap is higher at 6.02 eV [124] than for GaN[106].

The substrates were prepared for the spin-on resist layer by soaking in room temperature piranha solution for 15 minutes. The piranha solution is a mixture of 3:1 parts sulfuric acid (H_2SO_4) and hydrogen peroxide (H_2O_2), used to remove organic matter residues and make the surfaces hydrophilic to improve the resist adhesion. The samples were rinsed thoroughly in deionized water (DI) and dried in an oven at a constant 90 ℃ for 15 minutes. Alternatively, a short 5 minutes oxygen plasma achieved the same effect in cleaning and improving the adhesion on the wafer surface.

2.1.2 Nanoimprint lithography

The resist mask pattern has a large impact on the NR array because the pattern directly causes the initial diameter of the NR to create large arrays of identical NRs. Nanoimprint lithography (NIL) is an excellent method to obtain high nanometer resolution, reproducible, large area patterning at low cost. The nanometer resolution is achieved as it is a contact method, without limitations by the optical diffraction limit or scattering effects into the resist. NIL patterns at nanometre scale are created by the mechanical deformation of an acrylate resist. The patterns were available from nanoimprint PET films masters, which had a bold relief hexagonal pattern of 300 and 600 nm diameter holes at 0.6 and 2 μm respectively periodicity or pitch distance. The larger NR diameters and pitch can be obtained by photolithography as well, however, the smaller NRs and high uniformity require nanoimprinting. The variety of patterns and diameters with nm resolution is only limited by the availability of NIL masters.

Samples with planar GaN film were spin coated with a resist in an air atmosphere. The resist used was a 16% acrylate brought to clean-room temperature. The resist was spun for 1 minute at $2500 - 3000$ rpm and then heat cured at 150 ℃ on the hot-plate for 2 minutes to remove most of the solvent.

The pattern was impressed into the resist by the pressure of a hand-held roller which was rolled once onto the wafer substrate. The hand-held nanoimprint rolling process has proved to produce reliable and reproducible patterns on different sample sets, produced at different time periods during this study. The imprinted acrylate was exposed to 1 minute of UV curing to cross-link and harden the acrylate. The profile was in-filled by a second spin coating with HSQ, using the same spin parameters. Heat curing on a hotplate for the HSQ was done for 3 minutes at 200 ℃. Different plasma etching chemistries were used to etch selectively the resist and the HSQ layer.

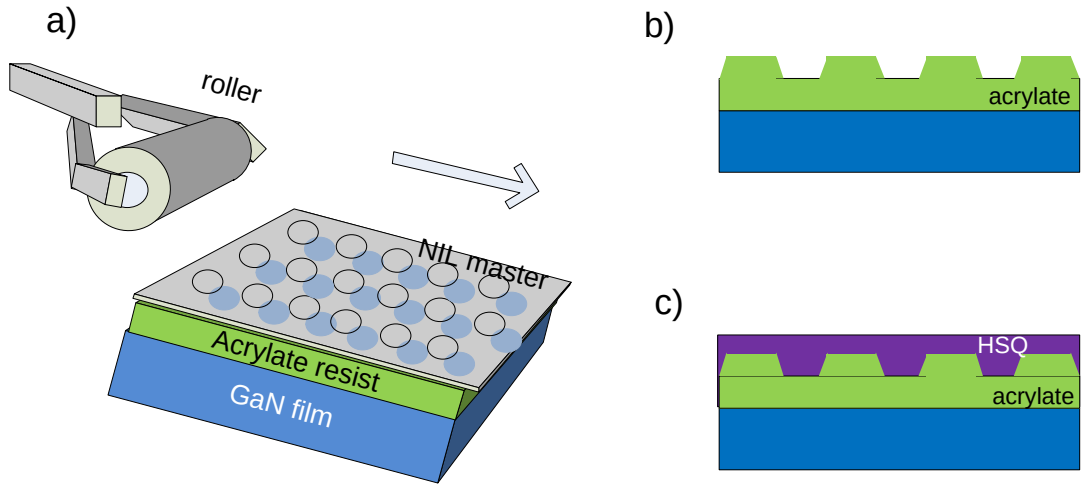

Figure 2-1: NIL process: a) The acrylate was spin coated onto GaN film and impressed with a NIL master by mechanical deformation of the resist. b) the acrylate undergoes cross-linking under 1 minute UV and the master was removed c) planarization with HSQ and thermal curing

2.1.3 Induction coupled plasma etching

Induction coupled plasma etching (ICP) is a highly directional and anisotropic dry etching method widely used in semiconductor processing. The etching is achieved mainly by chemical reactions from reactive fluorine and chlorine atoms or molecules, called radicals, generated by breaking the chemical bonds of the trifluoromethane (CHF_3) or Cl_2 gasses introduced into the plasma chamber when the potential discharge is turned on. Physical sputtering with energetic Ar ions also play a role, however, the density and lifetime of radicals are higher than for ions, as breaking the bonds requires lower energies than accelerating ions, therefore the chemical process has prevalence.

The stages of etching are summarized in Figure 2-2. First, the plasma discharge dissociates the etching gas molecules by impact with electrons accelerated by the plasma. CF_4 or CHF_3 gasses dissociate resulting in a fluorine radical and an electron. The second step involves diffusion of the radicals to the sample surface where they are adsorbed (step 3). Complex chemical reactions take place at the sample surface (step 4) which result in volatile reaction products. Step 5 involves the desorption of reaction products from the sample surface. This step can be enhanced by physical sputtering

with Ar ions and controlling the temperature of the sample. Last, the reaction products are diffused into the chamber gas volume. By-products occurring in the chamber are expelled by the pumping system.

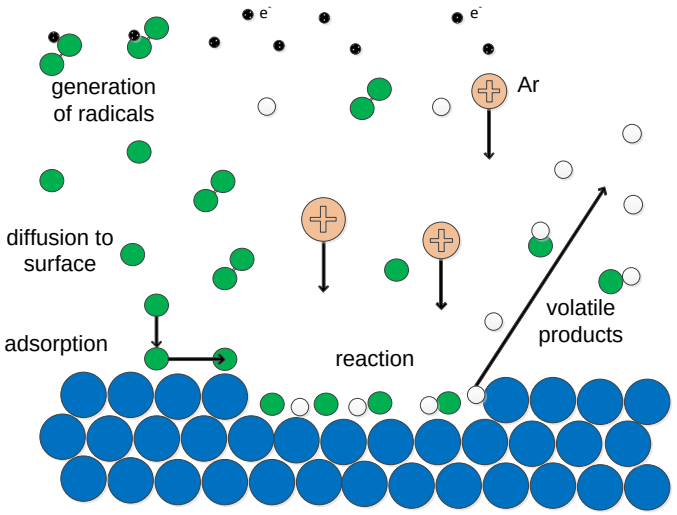

Figure 2-2: Plasma etching is both a chemical and a physical process. Radicals react at the an exposed sample surface and energetic ions remove the volatile chemical reaction products.

Etch profiles

Etching profiles are shown in Figure 2-3 for chemical a) and dry plasma b-d) etching. Chemical etching results in an isotropic and hard to control lateral profile. In dry plasma a highly directional profile can be achieved even for a purely physical sputtering process by Ar ions in Figure 2-3 b), however, angled facets can also be seen at the bottom of the profile.

If the etch is a combination of chemical and physical processes at low pressure and high power the sidewalls obtained can be vertical due to the radicals driven process in Figure 2-3 d). Plasma etching by a low power setting and relatively higher pressure can produce a more isotropic profile and an undercut (see Figure 2-3 c) if desired. Verticality can also be maintained if an etch is done in with a low ratio of fluorine to carbon atoms in the chamber for fluorine based processes. In this case, a polymer layer is deposited on the sidewalls inhibiting further etching. However, this involves a further step of removing the polymers in a strong acid.

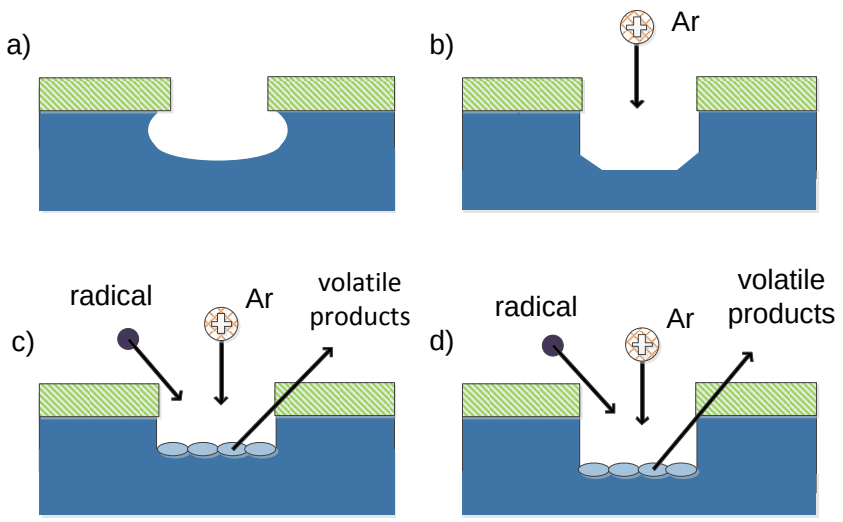

Figure 2-3: Typical etching profiles achieved with a) chemical wet etch produces a difficult to control undercut, b) plasma etch with Ar-only is similar to sputtering, leaving side edges, c) RIE for which both ions and radicals are acting to etch the sample, d) ICP etching with higher selectivity and etch rates compared to RIE.

Induction coupled plasma equipment

In Figure 2-4 the construction of the Oxford Plasma Pro System 100 Cobra, induction coupled plasma (ICP) system used in this work, is shown. A capacitively coupled plasma source is an improvement on a reactive-ion etching (RIE) chamber, by application of an additional radio frequency (RF) source. In an RIE chamber, the plasma consists of a top and a bottom electrode between which a potential difference controlled by a radio frequency source operating at 13.56 MHz applies a fast alternating current to accelerate the low mass gas electrons and increases their kinetic energy. Inelastic collisions between the accelerated electrons and the heavy, slow gas atoms generate ions, electrically neutral radicals, and additional electrons as well. The radicals are chemically reactive with the sample surface and are responsible for the effective chemical etching and volatile products on the sample surface. The sample was placed on the bottom electrode, the cathode, where most of the acceleration of ions and voltage drop or V_{bias} occurs. The plasma discharge observed in the chamber is due to relaxation to lower energy levels of energized electrons. The etch depth and anisotropy is limited (Figure 2-3 c), as high forward power has to be used to improve directionality, but highly energetic Ar ions can damage the device being fabricated.

An improvement on the process involves using a second RF source for an ICP etcher. In Figure 2-4 this source can be seen as a coil wrapped around the RIE region, which generates a magnetic field to impart a helical motion to the electrons in the plasma. This ICP configuration can separate control on ICP power, and achieve a dramatically higher density plasma at relatively low RIE ion energy forward power. The ICP process increases the etch rate by dissociating the chamber gasses into a higher number of radicals and more electrons. The ICP process flexibility results in precise etch profiles (Figure 2-3d) with higher selectivity than in RIE.

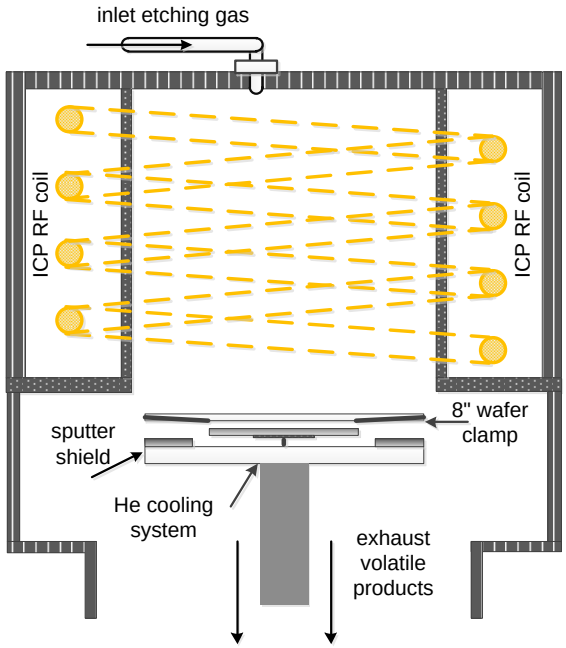

Figure 2-4: ICP chamber. Samples up to 8" in diameter can be mounted on the helium cooled holder. Two separate RF sources apply separate forward power for RIE and ICP make this type of plasma etching highly versatile.

Etching temperature is the parameter with the highest effect on directionality, generally higher temperatures are used to obtain deep vertical sidewalls. Chamber pressure influences the ion density and ion directionality, typically 9 mTorr was used to maintain a stable plasma. At low pressure, a longer mean free path between collisions means better directionality, but also implies a reduction in selectivity. Selectivity is defined as the ratio of target material etch rate, relative to the rates of the other materials being etched.

Etching resists

One of the advantages of plasma etching is the selective chemistry of different resists used. The HSQ resist is susceptible to CHF_3 plasma while the acrylate resist layer appears unaffected. Partial etching of the HSQ layer was done to expose some of the acrylate top structure, without removing all the HSQ as seen in Figure 2-5 b). A subsequent 2-minute oxygen RIE plasma was used to remove the exposed acrylate resist without affecting the HSQ (Figure 2-5 c)). In this step, a layer of acrylate or acrylate pillars must remain to support the remaining HSQ. This process creates a regular network of holes in the resists to expose the GaN surface between HSQ-on-acrylate pillars for a follow-up metal deposition step.

Metal mask

A metal mask of gold and nickel (10 nm Au, $150-200$ nm Ni) was deposited by electron beam evaporation to place metal dots on the GaN surface. An electron beam is used to heat the metal placed in a crucible to evaporation temperatures. At 6×10^{-6}mbar chamber pressure the metal atoms evaporated from the crucible will reach the surface of the sample on which the atoms condensate. The sample was mounted on a rotating holder to improve deposition homogeneity.

The mainly Ni metal mask requires an intermediary thin Au layer on GaN, as complexes formed at the Ni-GaN interface can inhibit MOVPE regrowth, even after complete metal mask removal. The metal mask was left to cool down for 15 minutes in the evaporator chamber to prevent oxidation and delamination. A lift-off step in hydrofluoric acid (HF) attacked and removed the HSQ. The acrylate pillars were removed by 2 minutes mild oxygen plasma, leaving the GaN film covered in a hexagonal array of metal dots to mask (Figure 2-5 e) and Figure 2-6 a)).

GaN nanorod etching

ICP etching is a chemical process as well as a physical process. For GaN etching a Cl_2/Ar gas mixture was used, with a ratio of 50/10 standard cubic centimeters per minute (sccm). Chlorine is a strong oxidizing agent and reacts on the surface of the GaN. Ar ions increase the energetic ion bombardment, physically removing polymers and volatile compounds formed at the sample surface and enhancing etch anisotropy.

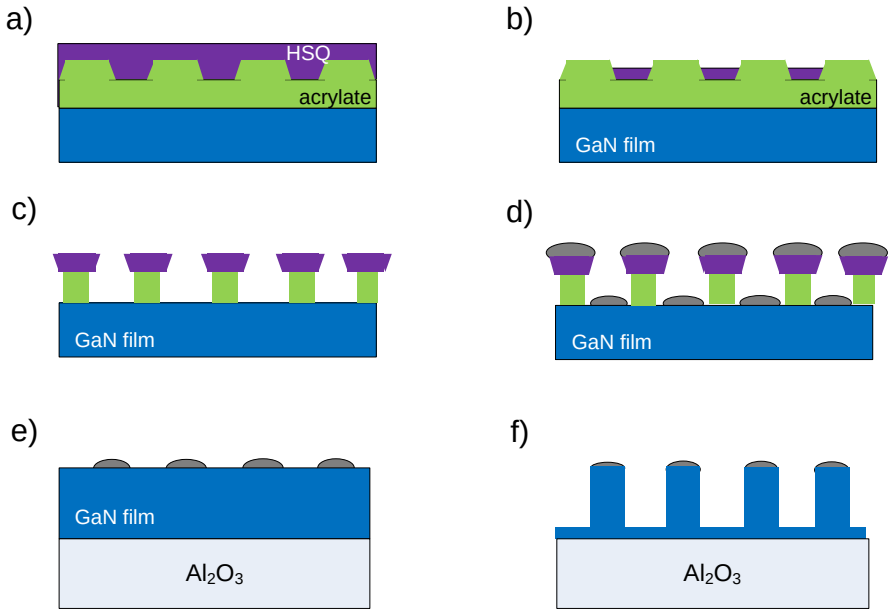

Figure 2-5: Nanorod template a) two layer resist of acrylate and HSQ, b) partial removal of HSQ to expose the acrylate, c) O_2 plasma removes the acrylate, d) Au/Ni metal deposition with the e-beam evaporator, e) Metal mask dot array after metal lift-off in BOE HF and mild O_2 plasma to remove HSQ and acrylate respectively, f) GaN cores after plasma etching with an underlying continous GaN for current conduction.

The metal mask [1] provides a good selectivity for GaN etching [125]. Furthermore, etching GaN at high temperature (150 ℃) improved the verticality of the nanorods and produced a vertical sidewall in Figures 2-5 f) and 2-6 b) [18]. Achieving a vertical sidewall is highly important as re-growth on tapered sidewalls would result in crystal facets different than the *m*-plane. The pressure of the etching process was 9 mTorr. After etching, the remaining metal mask was removed in 1:3 (HNO_3:HCl) aqua regia solution. The various etch processes are summarized in Table 2.1.

Alternating sequences of etching and cool-down of 1 minute each were used. The sequence resulted from the optimization of the etch rate. It was observed that continuous etching would lead to a variable etch rate and loss of sidewall verticality, due to the local temperature increase at the etch site. During the cool-down, only the plasma gases are pumped into the chamber, without striking the plasma. A GaN film of 4

[1] Reprinted from Shields, P. A. , Allsopp, D. W. E.,"Nanoimprint lithography resist profile inversion for lift-off applications",*Microelectron. Eng.* 88, 3011–3014 (2011), with permission from Elsevier, doi.org/10.1016/j.mee.2011.04.063.

Table 2.1: Plasma etch parameters.

Material	Press.(mTorr)	Temp. (°C)	ICP(W)	RIE(W)	Gas(sccm)	Rate (nm/min)
Acrylate	10	20	0	125	O_2 25	∼300
HSQ	10	20	300	50	CHF_3 25	50
GaN	9	150	800	120	Cl_2:Ar 50 : 10	∼450

µm thickness was typically etched in 8 cycles of etch/cool-down. As an indicator of reproducibility, a stable DC bias from sample to sample or from cycle to cycle was used to verify the etching. A key advantage of top-down plasma etching is that the NR diameters obtained are highly uniform[2], even on large 4 or 6-inch wafers [125, 102].

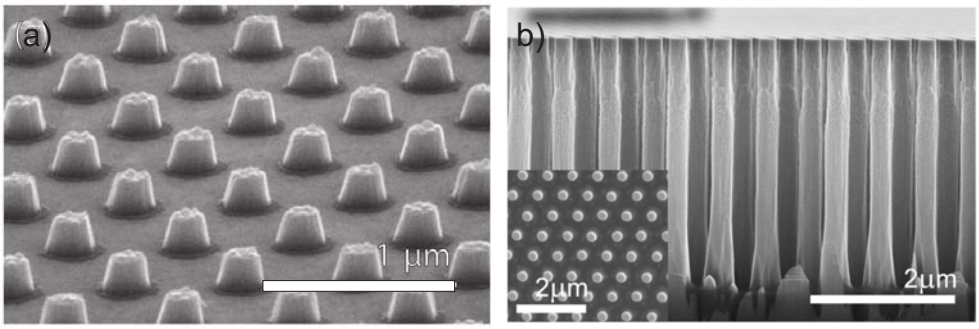

Figure 2-6: Metal nanodots mask on GaN film, b) ICP etched tall NRs with vertical sidewalls (reprinted from refs. [125, 102] with the permission of Elsevier and AIP publishing).

2.1.4 Electron beam lithography

An alternate patterning method used was electron beam lithography (EBL) for which a resist is exposed and patterned by the electron beam in the SEM. This method has a significant advantage in that it is highly customizable because different pattern periodicity and different diameters can be obtained on the same sample. However, it also has limitations as it is very time-consuming and the patterns produced to cover a small area. It is thus a great research tool, but with reduced practical use if high output is desired. The Hitachi S-4300 scanning electron microscope with a thermal field emission electron gun and Elphy nanolithography stage were used to obtain a range of patterns for resist hole diameters of 200, 300, 400 and 500 nm and pitches of 500, 1000,

[2]Reprinted from Le Boulbar, E. D., Gîrgel, I., Lewins, C. J., Edwards, P. R. Martin, R. W., Šatka, A., Allsopp, D. W. E. Shields, P. A., "Facet recovery and light emission from GaN/InGaN/GaN core-shell structures grown by metal organic vapour phase epitaxy on etched GaN nanorod arrays", *J. Appl. Phys. 114*, 94302 (2013), with the permission of AIP publishing.

1500 and 2000 nm. By optimizing the resist system and beam energy dosage, the EBL features can be reduced to $\sim 10-50$ nm if high-resolution HSQ resist is used [126, 127]. In this work, I used EBL on a two resist system of a low molecular weight methyl methacrylate (MMA) polymer and a higher molecular weight poly-methyl methacrylate (PMMA). The lower molecular weight MMA is more sensitive to the e-beam than the PMMA, therefore the MMA resist develops with an enhanced undercut to create a lift-off profile. The MMA was spin-coated first at 2500 rpm for 1 minute, with a heat cure on the hot-plate of 1 minute at 150℃ to obtain a $500-700$ nm layer thickness. The PMMA was then spin-coated on top of the MMA, at the same parameters, with a change in the curing temperature of 180 ℃, for a thickness of $200-250$ nm per layer. On top of the resists prior to exposure, a thin $5-10$ nm of Al layer was deposited by e-beam evaporation. The Al layer limits sample charging and improves exposure uniformity.

The MMA/PPMA system was exposed by the electron beam of the SEM. The exposure dose from the SEM was measured by running a current through the Faraday cup on the SEM holder with an ammeter measuring the current. It is important to avoid accidental resist system exposure by the electron beam. Therefore most of the initial focus and alignment corrections need to be done at the edges of the sample. A write-field correction was critical in achieving uniform patterns, with reproducible size features across the sample, especially as for write-field stitching was required. Exposure parameters such as area dose and beam current were identified. Each feature was exposed and written one at a time, making the method time consuming. The stage was moved, then a settle down period reduced the stage oscillations and a new feature was exposed.

After the resist was exposed the Al layer was removed in a H_3PO_4:HNO_3:H_2O wet etch. The MMA/PMMA was developed in a 1:3 methyl-isobutyl-ketone: isopropyl alcohol (MIBK:IPA) solution for 1 minute. The samples underwent a deposition of Au/Ni metal mask deposition in the e-beam evaporator, similar to the process described previously. Finally, a bath in acetone removed the MMA/PMMA resists to obtain a metal dots array on the GaN film. These processes created the lift-off profile similar to the NIL method. The mask was used to plasma etch GaN NRs as described.

2.1.5 Direct laser mask writer

An alternative to the NIL method was the PG101 375 nm laser (18 mW power) mask writer used to create patterns for etching and for metal contacts in electrically driven

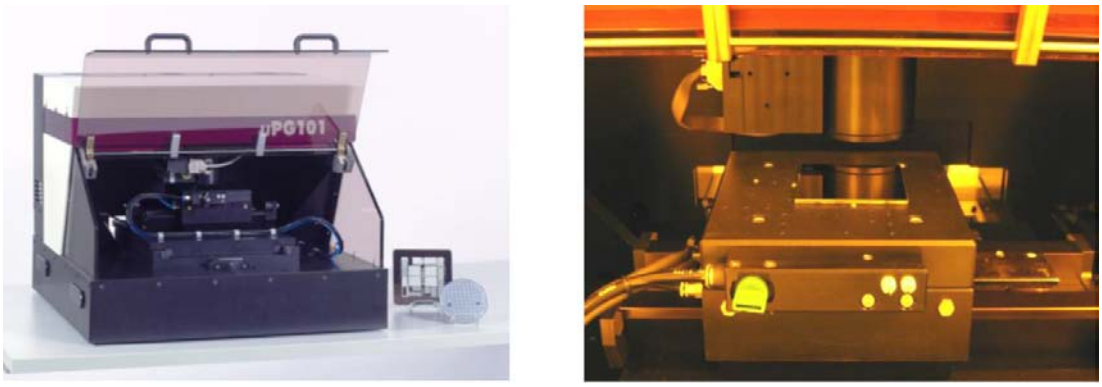

Figure 2-7: Heidelberg µPG101 tabletop laser micro-pattern writer

core-shell LEDs. This method has the advantages of speed and high output, however at a lower resolution as the minimum size of the features is 1 µm. The AZ n-LOF 2 µm negative resist was cured for 2 minutes on the hot-plate and exposed by the laser beam to obtain a lift-off profile. A power series was optimized to obtain the best dose (30%) for well-developed features. The resist was then post-baked for 1 minute and developed for 70 seconds in MIF 826 solution. An Au/Ni layer was deposited in the e-beam evaporator. After the metal deposition cool-down the samples were put in a Microposit 1165 stripper solution at 60 ℃ warm bath for 5 minutes for the metal lift-off process.

2.1.6 MOVPE re-growth

Metal-organic vapour phase epitaxy (MOVPE) is the crystal growth process by which the core-shell structures were obtained. MOVPE technology and reactors are largely used in the electronics and optoelectronics industries to obtain III-V compounds with precisely controlled layer thickness to obtain specific optical and electrical properties. The desired atom species are chemically bonded to complex organic liquid precursors. To obtain GaN crystals the precursor sources are trimethyl-gallium $Ga(CH_3)_3$ (TMGa) and ammonia (NH_3). A purified carrier gas, hydrogen, nitrogen or a mixture of the two, *bubbles* through the liquid carrying precursor molecules towards the reaction chamber.

The Aixtron 200 MOVPE reactor in this work is a horizontal-bed reactor (Figure 2-8) with a 2-inch susceptor on which a sample wafer can be mounted. All the recipes were made and run with the Aixtron software. The high temperature ($800 - 1050$ ℃) in the chamber breaks down the precursors and the Ga and N atoms react on the substrate surface. Nuclei are formed when a critical amount of molecules remain on

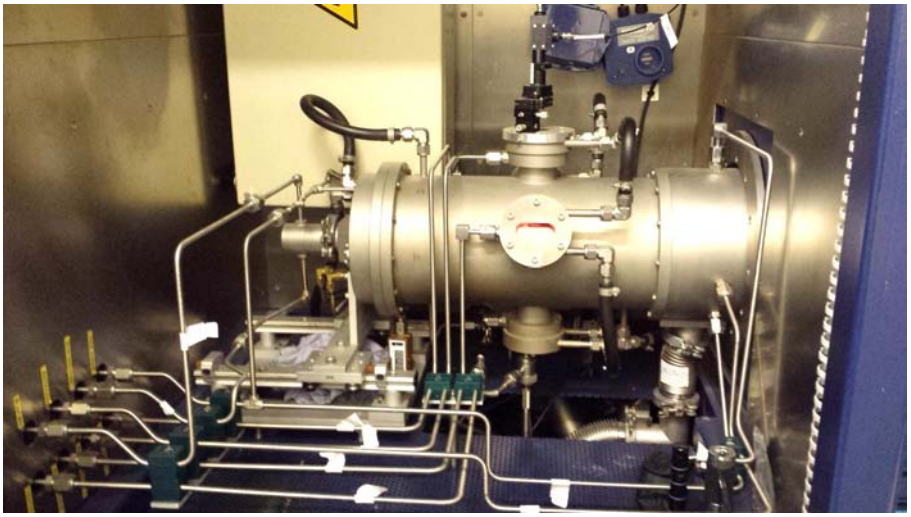

Figure 2-8: MOVPE flatbed Aixtron 200 reactor used in the work.

the substrate surface. A wetting layer is formed and further adatom adsorption grows the GaN crystal layer by layer. The reactor pressures used were from low $50-300$ mbar to 500 mbar, in the case of p-GaN in situ annealing. Changes in precursors gas flows and growth parameters such as temperature, pressure and time affect the properties of the crystal on the atomic scale. For a more comprehensive discussion on GaN growth please see refs [23, 26, 30].

In this work GaN nanorods were obtained by plasma etching an existing GaN film. The etched GaN cores are used as a template for the growth of successive layers of InGaN/GaN semiconductor shells, this succession making it a core-shell structure. After plasma etching, the remaining metal mask was removed in aqua regia solution. During etching the GaN NR accumulate temperature resilient polymers on the NRs surface which inhibit MOVPE growth and could result in parasitic growth, therefore the samples were cleaned. The clean consists of a 1 minute soak in buffered oxide etchant (BOE 5:1), based on a mixture of 5 parts 40% ammonium fluoride (NH_4F) and 1 part dilute 49% HF.

Passivation at the bottom of the GaN NR is necessary for controllable growth and electric current path insulation. During MOVPE growth the 3D structure of NR will adsorb Ga and N atoms from the gas phase on all the surfaces. To prevent growth between the NR bases, a spin-on-glass (SOG) solution, Dow Corning XR1541 HSQ, was applied on the NRs as shown in Figure 2-9 a). After spinning, at the NRs base a thicker HSQ layer was obtained, than on the sidewalls because of the HSQ viscosity.

A gradual hot-plate treatment from 150 to 450 ℃ and back for $\sim$ 30 min and 10 min respectively, was used to cure and harden the HSQ. Another curing for 2 hours under a nitrogen atmosphere at 550 ℃ in a horizontal tube furnace further hardened the HSQ. The heat curing was necessary to obtain a controlled HSQ etching rate for a follow-up BOE 100:1 etches to approximately 10 nm/min. As the sidewalls are covered with a thinner layer than the base area, a $\sim$ 30 seconds etch cleared the passivation layer from the sidewalls, but maintained $\sim$200 nm of HSQ at the NR's base as displayed in Figure 2-9 b).

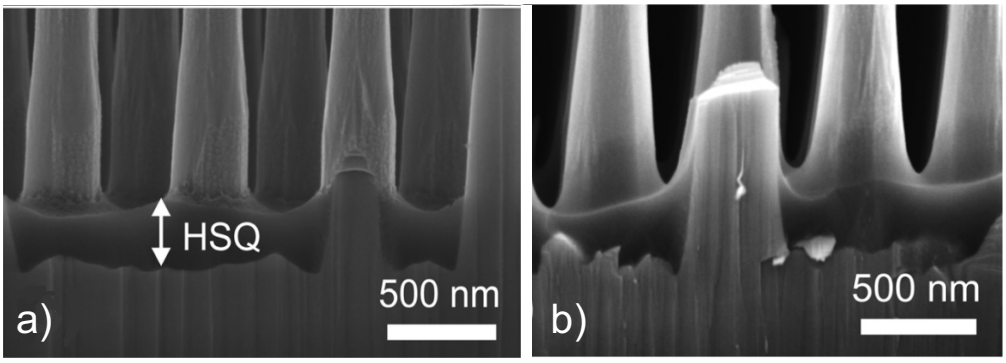

Figure 2-9: a) HSQ passivation layer covers the NRs base and sidewalls, b) after 30s BOE 100:1 etch the HSQ was removed from the sidewalls and maintaind at the NRs base as seen in the different contrast between base and rods (reprinted from ref. [102] with permission from AIP Publishing).

Passivation occurs naturally on the Si substrates for which the GaN was etched completely to the substrate. The Si surfaces react in NH_3 atmosphere and high temperature to form SiN_x in the MOVPE chamber, which inhibits growth from the base of the NRs. Diagram 2-10 shows the epitaxy steps for core-shell NRs. The facet recovery was optimized by Dr. Emmanuel Le Boulbar in ref [102]. Using the new 2 µm template, the facet recovery and subsequent epitaxy steps: active area region growth, p-GaN and annealing were implemented and optimized by myself.

The GaN regrowth step recovers the hexagonal crystal structure and repairs surface damage on the cylindrical etched NRs. This facet recovery step was carried out at $900-950$ ℃ without doping. Different regrowth times from 4 to 15 minutes have been used to obtain a different thickness of GaN sidewall. The uniformity with and without passivation is discussed in the results section 3.3. Detail discussion on the parameters for the different core-shell layers is given in section 6.1.

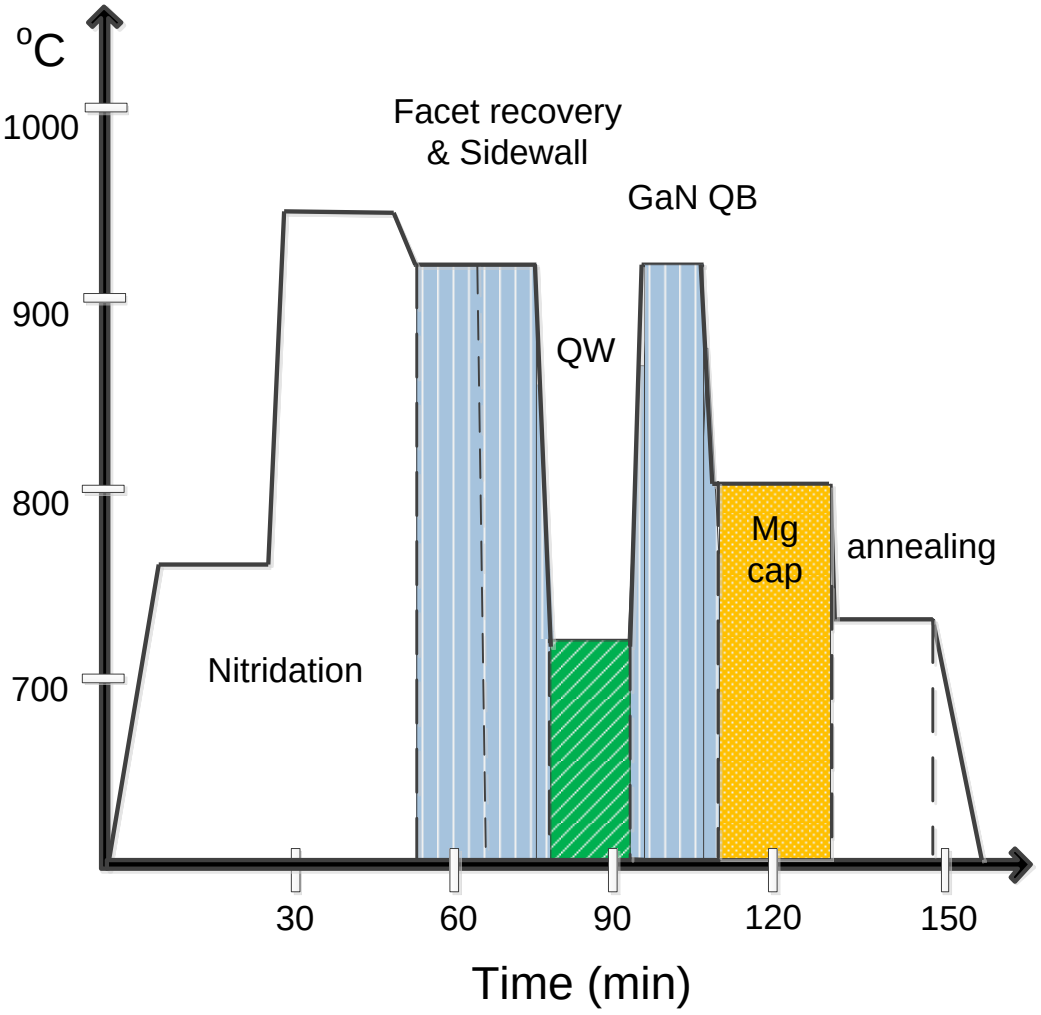

Figure 2-10: Outline of the main growth stages inside the MOVPE reactor. The GaN growth is 16 min, InGaN/GaN QW/QB are grown for 6 minutes, p-GaN and annealing for 40 and 20 min respectively (not drawn to scale).

2.1.7 Core-shell structure

A schematic of a core-shell structure is shown in Figure 2-11. A sequence of MOVPE growths at different reactor parameters are necessary to obtain the structure starting with the etched GaN core. The growth steps on the etched template were accomplished during the same reactor growth run, without removal of the sample.

Because the GaN cores were already n-doped, there was no need for further n-doping with silane. The MOVPE facet recovery step was done to repair etch damage and provide a dimensionally uniform hexagonal facets. Most of the samples were In-

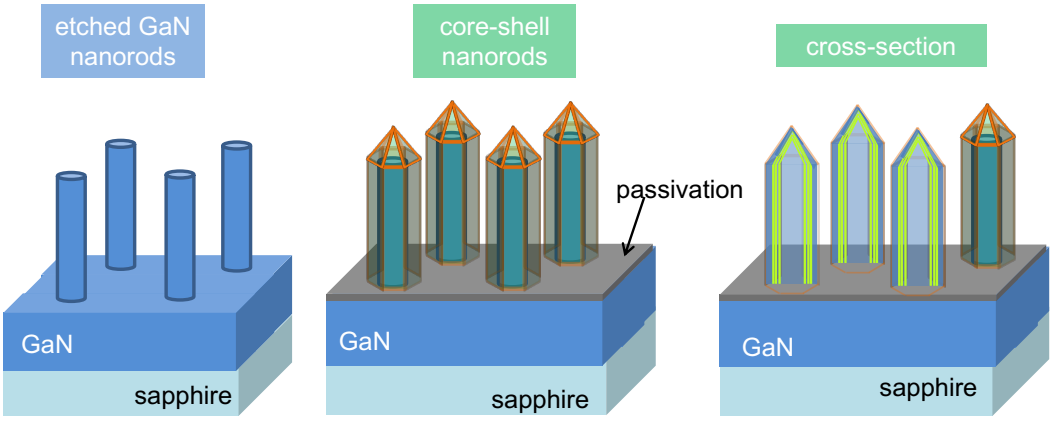

Figure 2-11: Core-shell structure obtained from etched GaN cores and regrowth on passivated GaN. A cross-section through NRs shows multiple quantum wells (MQW) covered by a p-GaN cap layer.

GaN/GaN SQW. The precursor used for indium was trimethyl-indium (TMIn). For MQWs the same process used for SQW was repeated. Because the InN fraction is much reduced at temperatures above 800 ℃ the switch between growth temperatures of GaN and InGaN has to be done carefully. For the InGaN, the temperatures are reduced and gas flows are stabilized before precursor injection into the growth chamber. For the GaN barrier, the TMIn flow is stopped and the temperature is raised gradually under a flow of TMGa and NH_3 up to the normal GaN growth temperature. The QB layers were typically grown for $6 - 10$ minutes. Finally, a cap layer p-GaN layer doped with Mg atoms using bis(cyclopentadienyl)magnesium (Cp_2Mg) precursor provides hole carriers for the core-shell structure. These structures were then used for planarization with HSQ and deposition of metal contacts.

A series of Mg-doped GaN were grown as a homojunction on the GaN template and on core-shell LEDs, to investigate p-type doping properties on NR. P-type doping is difficult, as less than 1% of Mg atoms can be activated at room temperature to provide active hole carriers [111]. The activation was done by annealing in the growth reactor for a period of 20 minutes at 720 ℃ under a nitrogen atmosphere.

2.1.8 ITO and contacts

Indium tin oxide (ITO) was deposited to obtain a uniform current spreading layer on the nanorods. The deposition was done with the e-beam evaporator on NR samples mounted in the chamber at an angle, to cover uniformly the m-plane sidewalls as seen

in Figure 2-12. The $75 - 120$ nm ITO layer on the NRs required annealing to obtain transparent and conductive films. Effective annealing was achieved on a hot plate ($300 - 350$ ℃) in air atmosphere for 5 minutes.

A single Fox 25 (thick HSQ) layer, was spin coated to infill the NRs and to planarize the core-shell NR structure. The HSQ covers the NR slightly above their tip. The spin parameters used were 2000 rpm for 1 minute, with a hot-plate baking of 1 minute at 200 ℃. The layers were exposed to CHF_3 plasma to back-etch the HSQ from the NR tips, however, this step likely may have damaged the conductivity of a set of samples, although the ITO layer covering the NRs did not seem to suffer any physical damage in the SE images. Instead a short BOE 100:1 HSQ dielectric back etch is recommended, avoiding a plasma process.

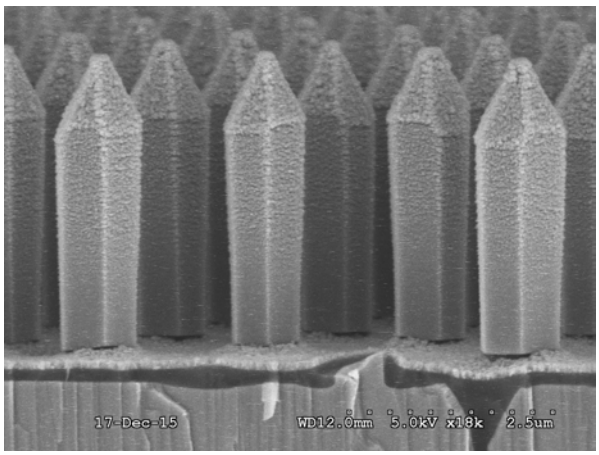

Figure 2-12: NRs covered by angled ITO deposition.

A second ITO deposition of 300 nm thickness was accomplished on the planarized structure to connect the arrays of NRs. Metal contacts for the p-type and n-type in a structure of Ti/Al/Ni/Au were deposited using the e-beam evaporator. Additional information on processing is provided in Chapter 6.

The intermediary steps towards the core-shell LED and the electrically driven device were characterized with a large array of tools specific for semiconductors as discussed in the next section.

2.2 Characterization tools

2.2.1 Scanning electron microscope

The scanning electron microscope (SEM) is widely used in semiconductor fabrication to verify dimensional characteristics. For this work, a large part of the planar SEM images was used together with the National Instruments Vision Assistant software to measure and extract statistical data on the uniformity of nanorod diameters for the series of growths performed. Typically this software is used for automated optical inspection of mechanical or electronic components. All the image collection was done using a Hitachi S4300 thermionic SEM at the same magnification (6000 $\times$), and were processed in Vision Assistant with identical settings for all images. The images were captured in secondary electron (SE) mode from planar view at 5 kV accelerating voltage to obtain low penetration into the samples and to increase contrast at small edges for high resolution necessary for image processing. The image size was 16×21.3 μm^2, identifying approximately $\sim$ 1000 NRs per image on 0.6 µm pitch samples and 80-90 NRs per image in the 2 µm sample sets, sufficient to extract statistically meaningful conclusions about the evolution of NR diameter for the different growths.

The algorithm for image processing identified edge outlines on the NR diameters which were overlayed on the initial SE image to verify the algorithm's accuracy. The steps programmed into Vision Assistant and their effects in succession can be seen in Figure 2-13: pixel calibration to real word units, thresholding, application of a low-pass smoothing filter on the NRs, removing incomplete NRs at image borders, object dilation/erosion to 'close' the outline of the objects and finally extract the NR outline. The threshold uses a set grey intensity limit to assign a value of 1 or 0 for the individual pixels in the image, transforming the SEM image into a binary image and identifying individual NRs. The threshold and smoothing filter particle size were the most sensitive parameters of the method and their change can cause differences in measurement values of $\pm$10 nm, for which it was reasoned to maintain the algorithm for individual series of growths.

Additional SEM systems were used by our collaborators at the University of Strathclyde and the Slovak University of Technology, equipped with other characterization tools, namely cathodoluminescence and electron-beam-induced current probes, which are described in the following sections. Electron beam lithography on the Hitachi Bath system was also used for patterning experiments.

The method described above demonstrated sample characteristic information can be

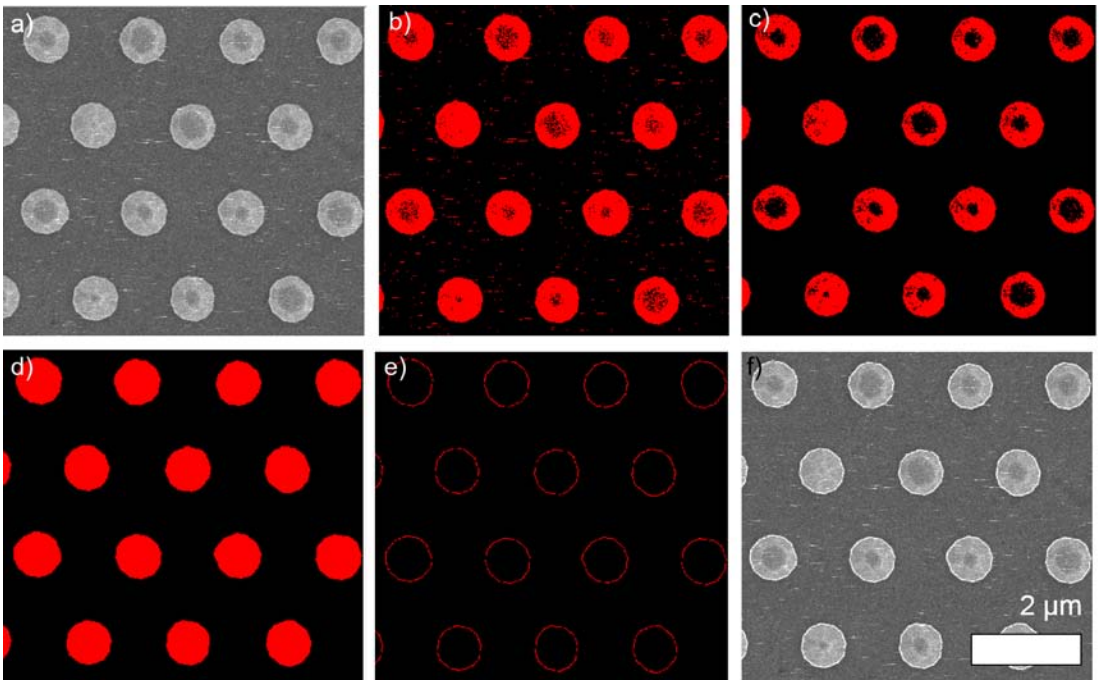

Figure 2-13: a) cropped SE image, a full image contains over 80 NRs, b) a threshold to the SE grey intensity transforms the SE into a binary image, c) application of a low band pass filter improves contrast at the NR edges, d) dilation, erosion and fill of NR interiors, e)extract the gradient or outline at the NR edges, f) overlay of diameter outline and NR SE image to verify accuracy of algorithm.

reliably extracted from planar SEM images on a large number of NRs.

2.2.2 Atomic force microscopy

Atomic force microscopy (AFM) is used to obtain high-resolution topography images of surfaces in a wide range of applications from microelectronics to medicine. For GaN NRs AFM analysis can reveal information about the uniformity of the nanorod template for core-shell structures as it is important for device manufacture. Subnanometer AFM resolution reveals new light on the quality of regrown surfaces and growth mechanisms. The equipment used was a Digital Instruments Nanoscope IIIA, a standard configuration AFM.

Figure 2-14 shows a typical AFM setup with a sharp tip on the end of a flexible cantilever scanning a fixed sample surface in a raster motion. A laser beam is focused on the back of the reflective cantilever. The beam is reflected back onto a photodetector that records the change in intensity of the laser beam caused by cantilever deflection

due to surface changes. The variations in intensity reproduce the topography features of the sample. The tip height relative to the sample and the oscillations of the cantilever is constantly corrected by a proportional–integral–derivative (PID) feedback loop. The feedback gains need to be high enough so that the Trace and Retrace scans correspond to each other for an accurate mapping.

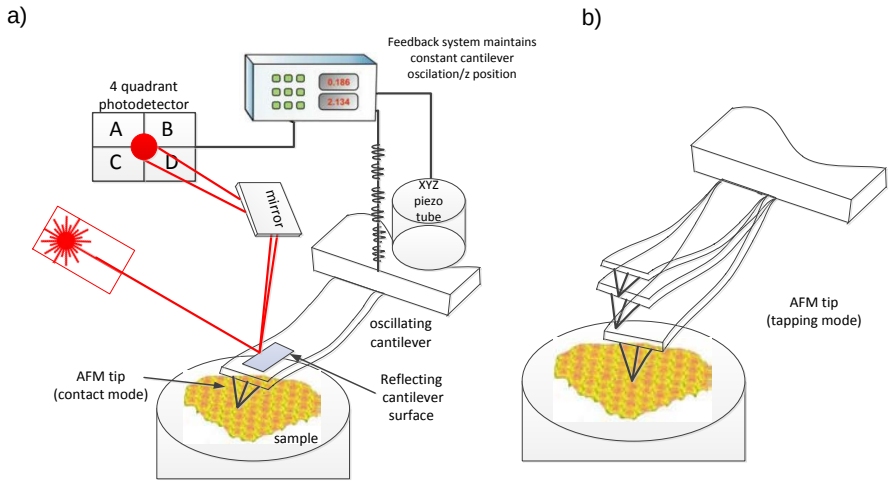

Figure 2-14: Schematic of typical AFM construction and operation in a) AFM in contact mode moving on the sample surface, b) the tip is mechanically oscillated near its resonance frequency to maintain the cantilever amplitude or phase setpoint.

Two imaging modes were used for the AFM analysis on NRs, contact mode, and tapping mode to obtain topography information about the NR heights and sidewalls respectively. In contact mode, a standard tip (Bruker MPP-11100-10 with tip radius 10 nm) is dragged on the sample surface while the feedback loop maintains a constant force between tip and sample. The height of the NRs and lateral deflections are used to map the sample surface. For tapping mode, the cantilever was oscillated causing the (Tap300-G) tip to probe without continuous contact the NR sidewalls and the changes in frequency and amplitude were monitored by the feedback loop to maintain the tip-sample interaction constant. Data processing of the scans was done with Gwyddion and Matlab software.

2.2.3 Scanning Transmission Electron Microscopy

Image contrast in transmission electron microscopy (TEM) for GaN crystalline samples is determined by the diffraction contrast of an energetic electron beam transmitted

through a thin sample. Changes in intensity of the TEM image are due to changes in the crystal orientation relative to the electron beam, or in local variations caused by crystal defects and sample thickness changes. In the bright-field (BF) imaging mode, an aperture is placed in the back focal plane of the objective lens which allows only the direct beam to pass. Thinner areas and lighter atoms areas appear with bright contrast while thicker areas and heavy atoms attenuate the beam and appear darker. In dark-field (DF) images, the direct beam is blocked by the aperture and only the strongly interacting diffracted beams pass towards the objective aperture, providing information on potential defects and stacking faults.

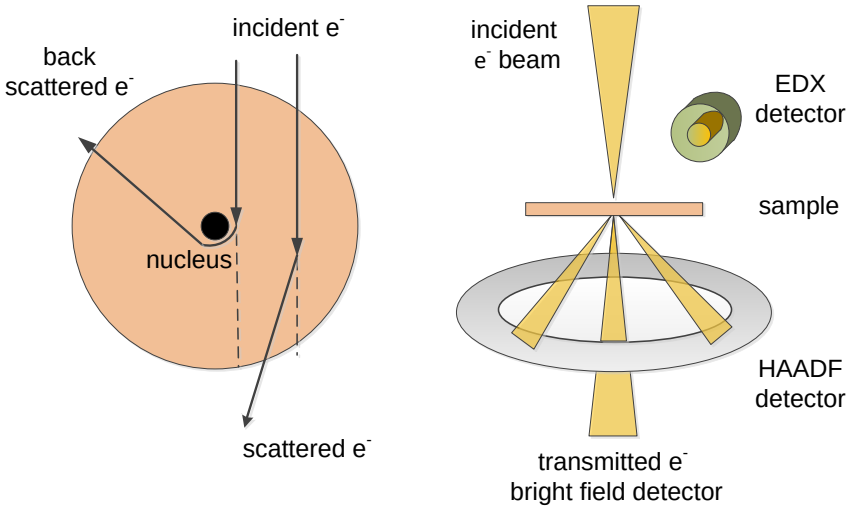

Figure 2-15: a) elastic electron scattering by Coulomb interaction b)HAADF detector

In scanning transmission electron microscopy (STEM) the strong Coulomb interaction of electrons with the positive charge of the atom core, causes deflection to the electrons path, leading to high angle scattering (Rutherford scattering). Capture of these electrons by a high-angular-annular-dark-field (HAADF) detector are used in STEM imaging (Figure 2-15). An advantage of HAADF mode is its chemical sensitivity under certain collection angles and providing corresponding Z-contrast information. A narrow electron beam is focused into a narrow 2 nm spot which is scanned over the sample in a raster motion similar to SEM. Energy dispersive X-ray spectrometry (EDX) measurements with high composition sensitivity can be made at the same time allowing for direct correlation of image and alloying quantitative data. EDX makes use of the characteristic X-ray spectrum emitted by a sample bombarded with the focused electron

beam to obtain a localized chemical analysis.

Sample preparation for planar and side view cross sections was done using the focused ion beam (FIB) method to thin down the cross sections to $100 - 200$ nm thickness with a Si ion 30 kV beam down. The sample preparation was done at the University of Leeds by Dr. Michael Ward and Dr. Pierre-Marrie Coulon. The STEM analysis was carried out at the University of Cambridge by Dr. Lata-Suman Sahonta. A Tecnai Osiris STEM operating at 200 kV was used, with high-angle HAADF Z-contrast images showing regions of high indium content in brighter contrast.

2.2.4 Photoluminescence and micro-photoluminescence

Photoluminescence and micro-photoluminescence (μ-PL) are widely used tools in semiconductors study, providing information on bandgap, doping, impurities, and defects. A laser beam with energy higher than the bandgap of GaN excites electrons from the valence band to the conduction band and electron-hole pairs are generated. The recombination of electron-hole pairs can occur non-radiatively by phonon emission or with light emission, at a signature wavelength for the semiconductors or alloys studied. PL measurements offer a fine control over the excitation densities.

A Renishaw inVia μPL spectrometer was used with a 325 nm laser source and a 2400 lines/mm grating. Measurements were typically carried out with an optical power $\sim$ 0.135 mW to obtain a good signal to noise ratio and avoid CCD saturation. The 40×, 0.5 NA objective provided a spot size of 0.8 μm. A second 405 nm conventional PL system for which the emission was captured and analyzed with a 600 lines/mm grating spectrometer was used for quick assessment of InN fraction and to compare PL with EL signal in Chapter 6. All measurements were carried out at room temperature.

2.2.5 Cathodoluminescence

Materials under exposure from an energetic electron beam absorb an amount of energy through inelastic collisions. The transferred energy can produce backscattered electrons, low energy secondary electrons, Auger electrons, X-rays, phonons, photons, an electron beam induced current (EBIC), information which can be quantified by a variety of detectors, as shown in Figure 2-16. The primary electrons are highly energetic and get scattered several times inside the crystal before they lose their energy or are scattered back from the crystal. The energy of X-rays and Auger electrons is still high, therefore they contribute to re-scattering and toward the secondary electron

population. The lower energies of the secondary electrons ($2 - 50$ eV) are responsible for the transfer of their excess energy to electrons in the valence band. Once an electron from the valence band is promoted, it leaves in its place an uncompensated positive charge or a positive 'hole'. Photon generation and light emission occur for radiative recombination of electrons-hole pairs.

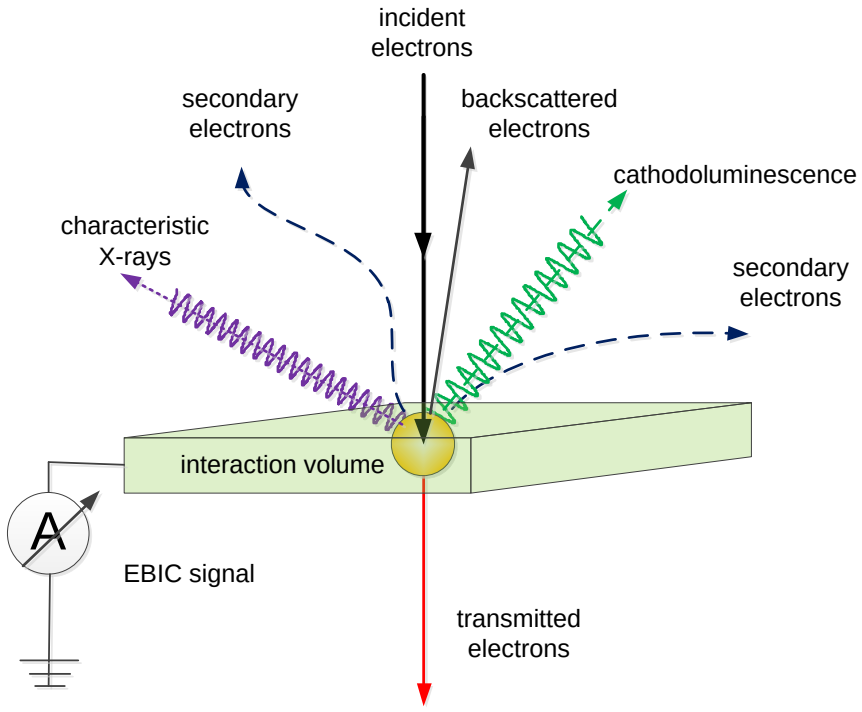

Figure 2-16: Information obtainable from the electron-beam and specimen interaction.

Light emission occurring due to e-beam stimulation is called cathodoluminescence (CL). Although the CL method offers less control over the excitation densities and less spectral resolution than PL, because of high excitation densities, the main advantage is the higher resolution and correlation between the scanned sample surface and emitted spectra. The CL emission is collected to obtain important information on the semiconductor such as alloy fraction, strain, crystal orientation, defects, doping and free carrier concentration. Defects can be identified from sudden changes in contrast in a CL map. Understanding defects are important to improve the crystal growth process, as electron-hole pairs can interact by non-radiative recombination at defect sites acting as carrier traps.

Cathodoluminescence hyperspectral images were acquired from various samples to correlate InN fraction with CL emission at high spatial resolution. A custom-built hyperspectral CL acquisition system on a FEI Quanta 250 field-emission-gun SEM at

the University of Strathclyde was used. The hyperspectral configuration enables fast acquisition of CL spectra at each point on the sample during the SEM raster scan [128].

In Figure 2-17 a schematic of the CL collection system is shown. When the electron beam is focused on a local spot on the sample, the light collection system gathers all the light emitted from the sample and directs it onto a spectrometer diffraction grating. A parabolic mirror in the SEM chamber focuses the collected light into a parallel and reversed image onto the spectrometer grating. The collected light reaches only partially beyond the spectrometer slit. This limits the field of view size and ensures the collection efficiency is maintained over the sampled area. The spectrometer is equipped with a 600 lines/mm diffraction grating and a cooled silicon CCD detector array. An advantage of the hyperspectral system is the acquired raw data can be examined outside of the acquisition time. The CL spectra were acquired at the University of Strathclyde by Dr. Paul Edwards and PhD candidate Chris Bryce. I performed one of CL core-shell sample analysis in Chapter 6 assisted by Chris Bryce at Strathclyde. All the samples spectra interpretation was done by myself in Bath using Dr. Edwards' Chimp software.

Instrument setup for spectra acquisition

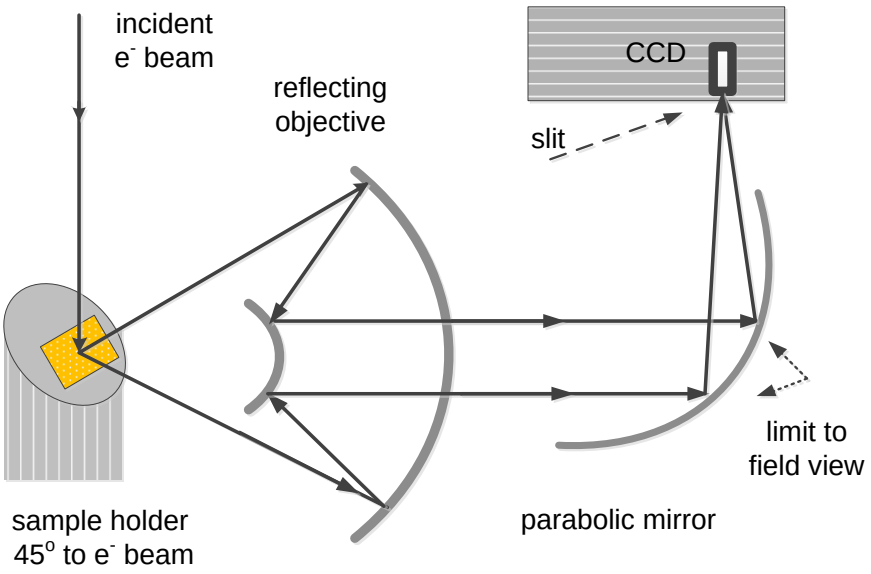

Figure 2-17: Optics setup for image collection in Strathclyde's hyperspectral CL system. Limiting the field of view ensures the collection efficiency is maintained of the sample area examined.

The calibration was done using the line from a phosphor standard at 630 nm. Once a vacuum of minimum 10^{-4}mbar was achieved, the initial SEM focus on the sample was done. Specific to the CL acquisition mode with a tilted sample holder, the samples' eucentric position or horizontal center of the objective lens was found. The SEM's magnification and correct focus are set to this eucentric reference position. When the sample height (in the Z-direction) is set at the eucentric, the sample can be tilted around its axis without the image of the sample moving across the screen. A final lens alignment step was done to check that the beam cross-over was correct and that focus and astigmatism were adjusted.

Once the GaN NBE peak was identified, the slit position was adjusted to maximize the GaN NBE signal. The parameters used for the hyperspectral capture can be different from sample to sample, however, unless otherwise stated the normal acquisition setup applies an accelerating voltage of 5 kV, a spot diameter size of 2 nm and averaging over 100 spectra. All the CL hyperspectral scans consisted of 200×200 pixels maps, with an individual pixel size of 25 nm in real space. Each hyperspectral CL map, depending on set scan size and step size, typically required between $20 - 60$ minutes.

A different CL setup on a SEM LEO-1550 was used by our collaborators at the Slovak University of Technology, by Prof. Alexander Šatka and Dr. Juraj Priesol to map magnesium dopant signal on NRs. An internal parabolic mirror in the SEM chamber and an external collimator were used to collect light to a spectrophotometer. Spectrally resolved CL maps were obtained using an electron beam of a very low accelerating voltage of 2 kV at room temperature.

2.2.6 Raman spectroscopy

Most of an incident laser beam passing through a molecule or crystal is scattered elastically, but some of the photons exit the sample with a changed energy level by $h\nu_m$ due to inelastic scattering as illustrated in Figure 2-18. Depending on the initial state, Raman shifted photons can be of a lower energy (Stokes shift) or higher energy (anti-Stokes), depending on the vibrational state of the sample under study. Raman scattering can reveal information about lattice strain, crystal quality, defects, alloy composition and dopant concentration. The strain in a heteroepitaxial structure is crucial for device fabrication. For GaN it is especially important to manage strain, as there are no native GaN substrates. Due to differences in cool-down rates and lattice constants between GaN and the non-native substrate, strain accumulation is inevitable in heteroepitaxial GaN, causing film cracking, threading dislocations and ultimately

Table 2.2: Raman-active modes allowed in planar wurtzite GaN in different scattering configurations $z(x,-)\bar{z}$ are parallel to the [0 0 0 1] direction).

Scattering geometry	Active mode	Frequency (cm^{-1}) (relaxed GaN [129])
$z(x,y)\bar{z}$	E_2^H	567.6
$z(x,x)\bar{z}$	E_2^H, $A_1^{(LO)}$	567.6 , 734
$x(y,y)\bar{x}$	E_2^H, $A_1^{(TO)}$	567.6 , 531
$x(z,z)\bar{x}$	$A_1^{(TO)}$	531
$x(z,y)\bar{x}$	$E_1^{(TO)}$	558.8
$x(y,z)\bar{y}$	$E_1^{(TO)}$, $E_1^{(LO)}$	558.8 , 741

reduced recombination efficiency. Raman spectroscopy is easy to use, relatively quick and non-destructive method to inspect the amount of strain in GaN.

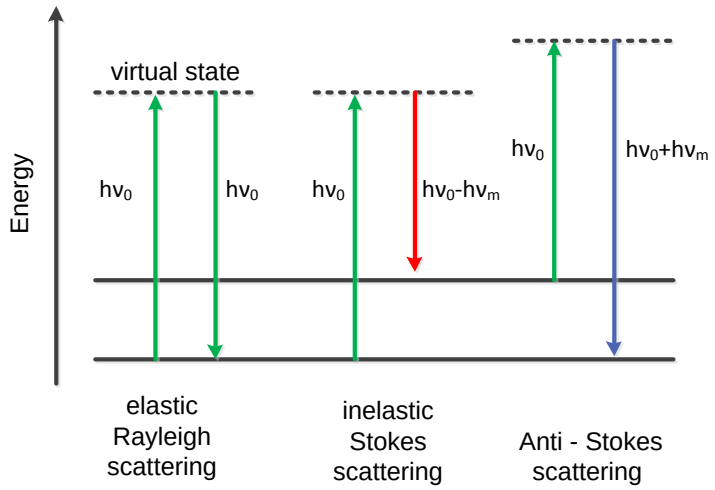

Figure 2-18: Raman transitions occur with loss of phonon vibration energy or increase in energy, if the molecule probed was already excited.

Atomic displacements and deviations from the ideal wurtzite crystal can be detected by vibrational shifts in the Raman-active phonon modes, by application of selection rules in different scattering geometries. The active modes are summarized in Table 2.2. The notation convention for letters outside the brackets indicate from left to right, the direction of the incident and scattered light respectively. The letters inside the brackets indicate the polarization state of the incident and scattered beams.

The A_1 phonon mode propagates parallel to the c-axis while the E_2 modes are sensitive to atomic displacements perpendicular to the c-axis. Typical wurtzite GaN strain values are summarized in the next chapter in Table 3.3. Because the GaN nanorods are three dimensional, the facets of the nanorods do not follow strictly the optical axes required by the selection rules. Thus for NRs the selection rules are relaxed and forbidden modes show up in the spectra. A more detailed discussion on Raman and GaN is provided in refs [130, 129].

The schematic of the Renishaw inVia Raman microscope system is shown in Figure2-19 and consists of a laser source and filter, optics for handling exposure and collection of light, wavelength filters, a diffraction grating and a CCD detector array. The light from the laser source enters the Raman microscope through a neutral density filter to remove any plasma lines. An optical beam expander consisting of two lenses with both their focus at the same point or confocal lenses, which broadens and maintains the beam collimated to limit stray light. A filter removes incoming wavelengths close in value to the laser wavelength. The laser light is reflected into the microscope where it is focused on the sample using an objective lens. A high-magnification objective provides a small focus spot and better spatial resolution. The light reflected from the sample is collected by the objective and directed again through the filter, where backscattered wavelengths close to the laser wavelength value are removed, leaving only Raman scattered wavelengths in the signal. The focused beam is passed through a slit and onto a prism and a diffraction grating. The slit value can be adjusted between $0 - 65$ μm, a narrower slit of 20 μm was found to provide the best resolution for NRs without saturation of the CCD detector. The diffraction grating disperses the signal which falls onto the other edge of the prism, from where it gets reflected through a focusing lens onto the CCD detector.

The setup in Figure 2-19 uses a visible laser source of 532 nm. For most of the present work the samples were measured with the Renishaw inVia Raman system at the University of Bath with an objective lens of 50×, 0.75 NA, and 1800 lines/mm diffraction grating for a focus spot of ∼1 μm. A set of Mg-doped sample set was measured in a higher resolution Renishaw inVia Raman microscope at Renishaw plc with a 150×, 0.95 NA lens and 3000 lines/mm and a focus spot of 0.3 μm.

Raman spectroscopy analysis for III-V semiconductors is a powerful characterization tool because it is a non-destructive, non-contact, requires a short acquisition time and little to no sample preparation. The shifts recorded by the spectra were used to interpret strain, morphology and dopant effects throughout this work.

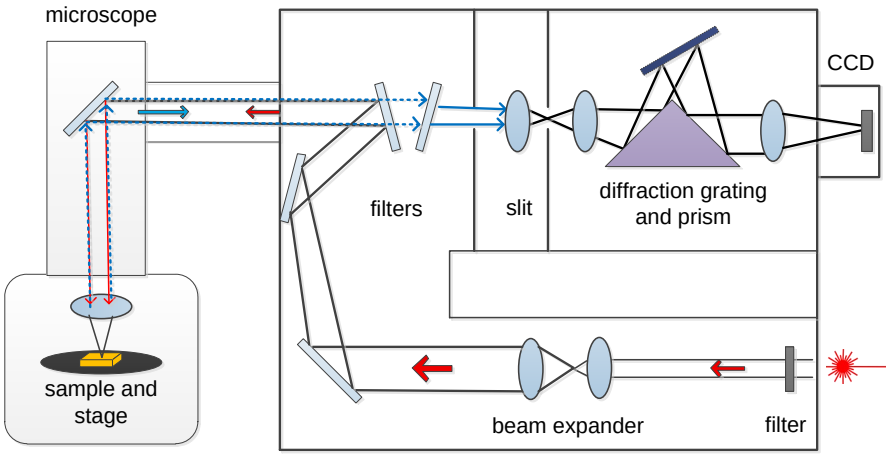

Figure 2-19: Renishaw inVia Raman microscope setup shows how the Raman scattered wavelenghts are detected.

2.2.7 Electron beam induced current

An incident electron beam from SEM probing a semiconductor sample generates mobile electron-hole pairs due to energy absorption from inelastic scattering with the atoms of the crystal lattice. The specimen acts as the collector of electric charge and the signal can be mapped to form a charge collection image [131]. The movement of carriers in the sample is random unless they are subjected to an internal electric field provided by a p-n junction. Figure 2-20 shows the setup at the Slovak University of Technology where the measurements were carried out.

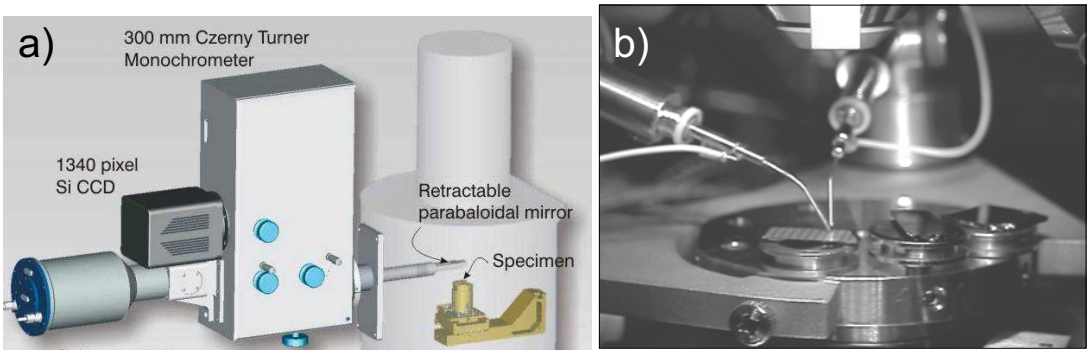

Figure 2-20: a) CL/EBIC system consisting of a Czerny-Turner monochromator, CCD detector and SEM chamber with sample holder, b) inside the SEM chamber, probes can be mounted to examine the sample's electrical characteristics.

Collection-current intensity and the space charge interaction in the sample can be used to locate the p-n junction's and its depletion width or space-change-region (SCR). The SCR depends on the dopant concentration and the voltage drop. A set of probes can apply the voltage , V_{bias}, to examine the SCR width and current-voltage characteristics. From this information, the p-n junction width, collection efficiency, transport efficiency, carrier diffusion lengths, and carrier concentrations could be determined. The method can also be used to locate impurities and electrically active defects such as dislocations, grain boundaries, and inhomogeneities. Electron-beam-induced-current is a great tool to determine electrical properties on NRs, otherwise difficult to examine individually or an array structure, where other factors such as the metal contacts [70] can change the electrical characteristics.

2.3 Conclusions

An overview of the cleanroom processing methods was provided starting with the substrate preparation and patterning, to profile transfer by plasma etching. Crystal growth in the MOVPE reactor for GaN facet recovery, the growth of InGaN active areas and of doped p-GaN shell were discussed. The processing approach for electrically driven light emitting devices was summarized. The characterization methods were introduced and describe. SEM and AFM were used to quantify the uniformity of the NRs. More detail is available in each of the chapters in which the characterization was used. The InGaN QW structures and doping were investigated by TEM, EDX and optical methods (PL, CL, Raman spectroscopy). Finally, EBIC and current-voltage measurements were used to determine electrical properties in prototype core-shell nanorod LEDs.

Chapter 3

Uniform GaN nanorods

Wafer size fabrication of core-shell LEDs requires a high geometry uniformity for nanorods (NRs) to achieve a narrow wavelength emission range. The nanorod diameter was demonstrated to have an impact on emission wavelengths [73]. NR height uniformity is important for the processing stages [58]. In the present chapter, the results on top-down plasma etching and MOVPE regrowth for GaN nanorods are discussed with emphasis on dimensional uniformity. The samples were prepared by Dr. Emmanuel Le Boulbar, and the sample characterization was done by myself. Scanning electron microscope images were used together with image analysis software to determine planar perspective NR diameter distributions, before and after MOVPE regrowth. AFM analysis provided an understanding of NR height variations and influence on regrowth by surface atom diffusion. Results in this chapter have been published ref [102]. Further results concerning GaN strain analysis and different NR diameter and pitch dimensions obtained by electron beam lithography are presented.

3.1 Plasma etched GaN nanorods

Nanorods were obtained by selective top-down plasma etching from planar GaN films, using a Ni nanodots mask (see section 2.1.2). The GaN on sapphire samples were 6 μm thick planar films. Additionally Si {1 1 1} substrates with a 2 μm planar GaN, on intermediary 0.5 μm AlN layer for lattice matching were used. The GaN on Si substrates were provided through the EU FP7 SMASH programme. Etching on the GaN films was accomplished with optimized parameters summarized in table 3.1. The GaN etch duration of 9 minutes resulted in ~ 4 μm tall NRs. More details on plasma

Table 3.1: GaN plasma etch parameters

Temp. (℃)	Pres.(mTorr)	ICP(W)	RIE(W)	Gas(sccm)	Rate(nm/min)
150	9	800	120	Cl_2(50): Ar(10)	450

etching optimization can be found in ref [125].

The nanoimprint patterns used in this work were the 0.6 μm pitch, 0.3 μm diameter and a pattern of 2 μm pitch, 0.6 μm diameter. The smaller dimensions pattern was used initially, and this chapter focuses on NRs obtained with that design. It was shown that due to NRs competing for adatoms, most of InN integration occurs at the tip [104], which is the effect we also observed [102]. Subsequently, the pattern was changed in the following chapters to the larger pitch and diameter. The choice of pitch and diameter determine the InN incorporation rate and fraction [73]. The two pattern parameters can give information on the density of NR on a planar surface, on the coverage or *fill factor* of a design. A smaller density of nanorods per unit area, or a smaller fill factor proved helpful in achieving uniform InGaN/GaN QW/QB growth [132].

The NR heights were controlled by the plasma etch depth. The Ni mask guarantees much deeper etching and vertical sidewalls than SiO_2 typically used for the top-down approach [104]. The taller NRs have the potential to increase the active area surface as long as InN can be incorporated on the sidewalls. A comparison between the different NR geometries by aspect ratio (height/diameter) is provided in Table 3.2. The table shows that even for shorter NR the surface area is superior to that of planar samples. The aspect ratio impacts clean-room processing for the deposition of contacts.

The 2 μm sapphire samples achieved roughly a 3.3 aspect ratio and an active area at least 2 × larger than a similarly sized planar GaN sample. The higher aspect ratio NRs used in this chapter and having 4 μm tall GaN cores at a pitch of 0.6 μm are expected to provide an equivalent $\sim 11\times$ active area relative to planar GaN. Some challenges remain with uniform InGaN integration on the high aspect GaN NR sidewalls, and are further discussed in section 4.5.5.

Maintaining uniformity in the GaN NR diameter is expected to provide a narrow emission spectral range because adatom incorporation and growth rate depend on the local environment. To quantify the effect of GaN regrowth, a method using statistical analysis was developed for scanning electron microscope (SEM) images for a large number of NRs. The same method was used throughout the work for different growth steps. The method described in section 2.2.1 uses thresholding and low band-pass filtering

Table 3.2: Active area increase over planar samples for different NR rod pitch and diameter.

NR pitch	2 μm(Al_2O_3)	2 μm(Si)	600 nm
Diameter (nm)	900	900	380
Height (nm)	3000	1500	4000
Aspect ratio	3.3	1.7	10.5
Fill factor	0.21	0.21	0.28
Nr rods/image	91	91	842
Active area	2.26	1.13	11.8

to determine nanorod edges. Equivalent NR diameters (Waddell disk diameter) were within ± 10 nm standard deviation for the 2 μm pitch samples between different SEM images. Etched cores in figure 3-1 a) show plasma etching maintained an excellent diameter uniformity on all sample sets. On average over 1000 NRs for 600 nm pitch samples and over 90 NRs on 2 μm pitch samples were quantified in each individual SEM image.

3.2 Regrowth of plasma etched GaN nanorods

Passivation of the GaN [0001] *c*-plane facets between the NRs is a step necessary to confine regrowth to the NR sidewalls. The passivation is visible in the dark contrast regions at the base of the NRs in Figure 3-1. Liquid hydrogen-siloxane (HSQ - DOW Corning XR-1541) was spin coated on etched NRs and heat cured to 550℃ (see section 2.1.6). The heat treatment changes the structure of the HSQ into SiO_2 and notably reduces the HSQ etch rate in buffered oxide etch (BOE) 100:1 solution. Due to the XR-1541 viscosity, at the NRs base, a thicker HSQ layer was achieved. After BOE exposure to an etch time of 30 sec for the 600 nm pitch samples, the thinner HSQ from the NR sidewalls was removed. As a consequence, during MOVPE growth only the sidewalls and the NR top surface experience GaN growth and increase the NR diameter by incorporation of Ga and N adatoms.

Regrowth on GaN etched cores was accomplished in the MOVPE reactor at ∼900 ℃, a pressure of 100 mbar, precursor flows of 9 sccm TMGa and 2800 sccm NH_3. In contrast to planar GaN growth, a lower TMGa flow rate ($< 20\times$) was necessary to limit the growth rate and the amount of lateral growth on NRs. In addition, the high ammonia flow reduces surface desorption of added Ga and N atoms. Several regrowth times were evaluated by their ability to reconstruct the GaN hexagonal facets and repair

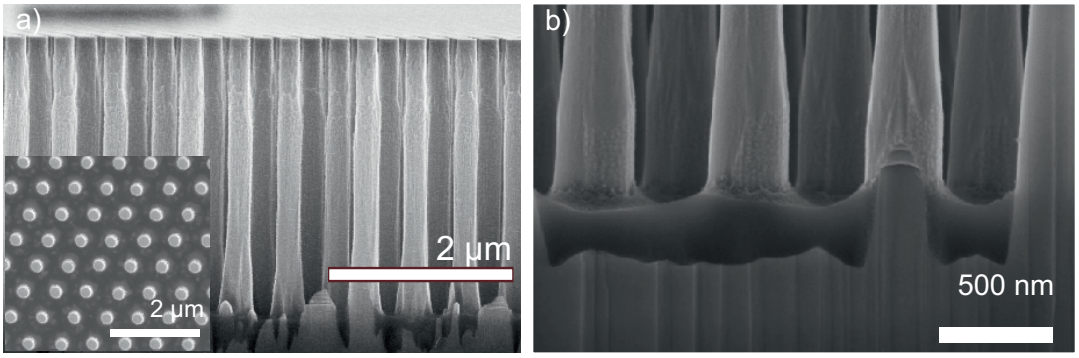

Figure 3-1: a) plasma etched GaN cores showing small diameter variations along the length of individual NRs and surface roughness at the NR tips ; the inset is a planar view of the highly uniform array of etched cores, b) cross-section view at the NR bases with HSQ pasivation layer in darker contrast. (Reprinted from ref [102], with the permission of AIP Publishing.)

any surface etch damage. Regrowth times were found to depend on the NR density or available GaN capture surface area available. On the 600 nm pitch 4 µm tall NR samples, a 30 minutes regrowth step provided good recovery of the m-plane facets [1]. On the 2 µm pitch samples for $2-3.5$ µm tall rods a regrowth time of $4-6$ minutes provided fully recovered m-plane facets for InGaN/GaN QW/QB growth.

A comparison of regrowth on the NR sidewalls is shown in Figure 3-2 with passivation a) and b), and without passivation c) and d), for 30 min and 60 minutes respectively. The regrowth repairs the NR width variations caused by etching damage along NR sidewalls. A longer regrowth time improves the sidewall verticality, yet the range of diameter values are more variable with increasing growth time, as shown by the distribution of diameters in the next section (3.3). Therefore, a regrowth of 30 minutes is optimum to maintain both diameter homogeneity and the vertical sidewall.

The un-passivated samples display a visible tapering in Figures 3-2 c) and d), caused by enhanced growth at the NRs base, and less growth at the pyramid tip. This can be explained by propagation of fast-growing high index planes upwards from the base toward the NR tips. The effect of the high index planes seems to aggravate for the 60 minutes un-passivated regrowth. The dimensions of the NRs and the amount of growth were determined from image analysis on SEM images.

[1] Reprinted from Le Boulbar, E. D., Gîrgel, I., Lewins, C. J., Edwards, P. R., Martin, R. W., Šatka, A., Allsopp, D. W. E., Shields, P. A., "Facet recovery and light emission from GaN/InGaN/GaN core-shell structures grown by metal organic vapour phase epitaxy on etched GaN nanorod arrays", *J. Appl. Phys. 114*, 94302 (2013), with permission from AIP publishing.

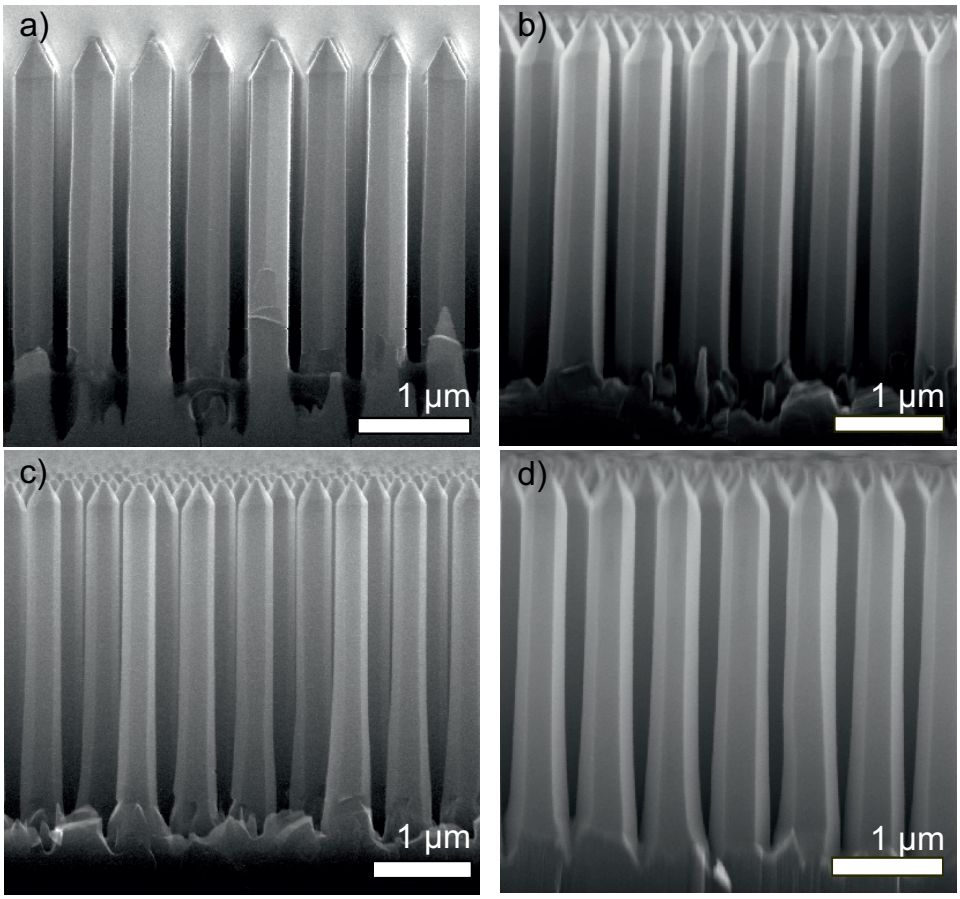

Figure 3-2: a) passivated 30 min GaN regrowth, b) passivated 60 min growth, c) not-passivated 30 min with wider NR bases, d) not-passivated 60 min regrowth. (Reprinted from ref [102], with the permission of AIP Publishing.)

3.3 Diameter uniformity

Individual SEM images at 6000× magnification capture a sample size area of 21× 16 µm^2. The SEM images were interpreted using the method explained in the SEM section (see 2.2.1). To quantify the uniformity obtained after regrowth, the inter-decile range (IDR) or the difference between the 10% and 90% diameter deciles, was used to illustrate the dispersion of NR diameter values. The values on the sides of each distribution correspond to the outer 10% and 90% deciles. Therefore the full IDR range covers the values shown in blue and green in Figure 3-3.

The etched NR cores with a narrow IDR variation of 9.2 nm, demonstrate the excellent dimensional control and large area reproducibility available with nanoimprinting and

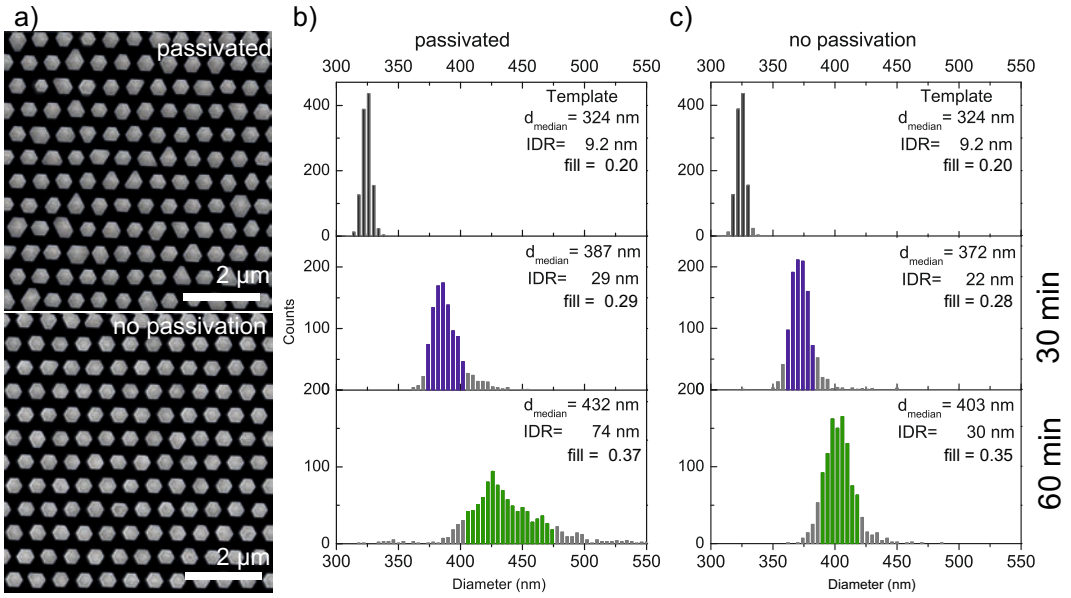

Figure 3-3: GaN regrowth shows evolution in NR diameters; a) selection from SEM images of NRs for passivated (upper) and not-passivated NRs (lower), b) Diameter distributions for passivated samples for etched template, 30 min and 60 min regrowth respectively, c) Diameter distributions for not-passivated samples. (Reprinted from ref [102], with the permission of AIP Publishing.)

plasma etching. The etched nanorod template had a corresponding fill factor of 0.20. Regrowth achieved an average diameter increase of 61 nm for 30 minutes, and the 60 minutes regrowth increased diameters by slightly more than 100 nm. The 30 minutes regrowth results in a fill factor of 0.29, after 60 min the fill factor approaches 0.37. The regrowth time and its effect on the fill factor can be used to control the NR thickness to achieve a given surface area.

Elongation of the NR sidewalls on random directions is visible on pairs of m-plane facets on the passivated sample in Figure3-3 a). This is believed to occur due to the close proximity of the NRs at 600 nm pitch , the neighboring rods are competing for the precursors available in the gas phase. The passivation has had little effect on diameter values distribution, however, it significantly impacts the sidewall profile.

3.4 Height uniformity

Height uniformity is important because NR height variation and the rod tip shape could increase the device processing difficulty. The initial planar film and the Ni mask

used in ICP etching are assumed to provide a highly uniform etched top surface. High-resolution cross-section SEM images confirm the local height uniformity of masked rods. Three types of GaN nanorods are studied: an initial etched nanorod array and two types of regrown samples, with and without the use of passivation.

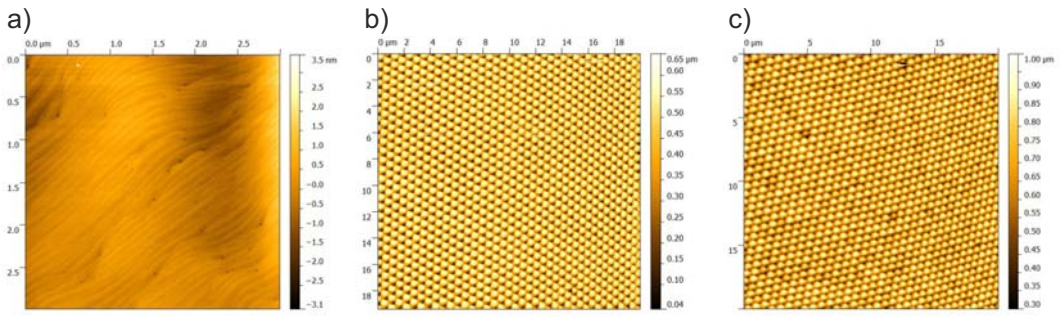

Figure 3-4: a) planar GaN film showing terraced GaN; b) etched GaN cores display very uniform heigths c) regrowth for 60 min shows an increase in height non-uniformity.

To measure NR heights the AFM tip is mounted normal to the NR template surface and brought in contact with the sample. An area of 19×19 μm^2 was scanned in contact mode and the initial AFM output can be seen in Figure 3-4. Only height variations are determined, because the Veeco SCM-PIC tip is too wide to access fully between the nanorods. Only about 0.50–0.75 μm of tip length enters between the rods for probing. Furthermore, since the AFM tip shape is pyramidal, the nanorod tips shapes are convoluted. Contact mode is desired because the oscillating motion in tapping mode can get the tip caught between the nanorods. Reconstruction of the exact surface features is not necessary, and the focus can be instead on the individual NR maxima. Local maxima can be used to build a height variation colour map. The maps were obtained using Matlab and the individual rod maxima determined from the raw AFM data.

The Matlab algorithm used to create the colour map identifies local maxima corresponding to individual nanorod tips. Once rogue points are removed, a median filter was applied to remove spikes. Smoothing by averaging adjacent points provides a smaller and more manageable data population. A matrix with a minimum separation element of 5 × 5 pixels in a 512 × 512 pixels image is chosen to remove double peaks. The minimum separation size needs to be a close match with the number of rods in the original AFM image. The results are color maps where the change in color tones indicate changes in NR height, as shown in Figure 3-5. The overlay dark blue dots indicate a single nanorod was taken into account.

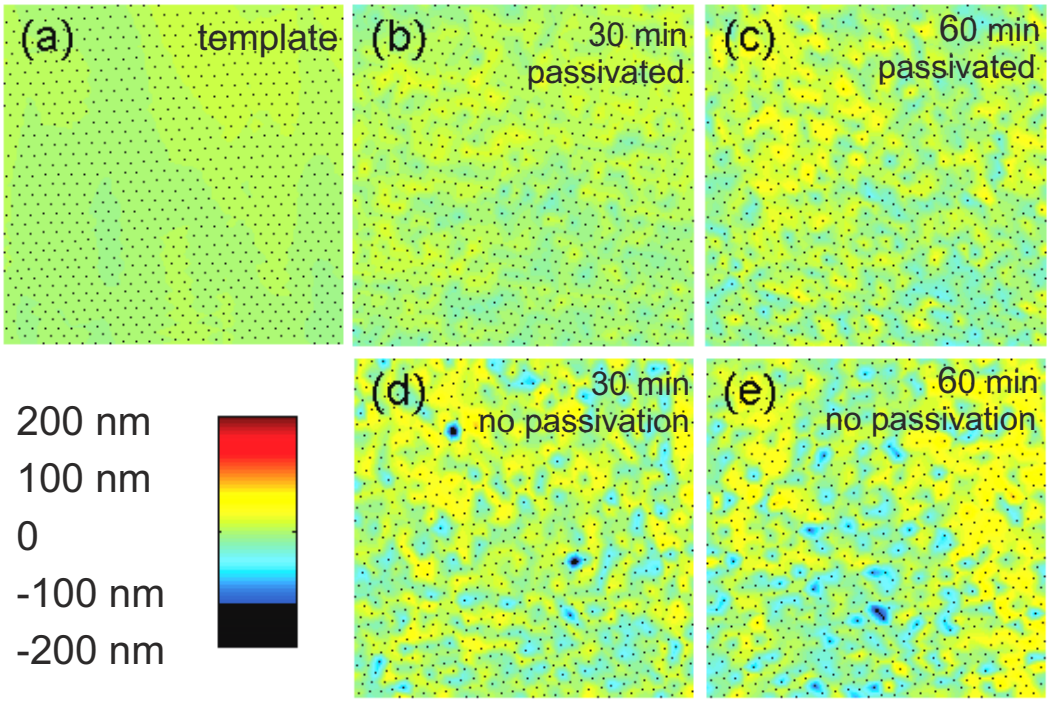

Figure 3-5: a) template map, b) heights variation on passivated samples for 30 min growth, c) map passivated 60 min growth, d) heights variation for 30 min growth with no passivation e) no passivation for 60 min growth. (Reprinted from ref [102], with the permission of AIP Publishing.)

The collected data supports the assumption that ICP etched nanorods provide highly uniform NR heights. The height variation expressed in IDR across a 19×19 μm^2 sample was only 12.6 nm. In Figure 3-6 it can be seen that within 30 minutes of regrowth, the IDR increased up to approximately 52 nm. Doubling the regrowth time to 60 minutes leads to rod heights IDR spread of 88 nm. As expected, increased growth time leads to more height variation. However, these variation values are very small if compared to bottom-up methods of growth, for which µm size variations are typical [90]. This amount of process control indicates plasma etching and regrowth provide an easily replicated process for reliable devices from batch to batch.

In order to understand the increase in height variation, Δh, can be related to diameter variation Δd, using equation 3.1, where θ is the angle between the $\{1\,\bar{1}\,0\,1\}$ semi-polar plane and the c-plane ($\sim 62°$). This relationship assumes a constant angle during crystal growth between the pyramid facets and etched core, as the relative growth rate of the corresponding crystal planes is constant.

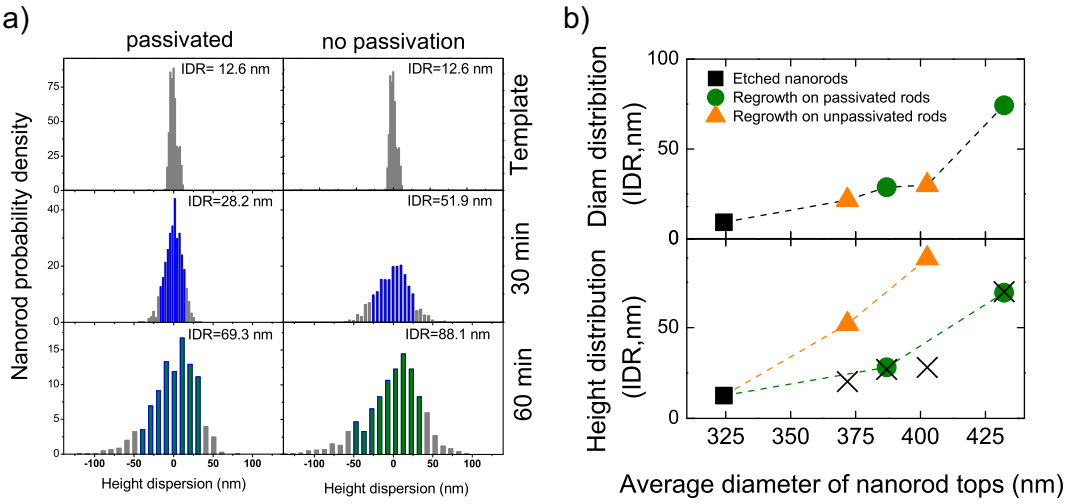

Figure 3-6: a) NR height distributions and IDR heights spread before and after regrowth for 30 and 60 minutes, with passivated and no-passivation samples, b) the lack of passivation shows a discrepancy between expected and measured NR height variations, indicating a reduction in vertical uniformity in samples without passivation.

$$\Delta h \approx \frac{\Delta d}{2 \tan \theta} \tag{3.1}$$

The crosses in Figure 3-6 indicate the expected height variation corresponding to equation 3.1. For passivated NRs, the measured data corresponds well to the theoretical height values. However for no-passivation samples the increase in height inhomogeneity cannot be correlated with diameter changes. The pyramid shape is formed in the early stages of the growth, as it is a more stable facet [78]. Thus the fast growing (0001) plane disappears and the only vertical growth component can be associated to the $\{1\,\bar{1}\,0\,1\}$ planes. This suggests NR to NR variable growth components on semi-polar planes could occur. The wider un-passivated NR bases capture the available Ga atoms and prevent their sidewall diffusion to the NR tip for incorporation. Because the passivated samples have a uniform sidewall, surface diffusion is unimpeded and the growth rate at the semi-polar surfaces can be more uniform from rod to rod.

3.5 Sidewall *m*-plane roughness

The previous section discussed how a tapered or non-$\{1\,0\,\bar{1}\,0\}$ planes could affect the NR heights. Because every subsequent growth step for core-shell structures is likely

to aggravate local inhomogeneities, the quality of the sidewall regrowth can influence the thickness and number of QW/QB which may be grown on the sidewalls. The existence of sidewall non-uniformities could also introduce surface states and surface recombination, and affect the internal quantum efficiency.

From the previous sections, the uniform contrast in SEM images indicated the surface uniformity of m-planes is high. Quantifying the surface roughness of the NR is a good challenge for AFM. Non-contact tapping mode was used to scan along the NR length, perpendicular to the sidewall. For measurements in contact mode, the tip had a tendency to get stuck between the NR, or damaged the rods and tracked the contours poorly. Two NRs were imaged partially without breaking them for their substrates. This method still creates problems and an improvement on the technique or equipment are necessary.

The AFM tip reproduces the hexagonal surfaces of the nanorods very well in Figure 3-7 a) for which two m-plane facets and the NR apex were probed by the AFM tip, while in figure b), three m-plane facets can be distinguished. The steps visible especially on the lateral side of the rods in Figure 3-7 a) are very likely AFM artifacts recorded for the tip slipping on the apex between the two facets, during amplitude and frequency adjustments. Ideally, the sample should be probed in the three facets configuration in Figure 3-7 b). Sharp features at the NR base caused by cleaving are visible in both samples. Surface roughness values were extracted from small areas from the centers of the facets. It is expected that the facets on which the tip is tracked perpendicular to the NR surface provide more reliable data.

Preliminary measurements reveal a root-mean-squared average surface roughness in the range of 0.6–1 nm on the un-passivated sample, and of $0.3 - 0.4$ nm on the passivated sample. Admitted the testing is not enough for a thorough conclusion and the two data sets have different resolution. The tip itself probes at different facet angles can have a significant effect on the measurement. However, even these preliminary results are encouraging as the surface roughness is similar to $\sim$1 nm measured in c-plane GaN crystals. This result implies GaN regrowth does not limit the thickness or surface quality of QWs that can be grown. A large number of QWs can be grown, which can improve the device internal quantum efficiency.

Summary on NRs uniformity

Statistical SEM image analysis and AFM measurements show top-down etching and regrowth can obtain uniform and reliable structures from batch to batch. Using pas-

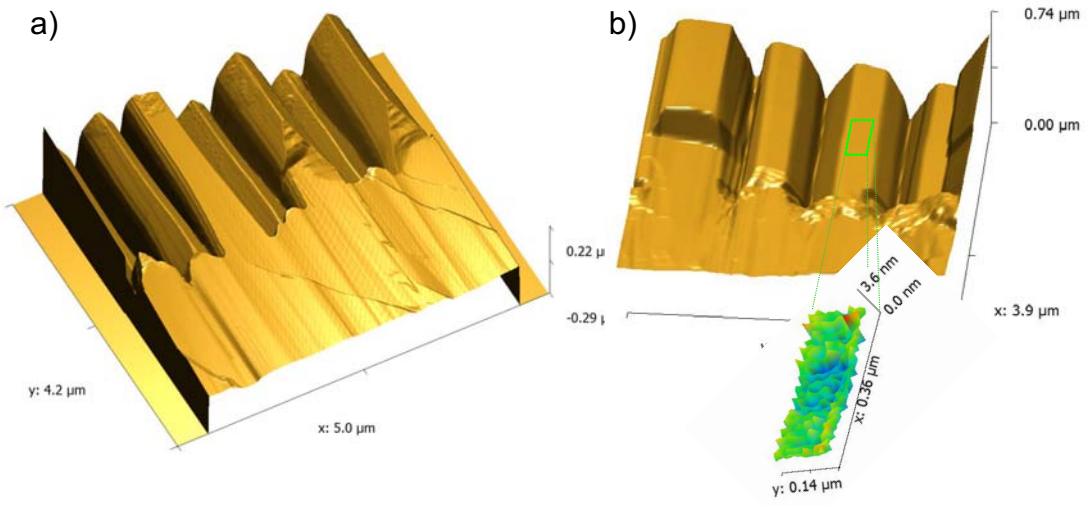

Figure 3-7: a) NRs with 2 facets at an angle to the AFM tip, b) NRs with 1 facet normal to the AFM tip, and two lateral facets; the inset shows and area from which NR facet roughness can be determined

sivation to block growth between the NRs, 80% of the diameters from over 1000 NRs showed a dispersion of $\sim$ 30 nm. Similarly, the majority of the nanorods were probed by the AFM tip within a 30 nm height variation. The AFM analysis for etched and regrown GaN nanorods has revealed the amounts of height variations that can be expected for regrowth. The AFM probe was used in both contact and tapping mode on the NR tips and on their sidewalls respectively. The sidewalls are vertical, uniform and reliably reproduced between different growths. Preliminary determination of surface roughness indicates quantum wells can be grown on crystal surfaces with small amounts of surface roughness of the GaN shell.

3.6 Effect of MOVPE regrowth on strain

Strain relaxation is an advantage of the GaN NR geometry compared to planar devices. With aspect ratios (height/diameter) larger than 1, the NRs behave as strain free GaN [62] which is significant in achieving higher InN fraction, due to an easier transition to a relaxed InGaN film from a relaxed GaN lattice than in planar compressive or tensile strained planar GaN.

Raman spectroscopy was used to detect strain changes in NRs, caused by processing and MOVPE growth steps. The E_2^H peak value provides information about strain

state and the crystal quality of GaN. The E_2^H mode is sensitive to phonon frequencies introduced in the lattice by atomic displacements perpendicular to the c-axis, while the TO and LO modes indicate possible displacements parallel to the c-axis. More on the method and interpretation of Raman spectra can be read in section 2.2.6 and in references [130, 129].

Figure 3-8 shows the effects of plasma processing and MOVPE regrowth respectively, on the E_2^H mode for GaN on sapphire substrates. The spectra are collected in $z(x,-)\bar{z}$ configuration, for which a reference planar undoped GaN film displays the E_2^H and the $A_1^{(LO)}$ peaks, the only peaks allowed in this configuration. The measured E_2^H GaN film value confirmed the initial GaN on sapphire film is in a compressively strained state. The well defined longitudinal optical (LO) phonon $A_1^{(LO)}$ at 734 cm^{-1} shows the sample is undoped. For n-type carriers in GaN, doping levels can be estimated (see section 5.1) from the shift of the $A_1^{(LO)}$ position, caused by phonon-plasmon coupling (LOPC)[129].

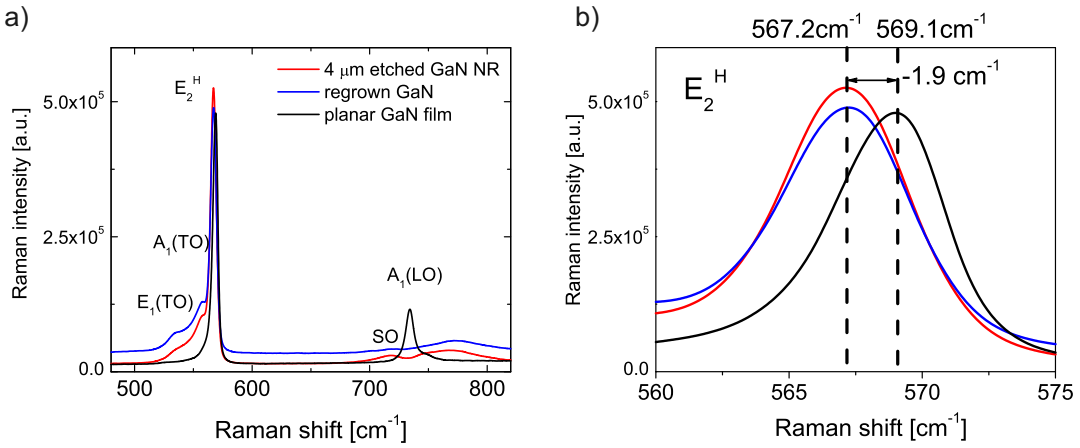

Figure 3-8: Raman spectra in $z(x,-)\bar{z}$ configuration for a) GaN film and NRs on sapphire substrate, b) the strain associated E_2^H peak shows relaxation of the compressively strained film occuring for etched and regrown GaN.

Plasma etching was carried out on ready-doped n-GaN on sapphire film template. The E_2^H experienced a frequency red-shift of ~ 1.9 cm^{-1}, to a value corresponding to relaxed GaN. Additional peaks, the $E_1^{(TO)}$ and $A_1^{(TO)}$ modes, are visible due to the new three-dimensional scattering geometry breaking the Raman selection rules when probed by the laser beam. Significantly the E_2^H peak has not changed its position value after the regrowth or facet recovery step.

The $A_1^{(LO)}$ phonon frequency is split by the decoupling of the LOPC mode in two lower and higher frequency branches[129], at $250-280$ cm^{-1} (not shown) and $760-780$ cm^{-1},

corresponding to the doping concentration. An additional band at $700 - 720$ cm^{-1} is visible only on the three-dimensional NR samples, which is argued to be related to a surface-optical phonon (SO) mode [133, 134]. The SO mode values were shown to depend on the NR diameter and surface roughness [135, 136].

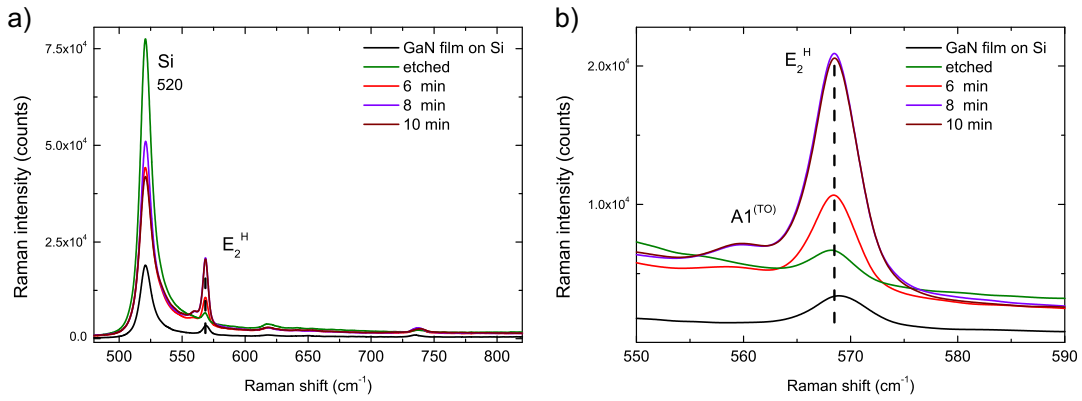

Figure 3-9: Raman spectra in $z(x,-)\bar{z}$ configuration for a) GaN film and NRs on Si substrate, b) increase of growth times for GaN NRs show no change in strain.

Figure 3-9 shows the dominant Raman peaks in GaN (undoped) on Si templates, and a constant E_2^H value with increasing NR diameter. Similar to the previous experiment, GaN films were plasma etched to a depth of 2 µm, which relieved a small amount of strain ($\sim$ 0.7 cm^{-1}). The etched sample (green line) seems to show a small offset, indicating that either the regrowth is causing a small amount of strain on the shorter NRs or it may likely be caused by the proximity of the very strong Si peak. The substrate also introduces another Si peak at $\sim$ 620 cm^{-1}. The $A_1^{(LO)}$ peak undergoes a small frequency shift of 3 cm $^{-1}$, indicating that etching can affect this peak, although to a small degree relative to the LOPC decoupling caused by doping impurities. The ability to control the sidewall without a change in strain and target a specific shell thickness could be used to control the fill factor to achieve uniform InN incorporation.

Table 3.3: Literature values for the Raman E_2^H peak in GaN films and for processed NRs in this work.

Substrate	GaN Sample	Planar E_2^H (cm^{-1})	NRs E_2^H (cm^{-1})	A_1^{LO} (cm^{-1})	Source
Al_2O_3	4 (µm) film	569.1	567.2	734	this work
Si(111)	2 (µm) film	568.9	568.5	734	this work
Al_2O_3	bulk GaN	568	–	–	Perlin [137]
Al_2O_3	1 (µm) film	570	–	750 (LOPC)	Harima [129]
Al_2O_3	$50-70$ (µm) film	567.6	–	734	Harima [129]
GaN	50 (µm) GaN	567.1	–	736.5	Goni [138]

Table 3.3 summarizes this work's results and contrasts them to literature values for

observed Raman GaN peaks in planar films. Plasma etching was shown to consistently release the strain from planar GaN templates. Constant E_2^H values for regrowth periods between 6 and 10 minutes suggest the NRs are maintaining their relaxed strain state.

3.7 Electron beam lithography

Electron beam lithography (EBL) provides flexibility to design bespoke patterns for NRs. Because different NR diameters are expected to incorporate distinct InN fractions [73], EBL was perfectly suited to investigate this effect.

A set of GaN etched NRs were obtained from GaN on Si-patterned by electron beam lithography, to study the effects of NR diameter and fill factor on growth rates. Figure 3-10 shows the quality of the Ni mask and of the etched NR structures obtained. Plasma etching achieved GaN NRs with several diameters 200/300/400/500 nm, and pitch sizes 0.5/1/1.5/2 µm. Although the exposure beam current (0.09 - 0.160 nA) was optimized for the poly(methyl-methacrylate) (PMMA/MMA) resist stack and the nanostructure sizes , the 200 nm NR diameter, as well as the 0.5 µm pitch size were not reliably obtained. A resist system using HSQ could produce higher resolution patterns [126]. However, to avoid a carrier depletion behavior caused by band bending and surface Fermi level pinning, the width of cylindrical NR should be larger than 280 nm [58]. Therefore in electrically injected devices NR dimensions smaller than 280 nm may have lower injection efficiencies.

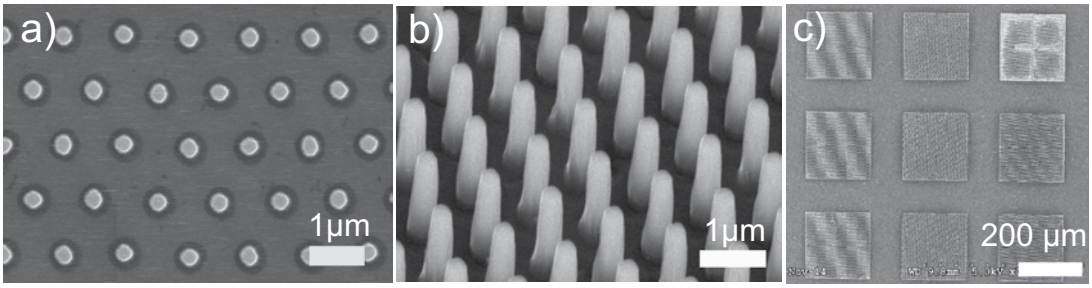

Figure 3-10: Electron beam lithography patterns a) Ni nanodots mask on GaN film, b) etched NRs with 300 nm diameter and 1 µm pitch c) map of EBL patterns.

Samples with the complete set of patterns were regrown in the MOVPE reactor and optimized growth parameters were determined. The use of high temperature (980 ℃) and low pressure (50 mbar) resulted in both *a*- and *m*-plane non-polar planes. The two non-polar planes are discussed in more detail in Chapter 4. It was quickly found that

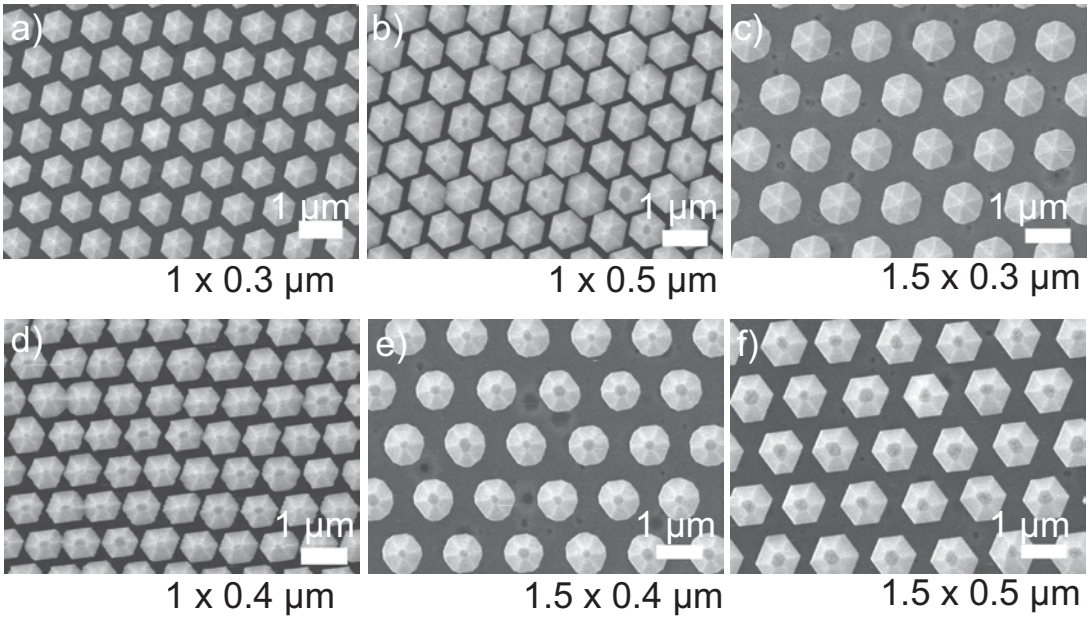

Figure 3-11: EBL patterned nanostructures. a) 300 nm diameter 1 µm pitch NRs, b) 0.70 highest fill factor, c) 300 nm and 1.5 µm, d) 400 nm and 1 µm, e) the low fill factor maintained both non-polar plane facets f) competition grown mode becomes dominant if the fill factor < 0.44.

due to the limited capture area of the small EBL samples, the growth rates were higher and easily lead to coalescence, compared to previous sets for which larger sample sizes were available. As a consequence, the TMGa precursor flow rate was reduced to only 3 sccm (other GaN samples typically grown with 8 sccm) and growth time reduced to 5 minutes.

Figure 3-11 shows a selection of GaN NRs after regrowth. In high density patterns, i.e. for all 1 µm pitch samples, regular and well defined *m*-plane facets can be seen.

Some of the NR seem to be slightly misaligned for the high fill sample in Figure 3-11 b), which may be explained by the ELB patterning of each individual feature at a time, or by local variations in available ad-atom collection spacing. Gas phase diffusion dominates for pitch distances of several microns. A growth mode dominated by neighbor competition occurs when the NRs are separated by less than 1.5 µm [139].

NRs in close proximity grow at a slower rate than NRs with a large free substrate surface area. Because the *a*-plane is more unstable and faster growing than the *m*-plane [140], the *a*-plane is observed only in the larger diameter, fast growing NRs with a lower fill factor (see Figure 3-11 c) and e)). Comparison between Figure 3-11 d)

Table 3.4: ELB pattern with NR pitch, diameters and fill factors

Initial pattern (pitch×diameter) μm	Diameter (nm)	$2\sigma(\pm)$ (nm)	fill factor
1.0×0.3	743	32	0.50
1.0×0.4	753	25	0.53
1.0×0.5	910	110	0.70
1.5×0.3	1008	20	0.47
1.5×0.4	980	20	0.37
1.5×0.5	1052	40	0.44

and e) indicates that with the increase in pitch size, a change in growth mode occurs. Moreover, comparison of Figure 3-11 f) with e) and c), proves that if the NR pitch drops below 1 μm, the *a*-plane is extinguished.

The EBL patterns provided an opportunity to study different NR fill factors during the same growth run. For NRs in close proximity a competition in the growth mode occurred when the fill factor was between $0.37 - 0.44$, with a threshold at ~ 0.44. Electron beam lithography patterns for MOVPE growth should be limited to a few patterns on individual samples because the growth rate can be very different depending on NR density. Furthermore, the growth rates may not transfer very well to larger area samples. Because the growth rates were very high due to the small GaN capture area, the EBL templates could not be exposed to a further MOVPE growth for a subsequent InGaN layer. InGaN growth is discussed in depth in the next chapter. Therefore the observation by Sekiguchi *et al.*[73] of distinct wavelength emission on different NR diameters could not be further explored. However it is very likely that a dependence of growth rate with NR pitch size and a threshold fill factor as showed by the EBL experiments, may be the cause of the influence of NR diameter on emission properties.

3.8 Conclusions

One of the most important advantages of NR structures for use in light emission is the high aspect ratio (height/diameter) and the increase ($> 4\times$ planar LEDs) in the size of the active area. Top-down etching is a method to obtain highly regular arrays of NRs, control the NR density, and obtain very good reproducibility at wafer scale by pairing with nanoimprint lithography.

Nanorod uniformity is crucial as dimensional uniformity confines the range of emitted

wavelengths. A passivation layer was used to block c-plane growth between the NRs, and obtain high-quality GaN films on the m-plane NR sidewalls. During GaN growths for 30 and 60 minutes, the majority (or 80% IDR) of NR diameter values were within a range of 30 nm (74 nm for 60 min) for NRs $\sim$ 400 nm in diameter. For no-passivation samples, high index planes were formed between the irregular NR bases, causing a loss of sidewall verticality and uniformity.

Passivation had an effect on NR heights as well because passivation provides a uniform m-plane, which atoms to diffuse toward the tip of the NR. The height uniformity was better maintained on the passivated samples, 80 % of NR tips are within $\sim$ 30 nm of each other's heights for 30 min of growth, while for un-passivated samples the range of values is almost double at 52 nm. Measurements of NR sidewall roughness have shown the NRs have similar roughness values to planar GaN.

Strain relaxation is another advantage of the NR structures. In planar LEDs, quantum efficiency is reduced by a piezoelectric field along the c-plane direction which increases with strain. Moreover, the InN fraction that can be grown on a GaN is limited by the strained GaN layer. The release of strain in the present work was measured on sapphire substrates to be up to ~ 2 cm^{-1}. Si substrates showed a smaller reduction (0.4 cm^{-1}) as the GaN dis not compressively strained on Si substrates. Importantly the strain did not change with increasing NR growth time and diameter, therefore, further regrowth on etched GaN cores can be carried out without significant introduction of strain.

Different NR diameters and pitch sizes were obtained using electron beam lithography. For NR fill factors smaller than 0.44, a growth mode threshold was observed for which the NRs compete for adatoms. The competition lowers growth rates and may have affected the incorporation of InN fraction onto the NRs as well. A comprehensive discussion on InGaN is given in the next chapter.

Chapter 4

InGaN growth

Blue and white light emitting diodes are based on the planar c-plane GaN/InGaN/GaN quantum well and quantum barrier (QW/QB) design proposed by Nakamura [10]. The new core-shell nanorod (NR) LED architecture makes use of the larger active area on non-polar NR sidewalls, [58, 104]. Heteroepitaxy of InGaN layers on the three-dimensional (3D) strain-free NRs and crystal plane dependent growth rates raise new design challenges. InGaN layers and QWs with different thickness and InN fractions results on the NRs, causing disparate emission wavelengths.

This chapter discusses results for InGaN shells growth on etched GaN 3D micro- and nano-size structures. InGaN growth under different temperature and pressure conditions was carried out to understand how these parameters influence the morphology and growth rates of InGaN shells. Optical emission properties and InN fractions were estimated by cathodoluminescence (CL) and energy dispersive X-ray spectroscopy (EDX). Understanding the evolution of InGaN layers is critical to the optimization of core-shell LED active areas on non-polar planes, and to the manufacture of eventual devices for solid state lighting. The results within this chapter on growth rates and CL characterization were published in ref [141], while the EDX analysis is currently under review in another journal.

4.1 Influence of strain on heteroepitaxial InGaN growth

InN and GaN are materials with different lattice parameters, a difference which causes the build-up of compressive strain in InGaN layers grown on GaN. Accumulated strain can generally be released by the formation of misfit dislocations (plastic relaxation)

or by lateral deformation (i.e. elastic relaxation) [142]. The increase in strain energy can be released by the formation of isolated, relaxed islands on layers above a critical nuclei size [75]. A growth mode transition occurs from a pseudomorphic strained 2D layer (Frank-van der Merwe) to a mixed 2D-3D mode on top of the strained layer (Stranski-Krastanov growth), as a means of elastic relaxation. The transition is associated with increased roughness [143] and increased InN fraction incorporation [144, 145]. Thus with thicker InGaN layers, the strain can be progressively relieved and more indium atoms are incorporated [146]. This may be a way to achieve longer wavelength LEDs and eliminate the *green gap*. However, planar InGaN films with high InN fraction are difficult to achieve because of potential phase segregation [83] caused by low miscibility of InN with the compressively strained GaN on sapphire substrates. In phase-segregated crystals, very high InN fraction areas (~ 0.8) linked to extended defects [142] may coexist with lower InN fractions, once the InN fraction becomes higher than 20% InN [83]. However, the strain in segregated layers should remain at the same values, as the miscibility and strain are two separate mechanisms [145]. By contrast, the NR sidewalls are free surfaces that allow easier strain relaxation and achieve higher InN incorporation than 2D layers with fewer defects. NR LEDs could provide longer emission wavelengths necessary for green and red LEDs, due to high InN fractions, without experiencing piezoelectric fields and emission blue shift associated with planar LEDs.

4.2 Nanostructures with non-polar *a*- and *m*-plane facets

The crystal shape under equilibrium conditions is determined by minimization of its total surface free energy. The atoms bond to the growing crystal's dangling bonds, which have different atom arrangement, depending on the crystallographic orientation, resulting in different surface energies and growth rates [147]. To reduce its surface energy, mechanisms of bond contraction and rotation are used, resulting in a slightly more energetically favorable and stable $\{1\,0\,\bar{1}\,0\}$ planes than $\{1\,1\,\bar{2}\,0\}$ planes [148].

The shape of a growing crystal can be studied with a polar plot of surface energies, or a *Wulff* plot. However, most crystal growth is achieved under non-equilibrium conditions, therefore a *kinetic* Wulff construct or ν plots showing growth velocities on individual planes (Figure 4-1) can be used to understand heteroepitaxy on the different crystal orientations.

Growth on GaN islands or nuclei takes place at convex facets, for which the fast growing

crystal planes, $\{1\,1\,\bar{2}\,0\}$ and $\{1\,0\,\bar{1}\,0\}$, grow to extinction, while the slow growing and stable $\{1\,\bar{1}\,0\,1\}$ and (0001) plane define the ultimate shape of the islands [80, 140]. This tendency is reversed on concave surfaces, for example, fast-growing planes are typically observed on dipped GaN surfaces [80]. Thus if the growth velocities are high on the Wulff construct [1] (Figures 4-1) b) and c), and the growth occurs at convex facets, the slowest growing facets are observed on the physical structures. The amount of facet growth and growth rates were determined in this work by measuring the facet size, before and after regrowth.

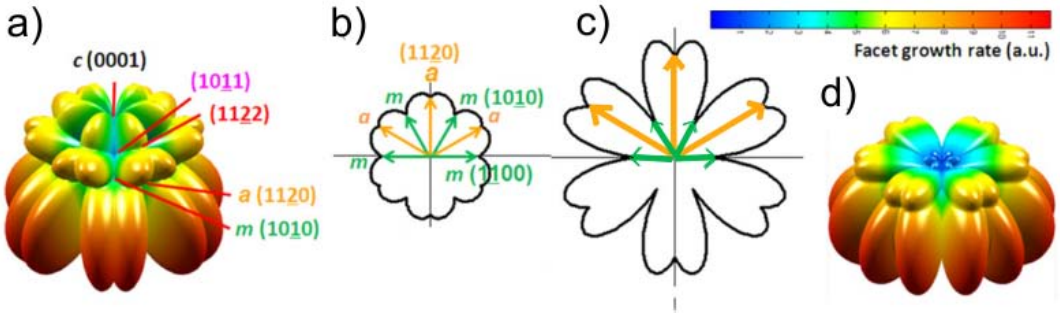

Figure 4-1: Kinetic Wulff plots for different reactor conditions for GaN growth. a) 3D ν plots within the m-plane for low-pressure conditions, b) 2D plot showing the relative growth velocities of a- and m-planes mapped onto the basal c-plane, c) 2D plot for high-pressure conditions showing the relative $\{1\,1\,\bar{2}\,0\}$ growth velocity is higher than for the $\{1\,0\,\bar{1}\,0\}$ plane, d) 3D plot high pressure (Reprinted and adapted with the permission of AIP Publishing from ref.[80]).

Using the Wulff ν-plot velocities from Figures 4-1 a) and b), corresponding to low pressure and low temperature, the m- and a- plane growth velocities are closer in magnitude to each other than for high temperature and high pressure, as shown in Figures 4-1 c) and d) [93]. MOVPE reactor parameters typically used to achieve high-quality GaN growth in the c-plane direction are high V/III ratio and high pressure ($200 - 300$ mbar) [149]. In literature and in the growth experiments discussed in this work up to this point, the $\{1\,1\,\bar{2}\,0\}$ a-plane can rarely be observed, due to its relatively high growth velocity and annihilation at high pressure. Changing any of the reactor parameters can change the relative growth velocities shown in Figure 4-1.

Two types of sample sets were prepared to study the InGaN growth on 3D faceted structures, obtained by top-down etching as described in section 2.1 and refs [18, 103]. Plasma etched large 3D GaN micro-disk cores were obtained for one set, and etched

[1] Reprinted from Sun, Qian, Yerino, Christopher D., Leung, Benjamin, Han, Jung, Coltrin, Michael E., "Understanding and controlling heteroepitaxy with the kinetic Wulff plot: A case study with GaN", *J. Appl. Phys. 110*, 53517 (2011), with the permission of AIP Publishing.

GaN NRs for the second set, both by using GaN on Si substrates. Micro-disks of 4 to 10 μm in diameter were patterned using direct laser exposure of the photoresist (nLOF 2020) and metal lift-off. The large micro-disks were chosen because they were considered better suited to quantify the changes in crystal growth by SEM over a long InGaN growth time.

Several growths were made to optimize the GaN template and achieve as many crystal facets as possible: *a*-, *m*-,*c*-, and the $\{1\,\bar{1}\,0\,1\}$ semi-polar planes. Starting from the Wulff ν-plots it was found experimentally that with a short GaN growth time of 5 minutes, and low-pressure conditions (50 mbar), the $\{1\,1\,\bar{2}\,0\}$ *a*-plane could be maintained. Also high temperature (1060 ℃) and a tri-methyl-gallium (TMGa) precursor flow of 8 sccm were used. The following sections discuss the effects of growth temperature and pressure on thick, relaxed InGaN layers for both types of samples.

4.3 GaN micro-disk templates

A template with micron-size diameter GaN disks was obtained to study the evolution of growth rates for InGaN layers under different reactor conditions. The large structures were selected because the SEM measurements have inherently greater tolerances than other methods, such as transmission electron microscopy (TEM). However, SEM has the advantage of quantifying the growth in a statistical manner for a large number of structures. The etched GaN provided micro-disks with different diameters ($4, 6, 8, 10$ μm), and respectively pitch sizes ($18, 24, 30$ μm). In Figures 4-2 a) the initial etched disks can be observed, and in Figures 4-2 b) and c) the different crystal facets after 5 min GaN regrowth can be distinguished: (0001) *c*-, $\{1\,0\,\bar{1}\,0\}$ *m*-, $\{1\,1\,\bar{2}\,0\}$ *a*-planes and $\{1\,\bar{1}\,0\,1\}$ semi-polar planes.

On the initial template, only GaN micro-disks with 18 μm pitch distance resulted in compact smooth surfaces and complete wurtzite crystal facets recovery for 5 minutes of regrowth. For the larger pitch distances, this growth time was insufficient and the crystal facets were only partially recovered. This can be explained if the growth on the larger pitch samples is driven by incident ad-atoms only, and contribution to growth from surface diffusions of Ga atoms on the Si substrate was significantly smaller. Therefore, the discussion on InGaN growth rates was focused on the 18 μm pitch and largest diameter disks, as their facets were completely recovered (see Figure 4-3). Furthermore, the surface area of semi-polar facets in planar-view SEM images decreased with larger disk radius (Figure 4-3). This indicates that for the smaller radius disks,

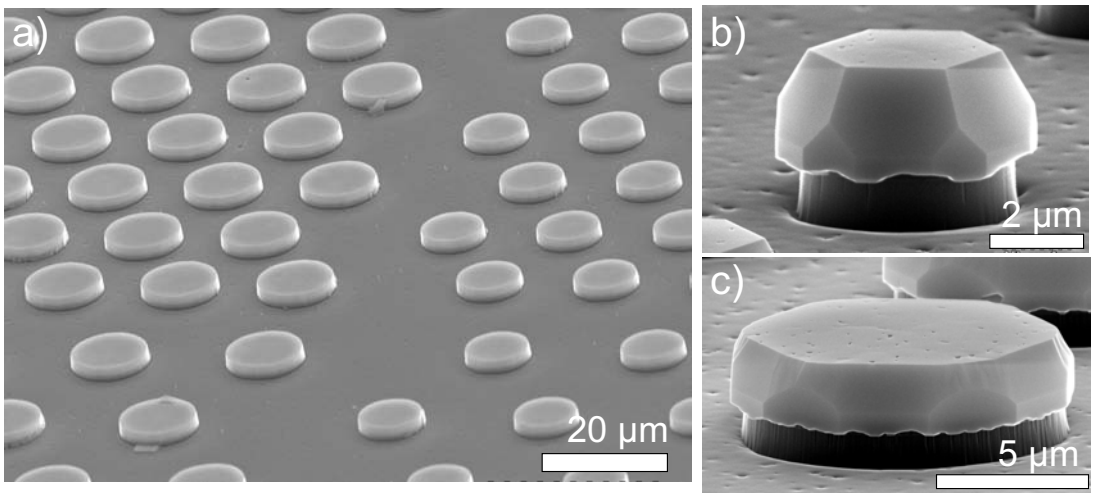

Figure 4-2: GaN micro-disks obtained after etching and regrowth. a) GaN template with plasma etched micro-disks of different diameters and pitch distances. b) regrowth with multiple facets on 4 µm disks, and c) regrowth on the larger diameter (10 µm) micro-disk

growth in the $\{1\,\bar{1}\,0\,1\}$ is preferential to the *c*-plane growth. This demonstrates that even for very large GaN *islands*, GaN MOVPE growth advances with the formation of pyramid $\{1\,0\,\bar{1}\,1\}$ facets and gradual extinction first of the non-polar planes than the *c*-plane. The surface of most crystal planes appeared smooth, while the *c*-plane showed some surface pitting. The surface pitting could be eliminated by a longer growth, however, this would reduce the surface of all facets in favor of the $\{1\,0\,\bar{1}\,1\}$ planes.

4.4 InGaN layers on micro-disk templates

Three separate sets of growth parameters were studied for InGaN layer growth of 30 minutes on a GaN template. The growth temperature and the pressure were alternately changed, starting with 750 ℃ and 300 mbar, second growth used 700 ℃ and 300 mbar, and last, a 750 ℃ and 100 mbar growth. The same flow of 200 sccm of tri-methyl-indium (TMIn) precursor was used on all the samples. The change in parameters caused modifications in the relative growth velocities of the crystal facets.

Figures 4-4 show the effects of growth on the micro-disks, from GaN template to the InGaN layer morphology. Considering first the semi-polar plane, after growth the $\{1\,\bar{1}\,0\,1\}$ facets appear smooth and their surface area is dominant in relative to the non-polar planes.

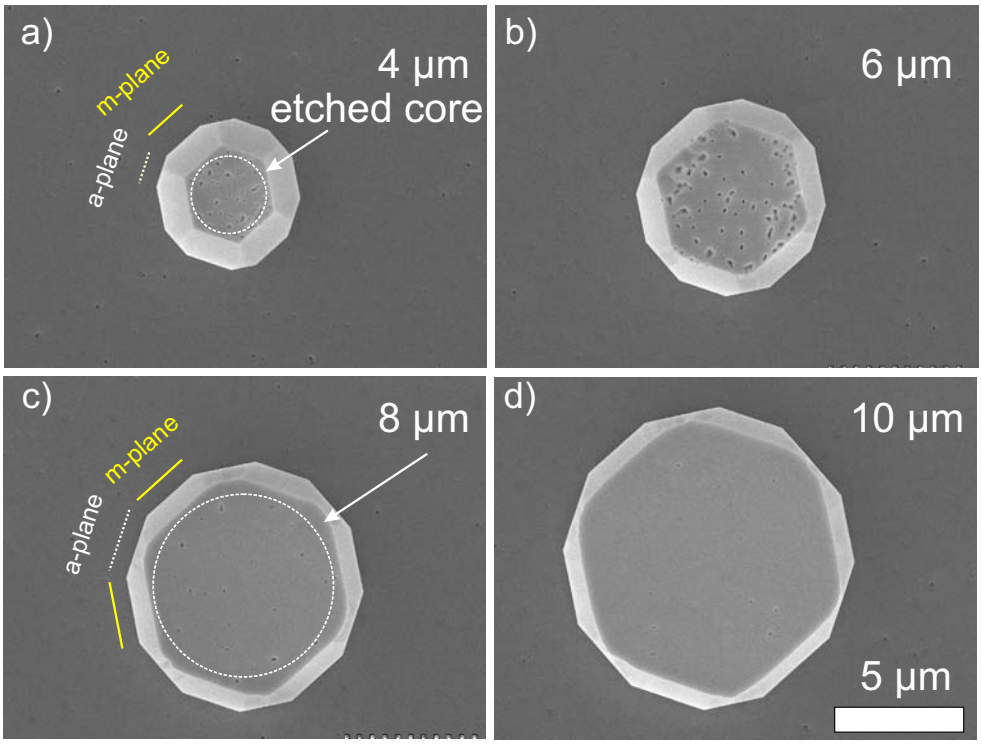

Figure 4-3: Micro-disks with different etched core diameters after 5 minutes of GaN regrowth recovered the crystal facets. a) regrowth on 4 µm etched core with *m*-plane and remaining small *a*-plane, b) 6 µm, c) 8 µm core with non-polar planes of similar lengths, d) 10 µm core for which shorter ad-atom surface diffusion improves the *c*-plane surface. The scans are taken using the same magnification.

Second, the remaining non-polar *a*-plane is rough and has a pitted surface, while the *m*-plane facets are smoother. Rougher surfaces can incorporate higher InN fraction, either because the roughness indicates relaxed layers able to accommodate more InN or the irregular surfaces have higher sticking coefficients improving adherence. However, these rough surfaces may also provide an increase in defects and surface states, reducing light emission by non-radiative recombination [150].

Third, the *c*-plane surface has a visibly rougher InGaN layer compared to the GaN template, indicating the InGaN films are thick and fully relaxed, similar to films in ref [151]. There are random depressions on the sample in Figure 4-4 b), which may be related to strain variations caused by threading dislocations in the GaN template or contamination during the fabrication process. The lower pressure sample in Figure 4-4 d) shows areas of different contrast on the *c*-plane, which are likely areas of coalescence into a continuous film or areas where the GaN was not completely covered or it could indicate separate materials absorbing differently the electron beam energy.

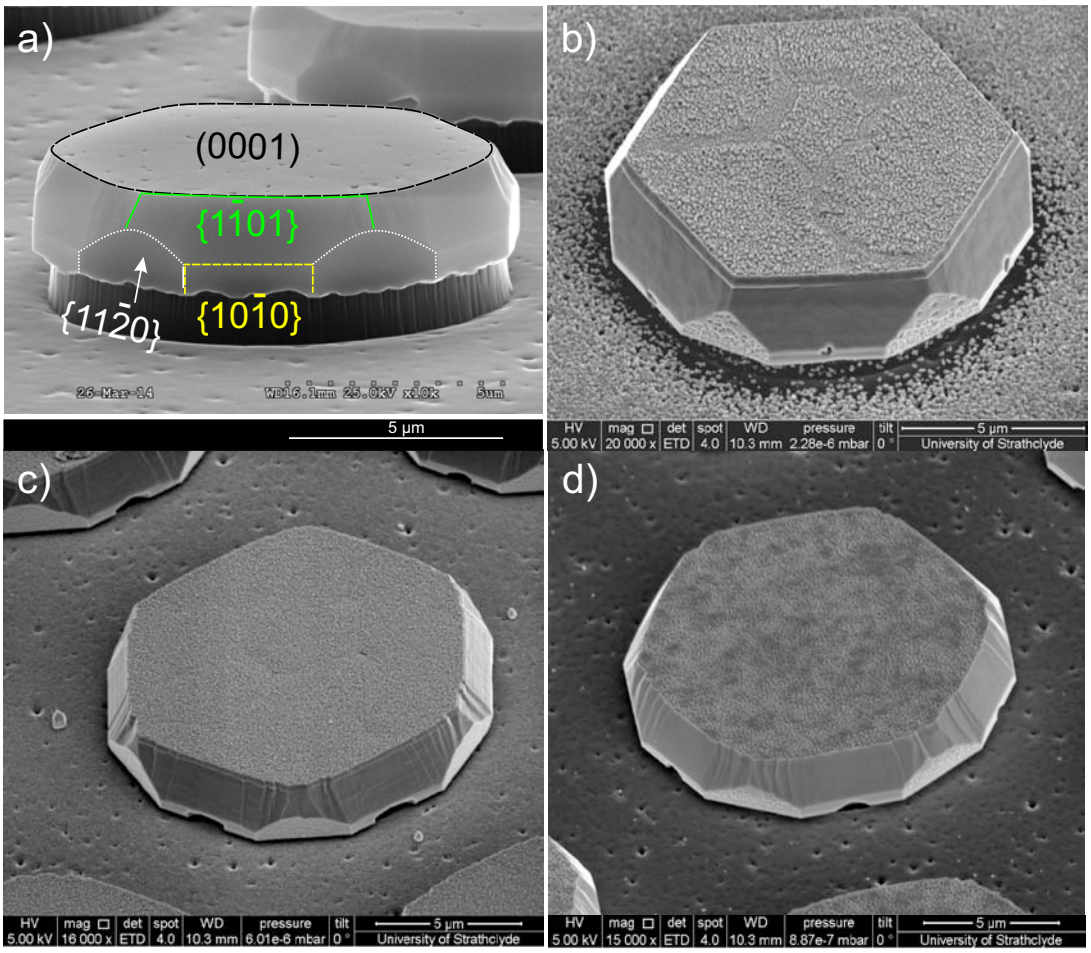

Figure 4-4: InGaN layers grown on GaN large disks template for 30 minutes. a) GaN template 5 min growth with (0001) c-plane, $\{1\,\bar{1}\,0\,1\}$ semipolar facets, $\{1\,0\,\bar{1}\,0\}$ m-plane, and $\{1\,1\,\bar{2}\,0\}$ a-plane, b) InGaN growth at 750 ℃ and 300 mbar c) InGaN 700 ℃ and 300 mbar d) InGaN 750 ℃ and 100 mbar.

The growth rate for the lateral sidewall expansion was determined from image analysis of planar SEM scans for the three samples, each image having $\sim\ 50-60$ micro-disks, with the aim to determine non-polar growth rates. Disk contours were extracted from individual SE images for each pattern. The diameter averages were calculated and considered to reflect the lateral, or sidewall growth rates and are shown in Figure 4-5. No distinction between a- and m-plane could be made, and the sidewall growth represents an average.

The InGaN layer on the sidewall at 750 ℃ and 300 mbar in Figure 4-4 b) was determined to have an average growth rate of ~ 17.5 nm/min. A lower temperature of 700 ℃ in Figure 4-4 c) led essentially to a doubling of the growth rate for InGaN and overall

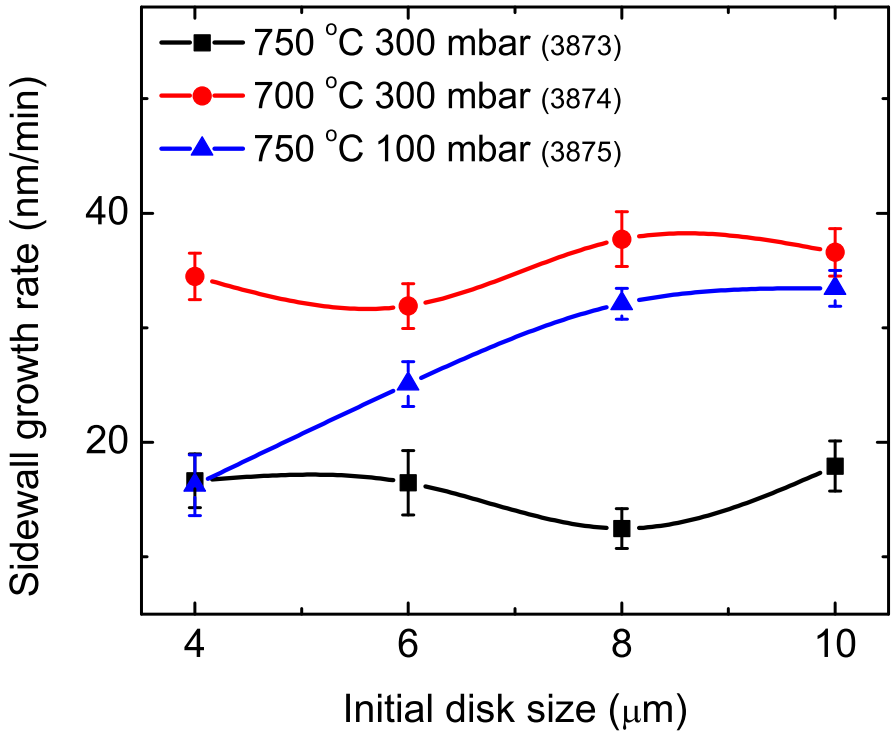

Figure 4-5: Dependence of InGaN lateral sidewall average non-polar growth rate with disk diameter and reactor parameters.

larger disk diameter due to increased indium capture efficiency and lower desorption at low temperatures [81]. Using a lower pressure in Figure 4-4 d) also promotes the gradual increase in semi-polar growth for larger disk diameters.

For both low temperature and low-pressure conditions the remaining non-polar facets are slightly smaller compared to the 750 ℃ and 300 mbar sample. Both sets of reactor parameters proved to encourage the semi-polar plane, which correlates to GaN growth evolution in ref [79]. The rapid increase in diameter would likely continue up to the point for which the non-polar facets are annihilated.

Studying the evolution of crystal planes with the aid of Wulff constructs can be very useful to guide the growth for multi-planar, three-dimensional-based devices. More information on InGaN layers was determined from a set of NR structures, including more accurate non-polar growth rates and emission spectra, which are presented in the next sections.

4.5 InGaN layers on core-shell nanorods

NR arrays were created with a top-down approach similar to the micro-disks, however, nanoimprinting was used to pattern planar GaN/AlN/Si(111) wafers [18]. A Cl_2/Ar plasma etched template consisted of GaN NRs in a hexagonal array pattern of $\sim$ 600 nm diameter and 2 µm pitch distance. Figure 4-6 a) shows a schematic of the GaN NRs fabricated by this process [2]. The initial planar film was an undoped 1.5 µm thick GaN, on top of a 0.5 µm AlN buffer layer for strain management. A thin layer on the Si surface is transformed into a SiN_x passivation layer by the MOVPE nitridation step. The SiN_x layer acts as a selective growth mask and limits re-growth only on the etched GaN cores, as shown in Figure 4-6 b).

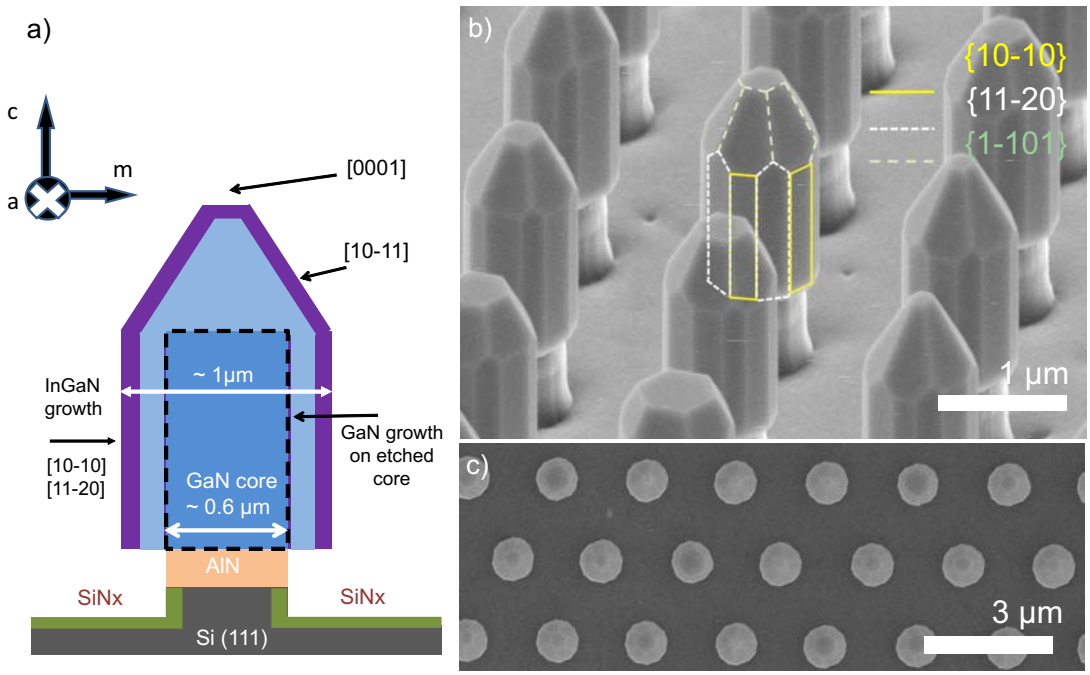

Figure 4-6: a)Schematic of a core-shell NR with etched GaN core and GaN/InGaN growth (not to scale), b) GaN template with various crystal facets, c) planar view of GaN template shows excellent diameter uniformity. Reprinted from ref [141] with permission from SPIE.

[2]Gîrgel, I. ,Edwards, P. R. Le Boulbar, E., Coulon, P.-M., Sahonta, S.-L. Allsopp, D. W. E., Martin, R. W., Humphreys, C. J., Shields, P. A. "Investigation of indium gallium nitride facet-dependent nonpolar growth rates and composition for core–shell light-emitting diodes", *J. Nanophotonics* 10, 16010 (2016). Copyright 2016 Society of Photo Optical Instrumentation Engineers. doi.org/10.1117/1.JNP.10.016010

4.5.1 Regrowth for GaN template

The MOVPE nitridation step was performed at 1050 ℃ for 10 minutes, during which only the NH_3 flow (1600 sccm) is turned on. A GaN nucleation step (4 min, TMGa 3 sccm) at 980 ℃ and a short GaN facet recovery step (5 min, TMGa 8 sccm) at 1060 ℃ were achieved in the MOVPE reactor. The pressure was set at 50 mbar to obtain NRs with as many crystal planes as possible, as shown in Figure 4-6 b).

The InGaN growth on the NR templates was performed during the same epitaxial growth as the micro-disks, thus the same conditions were applied: 750 ℃ and 300 mbar, 700 ℃ and 300 mbar, and finally 750 ℃ and 100 mbar. All the other reactor parameters were unchanged, with the TMIn and TMGa precursor flow kept constant at 200 sccm and 9 sccm respectively. The growth time of 30 minutes was chosen because InN can be easily lost to dissociation at the relatively high temperatures used [152]. The comparatively high temperatures were applied to limit the occurrence of point defects [51]. Furthermore, to determine reliable growth rates from the non-polar facets from SEM images, a longer growth time was required.

4.5.2 Uniformity of nanorod diameters

Image processing software was used to determine statistically the amounts of growth after each step. Once optimized to reproduce the exact contours of the NRs, the SEM images taken without changing magnification were processed, maintaining the image analysis algorithm unchanged. The effects of the different growth conditions on diameter distributions are shown in Figure 4-7 b). The lower temperature sample (700 ℃, 300 mbar) was analyzed by transmission electron microscopy (TEM) to examine the InGaN growth in more detail. The optical properties were assessed by cathodoluminescence (CL) hyperspectral imaging, to estimate InN mole fraction and determine emission characteristics, notably uniformity on the non-polar facets.

4.5.3 Effect of growth parameters on InGaN morphology

For micron sized GaN structures shown in section 4.4, the crystal planes are expected to have different relative growth rates [140], subject to growth parameters [93, 79]. However, it is unclear if the growth on rod-shaped nanostructures will be similar to the disk structures because of the different geometry. For example, the dimensions of the facets could be smaller than the diffusion lengths of Ga or In atoms, and the evolution of strain at the interfaces may be different, with impact on the InN fraction.

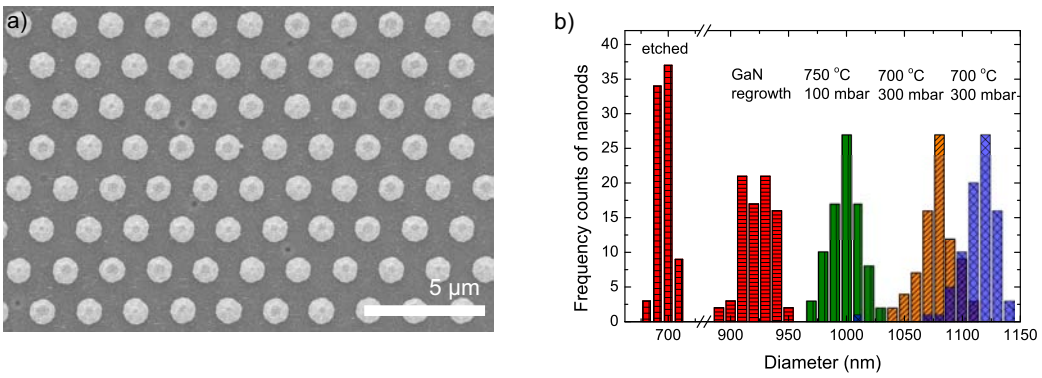

Figure 4-7: a) Planar SEM image used to estimate NR diameters on 700 ℃ 300 mbar sample b) Distribution of NR diameters for each processing step, and for each of the InGaN growth conditions (reprinted from ref. [141] with permission from SPIE.)

The GaN NRs maintained a residual [0001] c-plane in Figure 4-8 a) due to the short GaN facet recovery step. As with the disk samples, the semi-polar $[1\,\bar{1}\,0\,1]$ direction is slower growing and more stable, and with sufficient growth time, the NR tips would take the shape of a self-limiting pyramid [153, 154, 155]. However, unlike the micro-disks, the initial surface area of the $\{1\,\bar{1}\,0\,1\}$ facets relative to the non-polar surfaces is much smaller, therefore the non-polar facets on NRs can be maintained for longer growth times, and the measurements of lateral growth are pertinent for non-polar planes.

Figures 4-8 a-c) show SEM images of the three InGaN growth runs, in which the various crystal orientations are retained and can be identified: [0001], $[1\,\bar{1}\,0\,1]$, $[1\,1\,\bar{2}\,0]$, and $[1\,0\,\bar{1}\,0]$. The remaining c-plane surface shows an increase in roughness, indicating a layer of unstrained indium-rich growth [156]. Temperature and pressure have a dominant impact on the InGaN growth rates and the a- and m-planes, with influence over the relative facet size and surface roughness. The size of the a-plane is determined by the initial GaN template, where high temperature and low pressure changed the relative growth velocity difference between the two non-polar planes. Starting from the faceted GaN core, the use of a relatively high temperature (750 ℃) for InGaN growth, has reduced the proportion of a- to m-plane. This can be explained by an increase of the relative growth velocity of the $\{1\,1\,\bar{2}\,0\}$ facet at a higher temperature. Furthermore, there is a tendency for indium atoms to stick at the apexes between planes, which create more irregular surfaces where the adatoms are more readily captured [102].

At 700 ℃ and 300 mbar the relative growth rates of the non-polar planes are closer in value, causing a different a- to m-plane surface ratio. Also, the indium desorption

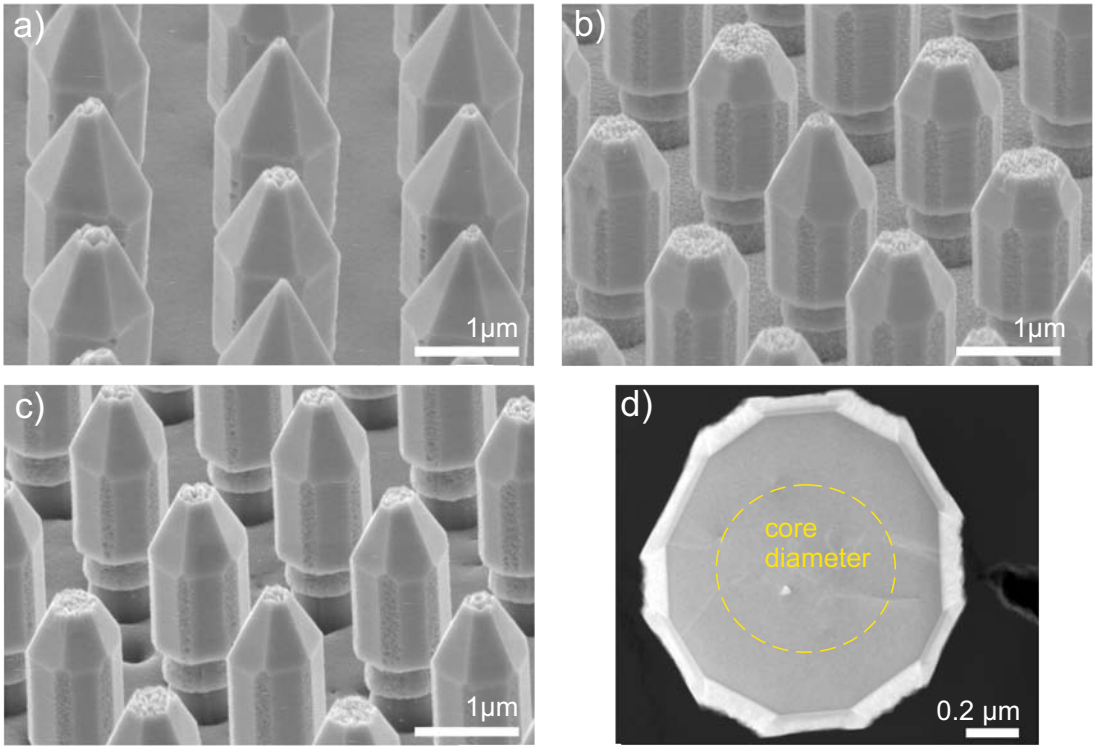

Figure 4-8: a) Angled view of 750 ℃ 300 mbar NR sample with very little *a*-plane remaining, b)NRs on 700 ℃ 300 mbar sample with rough non-polar and *c*-plane surfaces c)NRs on 750 ℃ 100 mbar sample with apparently smoother *m*-facets d)TEM cross-section plan-view through a NR grown at 700 ℃ 300 mbar with *m*- and *a*-planes. (reprinted from ref. [141] with permission from SPIE.)

and diffusion length are both lower, making the incorporation of more indium atoms possible. In ref. [147] it is indicated that a statistical roughening of the surfaces can be expected on the $[0\,0\,0\,1]$ and $[0\,0\,0\,\bar{1}]$ directions, if the diffusion length becomes shorter than the mean distance between binding sites. Similarly, this could explain the roughening of the sidewalls in Figures 4-8 c) and b), especially visible for the *a*-plane.

Reduction of the growth pressure to 100 mbar, at a temperature of 750 ℃, had the effect of reducing the InGaN growth rates of both the *a*- and *m*-planes from 3.2 nm to an average rate of ∼1.3 nm/min. The size of the *a*-plane is determined by the initial GaN template. The presence of residual $\{1\,1\,\bar{2}\,0\}$ *a*-planes on this sample, by contrast to the other sample at 750 ℃ (Figure 4-8 a)), indicates the relative growth velocity in the Wulff $\nu-$plots are affected by pressure. Alternatively, because of the lower growth rate, the *a*-plane has not had sufficient time to be extinguished.

In summary, high temperature (750℃) has reduced the proportion of *a*- to *m*- plane,

because of the relative increase of the $\{1\,1\,\bar{2}\,0\}$ facet growth velocity. The reduction in growth pressure tends to increase indium surface diffusion [157] because low pressure reduces the indium atom collision probability. This has had the effect of reducing the overall growth rate on the non-polar planes. Within the range of growth parameters available, the a-plane grows as fast as, or faster than the m-plane, suggesting that finding a growth recipe to create a substantial a-plane surface area would be difficult to achieve for a core-shell device through a growth process alone.

4.5.4 Non-polar growth rates on core-shell nanorods

Table 4.1 lists the combined average growth rates of the non-polar planes obtained from the image analysis method for the three NR samples used. The growth rates were determined from SEM images and from the radial cross section (i.e. plan view) TEM image of a single NR. The SEM and TEM were calibrated differently, which explains the discrepancy in measured diameters on the same sample. Image processing for the TEM data was done in a similar manner to the SEM data. The growth rate from the TEM image was determined to be 2.3 nm/min on the m-plane, and 3.1 nm/min on the a-plane, making the ratio of m/a growth rates of 0.74, for 700 ℃ and 300 mbar.

Table 4.1: Non-polar growth rates on nanorods corresponding to the three sets of InGaN growth parameters (reprinted from ref. [141] with permission from SPIE.)

Sample	Method	Diameter (std.dev) (nm)	Sidewall thickness (nm)	Avg. growth rate non-polar facets (nm/min)
GaN regrowth	SEM	923 (13)		
750 ℃ 300 mbar	SEM	1113 (17)	95.2	3.2
750 ℃ 100 mbar	SEM	999 (13)	37.9	1.3
700 ℃ 300 mbar	SEM	1079 (15)	78.0	2.6
	TEM	1265	84.6	2.8

Examining the TEM lamella in Figure 4-8 d), it is worth mentioning that the GaN facets grow seamlessly at the etched interfaces, because there is no contrast difference between the GaN core and overgrown GaN facets. However, the InGaN shell is immediately distinguishable. Furthermore, the different contrast within the InGaN growth on the GaN m-plane facet indicates a possible change in InN mole fraction after an initial critical layer was grown, probably related to a change in strain or in growth mode.

The results confirm that the InGaN growth rates and InN mole fraction are strongly

dependent on the crystal plane orientation and growth parameters. The latter can be used to alter the relative growth rates between the m- and a-plane, leading to a different surface size of the $\{1\,1\,\bar{2}\,0\}$ facet. Roughness on the crystal facets, caused by either relaxed InGaN growth resulting from a 3D growth mode, or rapid InN incorporation related to the short diffusion length of In, is likely to cause local variations in the InN mole fraction and a widening of luminescence emission spectra.

4.5.5 Cathodoluminescence characterization on nanorods

Cathodoluminescence hyper-spectral imaging was used to determine the emission characteristics of the thick InGaN shells on the different facets of the NRs. Using the energy versus composition equation 4.1, and a bowing parameter of $b \sim 2.8$ eV for relaxed [158] InGaN layers (or b =1.43 eV for strained layers [159]), the emission peak energy can be used to estimate the InN fraction for InGaN layers (see Figure 4-9). Band gap values[3] used to fit equation 4.1 are dependent on measurement temperature and strain (i.e. E_g^{GaN} was considered at 3.42 eV for room temperature, and 3.478 eV for low temperature measurements, while E_g^{InN} values range between ~ 0.66 eV in strained layers and ~ 0.8 eV for relaxed layers).

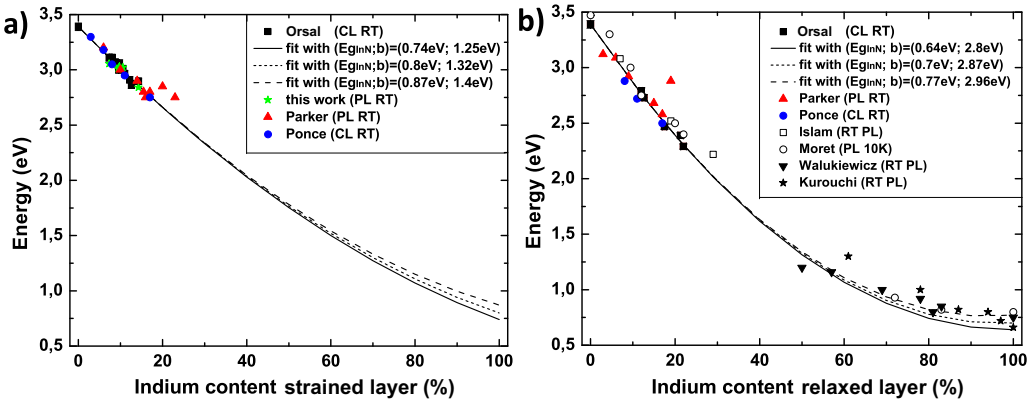

Figure 4-9: Evolution of InGaN bandgap with composition for a) strained and b) relaxed layers. (Parker[143], Walukiewicz[160], Ponce[161], Kurouchi[162], Moret[158], Islam[163], (adapted from ref.[164], with permission of The Optical Society).

$$E_g^{InGaN} = xE_g^{GaN} + (1-x)E_g^{InN} + bx(x-1) \tag{4.1}$$

[3]Republished from G. Orsal, Y. El Gmili, N. Fressengeas, J. Streque, R. Djerboub, T. Moudakir, S. Sundaram, A. Ougazzaden, and J.P. Salvestrini, "Bandgap energy bowing parameter of strained and relaxed InGaN layers", *Opt. Mater. Express 4*, 1030-1041 (2014), with permission of The Optical Society

The estimated InGaN layer widths were sufficiently large to consider the quantum confinement effect negligible, therefore the photon emission energy provides a good estimate of the band gap and composition. Hyperspectral CL measures a full spectrum from each point on the sample surface scanned by the electron beam. CL spectra were collected at room temperature for a beam energy of 5 keV and step size of 25 nm, to create 200×200 pixel maps. Figures 4-10 a-c) show *real color images*, calculated from the chromaticity coordinates of the collected spectra.

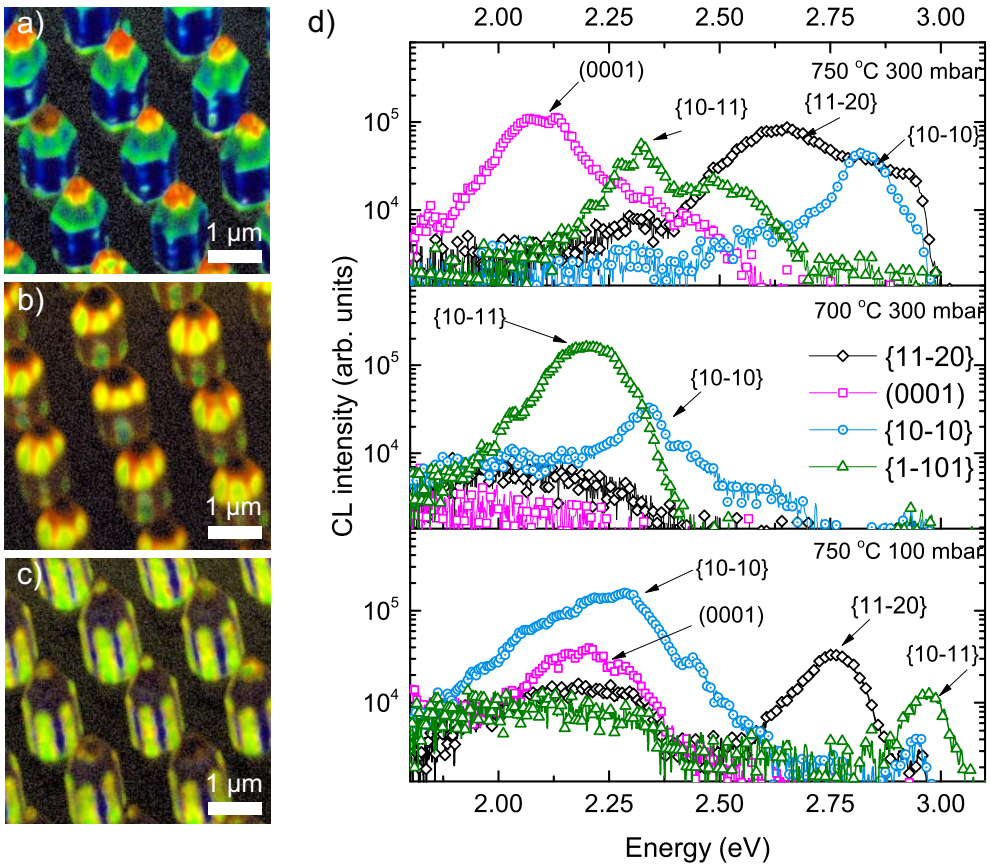

Figure 4-10: Real color maps of the three sample sets and growth parameter sets used: a)750 ℃ 300 mbar, b)700 ℃ 300 mbar, c) 750 ℃ 100 mbar. d) Spectra of each sample set, with InN fractions dependent on the different crystal facets. (Reprinted from ref. [141] with permission from SPIE.)

The CL maps in Figures 4-10 a-c) prove that each sample emits at different wavelengths, depending on the crystallographic facets and InGaN composition. Corresponding spectra extracted from the same hyperspectral datasets are shown in Figure 4-10 d) for the crystal planes mapped. The spectra were taken from representative areas on the NRs,

averaging 4×4 pixels from each facet.

The emission wavelengths and estimated InN fractions are summarized in Table 4.2. On all samples, the residual (0001) plane emission covered a wide wavelength range, from 2.05−2.28 eV, and with varying relative intensities from sample to sample. For the sample grown at 750 ℃ and 300 mbar (Figure 4-10a), the $\{1\,0\,\bar{1}\,0\}$ m-plane displayed emission with a main peak at 2.83 eV and a shoulder at 2.65 eV. The remaining $\{1\,1\,\bar{2}\,0\}$ a-plane was much smaller due its high growth velocity compared to the $\{1\,0\,\bar{1}\,0\}$ plane. The a-plane main emission was centered at 2.65 eV, and a high energy shoulder at 2.83 eV, likely from nearby m-planes. The $\{1\,\bar{1}\,0\,1\}$ semi-polar facets exhibit two emission peaks from the facet center (2.49 eV), and a lower energy peak (2.33 eV) towards the facet edges. The latter is caused by either enhanced InGaN relaxation at the facet apexes, or by increased indium atom incorporation in the localized regions or both.

For the 700 ℃ NR sample, no emission was identified on the rough a-plane, likely caused by surface states and non-radiative recombination [165] at high indium concentrations [166]. There were areas with emission peaks from the $\{1\,0\,\bar{1}\,0\}$ facets at 2.35 and 2.62 eV and a weak shoulder at 2.95 eV. This is probably caused by a varying indium fraction incorporation on the more irregular surfaces of this sample, while the 2.95 eV may originate from a likely underlying strained InGaN layer, observed in the TEM image (see Figure 4-8 d). The dominant emission for this sample originates on the $\{1\,\bar{1}\,0\,1\}$ semi-polar facets and is centered at 2.20 eV. Overall the decrease in temperature resulted in red-shifted emission on all the sample's facets, due to higher indium incorporation and reduced desorption rate.

The sample grown at 750 ℃ and 100 mbar shows a broad emission around 2.29 eV (see Figure 4-10c) which originates on the $\{1\,0\,\bar{1}\,0\}$ facets, with additional peaks at 2.43 and 2.95 eV, the latter possibly due to a strained layer. The $\{1\,1\,\bar{2}\,0\}$ planes have a distinct emission at 2.75 eV. The $\{1\,\bar{1}\,0\,1\}$ semi-polar planes emit at 2.97 eV with a low-intensity peak, and this emission intensity is reduced by one order of magnitude with respect to the other crystal facets. There is a corresponding increase in the emission from the defect-related "yellow band". The incorporation of a larger number of point defects at this pressure could explain why the main band emission peak is reduced.

The relative CL emission peak intensities can give some indication of the variation in crystal quality with growth parameters. For both a- and m- non-polar planes, higher CL intensities were obtained at a higher temperature and lower pressure. In contrast, the emission intensity for the semi-polar $\{1\,\bar{1}\,0\,1\}$ plane was enhanced by lower temperature and higher pressure, also leading to high InN fractions being incorporated. However,

the latter conditions may limit emission from the m-plane.

Table 4.2: Observed CL peak emission energy and InN mole fraction, as a function of the bandgap energy. (Reprinted from ref. [141] with permission from SPIE.)

Sample	750 ℃ 300 mbar			700 ℃ 300mbar			750 ℃ 100 mbar		
Plane	$m-$	$a-$	$\{1\,\bar{1}\,0\,1\}$	$m-$	$a-$	$\{1\,\bar{1}\,0\,1\}$	$m-$	$a-$	$\{1\,\bar{1}\,0\,1\}$
Peak (eV)	2.83	2.65	$2.33-2.49$	$2.35-2.95$	–	2.20	$2.29-2.95$	2.76	2.97
InN (%)	13	17	$25-20$	$24-14^a$	–	27	$25-14^a$	15	13^a

[a]Value determined using a strained InGaN bowing parameter[159]

Table 4.2 shows the InN mole fraction estimated from the CL peak emission energy. The decrease of the growth temperature from 750 to 700 ℃ led to the increase in InN mole fraction, estimated by CL to be from $13-24\%$ on the $\{1\,0\,\bar{1}\,0\}$ plane, and from between $20-30$ % on the different regions of the $\{1\,\bar{1}\,0\,1\}$ plane. As can be seen in Table 4.2, at 300 mbar the average InN mole fraction is higher on the $\{1\,1\,\bar{2}\,0\}$ and $\{1\,\bar{1}\,0\,1\}$ (17% and $20-25$ % respectively). On the $\{1\,0\,\bar{1}\,0\}$, for which the InN fraction is estimated at $\sim$ 13%. This result indicates that, despite the thick shell and the likelihood of unstrained growth, the above-mentioned growth conditions still limit the InN fraction incorporation efficiency on the m-plane.

The reduction in pressure from 300 mbar to 100 mbar, at a constant temperature, has caused a change in the InN mole fraction between the non-polar planes. A greater indium composition resulted on the $\{1\,0\,\bar{1}\,0\}$ facets (25%) than on either the $\{1\,1\,\bar{2}\,0\}$ (15%) or on the semi-polar $\{1\,\bar{1}\,0\,1\}$ planes (10%). For the latter, given the high possibility, the layer is in fact strained, the $\{1\,\bar{1}\,0\,1\}$ composition may be $10-13\%$, if a strained band bowing parameter is considered [159]. This was unexpected as the growth rate was low on this sample (see Table 4.1), and both low pressure and high temperature cause high diffusion lengths for the indium atoms. However from work on c-plane [167, 168] and planar thin films on a-plane [169], it was found that low pressure can increase indium incorporation. This was suggested to be caused by the suppression of indium desorption, with enhanced gas mass transfer rates of precursor species through the boundary layer [167], as the diffusion of gasses varies inversely proportional with pressure [170]. The measurements reported here show that low pressure encourages high InN incorporation efficiency on the m-plane, thus allowing InGaN layers with a high InN mole fraction to be obtained.

4.6 TEM and EDX analysis on InGaN/GaN on core-shell nanorods

The NR sidewalls are free surfaces that allow easier strain relaxation and higher InN incorporation than in 2D layers. Therefore, NR LEDs could provide longer the emission wavelengths necessary for green and red LEDs.
For growth of planar [0 0 0 1] InGaN on compressively strained [0 0 0 1] GaN, a thin pseudomorphic strained layer achieved with a short growth time and a limited InN fraction can be grown [144, 145]. With longer growth, higher InN fraction may be incorporated, however, the layer experiences an increase in strain. To release accumulated strain energy, the growth mode changes to a mix of planar and island 2D-3D growth, or Stranski-Krastanov (SK) growth mode. In the SK mode, the relaxed islands or nano-pyramids can more readily capture indium [145]. A graded InN fraction within in the layer was associated with the increase in InGaN layer thickness and strain relaxation [171, 146]. In this work the various crystal orientations were retained on NRs and were identified as the [0 0 0 1], [1 $\bar{1}$ 0 1], [1 1 $\bar{2}$ 0], and [1 0 $\bar{1}$ 0]. A comparison study of the previous CL estimates for InN fraction was carried out using energy dispersive X-ray spectroscopy (EDX) measurements, to understand the InGaN evolution on the mentioned planes.

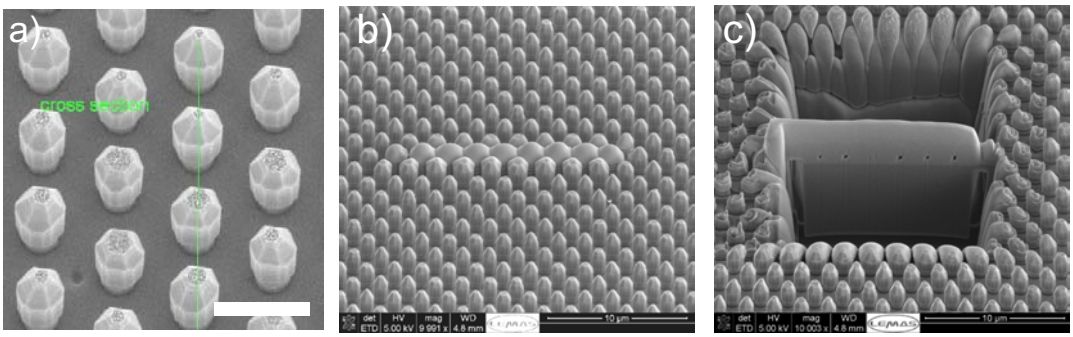

Figure 4-11: Focused ion-beam cross-section preparation: a)SEM image showing cross-section direction b) electron beam induced platinum deposition envelops NRs in a 15×2 µm platinum layer c) Si ion beam etching of trenches around and on the sides of the slab with NRs.

Planar and side view cross-sections on the 700 ℃ 300 mbar sample were prepared for TEM-EDX measurements (see Figure 4-11). To reduce the sample cross-section, a focused Si ion beam (30 kV) was used to achieve a $\sim 100 - 200$ nm section thickness through the NRs. To image the sample a Tecnai Osiris scanning-transmission electron

microscope (STEM) was operated at 200 kV and the high-angle annular dark-field (HAADF) Z-contrast images showed regions of high In content in bright contrast. The EDX spot size was approximately 2 nm with similar size interaction volume. The sample preparation was done by Dr. Michael Ward at the University of Leeds. The EDX measurements were carried out by Dr. Suman-Lata Sahonta at the Cambridge Center for Gallium Nitride.

A close-up planar section through a NR and overlayed EDX maps are shown in Figures 4-12 a-d). A change in the TEM contrast can be observed on the $\{1\,0\,\bar{1}\,0\}$ m-plane facets, which corresponds to a change in EDX InN concentration from $\sim 13-15\%$ at the GaN interface, to 20% towards the InGaN surface layer (Figures 4-12 b-c). The change indicates a likely transition from a pseudomorphically strained InGaN-on-GaN layer to partially or fully relaxed InGaN layer [142]. The EDX maps in Figures 4-12 b) and d) reveal that the a-plane facet undergoes a similar transition, from an initial lower InN fraction of 12%, to a higher InN incorporation in the upper layer to $\sim 25-35$ %. The distribution of InN appears less uniform in the a-plane and takes the shape of InN-rich (35%) stripes. The apexes between the two non-polar facets (Figure 4-12) show a similarly high concentration, with the m-plane in the vicinity of the apex increasing to 25%. The stripes build up on the pseudomorphically strained InGaN and do not start on the immediate GaN interface (Figure 4-12b). It can be concluded that the presence of a-plane on the template, either intentional or as a case of insufficient facet recovery growth time, can result in regions of high indium content at the apexes of the NRs.

In Figures 4-12, the total InGaN layer thickness on the m-plane was measured as $\sim 63-75$ nm. However, as was shown in the EDX maps, two different InN fractions are grown. The thickness of the likely strained layer at the GaN interface was measured as $\sim 22-25$ nm. The neighboring a-planes are visibly thicker $\sim 87-94$ nm. The likely a-plane strained layer at the GaN interface was measured to be $7-9$ nm. The surface facets on the a-plane are highly irregular and look pyramidal, which may indicate a relaxed SK growth mode. The increase in thickness in the apex area between the two non-polar planes, as seen in Figure 4-12, can be explained by the growth front advancing from the convex surface formed by the a- and m-planes. It can be speculated that during the early stages of the InGaN growth, the InGaN layer is first relaxed at the apexes. This may explain the fact that a build-up and increase in InN fraction occurs at these relaxed sites as observed in [104, 102].

Figures 4-13 a-d) show cross-sections of a single NR, with the a-, c-plane, and the $\{1\,\bar{1}\,0\,1\}$ semi-polar plane. Similar to the planar sections in Figure 4-12, the a-plane has a rough surface (Figure 4-13 b-c) and shows a graded transition from the GaN

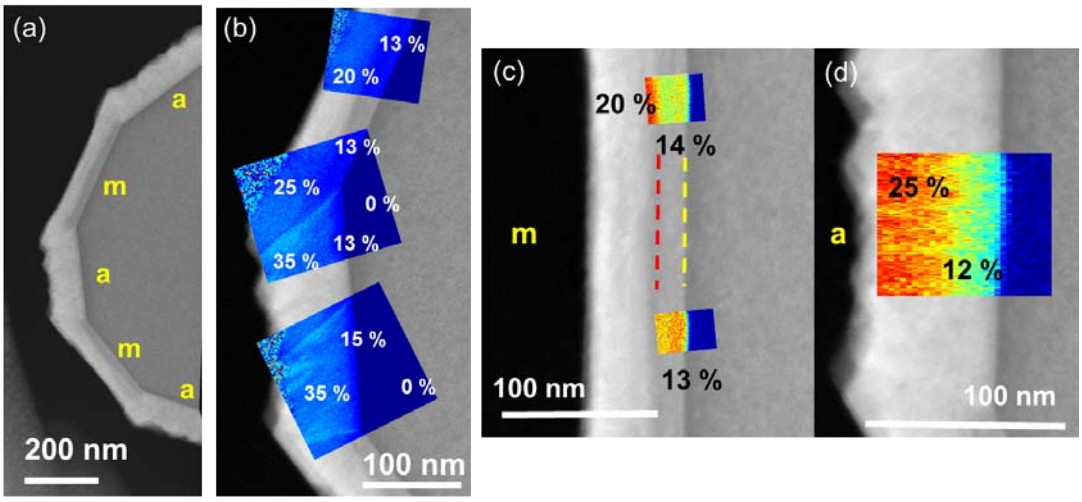

Figure 4-12: Map of InN fraction on planar crystal planes on NRs. a) NR planar view with *m*- and *a*-facets, b) EDX analysis on InN fraction at the apexes at the non-polar facets, c) detail view on *m*-plane with two distinct fractions of 20% and ∼13-14% InN, d) *a*-plane with distinct InN fractions, perspective on the semi-polar plane.

interface (14% InN) to higher InN fraction (26%). The growth in the [0 0 0 1] direction in Figure 4-13 c) occurs with fast incorporation of rich InN nuclei (35%). Further growth around the rich nuclei appears to form relaxed nano-pyramid shapes. The semi-polar plane achieves a 20% InN incorporation from a 30 nm thick layer with local geometry variations observed in Figure 4-13d). A thin intermediary layer of $2-3$ nm likely exists on the semi-polar plane, although the resolution is limited by the thick lamella.

Summary on InGaN integration

Both CL and EDX analyses indicate similar changes for InN fractions with crystal orientations and growth parameters. CL may overestimate the InN fraction on the semi-polar facets (27% vs 20%) because of a larger excitation spot or local sample variation. EDX showed that fast-growing *a*-planes result in local InN-rich regions, and perhaps cause a decrease in CL emission (Figure 4-10 b)) due to an accompanying increase in non-radiative defects. Single CL peak luminescence was observed for thin and possibly strained InGaN layers, below the critical layer thickness, while multiple and wide emission peaks were present in thick and relaxed layers. At 5 keV the CL electron beam has a penetration depth of $\sim$ 200 nm and could indicate luminescence peaks for both strained and relaxed InGaN layers. In EDX measurements the non-

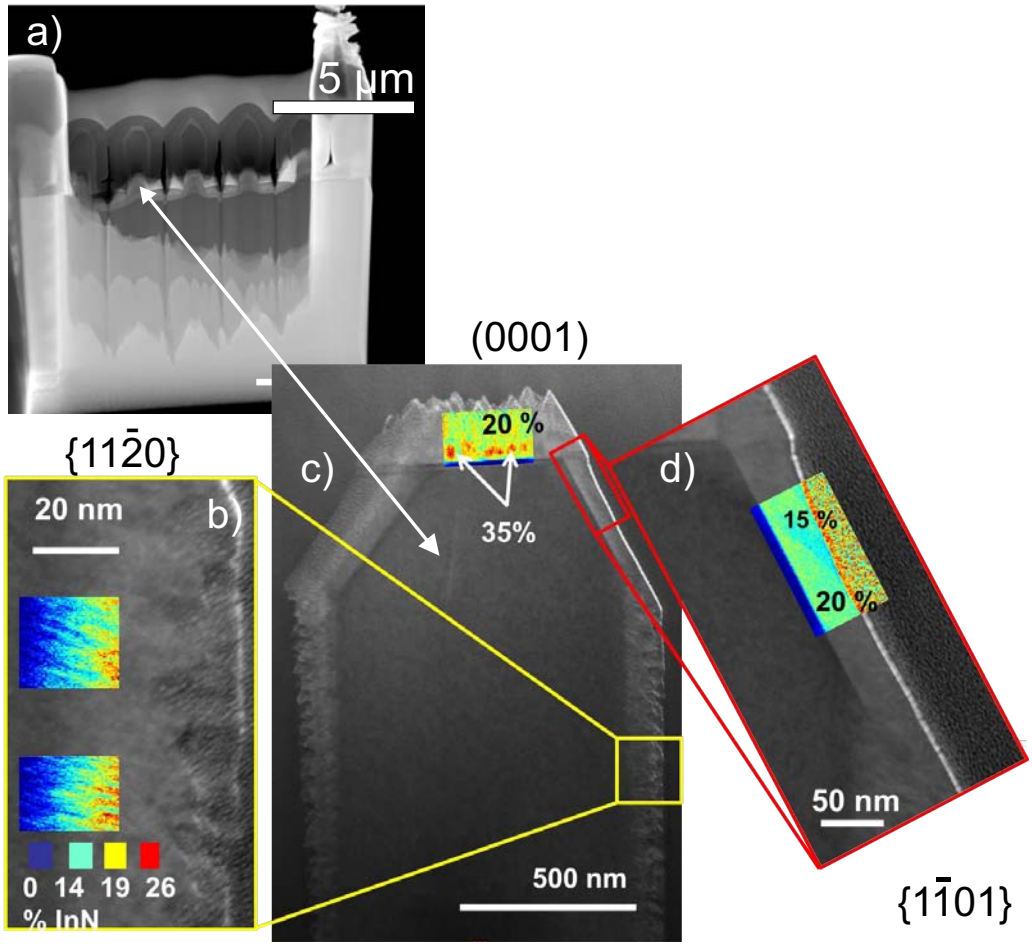

Figure 4-13: Map of InN fraction on different crystal planes on NRs. a) TEM comb of cross-section NRs, the 2nd NR was examined. b) close up of *a*-plane cross-section c) close up of NR with a top *c*-plane with clusters of rich InN d) perspective on the semi-polar plane.

polar facets showed that InN incorporation starts with a likely strained InGaN layer and progresses with increasing strain relaxation towards a higher InN fraction. There was a large contrast between the smooth surface and integration on the $\{1\,\bar{1}\,0\,1\}$ *m*-plane and the non-uniform and rough $\{1\,1\,\bar{2}\,0\}$ *a*-plane.

4.7 Conclusions

GaN templates of high-aspect ratio nanorods with (0001),$\{1\,0\,\bar{1}\,0\}$, $\{1\,1\,\bar{2}\,0\}$ and $\{1\,\bar{1}\,0\,1\}$ facets were fabricated to study the effects of pressure and temperature on the growth

rates of non-polar planes. The nanorods revealed that the combined non-polar growth rates varied from 1.3 to 2.8 nm/min with growth parameters. Using TEM the *a*- (3.1 nm/min) and *m*-plane (2.3 nm/min) growth rates were determined, for the InGaN sample grown at 700 ℃. The reduction in pressure to 100 mbar led to lower growth rates overall, but to more efficient InN mole fraction integration on the $\{1\,0\,\bar{1}\,0\}$ *m*-plane.

Each growth led to a different set of CL emission peaks, and different InN fractions were incorporated on each facet. The InN mole fraction was estimated by comparing the measured CL emission peak with previously published data. EDX data showed similar InN fractions and the evolution of InGaN layers, from an initially strained layer with low InN, to a richer InN fraction and relaxation with growth time. Relaxation can explain the tendency in other current studies [104, 172] for the existence of In-rich regions at the *m*-plane and semipolar plane junction and of wide spectra. However unlike those studies, the present array of high-aspect ratio NRs and large pitch, showed under careful control of reactor parameters, uniform layers of green-yellow emitters with a high InN mole fraction on the $\{1\,0\,\bar{1}\,0\}$ *m*-planes could be achieved.

Chapter 5

Doping for GaN nanorods

Electrical devices based on core-shell structures require the presence of doping impurities in the n-GaN and p-GaN layers to provide free carriers. This chapter focuses on p-GaN doping, particularly on the growth and characterization of p-n homo-junctions on NRs. A very good control of the doping concentrations and p-n junction thickness are required, subjects yet insufficiently understood for their application to core-shell NRs. Different growth parameters and dopant flows were used to achieve doping on NRs and the resulting samples were characterized by μPL, CL and Raman spectroscopy. Optically sensitive Mg-doping-related emission peaks were observed and used to estimate carrier concentrations. Similarly, changes in lattice vibrational modes occur due to Mg doping. The combination of non-contact optical methods was applied to analyze the uniformity of magnesium incorporation on the NR sidewall. This approach is of high interest as conventional electrical methods such as the Hall effect cannot be applied to nanorods, because a reliable Van der Pauw geometry and low resistance ohmic contacts are very difficult to achieve.

The samples were processed, grown by MOVPE and characterized with μPL by myself, and further characterization by CL was performed by Prof. Alexander Šatka and Dr. Juraj Priesol from the Bratislava University of Technology. Raman characterization was done on a high-resolution Renishaw in Via spectrometer with the help of Dr. Timothy Batten from Renishaw plc. The findings are under review for publication.

5.1 N-type doping on nanorods

A semiconductor with a majority of carriers in the conduction band (electrons) is classed as n-type. The impurity element needs to have a higher number of valence electrons than the semiconductor. Impurity atoms of Si provide nearly free electrons in the GaN lattice. Silane (SiH_4) precursor is typically used for GaN n-doping, which substitutes a Si atom onto a Ga site [173]. The GaN on sapphire templates used in this work were already doped to 3×10^{18} cm^{-3} electrons.

Impurities incorporate into the crystal lattice and introduce new Raman resonances or modes, particular to the impurity, which for concentrations higher than background levels can with Raman spectroscopy. Different impurities or defects can thus be detected by Raman vibrational modes, although the modes interpretation can be complicated. The epitaxial GaN films used as templates in this work had been n-doped and the presence of Si atoms was confirmed by Raman measurements. Figure 5-1 a) shows the Raman spectra of a measured undoped planar GaN film on sapphire.

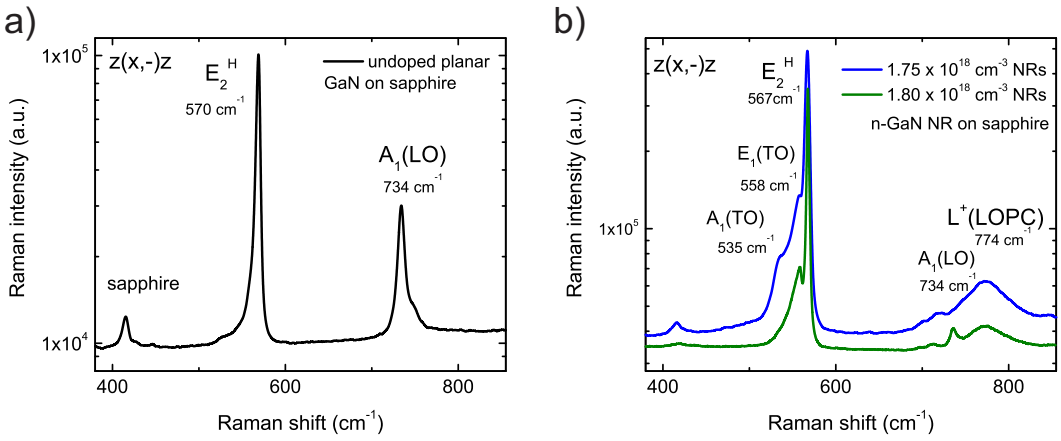

Figure 5-1: a) Raman spectra in log scale for planar undoped GaN in $z(x,-)\bar{z}$ (no polarization) configuration, b) coupling effect of n-type impurities in the L^+ LOPC and shift of the $A_1^{(LO)}$ peak; the other GaN characteristic peaks are visible for NR samples due to the breakdown of the selection rules.

Using Figure 5-1 b) the doping levels for n-type GaN can be estimated from the shift of coupled $A_1^{(LO)}$ position by contrast to the uncoupled position in the undoped sample. The shift was caused by the longitudinal optical phonon-plasmon coupling (LOPC) [129]. The LOPC indicates electronic states and lattice vibrations introduced with n-doping. The LOPC mode consists of lower (L^- -not shown) and higher frequency (L^+) branches, and the increase concentration of n-type carriers broadens the LOPC

L^+ branch, observed in Figure 5-1 b), and shifts the LOPC to higher frequencies.

The carrier density was estimated using a simplified formula in expression 5.1, for which the damping rates of the phonon and plasmon are neglected and the phonon frequency is determined from the $A_1^{(LO)}$ shift ($\Delta\omega$), relative to its uncoupled position at 734 cm^{-1}. The estimate is lower than the GaN data sheet (3×10^{18} cm^{-3}) for the two samples, which indicates that either the resolution of the method is not sufficient or that the formula should be completed with the additional material characteristics in ref [129], which were not known.

$$n = 1.1 \times 10^{17} \Delta\omega^{0.764} \tag{5.1}$$

5.2 Magnesium p-type doping on nanorods

Magnesium is currently the only effective impurity with fewer valence electrons than GaN, which can reliably provide free hole carriers. Because of the high ionization energy of Mg ($\sim$ 200 meV), it is necessary that high Mg atom concentrations ($\sim$ $10^{19} - 10^{20}$ cm^{-3} Mg atoms) have to be incorporated in the GaN lattice, to ensure that a sufficient number of free holes ($\sim 10^{17} - 10^{18}$ cm^{-3}) can be obtained for electron-hole recombinations [109].

The number of free holes is limited during the growth stage, due to the tendency of hydrogen found in the MOVPE reactor (either from the NH_3 precursor or due to contributions from the carrier gas) to bond to, and passivate the Mg atoms[7]. The high number of passivated Mg-H bonds can result in high electrical resistance. The annealing process decreases the resistance of the p-GaN.

Incorporation of Mg during MOVPE with bis(cyclo-penta-dienyl)-magnesium (Cp_2Mg) precursor introduces characteristic features in the μPL and CL spectra, originating from Mg atoms and likely from several other compensating complexes. The main luminescence peak at 3.27 eV has been commonly attributed to a donor-acceptor-pair (DAP) transition [174], between a Mg acceptor level and a donor level involving hydrogen [175, 176, 177]. Activation by thermal annealing process was shown to correspond to dissociation of Mg-H bonds [7, 175]. Once the Mg-H bonds are broken the isolated Mg acceptor level is considered active.

Magnesium related PL emission at low temperature (4K) on planar layers as well nanowire arrays, show similar emission wavelengths and peak positions as described in refs [177, 178, 179]. In highly Mg-doped GaN ($> 10^{18}$ cm^{-3}), at least one further luminescence peak has been observed at 3.15 eV and has been attributed to Mg-related

Table 5.1: Summary of literature values for Mg related optical transitions.

Peak energy (eV)	Assignment	Mg conc.(at.) (cm^{-3})	Conditions and refs.
3.287	DAP	$< 1 \times 10^{18}$	2K [182]
3.275	DAP2	8×10^{17}	2K [182]
3.256	DAP3	$> 2 \times 10^{18}$	2K [182]
3.27	DAP	$1 - 2 \times 10^{19}$	4K/10K [177, 178]
3.22	DAP	2×10^{18}	300K [181]
3.15	DAP2 or LO1	2×10^{19}	2K/300K [177],[181]
3.14	DAP2	3×10^{19}	4K [183]
3.08	DAP-LO2	2×10^{18}	300K [181]
2.90	deep DAP	1×10^{20}	[184, 185]

DAP type recombination by a perturbed state near a Mg acceptor site or to surface defects [180]. In room-temperature PL measurements, the Mg emission peaks have similar positions, although small shifts and peak broadening was observed [181]. Table 5.1 summarizes known Mg related luminescence peaks.

A reduction in the number of available hole carriers can occur due to the formation of intrinsic compensating donors or complexes, possibly involving isolated V_N or Mg-V_N pairs at high Mg doping levels (see Figure 5-2)[111]. The high levels of doping were shown in the same work to be unrelated to the formation of different Mg phases, or to a solubility limit of Mg in GaN. High Mg incorporation on planar layers has also been associated with an increase in GaN resistivity and presence of a wide blue luminescence band. The blue luminescence (BL) observed at $\sim 2.70 - 2.9$ eV is considered to be a transition between the substitutional Mg_{Ga} acceptor and a deep donor level, possibly a nitrogen vacancy V_N [109, 110] or other complexes involving a hydrogenated vacancy Mg-V_N-H [176, 186, 185].

The increase in electrical resistivity is likely caused by transitions between the Mg acceptor and the deep donor, and can be linked in PL spectra to the increase in the intensity of the BL band. With ever-larger numbers of Mg atoms incorporated in the lattice, the distance between the deep donor and the Mg atom is reduced, causing an increase in the number of lower energy transitions. Exceeding a Mg density of 2×10^{19} cm^{-3} triggers self-compensation [110], and predominant blue luminescence [187].

A different perspective to ref [175] is provided in ref [188], which considers the Mg-H responsible for the 3.27 eV DAP emission, however the BL emission is attributed to the isolated substitutional Mg_{Ga}. In ref. [189] it is proposed that the V/III ratio determines the dominant emission peak, with samples achieving similar conductivity,

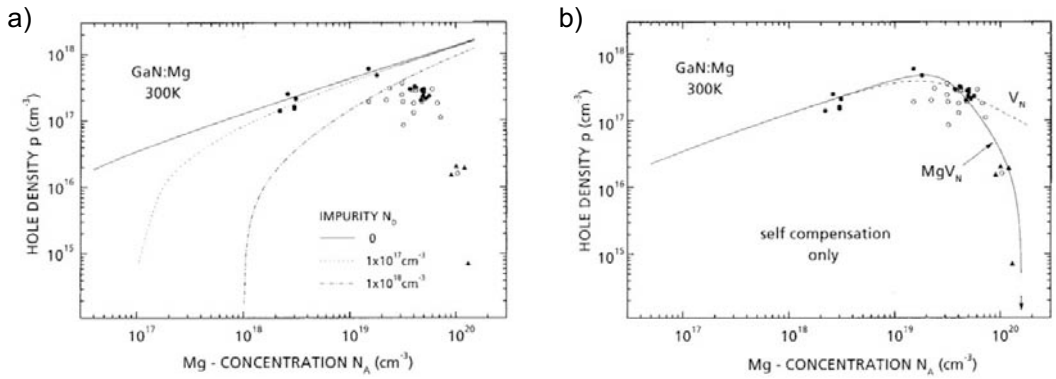

Figure 5-2: Hole concentrations in planar p-GaN measured by Hall effect. a) the curves represent calculated hole density values used to estimate approximate hole concentrations [111]. b) high densities of Mg atoms are related to the onset of self-compensation and formation of Mg-V_N and other vacancy related complexes. (Copyright 2000 by the American Physical Society)

whether their main PL emission is in the DAP1 or in the BL range.

By comparison, in MBE higher active Mg hole concentrations can be achieved because hydrogen atoms do not passivate the p-GaN as in MOVPE [190]. From the perspective of optical Mg signatures, the low resistance MBE p-GaN obtained in ref [181], showed similar spectra to the MOVPE p-GaN obtained in the present work. If the main driving mechanism of the compensation[1] is the presence of V_N vacancies and vacancy complexes, the MBE p-GaN may also be resistive. With either type of method, optimization of growth parameters can be optimized to reduce the number of vacancies.

5.3 p-GaN shell growth

Figure 5-3 shows core-shell nanorods obtained by plasma-etched GaN followed by lateral regrowth with a Mg-doped p-GaN shell. A nickel nano dot metal mask of 2 μm pitch, obtained by nanoimprint lithography [18], was used as an etch mask.

Several sample sets were fabricated from etched nanorods: a 2-μm-thick undoped GaN on Si substrate with an intermediate AlN buffer layer for lattice matching, and the second set of 5 μm tall, n-doped GaN on a sapphire substrate. The GaN-on-Si substrate was etched through to the underlying Si, while the GaN-on-sapphire substrate was

[1]Reprinted with permission from Kaufmann, U., Schlotter, P., Obloh, H., Köhler, K., Maier, M., "Hole conductivity and compensation in epitaxial GaN:Mg layers", *Phys. Rev. B 62*, 10867–10872, (2000). Copyright by the American Physical Society, doi.org/10.1103/PhysRevB.62.10867

etched only to a depth of 3.5 µm, to retain a 2 µm conductive n-GaN layer below the NRs. To promote growth only on the NRs sidewall, the Si substrate and the GaN planar layer on sapphire were protected from regrowth by passivation. Passivation was achieved either by the high-temperature formation of SiN_x on the exposed Si, or by spin-coating HSQ for the GaN on sapphire NRs, to passivate the spaces in-between the etched NRs.

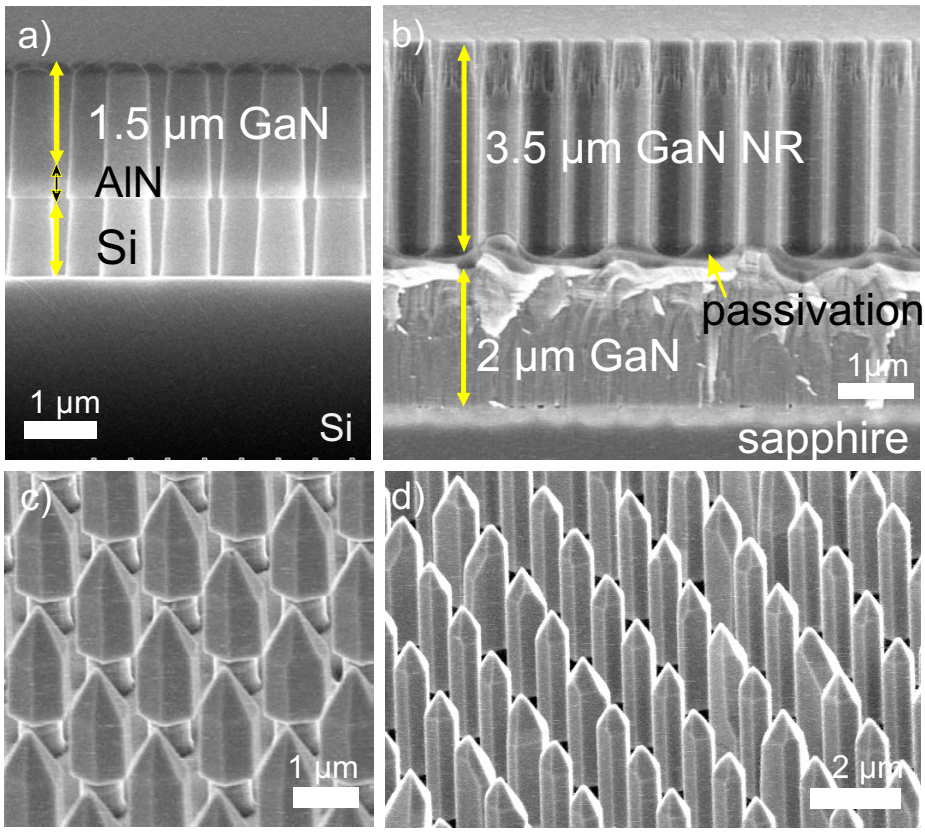

Figure 5-3: Succession of processing steps for GaN nanorods: a) plasma etched GaN-Si NRs, b) plasma etched GaN-sapphire NRs and a continuous GaN layer under the rods, c) regrown of 1.5 µm GaN-Si NRs, d) regrown of 3.5 µm GaN-sapphire NRs.

To identify a set of growth parameters for uniform p-GaN shells, growth temperatures of 700, 800, 900 and 1000 ℃ were examined using NRs on Si substrate only. Constant growth time of 10 minutes and precursor flow of 0.44 µmol/min Cp_2Mg, referred to as *medium* doping, were used. It was expected a high V/III ratio would provide high Mg incorporation [191], and optical emission without self-compensation. Annealing was performed at 620, 720 and 820 ℃ for 20 minutes under nitrogen gas in the MOVPE reactor. The different annealing temperatures were tested to determine an optimum

temperature to break the Mg-H or Mg-V_N-H bonds. The initial GaN regrowth for the undoped facet recovery step was done at an identical temperature (920 ℃), then the temperatures were varied during the p-GaN step. The samples were taken out of the reactor after growth, cleaved and then annealed with the different temperature conditions. It can be thus considered the samples growth and annealing parameters are consistent with each other.

5.3.1 Morphology dependence on p-GaN growth temperature

Figure 5-4 shows the size and shape of the nanorods obtained for different growth temperatures and 10 minutes growth time, using identical precursor flow. The NR diameters were determined from SEM images in a statistical manner for approximately $80 - 90$ NRs in each image.

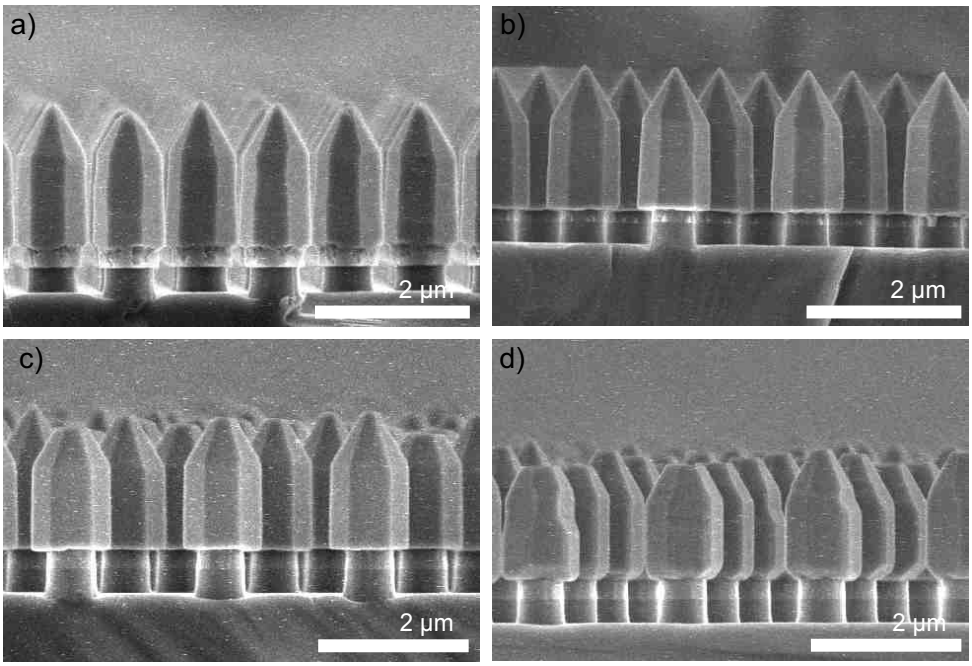

Figure 5-4: Effect of growth at different temperatures: a) 700 ℃ reduced growth rate and tapered sidewalls, b) 800 ℃ uniform heights and slight taper, c) 900 ℃ uniform diameter NRs and a remnant *c*-plane, d) 1000 ℃ variable height NRs with irregular facets.

At 700 ℃ the NRs in Figure 5-4 a) show only a small amount of lateral growth, probably due to the limited cracking efficiency of NH_3 at such a low temperature. The NRs are tapered and have a wider base diameter. The increase in growth temperature to

800 ℃ led to larger diameter NRs possibly due to an increased growth rate. The lower temperatures could reduce the diffusion length of Mg and Ga atoms, favoring incorporation at the NR bases. At 900 ℃ the sidewalls were practically vertical, however, they also show a residual polar c-plane on some of the NRs. This is caused by the change in relative growth rates between the c-plane and semi-polar facets occurring at this growth temperature. At 1000 ℃ the lateral growth rate increased further, however, the NRs were more irregular, with a few of the NRs showing different sets of semi-polar and m-plane facets. If compared to GaN only regrowth, the Mg doping seems to affect the relative crystal facet growth rates for high temperatures and favor tapering of the NRs at low temperatures.

The impact of different temperatures and of precursor flow on NR diameter is summarized in table 5.2. For 700 and 800 ℃ two values are given, corresponding to the base and to the upper-side of the NR m-plane. However, the SEM measurement method is not able to distinguish between diameter variations at the top and lower side on the NRs. The effect of precursor flow is thus more difficult to interpret because of the NRs taper. In the NRs on sapphire for which the tall NRs provide longer diffusion lengths and higher surface area, there was less taper and the tendency was for an increase in Mg precursor to reduce the diameter of the NRs (see Table 5.3). In either case, the variations in NR diameter depending on precursor are very small and within the error margins.

Table 5.2: The impact of growth temperature and Cp_2Mg flow rate on NR diameters.

Sample	Temperature [℃]	Cp_2Mg flow [µmol/min]	NR diameter [µm]	Std. dev (2σ) [nm]
GaN	920	–	0.776	±42
med	700	0.44	0.880 – 0.906	±29
med	800	0.44	0.896 – 0.916	±47
med	900	0.44	0.962	±20
med	1000	0.44	1.170	±39
low	800	0.30	0.919	±24
med	800	0.44	1.018	±24
high	800	0.71	0.965	±38

It should be mentioned the available NH_3 flow was reduced for all p-GaN growth relative to GaN stage (1900 scmm to 2800 sccm NH_3 respectively), to encourage high carrier concentration, low resistance [107] and doping without compensation [191]. From a facet uniformity perspective, the growths at 800 and 900 ℃ seem the most promising for core-shell growth.

5.3.2 Characterization dificulties for p-GaN nanowires

In contrast to planar doped layers for which the doping density and Mg activation can be measured using electrical methods, the three-dimensional geometry of core-shell structures requires alternative measurement methods. This is caused by the large number of individual NRs that can easily vary from sample to sample, as well as the different resistances occurring at contact surfaces for individual NRs,at the current spreading layers and metal contacts.

Characterization by optical means was chosen because these are non-contact, non-destructive and can reveal Mg atoms presence by optical transitions [182, 185] and changes within the crystal lattice [187, 192]. PL, CL, and Raman spectroscopy measurements were performed at room temperature. Although the characteristic Mg peaks are harder to resolve at that temperature, the spectra change introduced by Mg doping can still be identified and used to characterize the p-shell. For the measurements taken the emission intensities were normalized, because the collected peak intensity can vary due to minor differences in the focus procedure and due to light scattering occurring on the NRs. The measurements were repeated on several NRs to account for nanorod-to-nanorod variation. Detailed description of the equipment used and PL, CL and Raman measurements can be found in section 2.2.

5.3.3 Photoluminescence emission for Mg doping

Typical PL bands in planar GaN after Mg doping have been observed at ~ 3.27 eV in low and medium doped GaN [177], as well as blue luminescence $\sim 2.8 - 2.9$ eV emission for high Mg doping [187]. The position of these emission bands appears to be independent of the measurement conditions [193] or growth method [194]. Other emission bands such as the yellow luminescence ($\sim 2.18 - 2.2$ eV) have been associated with Si doping or with isolated nitrogen vacancies or crystal defects [195]. A red band (~ 1.8 eV) for p-GaN was determined by calculations to be caused by a Mg-V_N complex [196].

The μPL spectra of Mg-doped GaN-Si NR obtained with the growth temperatures discussed in the previous section are compared in Figure 5-5a) and b). The spectra of the samples are very similar for all growth temperatures before annealing. An exception is a sample grown at 1000℃, for which Mg incorporation in the shell has been found ineffective, probably due to p-GaN dissociation at high temperature. In all the samples the position of the DAP1 peak did not change significantly with growth temperature

or annealing. Figure 5-5 b) shows a slight intensity reduction in DAP1 after annealing, proving the breaking of Mg-H bond and activation of the Mg acceptor [197]. The decrease of the DAP1 intensity appears in Figure 5-5 b) to be more effective for p-GaN layers grown at lower temperatures.

The emission peak at 3.35 eV becomes more intense than the DAP after annealing. It is interesting to follow the evolution of this peak, because it is not at the expected NBE peak position. In the etched GaN on Si NR cores, the NBE can be distinguished in figure 5-5 c) at 3.4 eV. After the template undergoes facet recovery, new surface states may be introducing band bending and shifting the emission to the lower 3.35 eV energy. An observation can be made about the plateaus in the etched sample spectra, which can be associated with the AlN buffer layer.

The change in annealing temperatures from 620 to 820 ℃ has had little effect on the samples (not shown). However, if the thermal treatment is done at a too high temperature ($\sim$ 900 ℃), it can cause a substantial increase in the number of nitrogen vacancies and BL emission as in Figure 5-5 d) due to the likely p-GaN decomposition at high temperature.

The peak at 3.24 eV was more clearly observed after annealing, suggesting this feature may be connected to the Mg acceptor and another complex involving hydrogen. A peak at such a close value to the DAP1 energy has been related to another DAP pair transition (DAP3), for Mg impurity level above 5×10^{18} cm^{-3}, which in low-temperature PL was found at 3.256 eV in ref [182]. Furthermore, at a high level of activated acceptors, the "deep ground state" for the Mg acceptor is only 30 meV lower in energy than the "shallow transient state" of DAP1, which gets reduced by annealing [198].

Additional luminescence peaks related to Mg doping could be identified in the PL spectra. A weak luminescence at $3.15 - 3.16$ eV has been attributed to a DAP2 transition, corresponding to a deeper Mg_{Ga} deeper acceptor or a structural defect [185]. This emission wavelength was also observed at slightly lower doping (1×10^{18} cm^{-3}), and was suggested to be correlated with the formation of nano-basal-plane stacking fault defects (BSFs) perturbing the energy level of Mg acceptor [180].

Spectra features in the BL region are difficult to identify because the PL signal is noisy at room temperature. The intensities of these peaks indicate self-compensation or a limited number of deep (2.9 eV) donors. These spectral signatures are better visible in low temperature PL [193].

Phonon-assisted transitions caused by the coupling of phonons to the DAP were shown

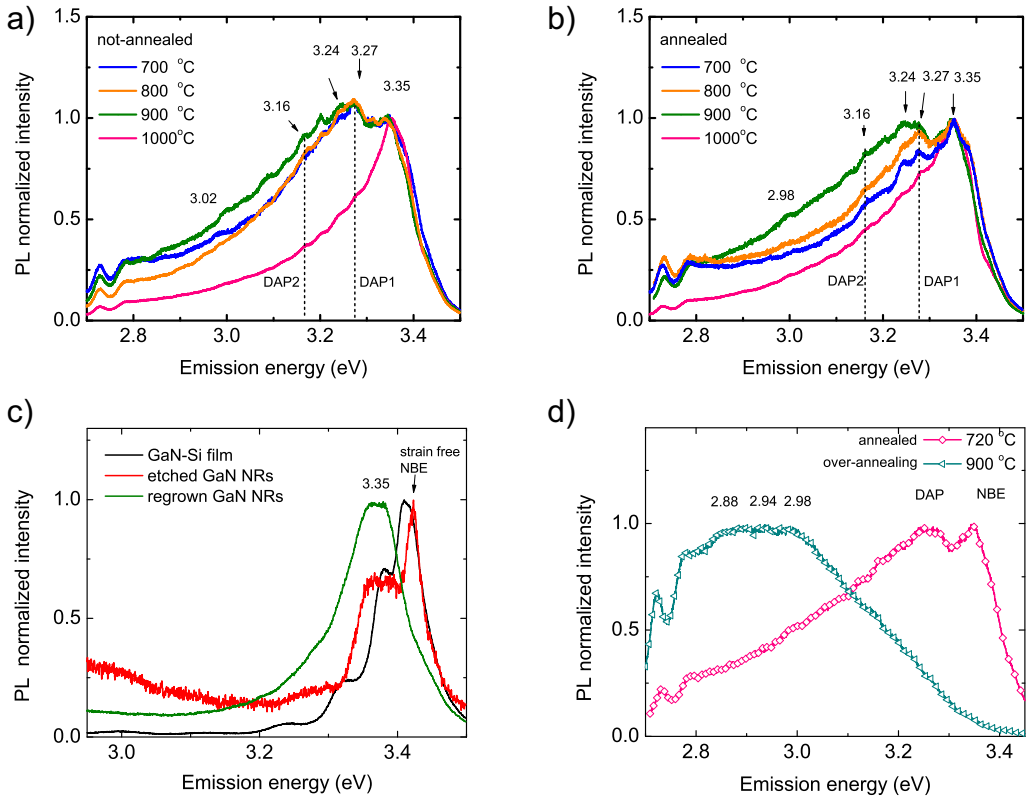

Figure 5-5: (color online) Normalized μPL spectra of core-shell NRs on Si substrate grown at different temperatures and constant *medium* doping: a) as-grown samples, b) thermal annealing has reduced the intensity of the DAP transitions, activating the Mg acceptor, c) evolution of emission peaks for the different stages of the template: GaN-Si film, etched cores and regrown samples, d) annealing at 900 ℃ could introduce a large number of V_N due to decomposition and generate the BL band.

in previous studies to occur below the DAP energy levels, for both NRs and planar layers. The phonon-assisted transitions or *DAP replicas* introduce additional spectra lines at regular intervals, while maintaining the shape of the original DAP peak [199, 200, 201, 183]. The value of the spacing between the 3.27 eV DAP1 and each of observed possible replica peaks at 3.20 and 3.12 eV, was $\sim$ 72 meV, and different from the expected $\sim$ 0.92 meV. This difference is likely caused by the 3D geometry and non-planar GaN , thus the phonon propagation direction is not strictly perpendicular or parallel to the crystal axis. The 72 meV spacing could be more closely associated to the E_1^{TO} mode. Potentially the mode originates from a mixing of modes due to the irregular scattering geometry, resulting in a quasi-LO mode [129]. The 3.08 eV peak could be a replica of the 3.15 eV DAP2 peak, however, its separation is larger than for the DAP1-replicas. This peak may also be traced to carbon impurities [150]. For

room-temperature spectra, the shape and values of LO replicas can only tentatively be associated with literature values, however, this is not in the purpose of the present work.

A small $3.31 - 3.32$ eV peak can be noted on the un-annealed samples, which was then reduced after annealing, indicating it too may be a complex or perhaps a surface DAP [150] sensitive to thermal treatment.

5.3.4 CL mapping for NRs on Si substrates

The effects of different precursor flow rates on the NR emission spectra were studied by cathodoluminescence. CL provides improved spatial resolution of p-GaN shell characterization because of its direct correlation between emission and the spatial origin of the emission. A low energy electron beam of 2 keV was applied to the individual NRs at RT to determine impurity atom distribution along the length of the NRs.

A sample set on Si substrate was grown under three different dopant flow rates, where the Cp_2Mg precursor flow was adjusted between:

- 0.30 µmol/min (*low*), or a Cp_2Mg/TMGa ratio of 0.98%
- 0.44 µmol/min (*medium*), ratio of 1.43% and
- 0.71 µmol/min (*high*), ratio of 2.26%.

Precursor ratios can be used to determine and predict the onset of electrical compensation [187]. The growth and annealing temperatures were kept constant across all the samples, at 800 ℃ and 720 ℃ respectively for 20 minutes.

The CL maps in Figure 5-6 show a comparison of the monochromatic CL emission peaks for the NBE (365nm) and the DAP1 (380nm) for medium and highly doped samples. The medium doped NRs display emission originating uniformly from the entire NR surface area. On the other hand, the highly-doped NRs in figure 5-6 e,f) show nonuniform DAP1 emission, mostly from the lower part of the semi-polar facets and from randomly distributed regions on the m-plane sidewalls. These inhomogeneities indicate a possible limit for Mg solubility in the GaN crystal. The difference between the two maps indicate that CL analysis using low accelerating voltages (2 keV) is an effective method to evaluate Mg doping uniformity. The CL maps were obtained from approximately 100 nm depth, as estimated from Monte-Carlo Casino software simulations, which can still probe partially the underlying GaN. When the accelerating energy was increased to $5 - 7$ keV, the nanorods showed uniform NBE emission from

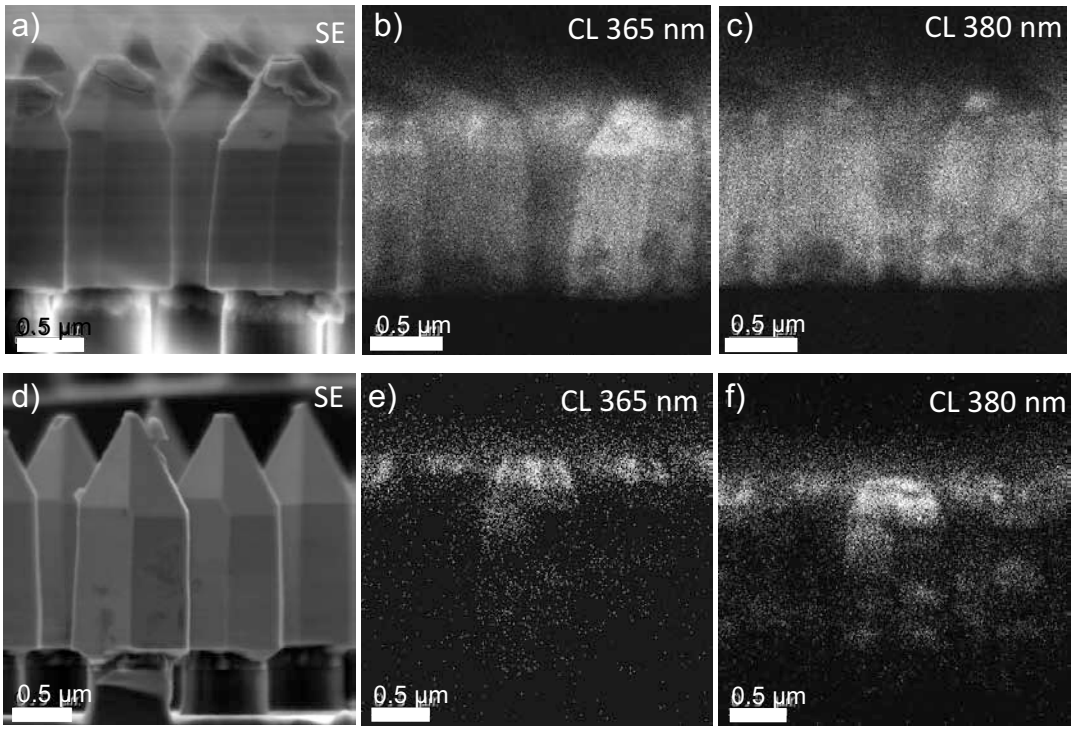

Figure 5-6: CL maps at 2 keV GaN on Si core-shell NRs with different Mg concentrations a) SE image of medium doped NRs, b) NBE emission medium doped NRs, c) DAP1 uniform emission from the entire m-plane and semi-polar facets for medium doping, d) SE image of highly doped NRs, e) reduced NBE emission intensity for highly doped NRs, f) highly doped samples display random areas of emission and reduced in uniformity for DAP1 transitions.

the entire *m*-plane area, proving that the semiconductor probed at 2 keV is mainly the Mg-doped shell.

The CL spectra measured from the *m*-planes of GaN-Si NRs are compared in Figure 5-7. The spectra indicate a greater red shift in CL emission caused by the increase in the Mg precursor flow, from unintentionally-doped to highly-doped p-GaN shells.

For the low doped samples, the emission at $\sim$ 3.35 eV dominates the spectrum and there is no clear distinction between the spectra of unintentional or low doped GaN-Si NRs (not shown). With the increase in Mg doping to medium level, the shoulder at $\sim$ 3.24 eV is more clearly observed in the CL spectrum. Further increase of Mg doping results in the emission from the DAP1 recombination at $\sim$ 3.27 eV becoming the dominant emission. The dominant emission together with the reduction in uniformity for highly doped samples could indicate that these samples have not achieved sufficient

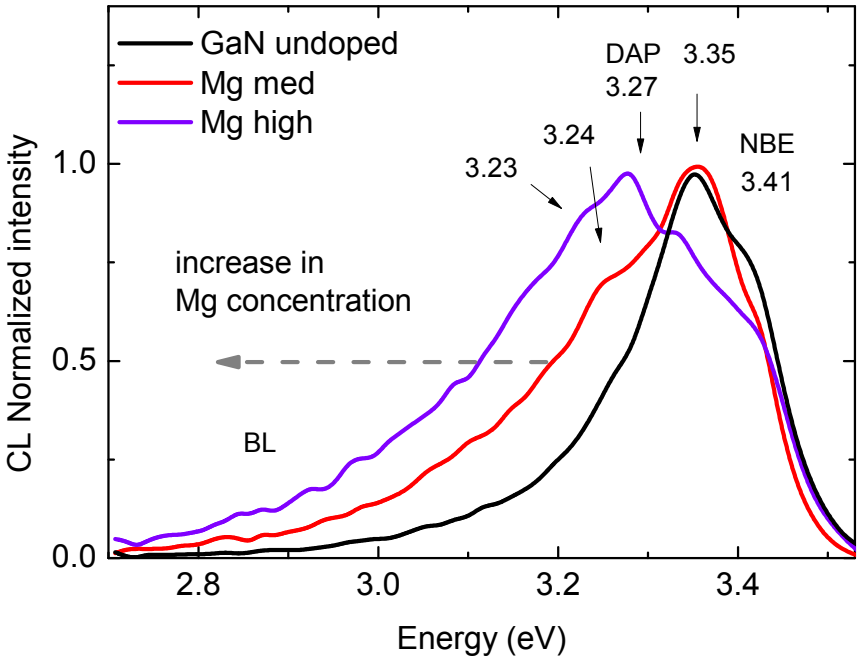

Figure 5-7: CL spectra of NRs for different Mg concentrations show a gradual shift toward lower energy transitions (DAP) with increasing Mg incorporation (2 keV, RT).

Mg incorporation. The second wide DAP2 emission shoulder at $\sim$ 3.15 eV can be identified only in the CL spectrum of the highly doped sample. Optical LO-phonon assisted replicas are not clearly resolved at room temperature.

5.3.5 CL for high aspect ratio NRs on sapphire substrate

A further set of samples was produced, to examine the uniformity of doping on higher aspect ratio NRs and to apply electrical contacts to the NRs. The 3.5 µm-tall NRs on sapphire were grown for 20 minutes for the p-GaN shell, using the same growth parameters and dopant recipes for *low, medium* and *high* Mg precursor flow, as in the above section. The samples were designed to drive electrical current, therefore a continuous n-GaN layer was kept below the NRs. The NR bases were passivated with HSQ prior to regrowth. No tapering was observed on the tall NRs. Tapering may occur on the short NRs because of lower atom surface diffusion length and incorporation also occurs on the exposed N-polar $\{0\,0\,0\,\bar{1}\}$ plane, which is not present on the tall NRs.

The NR diameters were smaller than for the short NRs, indicating that growth rates depend on available NR surface area. Because the thickness of the p-GaN shell thickness was reduced to $\sim 50-60$ nm despite doubling the growth time, annealing was reduced to 10 minutes, to prevent the risk of GaN dissociation. It was expected that Mg incorporation would increase the NR mean diameter value [202]. However, measurements showed growth rates are reduced when the Mg impurity flow was increased.

The monochromatic CL maps of tall core-shell NRs are shown in Figure 5-8, with emission peaks for the NBE (367nm), DAP peak emission (380 and 392 nm) and likely a phonon replica at 3.02 eV (410 nm). The tall NRs show a more uniform emission along the m-plane sidewall compared to short NRs, even for high doping. The uniformity may be related to the increase of available GaN surface area which is approximate 3× larger than for the short NRs. The emission at the DAP (380 nm) wavelength was more difficult to attribute to individual NRs. A reduction in CL NBE intensity from apexes in highly doped samples suggested an increase in non-radiative surface defects or an increase in complexes involving Mg-H bonds or V_N in these regions (Figure 5-8). Nitrogen vacancies have previously been proposed to form preferentially at the edges of nanowires and cluster together to be more energetically stable [203]. Vacancies were identified in positron lifetime spectroscopy as compensating the p-GaN growth and it was shown that annealing effectively reduced the number of V_N and Mg-V_N [204].

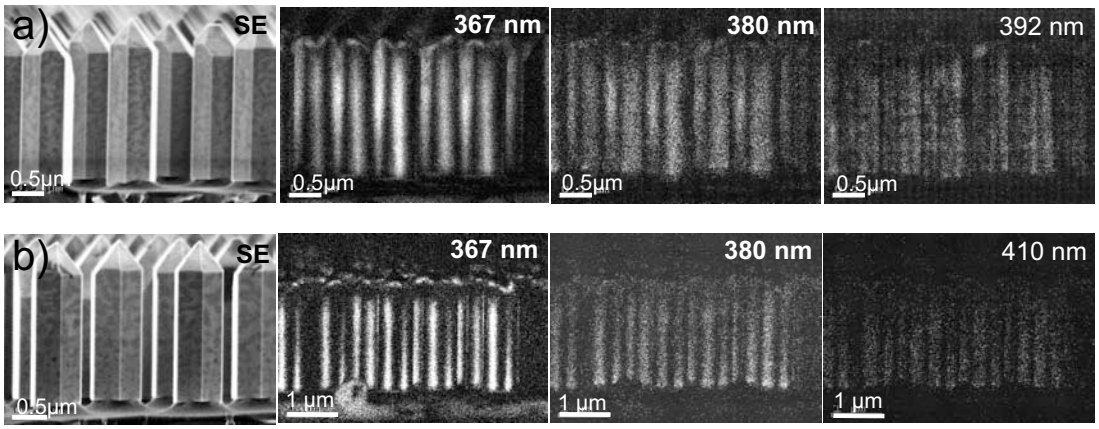

Figure 5-8: Monocromatic CL maps (RT, 2 keV) of p-GaN NRs on sapphire. a) medium doped NRs with emission from NBE and DAP peaks, the *m*-plane apexes show no emission, b) high doping seems to reduce the effective NBE and DAP emission surface area.

CL emission enhancement of individual NRs can be seen in the bright spots originating from the tips of the NRs at the 367 nm NBE wavelength (Figure 5-8). Furthermore, this emission follows the edge contours of individual rods at the apexes between the

semi-polar and m-plane facets. The effect may originate from the nanorod cavity due to resonant modes [179], as the enhancement is present even in undoped GaN NRs.

The increase in impurity flow has led to a high density of patchy contrast islands on the secondary electron images of the NRs as seen in the SE images in Figure 5-8. The islands may be a visible indication of incomplete Mg activation at the surface. Evidence of surface segregation occurring at high Mg flows which would appear as pyramid shaped defects and pyramidal inversion domains was not found. The pyramid defects can occur in highly doped planar p-GaN and are associated with local emission at $3.31 - 3.36$ eV [205].

Figure 5-9 a) shows corresponding CL spectra for the tall NRs with luminescence dominated by the 3.35 eV emission. The DAP peaks are present, however, they are less intense compared to the short NRs. The DAP1 transition appears as a weak shoulder to the main peak, likely due to a smaller contribution from the thinner p-shell ($50 - 60$ nm), resulting in the generation of free carriers and radiative recombination in the n-GaN core, even at the low 2 keV electron beam energy.

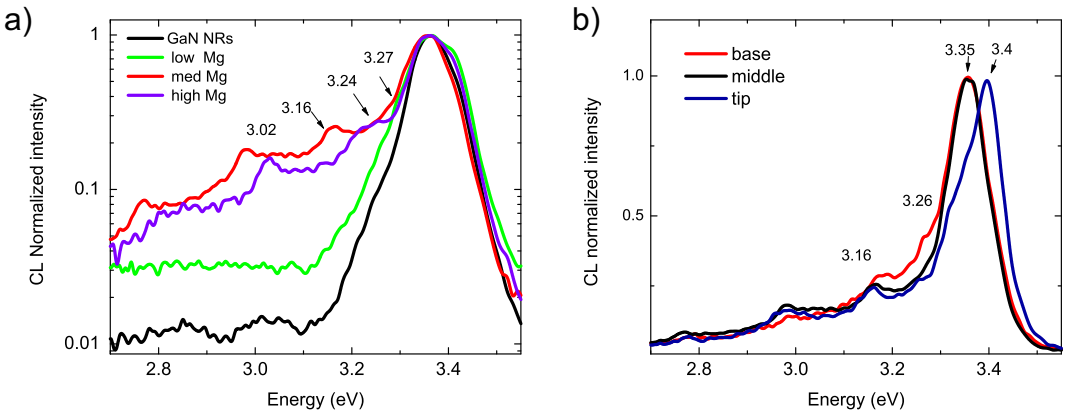

Figure 5-9: CL spectra (RT, 2 keV) on tall core-shell GaN NRs with *low, medium* and *high* doping. a) integrated CL signal from m-plane facets ($5 - 6$ NRs) show Mg signatures for medium and high precursor flow, b) CL spectra for different NR regions shows a stronger DAP peak at the NR base and a more intense NBE emission on the semi-polar NR tips.

The DAP peak at 3.27 eV [182], the absence of self-compensation and a lack of BL indicate a doping level below $\sim 5 - 7 \times 10^{18}$ cm^{-3} was possibly obtained. Correlation with ref. [111] gives a conservative estimate for active hole density in the range of $5 \times 10^{16} - \ 2 \times \ 10^{17}$ cm^{-3}.

Emission signatures expected in the BL range, $2.80 - 2.95$ eV for Mg-V_N [176], or defect emission for isolated V_N, did not change significantly with Mg doping or after annealing. One possible explanation could be the nitrogen rich environment affects the luminescence peaks, as it limits the amount of compensating complexes incorporated. Growth under nitrogen-rich conditions shows a predominant 3.27 eV peak and only decreases slightly after annealing, while samples grown with NH_3 or H carrier gas show strong compensation and BL [189]. In the same study, it was demonstrated that effective doping levels and annealing led to similar electrical resistivity for both types of samples, although their PL signatures are different. The high energy DAP is expected to be dominant for Mg atom concentrations up to 2×10^{19} cm^{-3}, however, the transition to resistive and compensated p-GaN with emission at 2.80 eV would occur abruptly above 3×10^{19} cm^{-3} Mg atoms [109].

5.3.6 Raman mapping of defects associated with Mg incorporation

Raman spectroscopy was used to detect and map phonon states introduced by the Mg doping. The E_2^H peak can be associated with strain variation caused by lattice inhomogeneities or by complexed formed during Mg doping [192]. To map the doped GaN NRs, a high-resolution Renishaw inVia Raman spectrometer with a 532 nm laser source, 3000 lines/mm grating and 150×0.95 NA objective was used. The laser power was 10 mW, the lateral spatial resolution was 0.3 μm, with spectral resolution of 0.01 cm^{-1}.

The NRs were mechanically scratched off the sapphire substrate and dispersed horizontally on a clean sapphire wafer to remove the contribution from the underlying n-GaN. AlN and Si pedestals remained attached to the GaN on Si NRs, even after removal from the substrate and hindered reliable measurement of the E_2^H peak frequency because of the intense Si peak at 520 cm^{-1}. Therefore only the samples on sapphire substrates are discussed.

GaN for planar LEDs is grown by heteroepitaxy on foreign substrates, and the resultant thin film undergoes compressive strain on a sapphire substrate, or tensile strain on a Si substrate, due to the lattice mismatch and thermal expansion mismatch between the substrates and the epitaxially grown layer. Information on strain can be determined from the Raman E_2^H mode frequency. Unstrained GaN films have values for the E_2^H peak in the range of $567.6 - 568$ cm^{-1} [129], depending on GaN thickness, growth technique or processing. In *c*-plane GaN-on-sapphire substrates the compressive strain results in E_2^H values of ~ 570 cm^{-1}, while on Si substrates, a tensile strained GaN has

may have a ~ 566 cm^{-1} E_2^H peak [206].

The present p-GaN shells have a thickness of between $40-60$ nm, covering a strain relaxed GaN core [62] of 720 nm diameter. Because of the relative thickness ratio of p-GaN to GaN, measurements of strain variations in the E_2^H peak were expected to be small, and a high spectral resolution system was required to detect the variations. Because the laser spot probes a volume of $\sim 0.5-1$ µm, the vibrational mode changes between the thick core and the thin p-shell could be better determined if their respective thicknesses could be more closely matched.

The NR Raman spectra can be influenced by small changes in the geometry of the NRs, because the observed modes change with the angle at which the laser beam is incident to the 3D surfaces [202]. Therefore a single scattering geometry and orientation of the NRs was considered and verified with the optical objective. This alignment is equivalent to using the $y(x,-)\bar{y}$ Raman selection rule, with the incident laser beam perpendicular to the NR's $\{1\,0\,\bar{1}\,0\}$ m-plane. In this configuration the Raman-active phonon modes are restricted to E_2^H, A_1^{TO} and E_1^{TO}, as seen in Figure 5-10 a). Spectra of individual dispersed NRs with identical orientation were collected and averaged to determine the position of the E_2^H peak.

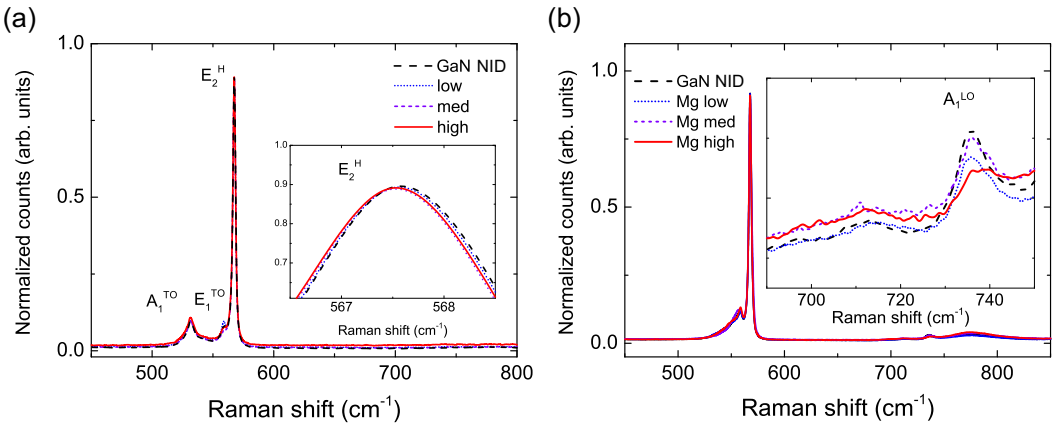

Figure 5-10: a) Normalized Raman spectra in $y(x,-)\bar{y}$ mode from dispersed rods for p-GaN shells with different Mg concentrations, the inset shows small change in strain with increasing Mg concentration, b) Normalized Raman spectra in $z(x,-)\bar{z}$ mode for laser beam parallel to the $[0\,0\,0\,1]$ direction,the inset shows the broadening of the A_1^{LO} peak with increasing Mg incorporation.

The inset in Figure 5-10 a) shows the Raman E_2^H peak shift towards tensile strain, from 567.56 cm^{-1} on regrown NRs, to 567.51 cm^{-1} for high Mg flow (Table 5.3). The NR shell thickness was determined from planar SEM images using image processing

Table 5.3: Variations for NRs thickness and for values of E_2^H mode with p-doping for *individual NRs* in $y(x,-)\bar{y}$ mode, and for *NR arrays* in $z(x,-)\bar{z}$ mode.

Sample	Shell thickness (2σ) [nm])	E_2^H individual NR (2σ) [cm^{-1}]	E_2^H array (2σ) [cm^{-1}]
GaN	diam.724(±20)	567.563 (±0.022)	567.563 (±0.026)
low Mg	62 (±39)	567.567 (±0.012)	567.566 (±0.014)
med Mg	49 (±20)	567.524 (±0.027)	567.523 (±0.030)
high Mg	39 (±27)	567.514 (±0.038)	567.515 (±0.044)

software. Kirste *et al.* proposed for planar layers that a compensating Mg-V_N complex occurring during Mg doping, causes the shift towards tensile strain. In the same study a sudden widening of the E_2^H peak width above 7×10^{18} cm^{-3} Mg atoms was associated with the start of self-compensation and reduction in crystal quality[192]. The current samples showed consistent E_2^H peak width, indicating no loss in crystal quality.

In addition to the detached NRs spectra, measurements were taken from standing NRs on the GaN-sapphire substrate, in a Raman configuration of $z(x,-)\bar{z}$ (Figure 5-10 b). The same amount of shift was observed on the array of standing NRs as with the dispersed NRs (Table 5.3). The standing NRs analysis provided information about doping from the $A_1^{(LO)}$ peak, observed in this configuration. In the case of n-type GaN, the doping levels can be estimated from the shift of the $A_1^{(LO)}$ position caused by the longitudinal optical phonon-plasmon coupling (LOPC)[129]. The LOPC indicates that electronic states introduced with n-doping are related to lattice vibrations as discussed in the first section of this chapter. However, the effect of the LOPC coupling is less clear in the case of p-type carriers.

The inset in Figure 5-10 b) shows incorporation of Mg atoms in the crystal lattice seems to cause a broadening of the $A_1^{(LO)}$ peak. Even if the concentration of hole carriers of the thin p-GaN sidewall was not sufficient to shift the $A_1^{(LO)}$ peak, its width has increased with Mg impurities as previously shown in ref [207]. For hole carriers below 10^{18} cm^{-3} it was argued the $A_1^{(LO)}$ does not change its coupled position[208]. However for hole concentration above 10^{18} cm^{-3}, the $A_1^{(LO)}$ or the coupled $A_1^{(LO)}-LOPC$ peak value was shown to shift gradually between $740-732$ cm^{-1} with increasing Mg incorporation, from 2.8×10^{18} to 2.9×10^{20} cm^{-3} Mg atoms in an MBE study [190].

Other Mg peak designations were observed in literature at 657 cm^{-1} and a series of peaks in the IR range [209]. However, it was shown previously that for hole densities in the range of 10^{17} cm^{-3} the 657 cm^{-1} peak is difficult to identify [202] and is not seen on the sample sets used in this work. It should also be considered that p-type carrier concentrations above 5×10^{17} cm^{-3} would likely trigger electrical self-compensation [111]. The NR geometry with the thin p-shell or noise levels may have prevented

reliable observation of IR spectra and were not further studied.

Uniformity of doped p-GaN shell

Dopant or defect distribution in the p-GaN layer will affect the current spreading ability of the doped shell through the layer conductivity. The CL analysis established the increase in emission non-uniformity of the DAP1 peak, caused by higher flow rates of Mg precursor. High-resolution Raman 2D mapping in $y(x,-)\bar{y}$ mode was used to investigate local variations in p-shell strain from individual NRs as a function of compensating defects incorporated in the lattice. Raman maps were obtained by scanning in a grid pattern at 0.1 µm step size on dispersed NRs. The signal was curve fitted and filtered by a minimum E_2^H peak intensity of 1000 counts to highlight the physical extent of the nanorod.

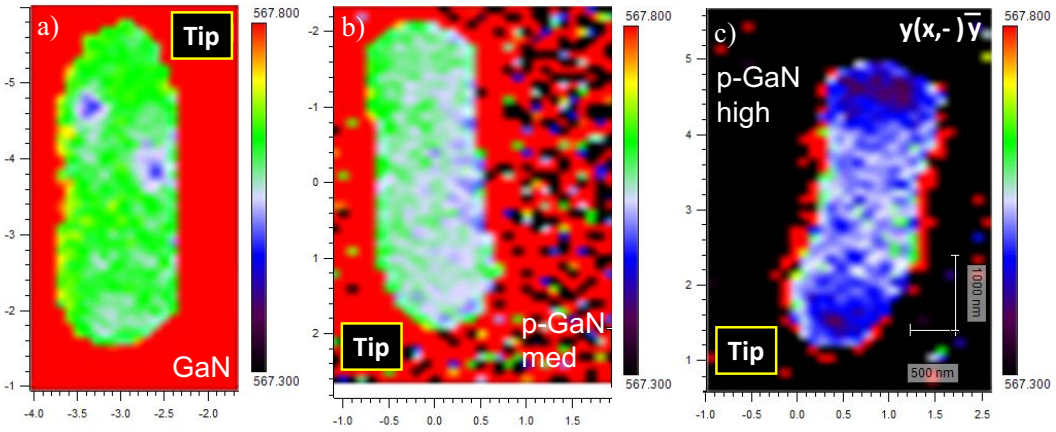

Figure 5-11: a) Raman map of E_2^H peak position along GaN only NR, b) E_2^H map for medium Mg doped p-GaN shell, c) E_2^H map for high doped p-GaN shows less uniform m-plane and variations at the NR extremities.

To study the possible location or distribution of compensating defects on the NRs, the Raman maps in Figure 5-11 were collected from each type of doped NR. For the case of GaN only in Figure 5-11 a), the E_2^H peak position does not change from tip to tip or from side to side, as the color is uniform across the sample. For the medium doped NR in Figure 5-11 b), gradual change in the E_2^H value from green to blue hues towards the tip. Examining the same image from the bottom of the NR, the different neighbor m-plane facets may be distinguished. The middle of the right-hand side of the NR also shows lower E_2^H values, and may indicate doping inhomogeneity on that facet. For the case of high doping in Figure 5-11 c), a larger shift in peak values is observed at the

tip and at bottom of the NRs. The sidewall color map covers hues from green to blue suggesting an increase in E_2^H non-uniformity. Moreover, the values of the E_2^H mode are on average 0.1 cm^{-1} lower on the high doped sample.

Crystallographic orientations determined by Raman spectroscopy

Considering Raman intensity maps from Figure 5-12, the ratio between the intensities of the E_2^H to $A_1^{(TO)}$ or E_2^H to $E_1^{(TO)}$ peaks can be used to map and identify different crystallographic orientations. In the $y(x,-)\bar{y}$ back-scattering geometry the highest E_2^H intensities are observed at the NR bottom and the NR apexes as these have the largest scattering sections. Using the Raman selection rules the color maps distinguish between the $\{1\,0\,\bar{1}\,0\}$ planes and the semi-polar $\{1\,\bar{1}\,0\,1\}$ planes. In Figures 5-12 b) and c) no minimum intensity filter was used in order to preserve the relative intensities of the individual phonon modes, corresponding to the change in crystal plane geometry. Because the laser beam samples partially the NR extremities, the signal map is wider than the NR true physical dimensions.

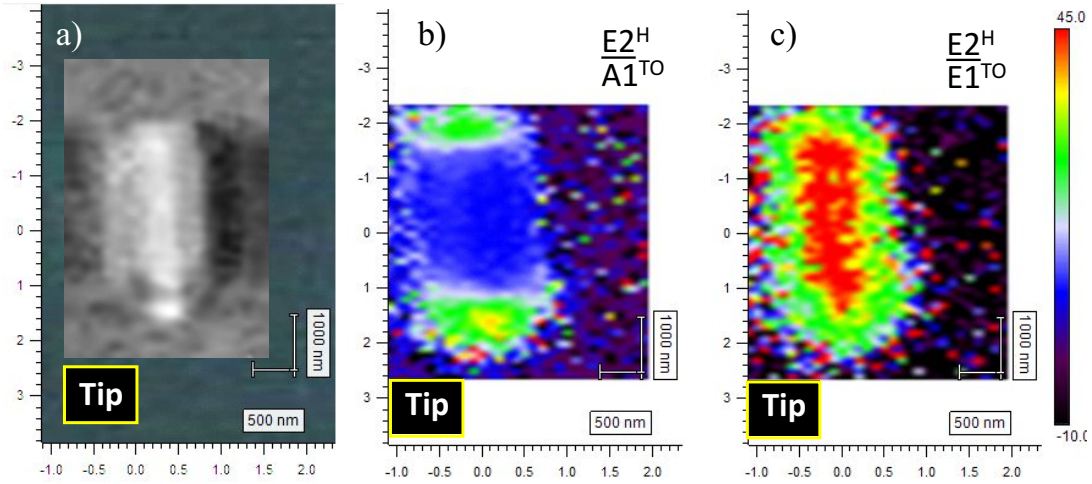

Figure 5-12: a) optical microscope detail of detached nanorod, b) intensity map shows how the ratio of E_2^H to $A_1^{(TO)}$ peaks provides distinction between m-plane and semi-polar planes, c) intensity ratio of E_2^H to $E_1^{(TO)}$ can be used to separate m-plane facets.

Similarly in $x(z,-)\bar{x}$ scattering geometry the selection rules indicate the $A_1^{(TO)}$ peak becomes dominant[129]. If this orientation was used, i.e. aligning the NR horizontally, the ratio of the $A_1^{(TO)}$ intensity to either the E_2^H or the $E_1^{(TO)}$ peaks, can be used to distinguish between the neighboring m-plane $\{1\,0\,\bar{1}\,0\}$ facets.

5.4 Conclusions

Complementary measurements of room temperature μPL, CL and Raman spectroscopy were used to identify Mg incorporation, p-shell growth parameters, map doping uniformity and estimate carrier concentrations for core-shell nanorods. The effects of different growth parameters, dopant concentrations and activation by thermal annealing were identified in the NRs.

A growth temperature of 800 ℃ was found to provide a reasonable growth rate and sidewall uniformity. The effective reduction of DAP after annealing at 720 ℃ for 20 minutes was observed. Potentially a p-GaN shell thicker than $\sim$ 50 nm would be necessary to limit penetration of the electron beam to the GaN core, and collect high-resolution CL emission from the p-GaN alone.

Donor-acceptor-pair transitions at 3.27, 3.24 and 3.16 eV indicate the presence of Mg atoms, although likely bonded to compensating hydrogen atoms. Potentially the Mg acceptor can form other compensating complexes such as Mg-V_N or Mg-V_N-H. Due to the high nitrogen component in the MOVPE growth environment, the 3.27 eV is a significant feature of the Mg spectra even at high impurity flow (0.71 μmol/min). Effective annealing, leading to mobile hole carriers, was demonstrated by the reduction in intensity of the DAP peaks. Several DAP replicas were observed with periodic separation to the DAP, with periodicity dependent on the geometry and the layer structure of the sample sets, for which clear identification at room temperature was not possible.

Magnesium incorporation in GaN is expected to compressively strain the lattice due to the Mg atom radius being larger than the Ga atoms radius [187]. By contrast, this work shows a small tensile strain shift of the E_2^H peak with increased doping was observed both in individual NRs and for arrays of standing NRs. This is attributed to the formation of compensating Mg-V_N or Mg-$V_N - H$ defects occurring at the same time with effective Mg doping shifting the E_2^H peak [192]. High-resolution Raman maps reveal that compensating complexes are uniformly distributed along the length of the $\{1\,0\,\bar{1}\,0\}$ m-plane nanorods for low and medium doping. The largest variation of the E_2^H was seen on the Raman 2D map for on m-plane sidewalls in the highest doped sample. In the medium doped samples, the range of E_2^H values was smaller indicating the p-shell was more uniform. This work shows that a Raman analysis in a high-resolution spectrometer can be used to rapidly verify Mg doping for core-shell structures. The Raman selection rules and the ratios of the different active modes can be used as a way to identify different crystal orientations on the 3D nanorod structures.

Chapter 6

Core-shell LEDs

The present chapter provides an fundamental perspective on the design, growth steps, process optimizations and device characterization for GaN-based core-shell LEDs. A review of the MOVPE growth of all the layers necessary for the three-dimensional structures is covered first, followed by a discussion on potential methods to contact and spread current uniformly into the NR array. Optical characterization of core-shell structures by photoluminescence (PL) is complemented by cathodoluminescence (CL) mapping to show the origin of light emission. Spectra obtained by electroluminescence (EL) and current-voltage (I-V) characterization conclude the discussion on the achieved prototype core-shell LED. Apart from EBIC measurements performed by Prof. Alexander Šatka and Dr. Juraj Priesol, as well as the CL analysis performed by doctoral candidate Chris Bryce, the experimental work was carried out by myself.

The device design and electrical characterization are meant to answer fundamental questions about the operation of a core-shell LED, rather than discuss exhaustively its characteristics.

6.1 Core-shell LED growth steps

Core-shell LEDs were obtained from GaN-on-sapphire substrates, by top-down etching and MOVPE regrowth. The tall structures in Figure 6-1 showcase one the advantages of this design, the high-aspect ratio NRs. The tall NRs are seen in Figure 6-1 a), and represent the initial etched cores with a passivation layer at the bottom of the NRs, which prevents growth between the NRs. The subsequent MOVPE growth results in GaN structures with a hexagonal cross-section, terminated with $\{1\,0\,\bar{1}\,0\}$ m-planes.

Figure 6-1 b) illustrates the complete core-shell NR. The radial growth of the active area on the non-polar m-plane exhibits another technological advantage of the structure: the QCSE becomes either null for $\{1\,0\,\bar{1}\,0\}$ or minimal for the $\{1\,\bar{1}\,0\,1\}$ planes, which improves the overlap of electron and hole wavefunctions [40], leading to increased efficiency and number of radiative recombinations.

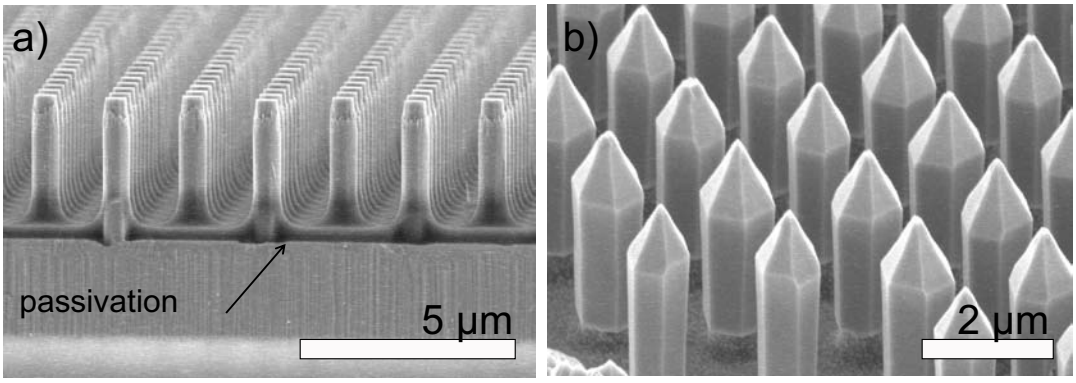

Figure 6-1: a) Etched GaN cores with base protected by a layer of ∼200 nm HSQ passivation b)Achieved core-shell structure used in optical and electrical measurements.

Sequential growth steps described in the previous chapters, build up the core-shell structure as shown in Figure 6-2. They include the etched GaN n-doped core, InGaN QWs to constrain carriers between undoped GaN QBs, and finally a conductive layer of p-doped GaN. On top of the core-shell LED the schematic shows a transparent conductive oxide layer (indium-tin-oxide ITO) for current spreading, a transparent dielectric spin-on-glass (HSQ) layer for insulation and planarization, and finally, metallic contacts complete the device structure.

Focusing on the active area first, radial InGaN/GaN QWs/QBs are grown on the m-plane sidewalls. In a previous section 3.7, and in recently published work from our group [132], the fill factor and temperature were shown to affect the InGaN shell's uniformity and indium incorporation respectively. The QWs were grown in temperature ranges of $650 - 750$℃, as covered in Chapter 4 and in refs [141, 132]. In Chapter 4 the sample with higher InN fraction on the m-plane, was obtained at 700℃ and showed the relaxed upper InGaN layer emitting at lower light intensity than the higher temperature sample (750℃), which in turn displayed single peak emission from a likely strained InGaN layer (see Figures 4-10a),b) and d)). In that case, it was concluded a concomitant increase in surface defects, proved by the increase in yellow-band luminescence, may occur for InGaN layers with thickness above $\sim 22 - 25$ nm, for which further growth results in a fully relaxed InGaN layer. An extended discussion on the relationship between QW

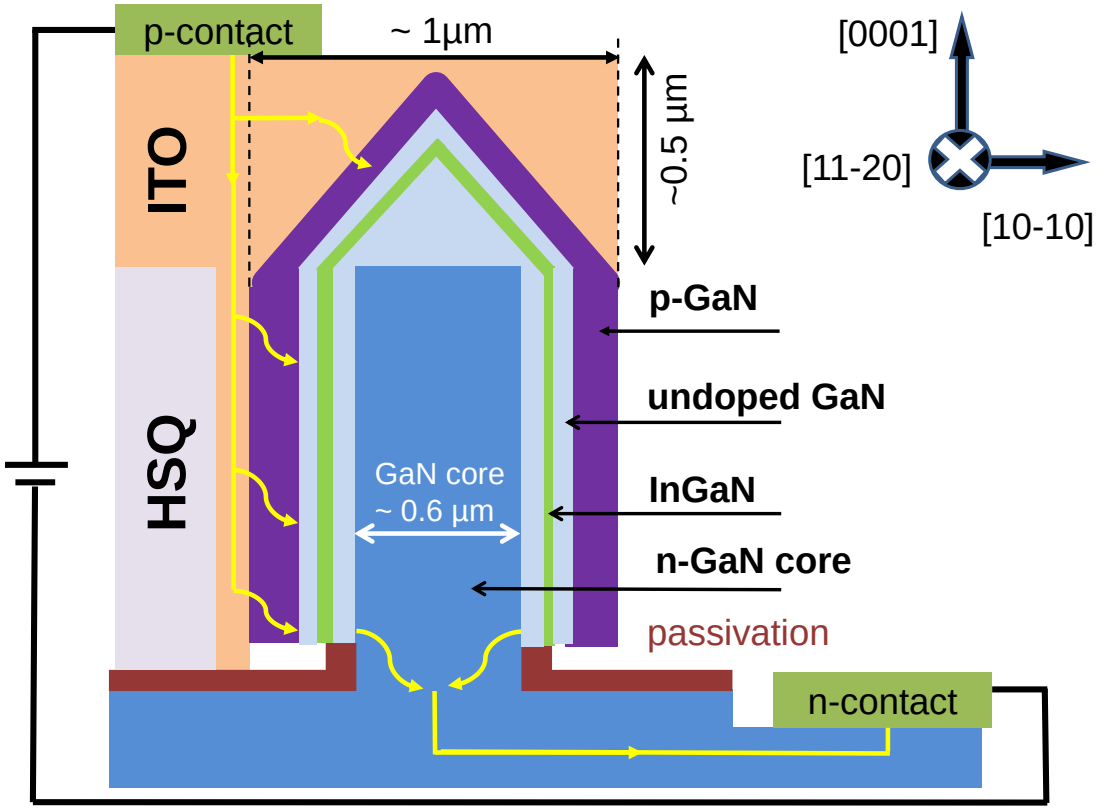

Figure 6-2: Proposed core-shell LED device structure comprising of sequencially grown GaN/InGaN/GaN/p-GaN layers, current spreading ITO layers, a dielectric HSQ layer and metal contacts.

thickness and maximum InN fraction on *c*-plane InGaN is provided in ref.[210].

The results in the sample set from ref [132] provided evidence that it is advantageous to reduce the InGaN growth temperature to achieve higher InN integration, obtaining a narrow QW and reduced number of defects, and this an improved emission uniformity and intensity. Results in that work showed uniform CL emission from a $\sim 10-11$ nm thick QW on the sidewalls of 1.5 µm tall NRs on Si substrates, after 6 minutes growth at 650°C. New sample sets were grown with thinner QWs on sapphire. Given a similar diameter to the Si substrate sample set (see Table 6.1), a rod height of $3-3.5$ µm, and growth time of $\sim 3-4$ minutes could achieve $\sim 2-4$ nm wide QWs, a thickness comparable to planar devices. The thicknesses of the InGaN/GaN QW/QB in Table 6.1 are estimates based on the TEM analysis in [132], while the p-GaN layer (sidewall thickness) was measured using the statistical SEM method (see section 2.2.1).

For core-shell LED samples 4650 and 4652, the different layers were grown in the

sequence found in Figure 6-3. For sample 4650 once the InGaN shell was grown, a single GaN QB was grown for 10 minutes, during a ramping procedure necessary to harmonize the two different temperature conditions for GaN and InGaN respectively. During ramping the pressure and temperature were changed from 300 mbar and 670 ℃ for the QW, to 100 mbar and 900 ℃ for GaN. For sample 4652 the same procedure was followed, however, a further 10 minutes GaN QB growth was done. Three periods of QW/QB were accomplished on sample 4652. Assuming the thickness of each QW and p-GaN layers are identical under the same parameters for the two samples, an estimate of $\sim$ 28 nm for 20 minutes QB can be made. Both samples were capped with a medium doped p-GaN layer with sidewall thickness $\sim$ 110 nm (see Table 6.1) grown for 40 minutes. For sample 4244, the QB was grown for only 6 minutes, because at the time, there was no information available to estimate layer thicknesses. The different growth rates for GaN can be explained considering the growths were accomplished under different conditions, and growth occurring during the ramping of pressure and temperature. GaN growth was done during ramping to protect the InGaN shell from decomposition. In two recent publications similar growth on *c*-plane was shown to produce very uniform thickness QWs, while direct growth at two separate temperatures showed discontinuities in the InGaN layer [211, 212]. In those studies, the discontinuous QWs showed superior CL intensity and narrower emission spectra, as InGaN defects underwent annealing. It is difficult to grasp the effect of noncontiguous QWs on core-shell devices, but growth at two very different temperatures on the *m*-plane can result in complete loss of InN or severe reduction in the InN incorporated [213]. Further TEM measurements on 4650 and 4652 could accurately determine the thicknesses and uniformity of the different core-shell layers.

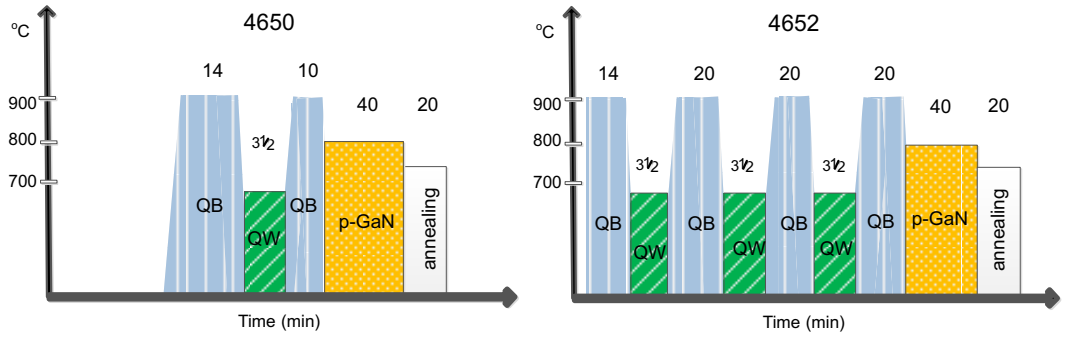

Figure 6-3: Growth steps and their respective duration for functional core-shell LED samples (not drawn to scale).

The p-GaN growth after an InGaN layer was grown resulted in a different morphology

Table 6.1: Summary of measured and estimated values for the different layers in NRs and core-shell structures.

Sample	InGaN QW (nm)	NR diameter (nm)	GaN QB (nm)	p-GaN sidewall (nm)
3833	$10-11$	938 ± 17	$7-8$	–
4244	$\sim 2-4$	887 ± 38	$\sim 3-4$	$\sim 49 \pm 20$
4650	$\sim 2-4$	1091 ± 91	$\sim 7-8$	$\sim 109 \pm 34$
4652 (3QW)	$\sim 2-4$	1188 ± 84	$\sim 8+20$	$\sim 109 \pm 34$

for p-GaN growth, compared to the GaN homo-junction growth described in the previous Chapter 5. The immediate difference observed was the lower p-GaN thickness on core-shell NRs. Another difference was observed with the lack of tapering of the NRs. The core-shell NRs in Figure 6-1 can be considered predominantly straight, although a slight increase in diameter can be observed at the top of the NR, likely caused by preferential InGaN growth at the apexes of m-planes and semi-polar facets. By contrast growth of p-GaN/GaN at 800℃ leads to NRs with wider bases (see Figure 5-4). Because the layers should be pseudomorphically strained, the difference in diameters may tentatively be explained if the indium atoms remaining in the chamber are reducing the GaN growth rate or increasing the diffusion length.

Reduced growth rate seems to be the case on the 3833 sample from ref [132], a 8 nm GaN-only cap-layer on the m-plane was achieved after 5 minutes of growth. This is a low value compared to the faceting growth rate (5.9 ± 2) nm/min or the p-GaN rate (2.7 ± 0.8) nm/min. On the 3833 sample the InGaN growth temperature was 650℃ for 6 minutes, resulting in a QW width of $10-11$ nm on 1.5µm tall NRs. The presence of indium could increase the solubility of Mg in GaN and efficiency of Ga atoms incorporation is reduced, reducing the overall GaN growth rate [214].

The increased solubility may have a positive impact on Mg incorporation. In fact co-doping Mg with InGaN has resulted in reduced number of V_N defects in recent studies [215, 216]. The final GaN QB or the p-GaN step could be extended to better understand the underlying process affecting the p-GaN. However, the thickness of the p-GaN was sufficient to have an effective rectifying behavior and recombination with light emission, as shown in the upcoming sections.

6.2 Device processing

An advantage of core-shell NRs created via top-down etching is a large number of highly uniform NRs that can be obtained. Processing NRs into a device of three-dimensional

(3D) nanostructures raises new challenges, which this work and other recent studies strive to address the problems [70, 172, 59]. Difficulties such as driving a uniform current through the 3D NR structure from top to bottom, having more resistive Mg shell than its n-core, enclosing the NRs in a transparent dielectric, connecting NRs in parallel and optimizing metal micro-contacts are of high interest. The effectiveness of the solutions proposed can affect the adoption of core-shell LEDs. The processing steps can be intensive, involving several resist spin-coatings, physical deposition, and lift-off procedures. Furthermore, imperfections in the patterning such as dust particles, non-optimum resist thickness can favor short-circuiting paths in the contacted NRs. The following subsections will discuss the difficulties, partial results and further optimization proposals that can be implemented for creating electrical contacts.

6.2.1 Pattern for core-shell LEDs

Ideally, large area nanoimprint masters should include patterns for the mask that separate individual LED devices, for example, $\sim 250 \times 250$ µm^2 (see Figure 6-4). Such dimensions are characteristic of planar LED structures. Individual devices obtained from NR arrays without NR-free regions in between, proved more challenging, but were possible with additional processing steps. From the experience gained in processing NRs to LEDs, a general guideline is that plasma etching and chemical processes should be kept to a minimum after the MOVPE growth is complete, as these methods could introduce non-radiative defects.

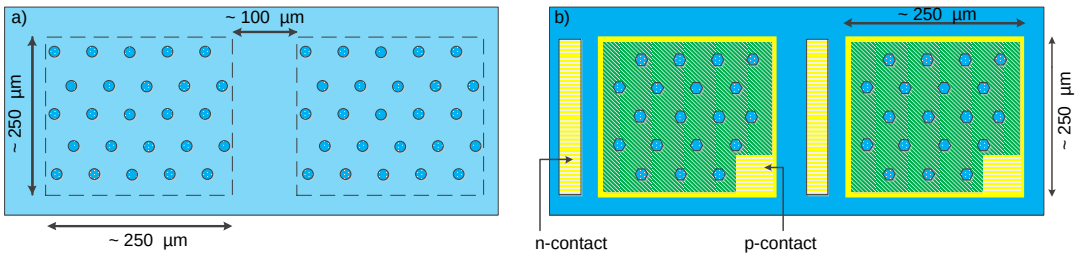

Figure 6-4: a) Nanoimprint master with regular spacing (dashes) between NRs for individual LED devices, b) Planar view of proposed core-shell LEDs with current spreading layers, encapsulated in spin-on-glass dielectric and with contact pads.

The plasma etching followed by passivation, MOVPE growth for GaN, InGaN/GaN and p-GaN layers would be carried out as described in the previous chapters.

6.2.2 Current spreading layer

The NR structure with the different layers for a core-shell LED is shown in Figure 6-5 a). A conformal ITO deposition shown in green in Figure 6-5 b), was deposited by rotating and angled e-beam evaporation to avoid NRs shadowing each other. ITO is a semiconductor oxide with a high donor density, which makes it an excellent choice for a transparent p-contact and a current spreading layer. This deposition method produces porous ITO films, whereas superior coverage can be achieved with sputtering deposition. An approach to connect the similar NRs without an indium based transparent conductor, using conformal GaZnO deposition instead, is discussed in ref [217].

Prior to ITO deposition, a second HSQ passivation layer was spin-coated on the sample to obtain a thicker passivation and better insulate the conductive ITO from the InGaN between the NRs and from underlying GaN. The exposed GaN in areas with nanoimprint imperfections or which suffered physical damage from sample handling can cause shorting. The HSQ parameters in section 2.1 were followed (2000 rpm, 300 ℃), but without the high temperature (550 ℃) anneal in N_2. Therefore excess HSQ from the core-shell NR sidewalls was removed in a 5 seconds 100:1 BOE etch. An additional passivation by PECVD was attempted as well in order to secure better insulation from the planar GaN layer. In PECVD passivated samples cork like rod tips are visible as in Figure 6-8 b).

The ITO layer was deposited using a rotating, angled sample support at 30°, 45° and 60°, to find the best configuration for uniform NR coverage without shadowing effects. The effect of the angle and of different film thicknesses achieved are shown in Figure 6-6. The best coverage and resistance were achieved at 30° angle and 350 ℃ annealing for 5 minutes (see Figure 6-6 a). Angled deposition also introduces voids in the ITO film, reducing its annealing temperature and increasing resistance, compared to non-angled films. Annealing was done on the hot plate in an air atmosphere, to achieve low resistivity and high transparency in a range of $100 - 300$ nm thickness films. Annealing under nitrogen atmosphere led to high resistance and opaque samples, without improvements from as-deposited characteristics. It is known that annealing ITO in the presence of O_2 introduces vacancies essential for a high number of carriers and low resistance [218]. Resistance was measured by the four-point-probe method on ITO films on glass slides obtained during the same deposition as the NRs.

The conformal ITO layer provides coverage on individual NRs, however neighboring NRs have to be connected to each other to ensure the spread of current uniformly through the LED device. This can be achieved with a second ITO layer. The space

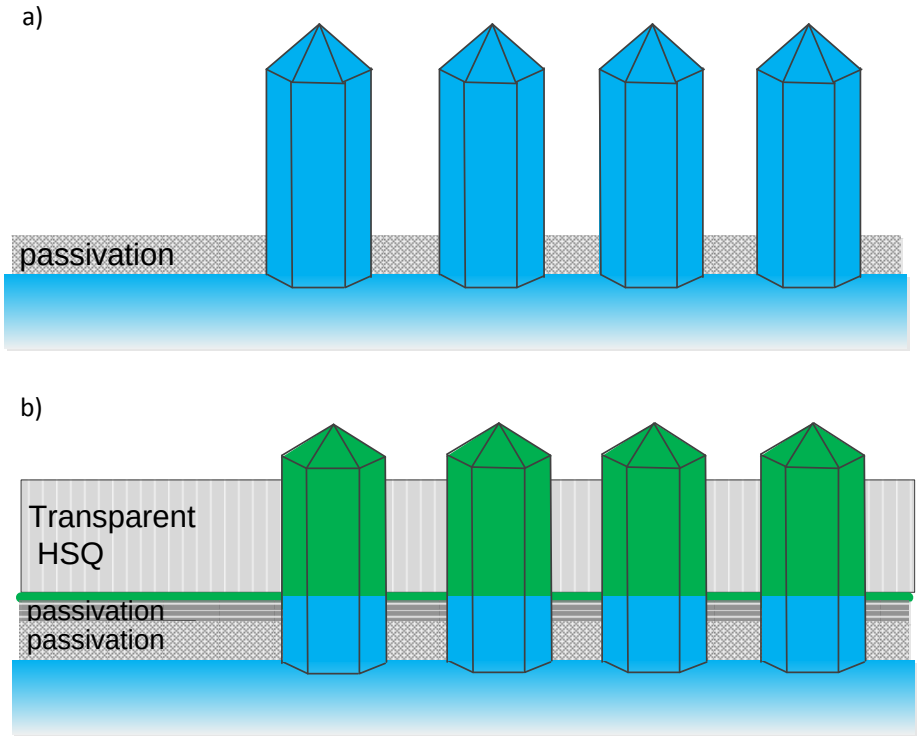

Figure 6-5: a) Core-shell NRs after MOVPE growth, b) NRs covered in a conformal ITO layer (in green) by angled e-beam deposition; this structure is spin-coated in a transparent HSQ layer for planarization and insulation.

between NRs can not be fully covered in ITO, especially for high-aspect-ratio NRs. A planarization step (see subsection 6.2.3) was used to fill the space between NRs with a transparent HSQ dielectric and make possible a second ITO deposition. The NR tips have to be exposed by an etch back step. This was attempted with plasma etching because of its highly controllable etch rate. Although plasma etching of the HSQ with CHF_4 showed no surface damage on the ITO protected NRs, it is possible thier conductivity was damaged. Thus alternatively a short back-etch step in BOE is preferable.

In later work it was found that the conformal ITO layer can still be a source of current leakage, thus it is preferable to limit the areas covered in ITO. It is proposed that a patterned deposition using a stencil or glass mask with the individual LED device profile be overlayed prior to the first ITO deposition. This provides less accuracy than a resist mask, however, the angled deposition or even sputtering deposition are likely to prevent easy removal or the resist after deposition.

In the initial work, for the second ITO deposition the entire sample was covered in

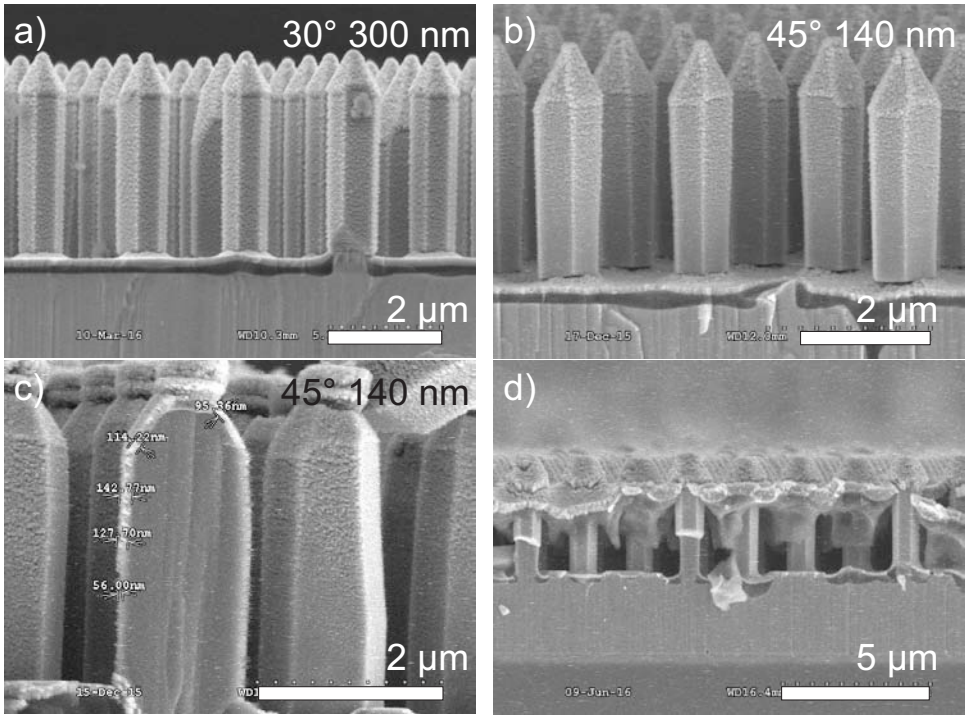

Figure 6-6: Different ITO coverage for a) 30° thick ITO on thin p-shell NRs, b) 45° 140 nm ITO on core-shell LED structure, c) detail on thick p-shell NRs showing different thickenss ITO at 45° deposition, d) planar ITO deposition on top of HSQ planarization layer and NRs.

500 nm thick continuous ITO layer as in Figure 6-6 d). Individual LED devices were attempted to be separated by exposure to a H_2O:HCl 50:1 solution. However because the diluted HCl solution infiltrates the ITO layer and peels it off non-uniformly and damages the ITO film, another method is proposed.

A metal deposition for a metallic p-contact pad can be achieved before the second ITO deposition, on the planarized HSQ layer and exposed NR tips. Metal lift-off can be complicated by the angled tips, thus the height of the tips, metal layer, and lift-off resist thicknesses should be carefully considered. The second planar ITO layer can be deposited in the inner perimeter of the p-contact pad, using another spin-on resist step and a photolithography step. A planar ITO layer of $100 - 300$ nm thickness can be obtained and annealed (see Figure 6-7 b). Successive annealing in identical conditions has shown that resistance does not change significantly with each heat treatment.

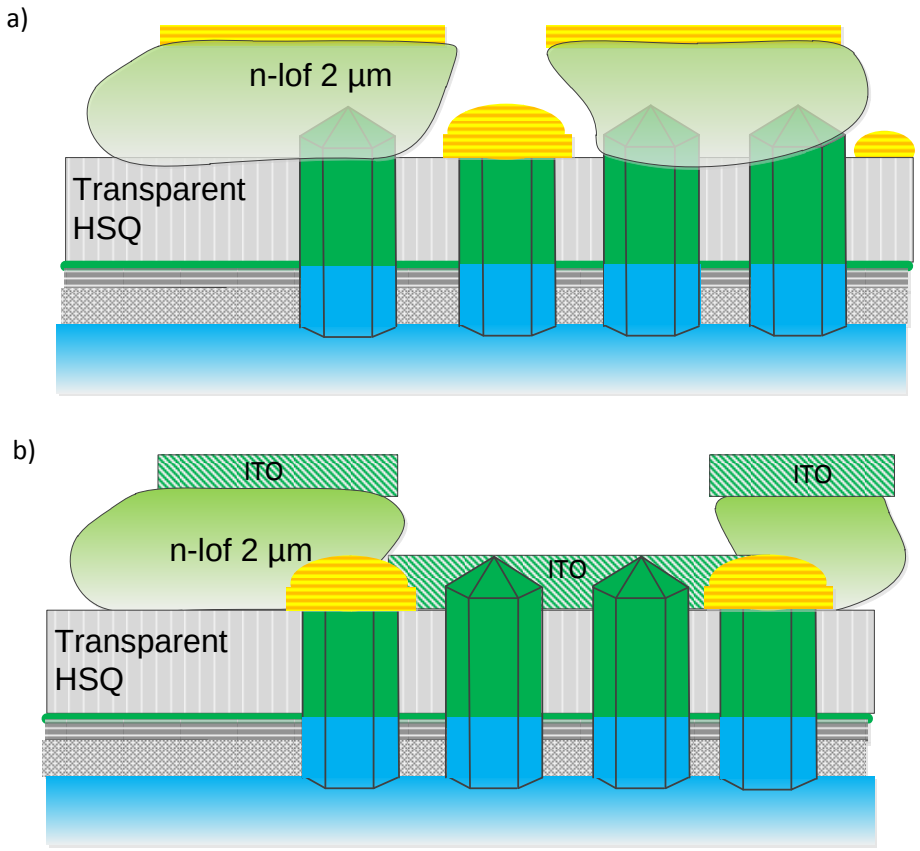

Figure 6-7: a) n-LOF for metal p-contact metal deposition on HSQ and NR tips, b) deposition of a planar ITO layer using n-LOF resist and a lift-off step.

6.2.3 Planarization

Planarization of the 3D structure with a transparent dielectric is necessary to place contacts, physically protect the NRs and as a means to spread the emitted and scattered light through the NR array. Several methods and resists were considered: PMMA, SU8, PDMS, and HSQ. Although PMMA was very easy to adjust for spin-rate and height, and coverage uniformity. SU8 offered excellent fill and height control with resist concentration, but all resists except for HSQ, experienced loss in transparency after the ITO annealing step at 300 ℃ necessary to reduce the oxide resistivity. PDMS used in ref [59] can be processed only up to 200 ℃, which does not provide transparent and conductive ITO. HSQ resulted as being the best material for the design considered and for non-flexible supports.

Planarization was achieved by spin-coating a thick ($\sim 2-3$ µm) and transparent HSQ as shown in Figure 6-5 b). When the spin rate was reduced to 2000 rpm, the NRs

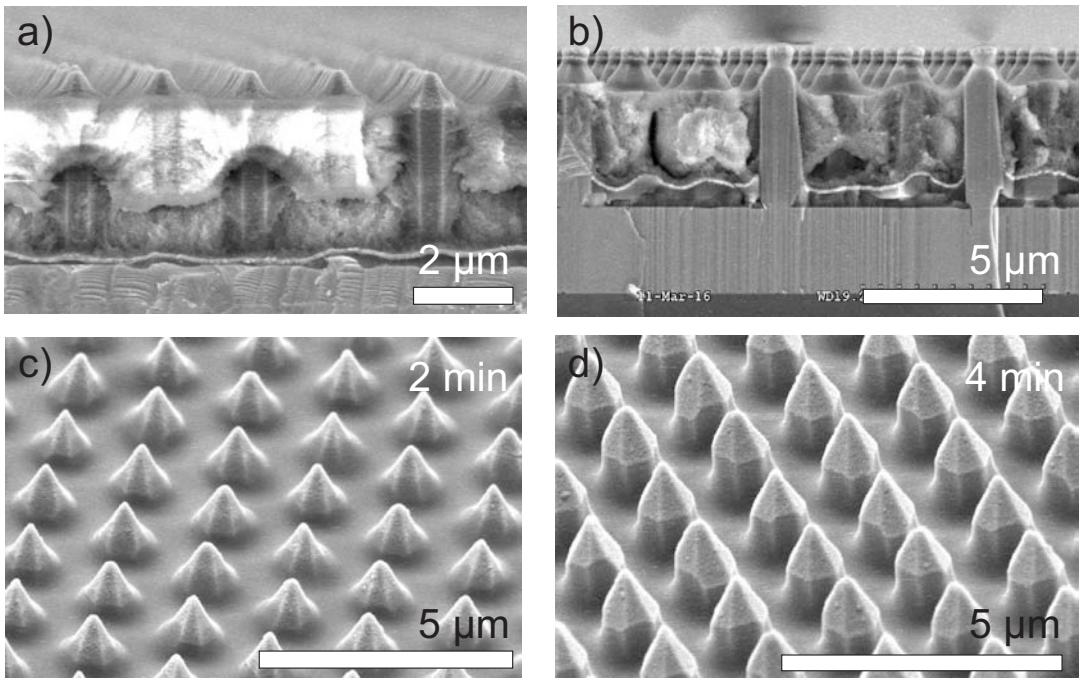

Figure 6-8: a) Cross-section of HSQ planarized NRs for LED sample 4244 with a single passivation layer, b) cross-section through planarized NRs with a 60 min (p-GaN) growth time and PECVD SiO_2 passivation, both samples show a thin ITO layer on the passivation, c) after 2 min of plasma back-etching, the HSQ is removed from the semipolar planes with no physical damage to the ITO, d) further back-etching exposes the m-planes.

were covered in a single layer of HSQ, although some voids were included. Alternately, multiple layers can be applied in a succession of spin-on-resist and hot plate curing, to adjust for the NR height. A glass transition can be achieved after reaching 300 ℃ curing temperature for 3 minutes on the hot plate. A gradual cool down ($\sim$ 50 ℃/min) was used to minimize HSQ cracking.

A plasma back-etch step was carried out to remove the HSQ from the top $\sim$ 500 nm of the NRs, as it provides a very controllable etch rate under CHF_3 chemistry (see Figure 6-8). However, it is unclear at this stage for these samples whether the fluorine affects the NR tips by the loss of hole carriers [219, 220]. Ref [172] showed that p-GaN can be affected by CF_4 plasma, but unlike the NRs in that study, these samples had an ITO buffer layer which was not physically affected by the plasma treatment. However the back-etch step or an immersion in HCl, done during the development of the process, damaged the sample on which the contact structure was placed, and it became unusable for light emission or current-voltage measurements.

An alternative to plasma back-etching is the removal of the top resist layer by a short (10 seconds) BOE etch. The risk of using BOE is the possible infiltration in the HSQ layer and its cracking. Note that measurements on ITO thin films on glass slides showed no change in resistance values or transparency after placing the ITO in BOE 100:1 even after 3 minutes.

6.2.4 Metallic contacts

The *p-contact* was obtained after spin-on of n-LOF resist, metal deposition, and lift-off. The n-LOF resist needs to be thick, as the tips of the NRs and the ITO layer raise the profile by ~ 1 µm and lift-off can be problematic. The resist was baked for 2 minutes, then exposed to 1.65 mW with the direct mask laser writer. Post-exposure baking of 2 minutes, developing for 90 seconds with MIF 826 ensured a good resist lift-off profile. The deposited metal alloy was Ti/Al/Ni/Au with 20/60/20/200 nm thicknesses. The most used p-contact metals are high work-function metals (Ni, Au) because they result in a low Schottky barrier height [221]. However, since contact optimization was not pursued and the p-contact did not need to be transparent, the same alloy was used for the p-contact as for the n-contact. After lift-off in hot 1165 solution the contact profile obtained is shown in Figure 6-9 a), with individual NRs visible in Figure 6-9 b). Please note that for these proof-of-principle devices the planar ITO layer was not divided into individual devices. For an optimized design, it was proposed in a previous subsection to first deposit the p-contact, followed by the planar (second) ITO layer deposition inside the area bordered by the metal pad squares. The p-GaN and ITO are not affected by the developer and stripper chemicals used, such as MIF 826, 1165 or acetone.

For the *n-contact* a fabrication design is proposed in Figures 6-10 a) and b). Long 250 µm and 50 µm wide Ti/Al/Ni/Au (20/60/20/100 nm) metal stripes for the n-contact could be placed in the ~ 100 µm spacing between individual devices. For the switch to 2 µm pitch NRs, the HSQ passivation thickness and coverage was observed to depend on the NR density, leading to areas of poor coverage and insulation between the NRs.

The etch rate for plasma-enhanced chemical vapor deposition (PECVD) and unannealed HSQ is ~ 500 nm/min [222], and experimentally observed at $1.0 - 1.2$ µm/min for the 300 ℃ 3 minutes cured spin-on HSQ. The thick HSQ layer is etched both in the vertical and lateral directions and since the lateral etching has to extend $5\times$ further than vertical etching, the devices should not be affected by the BOE. The spacing between the n-contact and the NRs could be further adjusted to consider chip dicing.

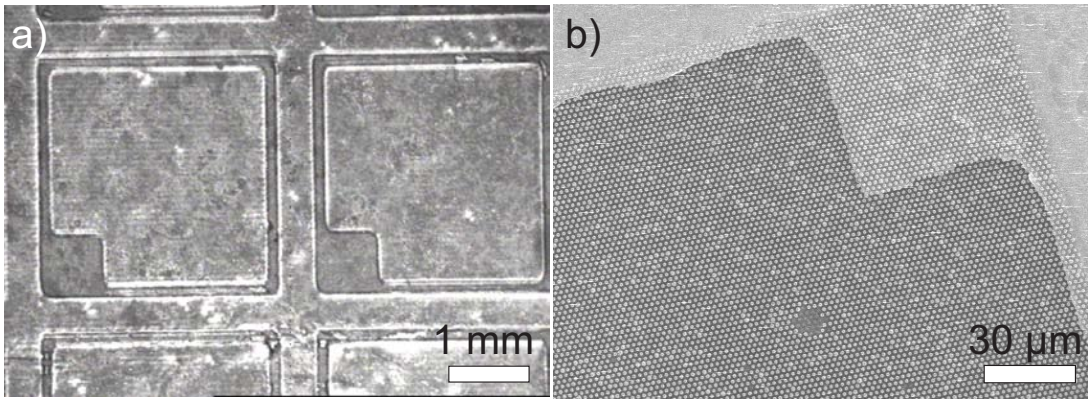

Figure 6-9: a) Optical microscope image of metal p-contacts on the ITO layer, b) SEM image of individual NRs covered in ITO and metal on the contact pad.

For the samples discussed which underwent electrical measurements in this work, the n-contact was placed at the edges of the samples using an indium bead soldered onto the underlying GaN. The mechanical removal of the passivation and scratching the GaN with a diamond scribe provided a reasonably reliable contact. While this would not be part of a commercial process, this method allowed for proof-of-principle electrical measurements to be made.

6.2.5 Alternative fabrication proceses

The metal contact methods discussed bring together traditional microfabrication methods. Planarization by MBE coalescence and transition to 2D p-GaN growth are proposed in literature which could work well on closely pack nanorods [223, 224, 67]. Coalescence is also likely to introduce defects local to those regions [30]. Other propositions are Ti/Au contacts from removable metal foils [225] or adoption of a flexible support and a Ag nanowire mesh [59]. A technique very recently proposed in planar layers grown in the $[1\,0\,\bar{1}\,0]$ direction based on n-contact on the substrate back-side and a p-contact on the epitaxy side with light extraction through the sapphire could also be adapted and explored [226]. Conductive Ag paste was used as a cheap and simple alternative to contact groups of NRs and investigate the important aspects of optical emission and electrical properties of core-shell LED.

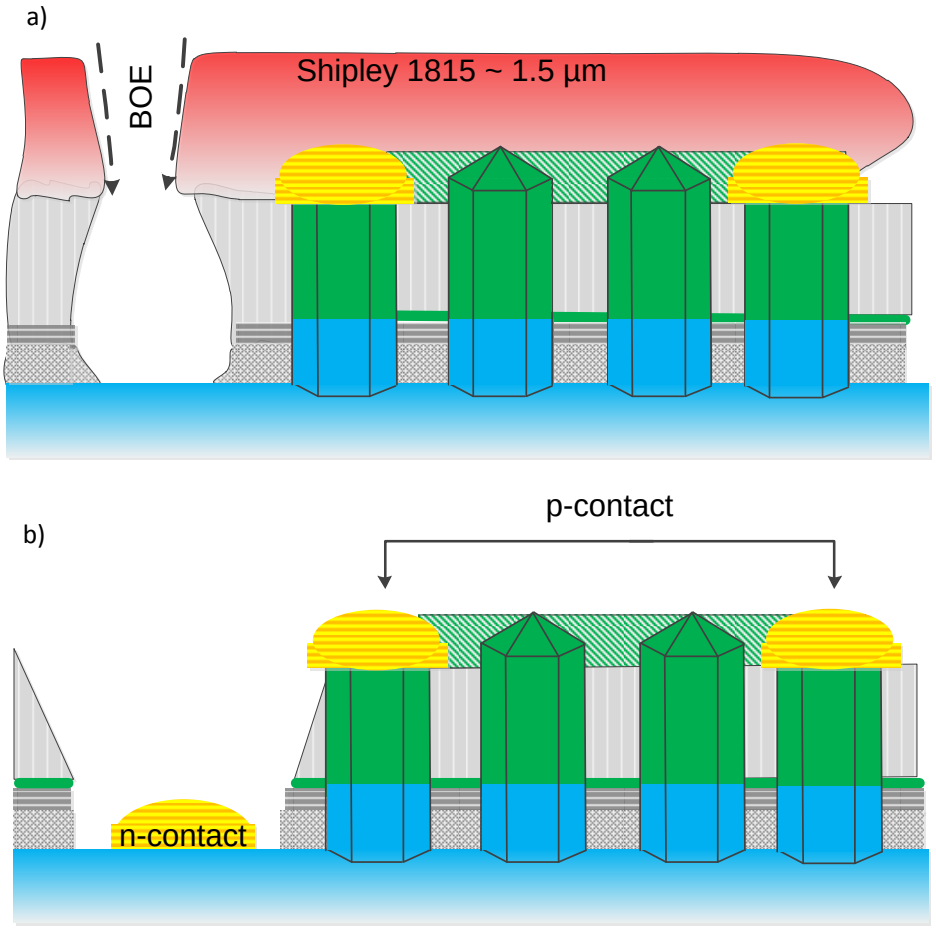

Figure 6-10: a) Spin-coated Shipley 1815 (BOE resistant), b) BOE etch to remove the HSQ for the n-contact deposition; the device is protected by the 5× larger amount of HSQ than needs to be etched laterally than vertically.

6.3 Light emission from core-shell LEDs

The following is a comparative discussion based on core-shell LED light emission under electrical, optical and e-beam injection. The excitation mechanisms are different for EL, PL, and CL, leading to dissimilar emitted wavelengths. For EL the top p-contact was replaced with a silver paste contact, because of shunting problems with ITO. With an improved passivation and a patterned ITO deposition, these issues could be avoided. PL emission from a 405 nm laser source with a focus spot ∼1 mm was used to excite the samples in the same area where the EL was probed from. Hyperspectral cathodoluminescence (CL) mapping provided a high-resolution perspective on the origin of the each emitted wavelength.

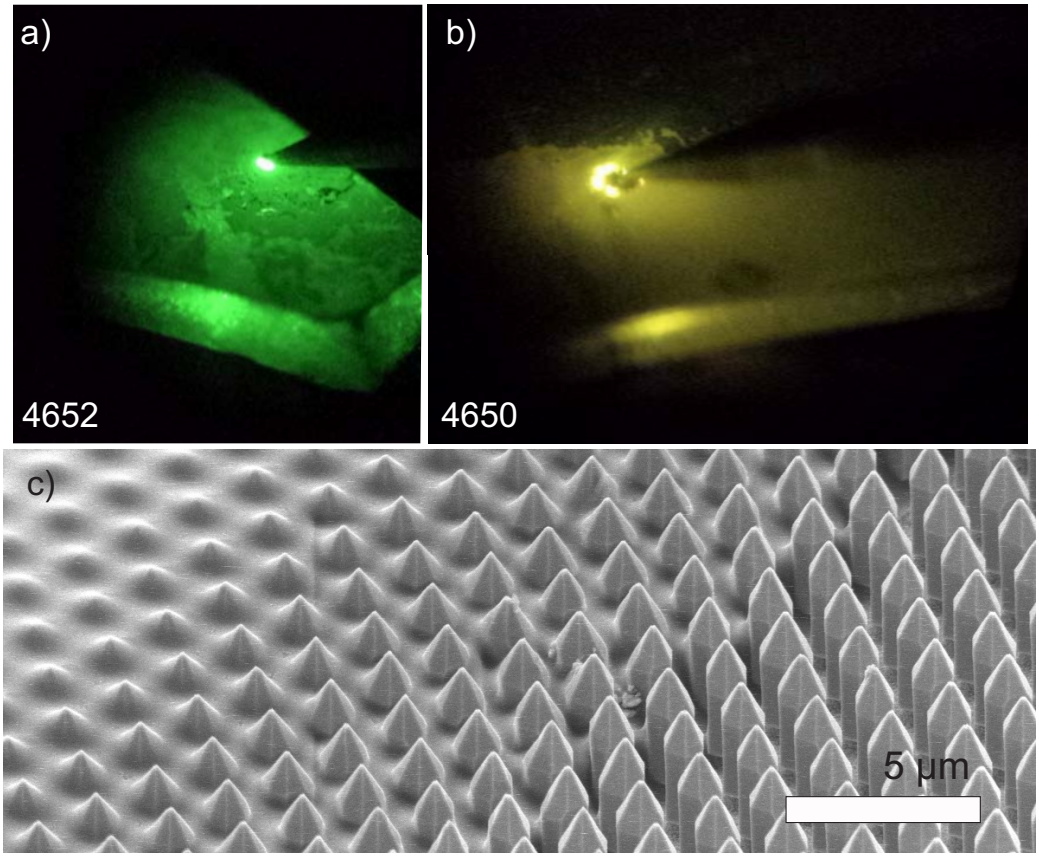

Figure 6-11: a) Green electroluminesce emission at 533 nm from the 3QW sample (4652) , b) green-yellow emission from the SQW sample (4650), c) spread of the silver paste between the NRs.

In Figure 6-11 the green and mixed green-yellow EL emission from samples 4652 (3QW) and 4650 (SQW) are shown magnified under an optical microscope. The emitted light originates from under the silver paste contact and from NRs at the contact boundary. The yellow emission is likely related to areas with irregular growth on the template, and its source is the Si-doped GaN [227]. The irregular rods in sample 4650 were caused by remaining passivation on the sidewalls and poor growth. Thus the analysis concentrates on the 4652 3QW sample.

The emission spectra obtained under optical and electrical injection are shown in Figure 6-12. The main PL peak was observed at ∼483 nm, and a second peak at ∼600 nm, likely related to the yellow luminescence (YL) band. Under electrical excitation, the emission was observed at $537-533$ nm with 10 V forward bias and 10 mA current. The main emission wavelengths possibly originate from the semi-polar facets, as it could provide a better current path, either due to the silver contact or due to a relatively

more resistive p-GaN on the *m*-plane facets. The main PL blue emission was caused by the incidence of the laser beam on the *m-plane* facets. This indicates that *m-plane* emission could be obtained if the NR contacts can be further optimized.

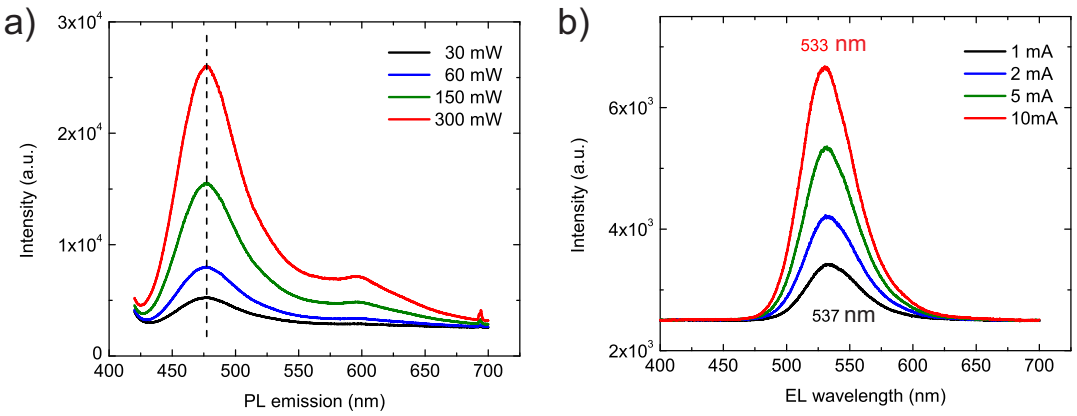

Figure 6-12: a)Sample 4652 PL spectra, b)EL spectra under forward bias.

The EL emission from Figure 6-12 b) shows a small blue shift of 4 nm with increasing current between $1 - 10$ mA. The blue shift in EL peak is likely caused by the combined suppression of the QCSE, due to the screening of the piezoelectric field, and by band filling of the localized states with excitons [228]. For polar facets and QWs, the conduction and valence bands bend subject to a strong internal field reducing the transition energy. For non-polar directions, lack of PL or EL shift indicates the absence of polarization-induced internal electric fields in the active region [229]. Carrier localization can reduce the screening caused by the QCSE [230]. The blue shift with increasing current or power intensity was observed in the EL spectra but not in PL. This could be explained by insufficient PL resolution.

Because of the high amount of electron carriers provided by the n-doped core, the electrons populate states within the conduction band, which push the electron quasi-Fermi level higher in energy and inside the conduction band. An electron from the top of the valence band can only be excited into the conduction band above the Fermi level, thus this appears as an effective increase in band gap (*Moss-Burnstein* or band-filling effect). The band-filling effect was observed in ref [231], where for QW thickness between $2.5 - 5$ nm, a quantum dot-like rich indium phase acts to blue-shift the emission with increasing power density. Competition between the screening of the built-in electric field and band filling effect was also observed in ref [232].

Real color mapping calculates the chromaticity coordinates of the CL spectrum from each point in the CL scan in CIE 1931 color space, and plots them as RGB real color

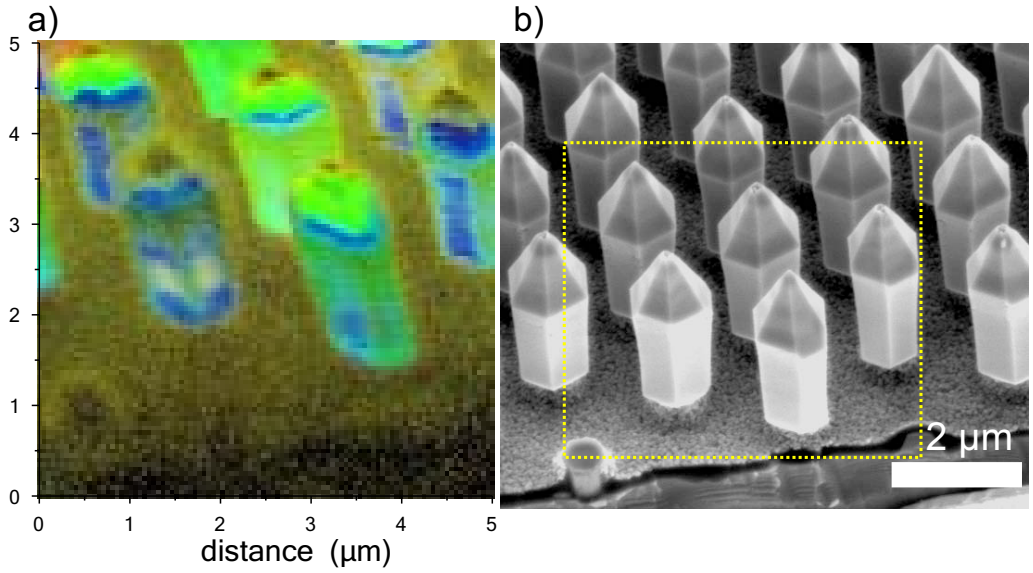

Figure 6-13: a) Real color CL map of 4652, b)SE NRs at 5 kV accelerating voltage.The images are distorted with respect to each other due to charging during acquisition.

CL maps as shown in in Figure 6-13 a). The hyperspectral CL map identifies the green emission (533 nm) originating from the semi-polar $\{1\,\bar{1}\,0\,1\}$ facets, while the blue (483 nm) peak emerges from the m-planes and from a small ring-area around at the apex of the semi-polar and m-plane facets.

Overall three LED samples were obtained with very similar growth parameters and capable of light emission: the 3QW (4652), SQW (4650) and an SQW with a thin p-GaN layer (4244) of $40-60$ nm. CL spectra from each of the samples are shown in Figure 6-14. The MQW spectra exhibit several peaks and troughs between $520-560$ nm due to resonant modes originating from the NR cavity due to either whispering gallery or Fabry-Perot modes [233].

In Figure 6-15 the different wavelength contributions to the CL signal on sample 4652 were separated, and each contribution was amplified relative to the green emission intensity. Two overlapping blue emission peaks are visible, which could indicate that the growth time was sufficient to create a pseudomorphically strained layer emitting at ∼455 nm and a partially relaxed layer with ∼483 nm emission. The two peaks correspond to $\approxeq 19-20\%$ InN when correlated to the band gap in either the strained or fully relaxed model [164]. Another overlap can be seen between Figures 6-15 a) and b), suggesting that green ($532-537$ nm) emission results from a fully relaxed InGaN layer, corresponding to ∼25% InN mole fraction.

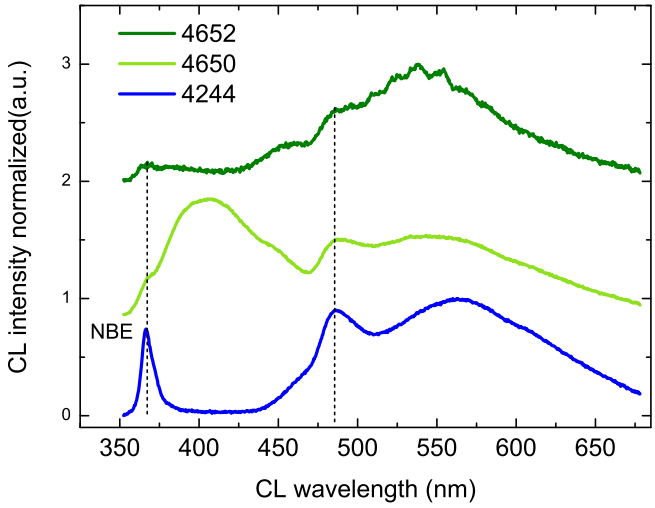

Figure 6-14: CL spectra from the different devices obtained SQW (4244, 4650) and MQW (4652).

In Figure 6-13 b) the SE image shows a darker contrast at the $\{1\,\bar{1}\,0\,1\}$ pyramid bases, which can be related to a more electron absorbing material, while the bright m-plane can indicate electron charging and a more resistive material. Figure 6-15 d) provides a highly amplified signal map of the DAP distribution on NRs, similar to maps seen in Figure 5-8. The DAP is a signature of Mg presence, however, in its hydrogen passivated state [177]. The samples were annealed to break the Mg-H bond, however not all bonds can be broken. Although it is the Mg-V_N complex that has been linked to resistive p-GaN [192], the complex characteristics emission 2.18 eV [196] cannot be distinguished from YL in the CL spectra. However, the presence of electrically inactive Mg-H related to the DAP is an indication of a reduced number of free hole carriers, and of a more resistive m-plane p-n junction.

Although samples 4244, 4650 had limitations, some lessons were learned from them. In Figure 6-16 the two samples showed they could maintain better emission uniformity than the MQW. Because the real color maps are dominated by yellow emission in Figures 6-16 a) and c), this indicates the n-doped GaN core is the source of emission. Emission from the n-doped core may be caused by the partial growth in sample 4650 or by the thin p-GaN sidewall in 4244.

Because most of the emission originates from the semi-polar plane further optimization of the MOVPE conditions is required to provide homogeneous emission from the m-planes. Higher index planes are likely formed due to 3D Stranski-Krastanov growth of the InGaN shell, and the variation introduced this way affects the uniformity of the

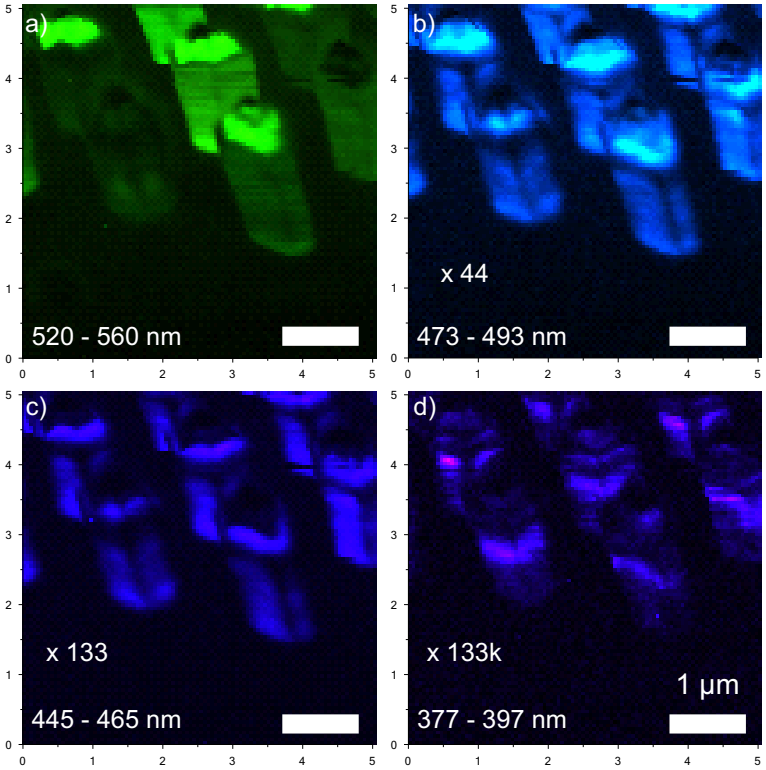

Figure 6-15: CL maps for sample 4652 at $5kV$ accelerating voltage; a) for emission in green ($520 - 560$ nm), two of the rods show uniform emission on both m- and semi-polar planes, b) blue emission, signal amplified $44\times$ in relation to green emission, c) another blue peak, likely from a strained layer, d) emission from Mg DAP; the scale bar represents 1µm.

GaN QB [213]. The growth mode can be adjusted by growth parameters, either by increasing slightly the temperature to achieve a higher desorption and uniformity or by reducing the pressure and thus the growth rate, as it was the case for sample 4244. Finally, the MQW sample provided the highest light intensity, visible by naked eye at normal room lighting from a non-optimized contact.

6.4 Electrical characterization

6.4.1 Electron beam induced current

The electron-beam-induced-current (EBIC) method is an excellent electrical characterization tool for probing semiconductor samples. It is especially useful in semiconductor

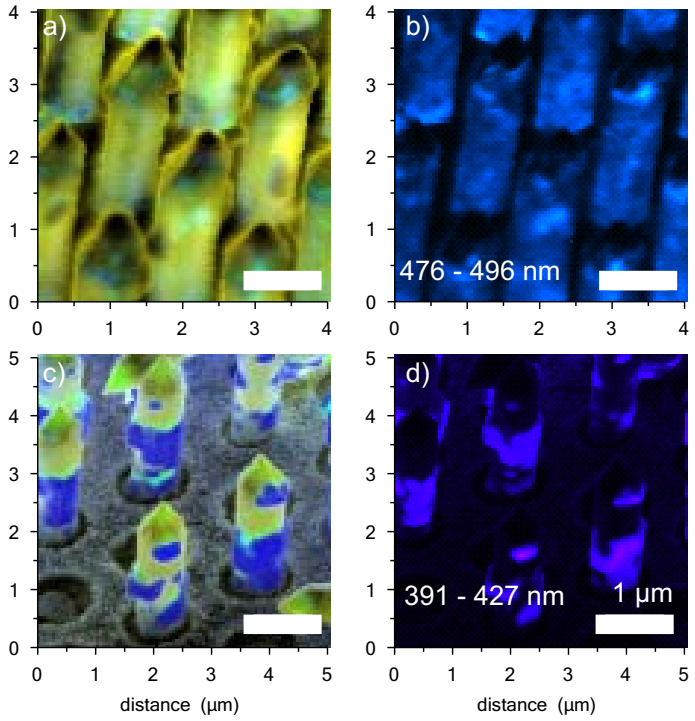

Figure 6-16: a) Real color CL map for 4244 obtained at 680 ℃, 150 mbar, 8 minutes InGaN, p-GaN 10 minutes , b) main emission from blue peak, c) real color CL map for 4650 obtained at 670 ℃, 300 mbar, 3'30" minutes InGaN, p-GaN 40 minutes, d) main violet peak emission.

nanostructures for which electrical contacts are difficult to attach, which have larger resistance compared to the probed sample. Also, EBIC is very useful in the case of small and irregular sample shapes, for which Hall effect measurements are not reliable. Its application to NRs can be seen in Figure 6-17 for which a current is driven through the tip of a nanorod and the underlying n-GaN. The EBIC measurements were performed by Prof. Alexander Šatka from the Slovak University of Technology on nanorod samples featuring p-n homo-junctions and on core-shell LED structures (sample 4244). A schematic of the CL/EBIC system was provided in subsection 2.2.7. A thorough perspective on the EBIC method is given in ref. [131].

Charge carriers are generated in a small area on the sample probed by the highly focused electron beam of a SEM. The collisions of energetic primary electrons with valence electrons in the sample produce an electron in the conduction band and a hole in the valence band. If the scanned sample area contains a p-n junction, the random movement of the generated carriers is ordered by the built-in electrical field of the junction. This leads to a separation of the electrons and holes so that they do not

recombine and instead form a current in the external circuit. A charge collection map shows the location of the p-n junction in the sample. Application of a voltage drop by nanoprobes across different regions of the sample provides information on the junction depletion width or space charge region (SCR), bias information, carrier diffusion lengths, and carrier concentrations and transport efficiencies at different biases. Local inhomogeneities and defects can be evaluated by EBIC.

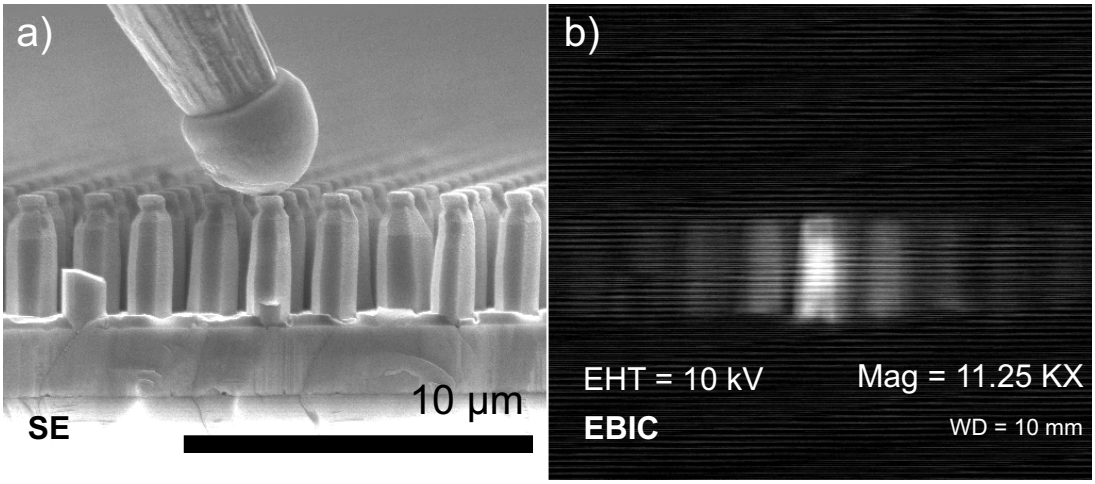

Figure 6-17: a) SE image of nanorods and EBIC probe used to apply a voltage drop across individual NRs; b) correspondig EBIC current map with contacted NR and current spreading to neighbouring NRs proving a good passivation.

Figure 6-17 shows GaN NRs with an overgrown p-GaN shell at medium doping level (0.44 µmol/min) contacted with a tungsten tip probe. The p-n junction is perceptible at 0 V U_{bias}, the EBIC signal becoming stronger with the increase of the reverse bias. In contrast, in forward bias the positive external electric field at the junction reduces the depletion region, encouraging majority carrier diffusion and reducing the drift of minority carriers across the depletion region. The charge-collection current displayed in EBIC maps increases with the probability of minority carrier recombination. The increase in collection current occurs for a wider junction area, obtained under reverse bias.

Figure 6-18 proves the current spreads preferentially in the NR-tip contact area. The signal from NRs is very local to the metallic tip due to the thin p-GaN layer, a thickness comparable to the hole diffusion length. After Mg doping, it is expected that the samples will experience an increase in resistance even after annealing, due to low mobility and a low number of carriers, as discussed previously in Chapter 5. For this reason, it was opted to enhance current spreading by deposition of an ITO layer on the

NRs. Several figures below prove the electron-beam deposited ITO formed relatively good ohmic contacts on the NR m-planes after annealing the ITO on the hot plate in an air atmosphere.

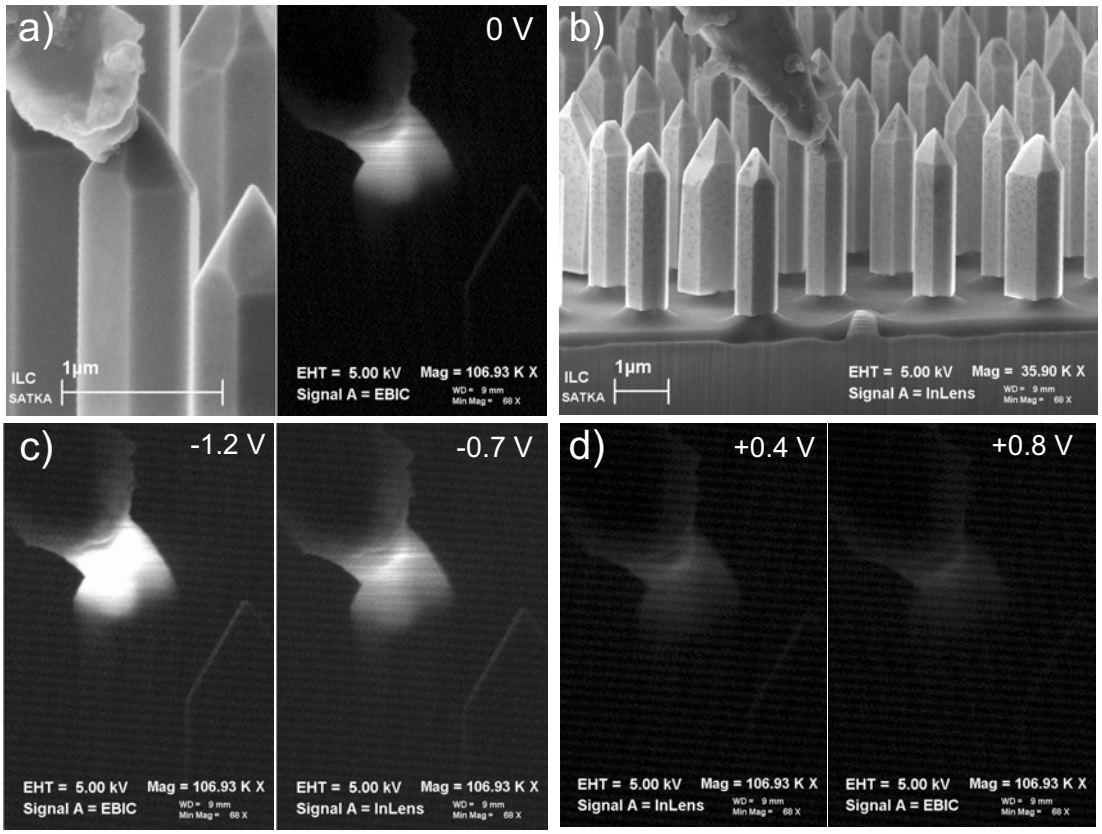

Figure 6-18: a) SE image and EBIC current map (medium Mg-doped NRs without ITO) at U_{bias}= 0 V shows current spreading only at the NR tip, b) SE image of an ensemble of NRs with one probe contacting a single NR, the second probe is on the underlying planar GaN, c) p-n junction under reverse bias indicates 'brighter' contrast and increasing current collection efficiency with increasing negative bias d) forward bias reduces the width of the SCR and displays 'darker' contrast with forward bias.

Direct proof of the p-n junction formation in NR can be seen in Figure 6-19, for which partial removal of the conductive ITO layer shows the underlying p-n junction in a bright, uniform contrast along the entire uncovered region. Unlike NR without an ITO layer in Figure 6-18, the current spreads along the entire NR. In Figure 6-19 b) the ITO was too thick to be penetrated by the 5 kV electron beam, but the uncovered region shows good charge collection from the p-n junction, and not from the GaN-ITO interface. At 10 kV acceleration voltage the 300 nm ITO can be fully excited with the increase in the charge collection volume.

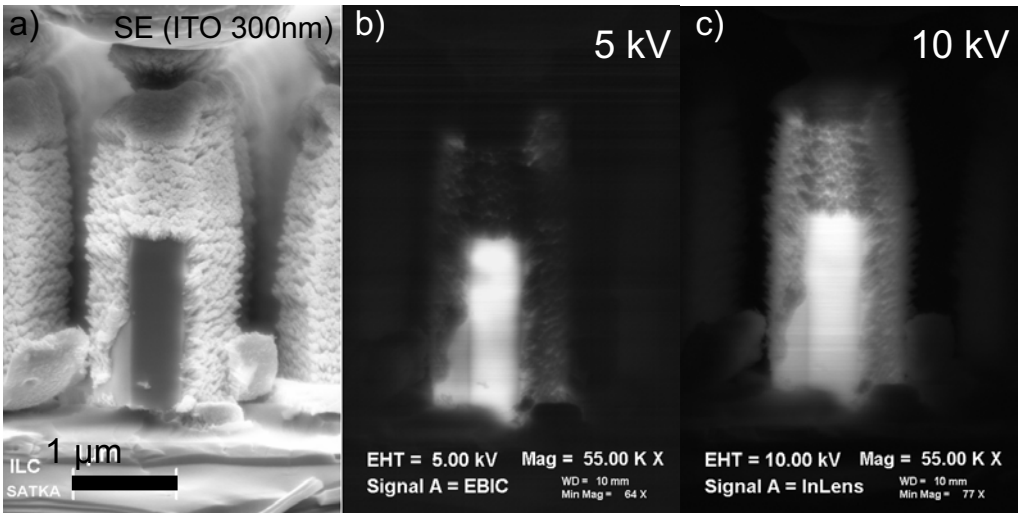

Figure 6-19: Direct proof of p-n junction with current spreading layer. a) SE image of NR covered in a 300 nm thick ITO layer, b) EBIC map with partial cover at 5 kV, charge collection is uniform on the NR sidewall, c) EBIC map of NR at 10 kV accelerating voltage,U_{bias}= 0 V.

A set of p-GaN-on-GaN NR samples was grown with 60 minutes p-GaN shell growth time to study the width of the p-n junction and optimize p-GaN growth. Apart from the growth time, the recipes (*low, medium* and *high* doping) were identical to the 20 minutes p-GaN NRs samples discussed in Chapter 5. The thicker NRs ($\sim 1147 \pm 48$ nm) were more easily split with cross-sections, which were necessary to determine the p-n junction width in EBIC. Figure 6-20 shows a cross-sectioned NR for which the different layers are identifiable from combined SEM and EBIC images. The false color EBIC map proves that most of the junction extends in the p-GaN layer, indicating a lower number of active hole carriers, relative to the electron carrier concentration. The width of the p-n junction measures $\sim 150 - 200$ nm. Darker contrast p-GaN on both sides of the NR indicate areas where the minority carriers have not been swept across the junction by the built-in field.

For a junction the width of the SCR is given by equation 6.1, where $\varepsilon_{GaN} = 9\varepsilon_0$. The built-in p-n junction potential is given by equation 6.2 as the V_{bi}. In equation 6.2 the U_{bias} is the external applied voltage, and N_d and N_a are the carrier concentrations for electrons and holes respectively [131], k_b is the Boltzmann constant, T is the room temperature in Kelvin. The n_i=1.9×10^{-10} cm^{-3} is the intrinsic carrier density in GaN.

$$w = \left[\frac{2\varepsilon_{GaN}(V_{bi} + U_{bias})}{q} \times \left(\frac{N_a + N_d}{N_a N_d}\right)\right]^{1/2} \tag{6.1}$$

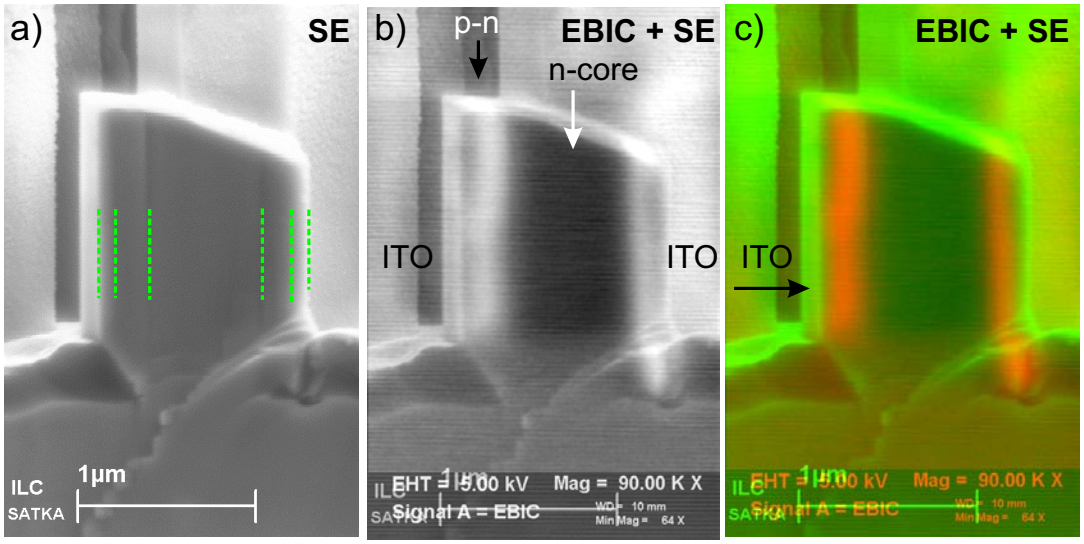

Figure 6-20: a) SE image of cross-sectioned NR with p-n junction with visible shell layers, accounting for the GaN n-core, thick p-GaN layer, and ITO current spreading layers on both sides, b) EBIC at U_{bias}= 0 V and overlayed SE display visible p-n junction, c) Overlay in false color of EBIC map and SE image, most of the signal originates from carriers on the p-GaN side of the junction.

$$V_{bi} = \frac{k_b T}{q} \times \ln\left[\frac{(N_a \times N_d)}{n_i^2}\right] \tag{6.2}$$

Using an average value of the p-n junction width of $w \sim 150 - 200$ nm as measured from Figure 6-20 c) and introduced in equation 6.1, the active hole carrier doping level for the medium Mg doped NRs was estimated at $N_a = 8 \times 10^{16} - 1.4 \times 10^{17}$ cm^{-3}. The electron carrier concentration for the GaN template used is known to be $N_d = 1 \times 10^{19}$ cm^{-3}. As specified by refs [109, 234] only a small percentage, likely lower than 1% of the Mg atoms can provide active hole carriers, the obtained N_a concentration agrees with estimates obtained from PL and CL measurements of $5 - 7 \times 10^{18}$ cm^{-3} Mg atoms in Chapter 5 and ref. [182]. The space charge widths on each type of material in the p-n junction is expected to be proportional to their respective carrier concentration [234, 113]. Because of the large difference between the n-GaN core and the p-GaN shell doping, most of the charge collection signal is obtained from the p-side.

Figure 6-21 shows two more sectioned NRs, under low doping (0.30 µmol/min) and 60 min growth conditions. Figures 6-21 b) and d) show a three-dimensional p-n junction, with a wider SCR at $250 - 300$ nm, corresponding to $\sim 3.5 - 5 \times 10^{16}$ cm^3 active carriers.

Figure 6-22 displays core-shell LED NRs contacted by probes. The current does not

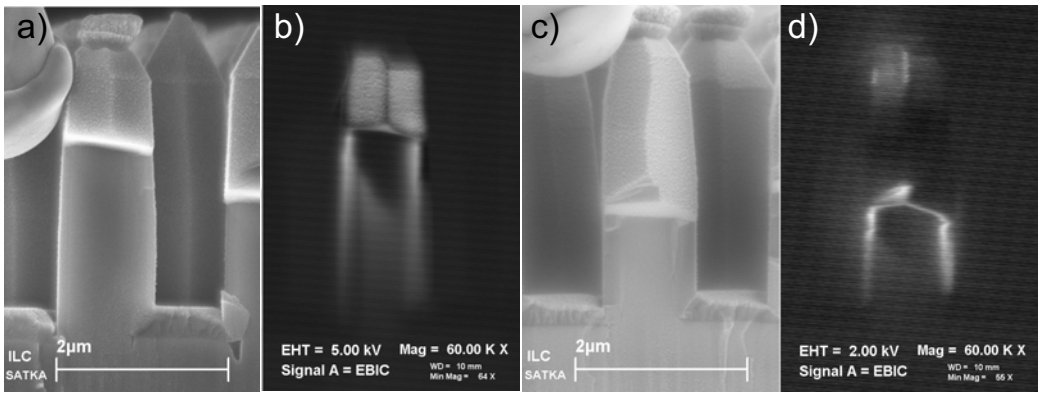

Figure 6-21: a) SE image of partially severed NR covered in $\sim$ 140 nm ITO, b) EBIC current map U_{bias}= 0V, with a wider p-n junction for low doped p-GaN, c) SE image of another NR d) a cleaved NR shows a 3D p-n junction.

spread to neighboring NRs due to a leakage between the ITO on p-GaN and bottom n-GaN layer. The observed increase of the EBIC signal toward the NR top demonstrates a decrease in resistance due to the thicker ITO. The EBIC maps reproduce the NRs geometry accurately, indicating the good contact and current spreading achieved within individual NR.

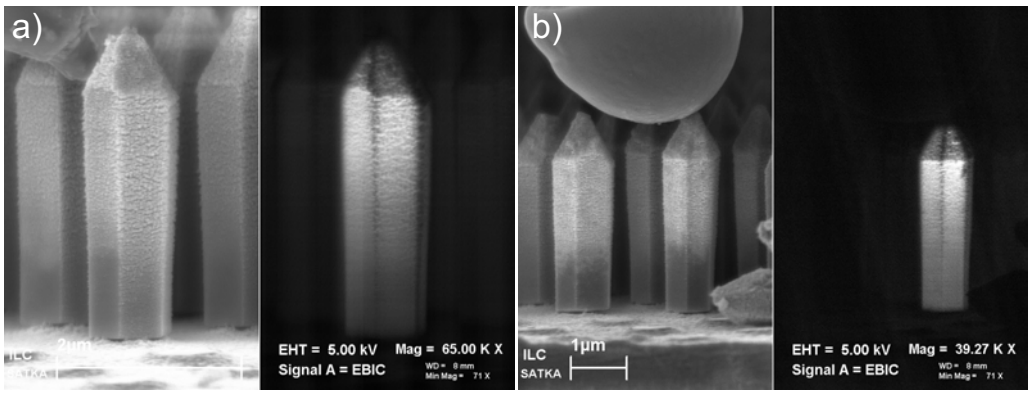

Figure 6-22: a)SE and EBIC map (U_{bias}= 0 V) of core-shell LED (sample 4244) covered in an ITO layer with a gradient of thickness, obtained under 45° deposition; b) different NRs contacted at the tip with a more resistive probe shows similar behavior and current spreading in the entire structure; dark contrast lines at the apexes of *m*-planes are similar to CL results, indicating crystallographic defects may acting as non-radiative recombination centers at the apexes.

Finally, the NR-LED was probed under different biases as shown in Figure 6-23. At high forward bias, the signal becomes too noisy. In reverse bias, the NR can be easily distinguished. Because of the ITO current spreading layer, the position of the probe

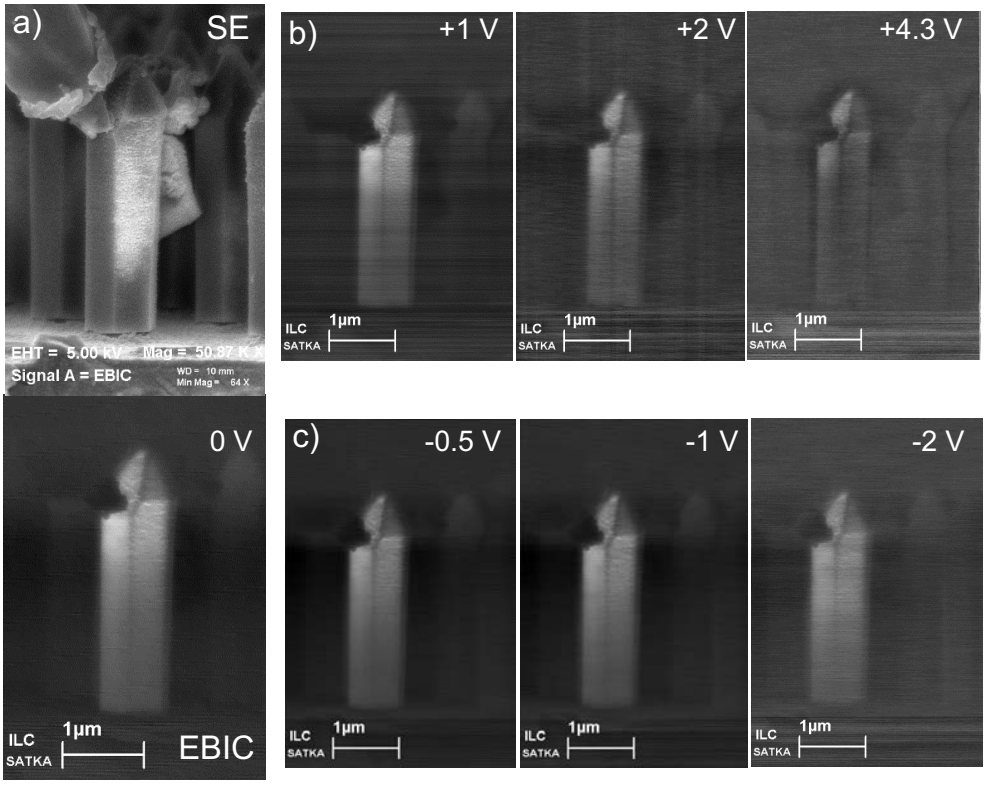

Figure 6-23: a) SE and EBIC map at U_{bias}= 0 V and 5 kV accelerating voltage for a core-shell LED NR, b) increasing forward bias results in reduced minority current and EBIC signal, c) under reverse bias the p-n junction and collection current are visible and uniform along the entire NR due to the ITO layer.

along the NR has no significant impact on the current collection.

6.4.2 Nanorod current-voltage characteristics

EBIC was applied to determine current-voltage characteristics from individual NRs by making a contact between the planar GaN and individual NRs with nanoprobes. Figure 6-24 a) shows a typical IV characteristic and rectifying behavior from an individual NR with a medium doped p-shell. The early onset of the threshold may be caused by the very low thickness of the p-GaN layer (49 ±20 nm) and traps or defect states occurring during the growth. Often a non-reliable contact to the rods, which can easily break or chip at the contact point. To improve current spreading in the NR, a layer of ITO was deposited. Due to areas of imperfect passivation, the ITO can get in contact to the underlying GaN. Thus the rectifying nature of the rods can not be observed (see Figure 6-24 b).

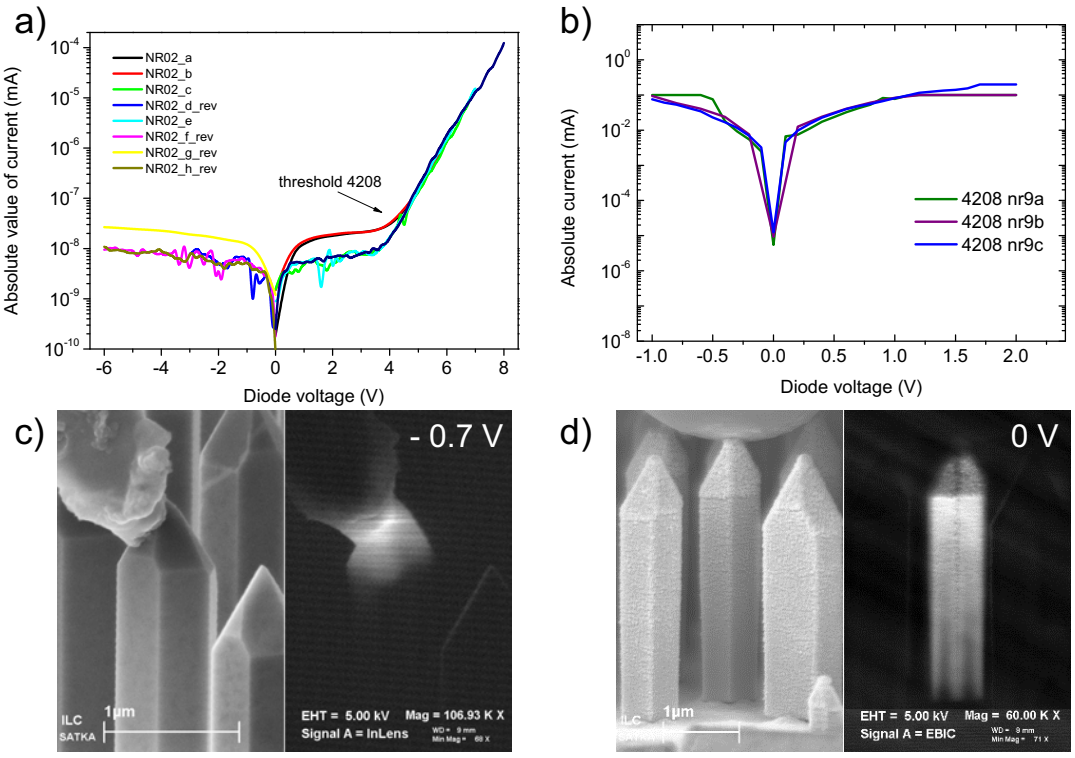

Figure 6-24: a) Current-voltage characteristics obtained from EBIC on an individual NR, b) I-V characteristic with shorting likely between the ITO and the n-GaN, c) SEM and EBIC map of NR without ITO under reverse bias, d) no forward or reverse bias could be put through ITO covered NRs, due to shorting on the planar GaN.

The EBIC measurements were complemented by standard I-V probe measurements on NR arrays. Because of the ITO issue, the p-contact was achieved by spreading a bead (~ 1 mm^2) of conductive Ag paste on the NRs. Limits were set to ± 10 V and 10 mA. Standard Au probes were used to perform the I-V measurements seen in Figure 6-25, under identical low light conditions, but without a dark box. Several measurements from different samples and sample regions were made to get a qualitative perspective on the I-Vs behavior. The thicknesses of the different shells mentioned in the Figure 6-25 caption are estimated from Table 6.1.

Comparing the three samples in Figure 6-25, the notable characteristics are rectifying behavior with high asymmetry on the log scale and relatively low reverse current. Some of the measurements were more erratic, which is likely if some NRs have been broken under the large probe contact. In particular, for reverse bias the thicker p-GaN and multiple QW/QB structure can withstand two orders of magnitude higher breakdown voltages. The 4652 MQW sample was grown with much thicker QBs. Sample 4650

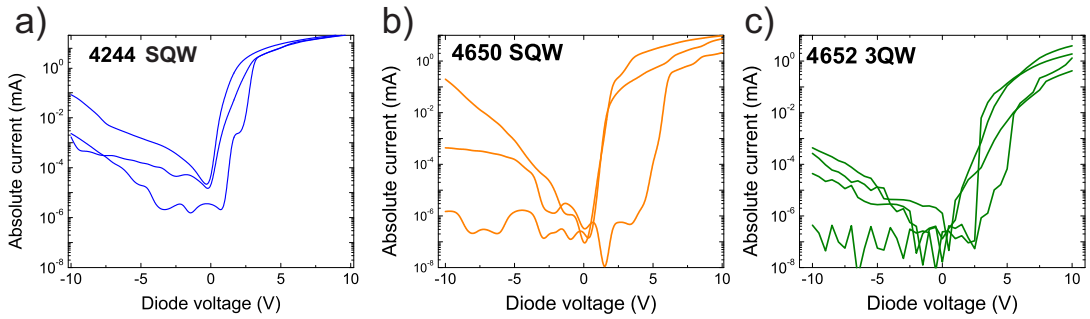

Figure 6-25: I-V characteristics for multiple measurements a) SQW at 680℃, 150 mbar, p-GaN shell 49 ±20nm, b) SQW at 670℃, 300 mbar, p-GaN shell 110 ±34 nm, c) MQW at 670℃, 300 mbar, p-GaN shell 110 ±34 nm.

has a similar p-GaN layer, but with a thinner QB leading to a wider range of reverse current measurements.

As determined from EBIC, the SCR likely extends over the whole p-GaN layer and over to the ohmic contact for U_{bias}= 0 V. However, using 3 V forward bias and equation 6.1, the SCR region was reduced to $\sim$ 50 nm, within the thickness of the p-GaN achieved for samples 4650 and 4652.

Figure 6-26 displays a comparison of I-V curves for the three LED samples and the p-n homojunction sample. The two samples with thin p-GaN shells have a low turn-on voltage, possibly due to narrow electron and hole potential barriers and their low resistivity. Also likely to lower the turn-on voltage are defects, trap states or a shunt resistance, possibly caused by broken rods that may be touching the planar GaN.

Higher turn-on voltages in samples 4650 and 4652 ($3.6 - 3.8$ V) must originate from the wider p-GaN shell. As indicated by these I-V characteristics, the values are in a reasonable range and similar to planar InGaN/GaN LEDs. Sapphire substrate LEDs with a band gap at 2.7 eV demonstrated a turn-on voltage at 3.5 V, and 3.7 V on Si substrates [235]. Lower turn-on voltages were achieved at 2.5 V (band gap 2.7 eV) in ref [236]. The turn-on value depends on the dopant concentration, hole mobility, and resistivity of the p-GaN shell. The wider p-GaN layer can be regarded as series of diodes with higher turn-on voltages to block injection of carriers until the applied voltage is high enough to turn on the junctions. Sample 4652 has a wider SCR because of the succession of QW/QB, resulting in higher serial resistance, as shown in Figure 6-26.

The I-Vs and EL spectra from section 6.3 were measured separately. The LED emission was observable with the naked eye for blue, green and yellow luminescence. The blue

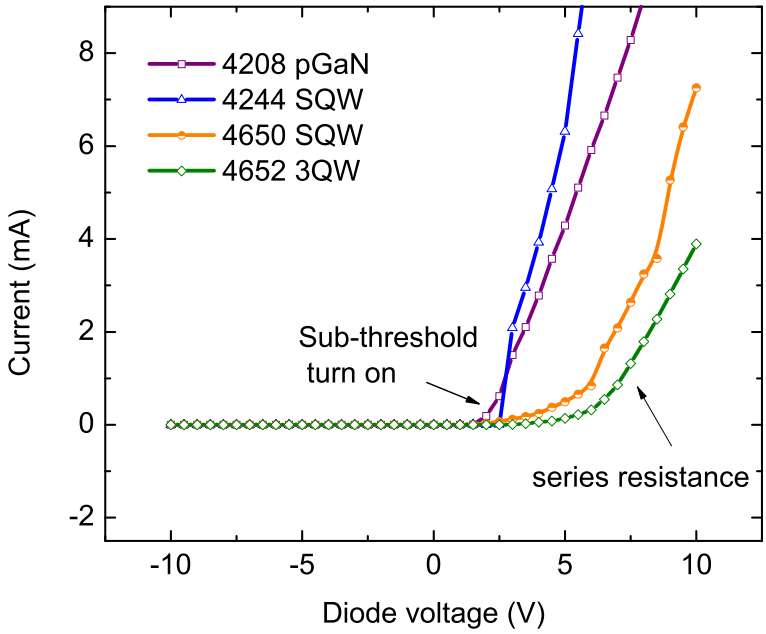

Figure 6-26: Thin p-GaN shell, trap states or shunt resistance causes early turn-on in this walled NRs, but increased series resistance with thicker p-GaN raised the turn-on voltage in the MQW NRs to ~ 3.8 V.

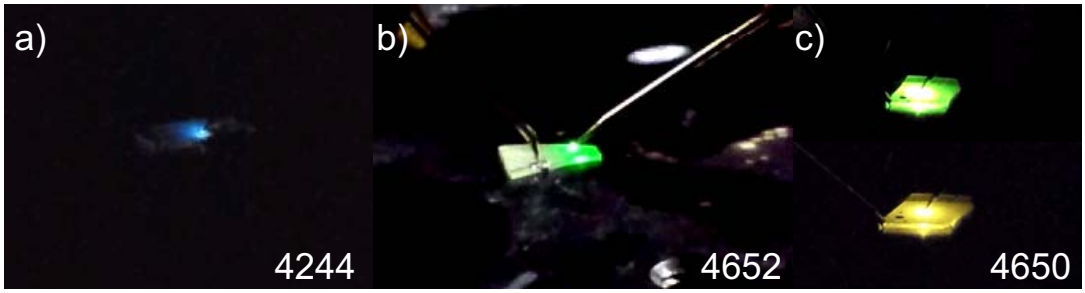

Figure 6-27: Electroluminescence showing: a) weak blue emission from sample 4244, b) 3QW (4652) visible green emission at normal room lighting, c) SQW (4650) emission in green-yellow with less intensity than the 3QW sample.

LED (4244) displayed only weak luminescence due to its thin barrier and p-GaN. Sample 4650 having partial growth could emit in green and yellow, depending on probed area. The MQW sample was the most robust structure with thick QB and p-GaN, and can be seen in Figure 6-27 b) under normal room illumination with bright green emission.

6.5 Conclusions

The sequence of MOVPE growth steps and parameters for the three core-shell LEDs samples achieved were reviewed and summarized. The current approach for device processing as well as potential improvements in device fabrication, such as the current spreading layer, planarization, and contacts were discussed. A challenge remains the quality of the deposition for the ITO transparent current spreading layer, as it tends to introduce shorting to the underlying GaN planar layer.

EL measurements were performed on the same areas as probed by PL excitation. The EL and PL spectra were different, most likely due to the current path favored by the contacts. While PL spectra indicated a dominant blue peak, as identified from CL mapping on the m-plane facets of individual NRs, the EL spectra were dominated by the green emission from the semi-polar planes. In CL measurements the NRs showed blue emission from the m-planes, with lower intensity. It is possible that local Mg inhomogeneities are causing the NRs m-plane sidewalls to be more resistive and block the current path through the entire NR.

EBIC I-V characteristics were determined from individual NRs and rectifying behavior was identified. ITO covered NRs led to considerable limitations as shunting could not be avoided. Traditional I-V measurements were performed on arrays of NRs contacted on small areas with silver paste. Rectifying behavior and the turn-on voltage of $3.6-3.8$ V were observed for samples with a p-GaN shell thickness of 110 nm ($\pm$34 nm). Higher electrical resistance was observed with increasing QB width and p-GaN thickness. The MQW LED was reliably measured and it provided visible 532 nm green emission to the naked eye in a room with day lighting.

Chapter 7

Summary, Conclusions and Outlook

The present work brings together results and arguments relevant to the development of vertical core-shell LEDs. The interest in the core-shell architecture is driven by its potential to solve technical challenges, such as the native GaN polarization in traditional c-plane LEDs or strained heteroepitaxial GaN growth, and to improve current solid state lighting technology by using the polarization free m-planes or by increasing the active LED area. The present work achieved several technical milestones, and comparable studies were pursued very recently [58, 104] and in parallel by a variety of growth techniques [217, 237, 59]. However, a distinguishing factor of this work is that wafer-scale-arrays of NRs were achieved by etching and MOVPE regrowth. Furthermore, the techniques provide high NR dimensional uniformity and high-aspect ratios. Second, the growth and characterization of the InN fraction have shown how to control the reactor parameters and obtain predictable alloy growth rates on the different crystal facets. Third, experimental results regarding p-GaN doping and its uniformity are given, especially as MOVPE based doping and crystal growth on NRs and NWs is not thoroughly discussed in the literature. And lastly, developing current spreading layers and metal contacts were essential in the fabrication of a proof-of-concept core-shell LED.

The major accomplishment of this work is the demonstration of a functional core-shell LED design in a prototype stage. The experiments revealed green light emission from the InGaN/GaN active layers. Light emission by electrical injection was possible due to the functional core-shell p-n junction on NRs. Furthermore, this was demonstrated for arrays of NRs, not only individual nanowires. The work aimed to explore and establish

guidelines to levy the advantages and mitigate the technical challenges of the core-shell nanorod LED structure. Next is a more detailed look at the challenges and solutions put forward during this study. Key results were achieved in:

- optimized a cleanroom process comprising plasma etching and MOVPE regrowth, resulting in high aspect-ratio and high uniformity GaN NRs
- examined InGaN incorporation and growth parameter, obtained cathodoluminescence emission from different wurtzite crystal facets
- controlled effective p-GaN doping and its uniformity on the *m*-plane
- integrated the MOVPE growth and developed processing for a current-injected core-shell LED prototype device.

Summary

High aspect ratio uniform nanorods

Top-down etching and *regrowth* were investigated, as the two methods combined can produce high-aspect ratio NRs ($3.5 - 5$ μm), while most *bottom-up* growth result in typically 0.5 μm tall NRs [104]. Another advantage of the top-down process is reproducibility to wafer size NR-LED templates. NRs with diameters of $\sim 320 - 470$ nm and 0.6 μm pitch distance were obtained as a template for a follow-up InGaN/GaN active area growth. After regrowth on the NR *m*-plane sidewalls, the best diameter and height uniformity were achieved for a 30 minutes GaN regrowth and by the use of an HSQ passivation layer between the NRs, blocking the *c*-plane growth direction. The emitted wavelengths and peak widths depend on the NR diameters [73]. The majority (80%) of the NR diameters had a 30 nm diameter range in a statistical size set of $\sim$ 1000 NRs. The etch-regrowth process was extended to the 2 μm pitch distance to study the effect on InGaN integration uniformity. This was because for the 0.6 μm pitch, the InN incorporated mainly at the NR tips. Additional samples prepared by electron beam lithography with intermediary NR pitch distances were grown, and it was found that NR with a period smaller than 1.5 μm are in a competition growth mode for the available adatoms in the gas-phase. This result suggests that closely packed NRs may not be an optimum design for uniform InN integration on the *m*-plane. The 2 μm period provided a better growth uniformity for the InGaN growth step [132]. Height uniformity and sidewall roughness on the GaN NR template were analyzed for the first

time by AFM on NR tips and on NR cross-sections. The AFM analysis proved experimentally challenging as the NR arrays can easily trap and break the AFM tips without further sample preparation. In more recent work, our group took a different approach and experimental setup to analyze the surfaces of individual NRs [213]. A further result from Raman spectroscopy investigation showed that he etched and regrown NRs are unstrained.

InGaN incorporation

The incorporation of InGaN on the NR non-polar sidewalls is complicated by the growth temperatures compatibility between the GaN (~ 950℃) and the InGaN ($\sim 650 - 680$ ℃) steps, and by atom migration from the base of individual NRs toward the tips [238]. Using a low growth temperature to limit surface diffusion can encourage the formation of surface defects on the InGaN layer. In this work a range of growth temperatures for GaN and InGaN were studied, the atom migration and the unstrained growth for thick InGaN layers were observed and discussed. A NR structure with both *a*- and *m*-planes was obtained on the GaN template to study the growth and integration of the InN fraction. Further experiments by cathodoluminescence provided insight into InN integration on different crystalographic facets ($\{1\,0\,\bar{1}\,0\}$, $\{1\,\bar{1}\,0\,2\}$, $\{1\,\bar{1}\,0\,1\}$, $(0\,0\,0\,1)$) by mapping the light emission from the nanostructures. From the thick InGaN layers typically two emission peaks were observed, likely caused by the coexistence of both strained and relaxed or partially relaxed layers. It was found from these experiments that a low growth pressure (100 mbar) can improve InGaN uniformity on the sidewalls and achieve higher InN fraction [141]. Also, the larger pitch distance at 2 μm between the NRs improved the incorporation uniformity of adatoms [132].

P-GaN doping

Mg doping on NRs and LEDs has been reported in previous studies, however, however, most cover self-assembled MBE NRs with variable diameter NRs, or gave little information on what basis of how the growth parameters were chosen, or present devices covered completely in p-GaN [74]. In this work, the doping uniformity of the magnesium shell was investigated by changing the precursor flows, p-GaN growth temperatures, p-GaN shell thickness and the annealing treatment to obtain active hole carriers. The samples were investigated by complementary CL, Raman spectroscopy, and electron-beam-induced-current (EBIC) measurements. Effective hole carrier-density was estimated from CL and EBIC at a conservative $2 - 5 \times 10^{17}$ cm^{-3} level. Traditional Hall

effect measurements cannot be completed on an irregular sample of NR arrays. Medium to high doping levels ($0.45 - 0.70$ μmol/min) and lower growth temperatures ($\sim 800 - 900$ ℃) than in typical GaN ($\sim 900 - 1050$ ℃) were found to incorporate a larger number of Mg atoms which could be activated. The effectiveness of an ~ 109 nm thick p-GaN core-shell layer was finally demonstrated by driving and measuring the electrical current and by the visible electroluminescence.

Core-shell LEDs

The vertical form factor of NRs can provide an enhanced LED active area and more light extraction from the unstrained, low-defect InGaN/GaN core-shell LEDs. The previous lessons about template optimization, InGaN growth parameters, and p-doping were brought together in the core-shell LED prototype. Uniform current-spreading on the NRs was achieved by the deposition of indium-tin-oxide (ITO) layers. However, due to leakage problems or processing problems related to the ITO, a setup using conducting silver paste was used to connect the NRs array. This change indicates the ITO as a current spreading layer should be deposited in a different manner, which was discussed in section 6.2.2. In the resulting devices, light emission in the blue range was observed from the $\{1\,0\,\bar{1}\,0\}$ m-plane and green emission from the $\{1\,\bar{1}\,0\,1\}$ semipolar plane, in both PL and CL measurements. For electroluminescence measurements, the 532 nm green emission was dominant, likely due to a selective current path on the lower-resistance semipolar planes. Finally, a current-voltage characterization was carried out and demonstrated on the prototype core-shell LEDs, showing a turn-on voltage of ~ 3.6 V for the ~ 1 mm^2 sized LEDs. A discussion of the important factors affecting the patterning and processing for core-shell LED designs was given.

Conclusions

This work shows it is possible to produce electrically injected core-shell InGaN/GaN LEDs in a process with high repeatability, by careful selection of the growth parameters and by using etched-and-regrown GaN nanocolumns. The initial etching mask pattern was obtained by highly uniform nanoimprinting. After plasma etching and regrowth, nanorod diameter uniformity was maintained. In the final device, the uniformity was important towards achieving consistent wavelengths from individual NRs and from individual devices. Although the core-shell LED showed in CL two emission peaks, these correspond to the different crystal facets (blue and green emission from the m-

plane and semipolar plane), however, the respective facets show uniform InN fraction. A series of growth parameters optimizations, as shown in this work, or different contact methods could be used to optimize single wavelength devices. The proof-of-principle device functioned with a single electroluminescence 532 nm peak and a high turn-on voltage of 3.6 V, likely due to high resistance electric paths in the p-GaN. Thus the device requires further optimization, especially in regards to the electrical contacts and chip packaging.

Challenges are still ahead for core-shell LEDs, however, this study and results from other groups illustrate the NR arrays can be developed into working devices, and that it is a matter of finding the optimum technical solutions for robust devices. From the process viewpoint, the core-shell LEDs involve additional processing compared to planar LEDs. However, current high brightness LEDs have a high degree of complexity and costs included in the packaging, thus a more efficient and brighter core-shell device running at a lower temperature could be competitive. It remains to be seen if the advantages of the new design can offset the additional processing.

Outlook

The experiments accomplished in this work covered fundamental topics concerning the core-shell structure, GaN and InGaN growth, functional active layers, doping, and device processing. Potential future development directions could be made to enhance the present design and understanding of core-shell LEDs. For the device developed in this work, the optimization of the current spreading layer is necessary because the location and type of contact on the NR were shown here and in other recent studies [70], to influence the resulting emission wavelength and the current path. In place of a wafer-wide deposition a patterned ITO deposition, individual LED devices size ITO coverage is proposed to avoid creating leakage paths between the p-GaN and the template due to imperfect passivation. Deposition by sputtering and using a stencil mask on the wafer for a high step difference between the NRs and the deposition mask are also proposed.

Accurate measurements and TEM inspection of the shell thicknesses can provide a better understanding of achieved QW/QB and p-GaN layers. This information would provide higher predictability on the growth times for each layer and on the growth parameters used. Studying the QW/QB growth temperature and growth pressure under different growth temperature procedures [211] could be further examined to obtain

more controllable InGaN/GaN layer interfaces and quantify these parameters effects on the internal quantum efficiencies. The addition of an electron blocking layer could increase the effective energy barrier in the QW region and prevent possible electron leakage into the p-doped shell [239]. A study on light extraction efficiency from multiple devices could indicate an optimum fill factor required to maximize the escape of light from between the NRs.

Understanding all the process stages and the processes repeatability will help determine whether NR LEDs are technically and commercially competitive compared to planar LEDs. Cost reductions are possible by the elimination of the phosphor coating and from the reduction in packaging costs [240]. For a core-shell LED the bulb or lens may prove unnecessary because the diffraction grating behavior of NRs increases light extraction [241]. A further direction for the core-shell architecture can be monolithic integration for white light LEDs. The different InN fractions (see Figure 4-10a)) can be considered an opportunity for color mixing and white light, on the same chip without the use of a phosphor layer. This aim could be achieved by using emission from the crystal facets or by using templates with small diameter variations on dense NRs [73], or even multi-section core-shell NRs [237]. Monolithic integration has been recently studied by using different growth steps [242, 59, 243].

Balancing the issues of processing, performance, reliability, and costs are necessary to continue the development of nanorod based devices. New advances in fundamental physics are likely once highly stable devices can be obtained. Robust devices using *m*-plane sidewall emission could be used to study the nature of droop. Core-shell LEDs could be a path towards reducing the green gap. Even at a proof-of-concept stage an intense green LED running at 10 mA was achieved in this work. Further work to the NR core-shell LED performance could lead to compact devices, highly efficient non-polar LEDs, functioning at lower temperatures and lower drive currents than traditional planar LEDs. Because the NRs are grown (or regrown) in the MOVPE reactor, and theoretically the substrates used can be Si wafers, the core-shell LEDs could be grown without strain on larger and cheaper Si wafers. Integration with Si, contact methods or the use of different NR diameters for monolithic white light, are current research priorities that can raise further interest in the development of nanowires/nanorods for core-shell LEDs for lighting.

Published work

Peer-reviewed journals

I. Gîrgel, S.-L. Sahonta, P. R. Edwards, P.-M. Coulon, E. Le Boulbar, D. W. E. Allsopp, R. W. Martin, C. J. Humphreys, and P. A. Shields, "InGaN shell morphology and composition on multi-faceted GaN nanorods," (2016, submitted).

I. Gîrgel, A. Šatka, J. Priesol, T. Batten,E. Le Boulbar, P.-M. Coulon, and P. A. Shields, "Optical characterization of magnesium incorporation in p-GaN layers for core-shell nanorods," (2016, submitted).

P.-M. Coulon, S. H. Vajargah, A. Bao, P. R. Edwards, E. Le Boulbar, I. Gîrgel, R. W. Martin, C. Humphreys, R. A. Oliver, D. W. E. Allsopp, and P. A. Shields, "Evolution of the m-plane Quantum Well Morphology and Composition within a GaN/InGaN Core-Shell Structure, "*J. Crystal Growth and Design*, 17(2),pp. 474-472, (2016)

I. Gîrgel, P. R. Edwards, E. Le Boulbar, P.-M. Coulon, S. -L. Sahonta, D. W. E. Allsopp, R. W. Martin, C. J. Humphreys, and P. A. Shields, "Investigation of indium gallium nitride facet-dependent nonpolar growth rates and composition for core–shell light-emitting diodes," *J. Nanophotonics*, vol. 10, no. 1, p. 016010, (2016).

E. D. Le Boulbar, P. R. Edwards, S. H. Vajargah, I. Griffiths, I. Gîrgel, P.-M. Coulon, D. Cherns, R. W. Martin, C. J. Humphreys, C. R. Bowen, D. WĖÀllsopp, and P. A. Shields, "Structural and Optical Emission Uniformity of m-plane InGaN Single Quantum Wells in Core–Shell Nanorods," *J.Cryst. Growth and Design*, vol. 16, pp. 1907 – 1916, (2016)

E. D. Le Boulbar, I. Gîrgel, C. J. Lewins, P. R. Edwards, R. W. Martin, A. Šatka, D. W. E. Allsopp, and P. A. Shields, "Facet recovery and light emission from GaN/InGaN/GaN core-shell structures grown by metal organic vapour phase epitaxy on etched GaN nanorod arrays," *Journal of Applied Physics*, vol. 114, no. 9, p. 094302, (2013)

International conference presentations

J. Priesol, A. Šatka, I. Gîrgel, D. W. EȦllsopp, P. A. Shields, F. Uherek, P. -M. Coulon and E. D. Le Boulbar ,"Electron-beam induced current and cathodoluminescence characterization of transparent contacts on core-shell nano-rod LED structures", *European Materials Research Society Fall Meeting*, Warsaw, Poland, Sept. 2016

I. Gîrgel, A. Šatka, J. Priesol, P. -M. Coulon, E. Le Boulbar, D. W. E. Allsopp, and P.A. Shields,"Optical characterization of magnesium incorporation in p-GaN layers for core-shell nanorods", *The 11th International Conference on Nitride Semiconductors, ICNS-11*, Beijing, China, Sept. 2015

D. W. E. Allsopp, I. Gîrgel, C. J. Lewins, E. D. Le Boulbar, S. O'Kane, P-M. Coulon, S. M. Lis, S. A. Fox, and P. A. Shields, "Impact of Size and Pitch on the Optical Properties of Ordered Arrays of InGaN/GaN Quantum Disc and Core-Shell Nanowires," *International Conference on Metamaterials*, New York, Aug. 2015

I. Gîrgel, P.R. Edwards, E. Le Boulbar, D.W.E. Allsopp, R.W. Martin, and P.A. Shields, "Investigation of facet-dependent InGaN growth for core-shell LEDs", *SPIE Photonics West*, 15vol. 9363, p. 93631V, San-Francisco, USA, Feb. 2015

E. Le Boulbar, I. Gîrgel, P. R. Edwards, R. W. Martin, S. L. Sahonta, A. Šatka, D. W. E. Allsopp and P. A. Shields "Investigation of the growth of GaN/InGaN core-shell structures by MOVPE on etched GaN nanorod arrays", *The 10th International Conference on Nitride Semiconductors, ICNS-10*, Washington D.C., USA, Aug. 2013

UK conference presentations

I. Gîrgel, A. Šatka, J. Priesol, P. -M. Coulon, E. Le Boulbar, D. W. E. Allsopp, and P.A. Shields,"Uniformity of magnesium incorporation in p-GaN layers for core-shell nanorods",*UK Semiconductors*, Sheffield, July 2015

I. Gîrgel, C. Bryce, P.R. Edwards, E. Le Boulbar, D.W.E. Allsopp, R. W. Martin, and P. A. Shields, "Understanding the effect of nanowire geometry on the active regions of core-shell emitters",*UK Nitrides Consortium*, Nottingham, Jan. 2015

I. Gîrgel, E. Le Boulbar, P. R. Edwards, D. W. E. Allsopp,and P. A. Shields,"Facet dependent incorporation of InGaN for LED", *UK Semiconductors*, Sheffield, July 2014

I. Gîrgel, E. Le Boulbar, D. W. E. Allsopp,and P. A. Shields,"AFM assessment of height variation and facet roughness introduced by GaN regrowth on GaN nanorod arrays",*Gallium Nitride Workshop*, Cambridge, July 2013

I. Gîrgel, E. Le Boulbar, D. W. E. Allsopp,and P. A. Shields, "Is Raman spectroscopy a good characterization method to monitor GaN/InGaN core-shell growth on GaN nanowires?" *UK Nitrides Consortium*, Cardiff, Jan. 2013

Bibliography

[1] Joseph D. Bergesen, Leena Tähkämö, Thomas Gibon, and Sangwon Suh. Potential Long-Term Global Environmental Implications of Efficient Light-Source Technologies. *Journal of Industrial Ecology*, 20(2):263–275, 2016. 1.1

[2] Christian Cajochen, Sylvia Frey, Doreen Anders, Jakub Späti, Matthias Bues, Achim Pross, Ralph Mager, Anna Wirz-Justice, and Oliver Stefani. Evening exposure to a light-emitting diodes (LED)-backlit computer screen affects circadian physiology and cognitive performance. *Journal of applied physiology (Bethesda, Md. : 1985)*, 110(5):1432–8, may 2011. 1.1

[3] Steven P. Denbaars, Daniel Feezell, Katheryn Kelchner, Siddha Pimputkar, Chi Chen Pan, Chia Chen Yen, Shinichi Tanaka, Yuji Zhao, Nathan Pfaff, Robert Farrell, Mike Iza, Stacia Keller, Umesh Mishra, James S. Speck, and Shuji Nakamura. Development of gallium-nitride-based light-emitting diodes (LEDs) and laser diodes for energy-efficient lighting and displays. *Acta Materialia*, 61(3):945–951, 2013. 1.1

[4] Stacia Keller and Steven P. DenBaars. Metalorganic chemical vapor deposition of group III nitrides—a discussion of critical issues. *Journal of Crystal Growth*, 248:479–486, feb 2003. 1.1

[5] I. Akasaki H. Amano, N. Sawaki. Metalorganic vapor phase epitaxial growth of a high quality GaN film using an AlN buffer layer. *Applied Physics Letters*, 48(1986):353–355, 1986. 1.1

[6] Hiroshi Amano, Masahiro Kito, Kazumasa Hiramatsu, and Isamu Akasaki. P-type conduction in Mg-doped GaN treated with low-energy electron beam irradiation (LEEBI). *Japanese Journal of Applied Physics*, 28(12 A):L2112–L2114, 1989. 1.1

[7] Shuji Nakamura, Takashi Mukai, Masayuki Senoh, and Naruhito Iwasa. Thermal Annealing Effects on P-Type Mg-Doped GaN Films. *Japanese Journal of Applied Physics*, 31:139–142, 1992. 1.1, 5.2

[8] Shuji Nakamura. GaN Growth Using GaN Buffer Layer. *Japanese Journal of Applied Physics*, 30(10A):1705 – 1707, 1991. 1.1

[9] Shuji Nakamura and Takashi Mukai. High-Quality InGaN Films Grown on GaN Films. *Jpn. J. Appl. Phys.*, 31(10B):L1457–L1459, 1992. 1.1

[10] Shuji Nakamura, Takashi Mukai, and Masayuki Senoh. Candela-class high-brightness InGaN/AlGaN double-heterostructure blue-light-emitting diodes. *Applied Physics Letters*, 64(13):1687–1689, 1994. 1.1, 4

[11] Fang Qian, Yat Li, Silvija Gradečak, and Charles M Lieber. Gallium Nitride-Based Nanowire Radial Heterostructures for Nanophotonics. *Nano letters*, 4(10):1975 – 1979, 2004. 1.1, 1.5.5, 2

[12] Fang Qian, Silvija Gradečak, Yat Li, Cheng-Yen Wen, and Charles M Lieber. Core/multishell nanowire heterostructures as multicolor, high-efficiency light-emitting diodes. *Nano letters*, 5(11):2287–91, November 2005. 1.1, 1.9

[13] Shuji Nakamura, Masayuki Senoh, Shin-ichi Nagahama, Naruhito Iwasa, Takao Yamada, Toshio Matsushita, Hiroyuki Kiyoku, and Yasunobu Sugimoto. InGaN-based multi-quantum-well-structure laser diodes. *Japanese Journal of Applied Physics, Part 2: Letters*, 35(1 B), 1996. 1.1

[14] Mathew C. Schmidt, Kwang-Choong Kim, Robert M. Farrell, Daniel F. Feezell, Daniel A. Cohen, Makoto Saito, Kenji Fujito, James S. Speck, Steven P. DenBaars, and Shuji Nakamura. Demonstration of Nonpolar m -Plane InGaN/GaN Laser Diodes. *Japanese Journal of Applied Physics*, 46(No. 9):L190–L191, 2007. 1.1

[15] Yuji Zhao, Shinichi Tanaka, Chih-Chien Pan, Kenji Fujito, Daniel Feezell, James S. Speck, Steven P. DenBaars, and Shuji Nakamura. High-Power Blue-Violet Semipolar \hkl{20-2-1} InGaN/GaN Light-Emitting Diodes with Low Efficiency Droop at 200 A/cm$ˆ{2}$. *Applied Physics Express*, 4(8):082104, jul 2011. 1.1

[16] R.J. Molnar, W. Götz, L.T. Romano, and N.M. Johnson. Growth of gallium nitride by hydride vapor-phase epitaxy. *Journal of Crystal Growth*, 178(1-2):147–156, 1997. 1.1

[17] R. Dwiliński, R. Doradziński, J. Garczyński, L. P. Sierzputowski, A. Puchalski, Y. Kanbara, K. Yagi, H. Minakuchi, and H. Hayashi. Excellent crystallinity of truly bulk ammonothermal GaN. *Journal of Crystal Growth*, 310(17):3911–3916, 2008. 1.1, 1.4.1

[18] Philip A. Shields, Maxime Hugues, Jesus Zúñiga Pérez, Mike Cooke, Mark Dineen, Wang Wang, Federica Causa, and Duncan Allsopp. Fabrication and properties of etched GaN nanorods. *Physica Status Solidi (C)*, 9(3-4):631–634, March 2012. 1.1, 1.8, 1.8, 1-14, 2.1.3, 4.2, 4.5, 5.3

[19] S. Strite. GaN, AlN, and InN: A review. *Journal of Vacuum Science & Technology B: Microelectronics and Nanometer Structures*, 10(4):1237–1266, 1992. 1.3

[20] Masakatsu Suzuki, Takeshi Uenoyama, and Akira Yanase. First-principles calculations of effective-mass parameters of AlN and GaN. *Physical Review B*, 52(11):8132–8139, 1995. 1.3

[21] I. Vurgaftman, J. R. Meyer, and L. R. Ram-Mohan. Band parameters for III-V compound semiconductors and their alloys. *Journal of Applied Physics*, 89(11 I):5815–5875, 2001. 1.3

[22] Stacia Keller, Haoran Li, Matthew Laurent, Yanling Hu, Nathan Pfaff, Jing Lu, David F Brown, Nicholas A Fichtenbaum, James S Speck, Steven P Denbaars, and Umesh K Mishra. Recent progress in metal-organic chemical vapor deposition of (000-1) N-polar group-III nitrides. *Semiconductor Science and Technology*, 29:113001, 2014. 1-1

[23] O. Ambacher. Growth and applications of Group III-nitrides. *J. Phys. D*, 31:2653–2710, 1998. 1.3, 2.1.6

[24] D. Schikora, M. Hankeln, D. J. As, K. Lischka, T. Litz, A. Waag, T Buhrow, and F Henneberger. Epitaxial growth and optical transitions of cubic GaN films. *Physical Review B*, 54(12):R8381–R8384, 1996. 1.3

[25] Huiyuan Geng, Haruo Sunakawa, Norihiko Sumi, Kazutomi Yamamoto, A. Atsushi Yamaguchi, and Akira Usui. Growth and strain characterization of high quality GaN crystal by HVPE. *Journal of Crystal Growth*, 350(1):44–49, 2012. 1.4.1

[26] S. C. Jain, M. Willander, J. Narayan, and R. Van Overstraeten. III–nitrides: Growth, characterization, and properties. *Journal of Applied Physics*, 87(3):965, 2000. 1.4.1, 1.4.2, 2.1.6

[27] A. Dadgar, M. Poschenrieder, J. Bläsing, O. Contreras, F. Bertram, T. Riemann, A. Reiher, M. Kunze, I. Daumiller, A. Krtschil, A. Diez, A. Kaluza, A. Modlich, M. Kamp, J. Christen, F.A. Ponce, E. Kohn, and A. Krost. MOVPE growth of GaN on Si(111) substrates. *Journal of Crystal Growth*, 248:556–562, 2003. 1.4.1

[28] Mingwei Zhu, Shi You, Theeradetch Detchprohm, Tanya Paskova, Edward A. Preble, Drew Hanser, and Christian Wetzel. Inclined dislocation-pair relaxation mechanism in homoepitaxial green GaInN/GaN light-emitting diodes. *Physical Review B - Condensed Matter and Materials Physics*, 81(12):1–6, 2010. 1.4.1

[29] Bernard Gil. Group III Nitride Semiconductor Compounds Physics and Applications. *Clarendon Press Oxford*, pages 19–69, 1998. 1.4.1

[30] Pierre Gibart. Metal organic vapour phase epitaxy of GaN and lateral overgrowth. *Reports on Progress in Physics*, 67(5):667–715, may 2004. 1.4.1, 1.5.2, 2, 2.1.6, 6.2.5

[31] Yukio Narukawa, Yoichi Kawakami, Mitsuru Funato, Shizuo Fujita, Shigeo Fujita, and Shuji Nakamura. Role of self-formed InGaN quantum dots for exciton localization in the purple laser diode emitting at 420 nm. *Applied Physics Letters*, 70(1997):981, 1997. 1.4.1

[32] R. A. Oliver, S. E. Bennett, T. Zhu, D. J. Beesley, M. J. Kappers, D. W. Saxey, A. Cerezo, and C. J. Humphreys. Microstructural origins of localization in InGaN quantum wells. *Journal of Physics D: Applied Physics*, 43(35):354003, 2010. 1.4.1

[33] Peter Lawaetz. Stability of the wurtzite structure. *Physical Review B*, 5(10):4039–4045, 1972. 1.4.2

[34] Christopher A. Schaake, Nicholas A. Fichtenbaum, Carl J. Neufeld, Stacia Keller, Steven P. DenBaars, James S. Speck, and Umesh K. Mishra. M -plane InGaN/GaN light emitting diodes fabricated by MOCVD regrowth on c -plane patterned templates. *Physica Status Solidi (C)*, 5(9):2963–2965, jul 2008. 1.4.2

[35] D. A. B. Miller, D. S. Chemla, T. C. Damen, A. C. Gossard, W. Wiegmann, T. H. Wood, and C. A. Burrus. Band-edge electroabsorption in quantum well structures: The quantum-confined Stark effect. *Physical Review Letters*, 53(22):2173–2176, 1984. 1.4.3

[36] G. Martin, A. Botchkarev, A. Rockett, and H. Morkoç. Valence-band discontinuities of wurtzite GaN, AlN, and InN heterojunctions measured by x-ray photoemission spectroscopy. *Applied Physics Letters*, 68:2541–2543, 1996. 1.4.3

[37] P Waltereit, O Brandt, A Trampert, Ht Grahn, J Menniger, M Ramsteiner, M Reiche, and Kh Ploog. Nitride semiconductors free of electrostatic fields for efficient white light-emitting diodes. *Nature*, 406(6798):865–8, aug 2000. 1.4.3

[38] Daniel F. Feezell, James S. Speck, Steven P. Denbaars, and Shuji Nakamura. Semipolar (20-2-1) InGaN/GaN light-emitting diodes for high-efficiency solid-state lighting. *IEEE/OSA Journal of Display Technology*, 9(4):190–198, 2013. 1.4.3

[39] J. Bai, B. Xu, F. G. Guzman, K. Xing, Y. Gong, Y. Hou, and T. Wang. (11-22) semipolar InGaN emitters from green to amber on overgrown GaN on micro-rod templates. *Applied Physics Letters*, 107(26), 2015. 1.4.3

[40] A. E. Romanov, T. J. Baker, S. Nakamura, and J. S. Speck. Strain-induced polarization in wurtzite III-nitride semipolar layers. *Journal of Applied Physics*, 100(2):023522, 2006. 1.4.3, 6.1

[41] Min-Ho Kim, Martin F. Schubert, Qi Dai, Jong Kyu Kim, E. Fred Schubert, Joachim Piprek, and Yongjo Park. Origin of efficiency droop in GaN-based light-emitting diodes. *Applied Physics Letters*, 91(18):183507, 2007. 1.4.4

[42] Y. C. Shen, G. O. Mueller, S. Watanabe, N. F. Gardner, A. Munkholm, and M. R. Krames. Auger recombination in InGaN measured by photoluminescence. *Applied Physics Letters*, 91(14), 2007. 1.4.4

[43] Justin Iveland, Lucio Martinelli, Jacques Peretti, James S. Speck, and Claude Weisbuch. Direct Measurement of Auger Electrons Emitted from a Semiconductor Light-Emitting Diode under Electrical Injection: Identification of the Dominant Mechanism for Efficiency Droop. *Physical Review Letters*, 110(17):177406, apr 2013. 1.4.4

[44] J. Hader, J. V. Moloney, and S. W. Koch. Temperature-dependence of the internal efficiency droop in GaN-based diodes. *Applied Physics Letters*, 99(18):2014–2017, 2011. 1.4.4, 1.4.4

[45] S. Hammersley, D. Watson-Parris, P. Dawson, M. J. Godfrey, T. J. Badcock, M. J. Kappers, C. McAleese, R. A. Oliver, and C. J. Humphreys. The consequences of high injected carrier densities on carrier localization and efficiency droop in InGaN/GaN quantum well structures. *Journal of Applied Physics*, 111(8), 2012. 1.4.4, 1.4.4

[46] Y. L. Li, Y. R. Huang, and Y. H. Lai. Efficiency droop behaviors of InGaNGaN multiple-quantum-well light-emitting diodes with varying quantum well thickness. *Applied Physics Letters*, 91(18):20–23, 2007. 1.4.4

[47] Ansgar Laubsch, Matthias Sabathil, Werner Bergbauer, Martin Strassburg, Hans Lugauer, Matthias Peter, Stephan Lutgen, Norbert Linder, Klaus Streubel, Jörg Hader, Jerome V. Moloney, Bernhard Pasenow, and Stephan W. Koch. On the origin of IQE-'droop' in InGaN LEDs. *Physica Status Solidi (C) Current Topics in Solid State Physics*, 6(SUPPL. 2):913–916, 2009. 1.4.4, 1.5.6

[48] Joachim Piprek. Efficiency droop in nitride-based light-emitting diodes. *Physica Status Solidi (A) Applications and Materials Science*, 207(10):2217–2225, 2010. 1.4.4, 1.5.6

[49] Shih-Chun Ling, Tien-Chang Lu, Shih-Pang Chang, Jun-Rong Chen, Hao-Chung Kuo, and Shing-Chung Wang. Low efficiency droop in blue-green m-plane InGaN/GaN light emitting diodes. *Applied Physics Letters*, 96(23):231101, 2010. 1-3

[50] Dario Schiavon, Michael Binder, Matthias Peter, Bastian Galler, Philipp Drechsel, and Ferdinand Scholz. Wavelength-dependent determination of the recombination rate coefficients in single-quantum-well GaInN/GaN light emitting diodes. *Physica Status Solidi (B) Basic Research*, 250(2):283–290, 2013. 1.4.5

[51] S. Hammersley, M. J. Kappers, F. C.-P. Massabuau, S.-L. Sahonta, P. Dawson, R. A. Oliver, and C. J. Humphreys. Effects of quantum well growth temperature on the recombination efficiency of InGaN/GaN multiple quantum wells that emit in the green and blue spectral regions. *Applied Physics Letters*, 107(13):132106, 2015. 1.4.5, 4.5.1

[52] Torsten Langer, Holger Jönen, Andreas Kruse, Heiko Bremers, Uwe Rossow, and Andreas Hangleiter. Strain-induced defects as nonradiative recombination centers in green-emitting GaInN/GaN quantum well structures. *Applied Physics Letters*, 103(2), 2013. 1.4.5

[53] Andrew M. Armstrong, Mary H. Crawford, and Daniel D. Koleske. Contribution of deep-level defects to decreasing radiative efficiency of InGaN/GaN quantum wells with increasing emission wavelength. *Applied Physics Express*, 7(3), 2014. 1.4.5

[54] Florian Furtmayr, Martin Vielemeyer, Martin Stutzmann, Jordi Arbiol, Sonia Estrade, Francesca Peiro, Joan Ramon Morante, and Martin Eickhoff. Nucleation

and growth of GaN nanorods on Si (111) surfaces by plasma-assisted molecular beam epitaxy - The influence of Si- and Mg-doping. *Journal of Applied Physics*, 104(3):034309, 2008. 1.5.1

[55] V. Consonni, M. Knelangen, L. Geelhaar, A. Trampert, and H. Riechert. Nucleation mechanisms of epitaxial GaN nanowires: Origin of their self-induced formation and initial radius. *Physical Review B*, 81(8):085310, February 2010. 1.5.1, 1.6.1

[56] Jun Hee Choi, Andrei Zoulkarneev, Sun Il Kim, Chan Wook Baik, Min Ho Yang, Sung Soo Park, Hwansoo Suh, Un Jeong Kim, Hyung Bin Son, Jae Soong Lee, Miyoung Kim, Jong Min Kim, and Kinam Kim. Nearly single-crystalline GaN light-emitting diodes on amorphous glass substrates. *Nature Photonics*, 5:763–769, 2011. 1.5.1

[57] L. Meshi, D. Cherns, I. Griffiths, S. Khongphetsak, A. Gott, C. Liu, S. Denchitcharoen, P. Shields, W. Wang, R. Campion, S. Novikov, and T. Foxon. The reduction of threading dislocations in GaN using a GaN nanocolumn interlayer. *Physica Status Solidi (C)*, 5(6):1645–1647, may 2008. 1.5.2

[58] Andreas Waag, Xue Wang, Sönke Fündling, Johannes Ledig, Milena Erenburg, Richard Neumann, Mohamed Al Suleiman, Stephan Merzsch, Jiandong Wei, Shunfeng Li, Hergo H. Wehmann, Werner Bergbauer, Martin Straßburg, Achim Trampert, Uwe Jahn, and Henning Riechert. The nanorod approach: GaN NanoLEDs for solid state lighting. *Physica Status Solidi (C)*, 8(7-8):2296–2301, jul 2011. 1.5.3, 2, 3, 3.7, 4, 7

[59] Xing Dai, Agnès Messanvi, Hezhi Zhang, Christophe Durand, Joël Eymery, Catherine Bougerol, François H Julien, and Maria Tchernycheva. Flexible Light Emitting Diodes Based on Vertical Nitride Nanowires. *Nano letters*, 15:6958 – 6964, August 2015. 1.5.3, 1.7, 1.9, 6.2, 6.2.3, 6.2.5, 7, 7

[60] Hiroto Sekiguchi, Katsumi Kishino, and Akihiko Kikuchi. Ti-mask Selective-Area Growth of GaN by RF-Plasma-Assisted Molecular-Beam Epitaxy for Fabricating Regularly Arranged InGaN/GaN Nanocolumns. *Applied Physics Express*, 1:124002, dec 2008. 1.5.3, 1-4

[61] Stephen D Hersee, Xinyu Sun, and Xin Wang. The Controlled Growth of GaN Nanowires. *Nano letters*, 6(8):1808–1811, 2006. 1-4, 1.7

[62] M. Hugues, P. a. Shields, F. Sacconi, M. Mexis, M. Auf der Maur, M. Cooke, M. Dineen, A. Di Carlo, D. W. E. Allsopp, and J. Zuniga-Perez. Strain evolution

in GaN nanowires: From free-surface objects to coalesced templates. *Journal of Applied Physics*, 114(8):084307, 2013. 1.5.4, 2, 3.6, 5.3.6

[63] E. Calleja, J. Ristić, S. Fernández-Garrido, L. Cerutti, M. A. Sánchez-García, J. Grandal, A. Trampert, U. Jahn, G. Sánchez, A. Griol, and B. Sánchez. Growth, morphology, and structural properties of group-III-nitride nanocolumns and nanodisks. *Physica Status Solidi (B)*, 244(8):2816–2837, aug 2007. 1.5.4, 1.9

[64] R. Armitage and H. Hirayama. M-plane GaN grown on m-sapphire by metalorganic vapor phase epitaxy. *Applied Physics Letters*, 92(9):092121, 2008. 1.5.5

[65] Yong-Ho Ra, Rangaswamy Navamathavan, Hee-Il Yoo, and Cheul-Ro Lee. Single nanowire light-emitting diodes using uniaxial and coaxial InGaN/GaN multiple quantum wells synthesized by metalorganic chemical vapor deposition. *Nano letters*, 14(3):1537–1545, 2014. 1-5, 1.5.5, 1.9

[66] Xiangfeng Duan and Charles M. Lieber. Laser-Assisted Catalytic Growth of Single Crystal GaN Nanowires. *Journal of the American Chemical Society*, 122(1):188–189, 2000. 1.5.5

[67] Yong-ho Ra, R Navamathavan, Ji-Hyeon Park, and Cheul-Ro Lee. Coaxial InxGa1-xN\GaN Multiple Quantum Well Nanowire Arrays on Si(111) Substrate for High-Performance Light Emitting Diodes. *Nano letters*, 13:3506–3516, 2013. 1.5.5, 1.9, 6.2.5

[68] A. L. Bavencove, G. Tourbot, J. Garcia, Y. Désières, P. Gilet, F. Levy, B. André, B. Gayral, B. Daudin, and Le Si Dang. Submicrometre resolved optical characterization of green nanowire-based light emitting diodes. *Nanotechnology*, 22(34):345705, aug 2011. 1.5.5

[69] F. Limbach, C. Hauswald, J. Lähnemann, M. Wölz, O. Brandt, A. Trampert, M. Hanke, U. Jahn, R. Calarco, L. Geelhaar, and H. Riechert. Current path in light emitting diodes based on nanowire ensembles. *Nanotechnology*, 23(46):465301, nov 2012. 1.5.5

[70] M. Tchernycheva, P. Lavenus, H. Zhang, A. V. Babichev, G. Jacopin, M. Shahmohammadi, F. H. Julien, R. Ciechonski, G. Vescovi, and O. Kryliouk. InGaN/GaN Core-Shell Single Nanowire Light Emitting Diodes with Graphene-Based P-Contact. *Nano letters*, 14(5):2456–65, May 2014. 1.5.5, 1.9, 2.2.7, 6.2, 7

[71] Kwang Choong Kim, Mathew C. Schmidt, Hitoshi Sato, Feng Wu, Natalie Fellows, Zhongyuan Jia, Makoto Saito, Shuji Nakamura, Steven P. Denbaars, James S. Speck, and Kenji Fujito. Study of nonpolar m-plane InGaN/GaN multiquantum well light emitting diodes grown by homoepitaxial metal-organic chemical vapor deposition. *Applied Physics Letters*, 91(18):4–7, 2007. 1.5.6

[72] X. Li, X. Ni, J. Lee, M. Wu, Ü. Özgür, H. Morkoç, T. Paskova, G. Mulholland, and K. R. Evans. Efficiency retention at high current injection levels in m -plane InGaN light emitting diodes. *Applied Physics Letters*, 95(12):13–16, 2009. 1.5.6

[73] Hiroto Sekiguchi, Katsumi Kishino, and Akihiko Kikuchi. Emission color control from blue to red with nanocolumn diameter of InGaN/GaN nanocolumn arrays grown on same substrate. *Applied Physics Letters*, 96(23):231104, 2010. 1.5.7, 1-6, 2, 3, 3.1, 3.7, 3.7, 7, 7

[74] Young Joon Hong, Chul-Ho Lee, Aram Yoon, Miyoung Kim, Han-Kyu Seong, Hun Jae Chung, Cheolsoo Sone, Yong Jo Park, and Gyu-Chul Yi. Visible-color-tunable light-emitting diodes. *Advanced materials (Deerfield Beach, Fla.)*, 23(29):3284–8, aug 2011. 1-7, 1.5.7, 1.9, 7

[75] J. A. Venables, G. D. T. Spiller, and M. Hanbucken. Nucleation and growth of thin films. *Reports on Progress in Physics*, 47(4):399, 1984. 1.6.1, 4.1

[76] Vitaliy Shchukin and Dieter Bimberg. Spontaneous ordering of nanostructures on crystal surfaces. *Reviews of Modern Physics*, 71(4):1125–1171, 1999. 1.6.1

[77] K. Hiramatsu, K. Nishiyama, A. Motogaito, H. Miyake, Y. Iyechika, and T. Maeda. Recent Progress in Selective Area Growth and Epitaxial Lateral Overgrowth of III-Nitrides: Effects of Reactor Pressure in MOVPE Growth. *Physica Status Solidi (a)*, 176(1):535–543, nov 1999. 1-9, 1.6.2

[78] Danxu Du, David Srolovitz, Michael Coltrin, and Christine Mitchell. Systematic Prediction of Kinetically Limited Crystal Growth Morphologies. *Physical Review Letters*, 95(15):155503, oct 2005. 1.6.2, 3.4

[79] Benjamin N. Bryant, Asako Hirai, Erin C. Young, Shuji Nakamura, and James S. Speck. Quasi-equilibrium crystal shapes and kinetic Wulff plots for gallium nitride grown by hydride vapor phase epitaxy. *Journal of Crystal Growth*, 369:14–20, apr 2013. 1.6.2, 4.4, 4.5.3

[80] Qian Sun, Christopher D. Yerino, Benjamin Leung, Jung Han, and Michael E. Coltrin. Understanding and controlling heteroepitaxy with the kinetic Wulff plot:

A case study with GaN. *Journal of Applied Physics*, 110(5):053517, 2011. 1.6.2, 4.2, 4-1

[81] Tomonari Shioda, Masakazu Sugiyama, Yukihiro Shimogaki, and Yoshiaki Nakano. Selective area metal-organic vapor-phase epitaxy of InN, GaN and InGaN covering whole composition range. *Journal of Crystal Growth*, 311(10):2809–2812, 2009. 1.6.2, 1-10, 4.4

[82] Y. Guo, X.L. Liu, H.P. Song, A.L. Yang, X.Q. Xu, G.L. Zheng, H.Y. Wei, S.Y. Yang, Q.S. Zhu, and Z.G. Wang. A study of indium incorporation in In-rich InGaN grown by MOVPE. *Applied Surface Science*, 256(10):3352–3356, mar 2010. 1.6.2

[83] I-hsiu Ho and G. B. Stringfellow. Solid phase immiscibility in GaInN. *Applied Physics Letters*, 69(18):2701, 1996. 1.6.2, 4.1

[84] G.B. Stringfellow. Microstructures produced during the epitaxial growth of InGaN alloys. *Journal of Crystal Growth*, 312(6):735–749, mar 2010. 1.6.2

[85] M.a. Sanchez-Garcia, E. Calleja, E. Monroy, F.J. Sanchez, F. Calle, E. Muñoz, and R. Beresford. The effect of the III/V ratio and substrate temperature on the morphology and properties of GaN- and AlN-layers grown by molecular beam epitaxy on Si(1 1 1). *Journal of Crystal Growth*, 183(1-2):23–30, jan 1998. 1.7

[86] K. A. Bertness, A. Roshko, L. M. Mansfield, T. E. Harvey, and N. A. Sanford. Nucleation conditions for catalyst-free GaN nanowires. *Journal of Crystal Growth*, 300(1):94–99, 2007. 1.7

[87] Jelena Ristić, Enrique Calleja, Sergio Fernández-Garrido, Laurent Cerutti, Achim Trampert, Uwe Jahn, and Klaus H. Ploog. On the mechanisms of spontaneous growth of III-nitride nanocolumns by plasma-assisted molecular beam epitaxy. *Journal of Crystal Growth*, 310(18):4035–4045, aug 2008. 1.7, 1-11, 1.7, 1.9

[88] R. K. Debnath, R. Meijers, T. Richter, T. Stoica, R. Calarco, and H. Luth. Mechanism of molecular beam epitaxy growth of GaN nanowires on Si(111). *Applied Physics Letters*, 90(12):123117, 2007. 1.7

[89] Robert Koester, Jun-Seok Hwang, Damien Salomon, Xiaojun Chen, Catherine Bougerol, Jean-Paul Barnes, Daniel Le Si Dang, Lorenzo Rigutti, Andres de Luna Bugallo, Gwénolé Jacopin, Maria Tchernycheva, Christophe Durand, and Joël Eymery. M-plane core-shell InGaN/GaN multiple-quantum-wells on GaN

wires for electroluminescent devices. *Nano letters*, 11(11):4839–45, November 2011. 1-12, 1.7, 1.9

[90] C. Tessarek, M. Heilmann, E. Butzen, A. Haab, H. Hardtdegen, C. Dieker, E. Spiecker, and S. Christiansen. The role of Si during the growth of GaN micro- and nanorods. *Crystal Growth and Design*, 14(3):1486–1492, 2014. 1.7, 1.7, 2, 3.4

[91] Yen-Ting Lin, Ting-Wei Yeh, and P Daniel Dapkus. Mechanism of selective area growth of GaN nanorods by pulsed mode metalorganic chemical vapor deposition. *Nanotechnology*, 23(46):465601, November 2012. 1.7, 1-13, 2

[92] W. Bergbauer, M. Strassburg, C. Kolper, N. Linder, C. Roder, J. Lähnemann, A. Trampert, S. Fundling, S. F. Li, H-H. Wehmann, and A. Waag. Continuous-flux MOVPE growth of position-controlled N-face GaN nanorods and embedded InGaN quantum wells. *Nanotechnology*, 21(30):305201, July 2010. 1.7, 2

[93] Qian Sun, Christopher D. Yerino, Tsung Shine Ko, Yong Suk Cho, In-Hwan Lee, Jung Han, and Michael E. Coltrin. Understanding nonpolar GaN growth through kinetic Wulff plots. *Journal of Applied Physics*, 104(9):093523, 2008. 1.7, 4.2, 4.5.3

[94] J. E. Northrup and J. Neugebauer. Strong affinity of hydrogen for the GaN(000-1) surface: Implications for molecular beam epitaxy and metalorganic chemical vapor deposition. *Applied Physics Letters*, 85(16):3429–3431, 2004. 1.7

[95] Kihyun Choi, Munetaka Arita, and Yasuhiko Arakawa. Selective-area growth of thin GaN nanowires by MOCVD. *Journal of Crystal Growth*, 357:58–61, oct 2012. 1.7

[96] Jana Hartmann, Xue Wang, Henning Schuhmann, Wanja Dziony, Lorenzo Caccamo, Johannes Ledig, Matin Sadat Mohajerani, Tilman Schimpke, Markus Bähr, Gerhard Lilienkamp, Winfried Daum, Michael Seibt, Martin Straßburg, Hergo-Heinrich Heinrich Wehmann, and Andreas Waag. Growth mechanisms of GaN microrods for 3D core-shell LEDs: The influence of silane flow. *Physica Status Solidi (A) Applications and Materials Science*, 212(12):n/a–n/a, aug 2015. 1.7

[97] Stephen Y. Chou, Peter R. Krauss, and Preston J. Renstrom. Nanoimprint lithography. *Journal of Vacuum Science & Technology B: Microelectronics and Nanometer Structures*, 14(6):4129, 1996. 1.8

[98] V. Ramesh, A. Kikuchi, K. Kishino, M. Funato, and Y. Kawakami. Strain relaxation effect by nanotexturing InGaN/GaN multiple quantum well. *Journal of Applied Physics*, 107(11), 2010. 1-14

[99] C. H. Chiu, T. C. Lu, H. W. Huang, C. F. Lai, C. C. Kao, J. T. Chu, C. C. Yu, H. C. Kuo, S. C. Wang, C. .F Lin, and T. H. Hsueh. Fabrication of InGaN/GaN nanorod light-emitting diodes with self-assembled Ni metal islands. *Nanotechnology*, 18(44):445201, 2007. 1.8

[100] Min Yann Hsieh, Cheng Yin Wang, Liang Yi Chen, Tzu Pu Lin, Min Yung Ke, Yun Wei Cheng, Yi Cheng Yu, Cheng Pin Chen, Dong Ming Yeh, Chih Feng Lu, Chi Feng Huang, C. C. Yang, and Jian Jang Huang. Improvement of external extraction efficiency in GaN-based LEDs by SiO2 nanosphere lithography. *IEEE Electron Device Letters*, 29(7):658–660, 2008. 1.8

[101] Qiming Li, Karl R Westlake, Mary H Crawford, Stephen R Lee, Daniel D Koleske, Jeffery J Figiel, Karen C Cross, Saeed Fathololoumi, Zetian Mi, and George T Wang. Optical performance of top-down fabricated InGaN/GaN nanorod light emitting diode arrays. *Optics express*, 19(25):25528–34, dec 2011. 1.8

[102] E. D. Le Boulbar, I. Gîrgel, C. J. Lewins, P. R. Edwards, R. W. Martin, A. Šatka, D. W. E. Allsopp, and P. A. Shields. Facet recovery and light emission from GaN/InGaN/GaN core-shell structures grown by metal organic vapour phase epitaxy on etched GaN nanorod arrays. *Journal of Applied Physics*, 114(9):094302, 2013. 1.8, 2, 2.1.3, 2-6, 2-9, 2.1.6, 3, 3.1, 3-1, 3-2, 3-3, 3-5, 4.5.3, 4.6

[103] Sergiy Krylyuk, Ratan Debnath, Heayoung P. Yoon, Matthew R. King, Jong-Yoon Ha, Baomei Wen, Abhishek Motayed, and Albert V. Davydov. Faceting control in core-shell GaN micropillars using selective epitaxy. *APL Materials*, 2(10):106104, oct 2014. 1.8, 4.2

[104] J.-R. Chang, S.-P. Chang, Y.-J. Li, Y.-J. Cheng, K.-P. Sou, J.-K. Huang, H.-C. Kuo, and C.-Y. Chang. Fabrication and luminescent properties of core-shell InGaN/GaN multiple quantum wells on GaN nanopillars. *Applied Physics Letters*, 100(26):261103, 2012. 1-15, 3.1, 4, 4.6, 4.7, 7, 7

[105] Ting-Wei Yeh, Yen-Ting Lin, Lawrence S. Stewart, and P. Daniel Dapkus. InGaN/GaN Multiple Quantum Wells Grown on Vertical GaN Nanorod Arrays. *To Be Published*, 2012. 1.9

[106] B. Monemar. Fundamental energy gap of GaN from photoluminescence excitation spectra. *Physical Review B*, 10(2):676–681, 1974. 1.9, 2.1.1

[107] P. Kozodoy, S. Keller, S. P. Denbaars, and U. K. Mishra. MOVPE growth and characterization of Mg-doped GaN. *Journal of Crystal Growth*, 195:265–269, 1998. 1.9, 5.3.1

[108] B. Monemar, P.P. Paskov, J.P. Bergman, A.A. Toropov, T.V. Shubina, S. Figge, T. Paskova, D. Hommel, A. Usui, M. Iwaya, S. Kamiyama, H. Amano, and I. Akasaki. Optical signatures of dopants in GaN. *Materials Science in Semiconductor Processing*, 9(1-3):168–174, February 2006. 1.9

[109] H Obloh, K H Bachem, U Kaufmann, M Kunzer, M Maier, A Ramakrishnan, and P Schlotter. Self-compensation in Mg doped p-type GaN grown by MOCVD. *Journal of Crystal Growth*, 195:270–273, 1998. 1.9, 5.2, 5.2, 5.3.5, 6.4.1

[110] U. Kaufmann, M. Kunzer, M. Maier, H. Obloh, A. Ramakrishnan, B. Santic, and P. Schlotter. Nature of the 2.8 eV photoluminescence band in Mg doped GaN. *Applied Physics Letters*, 72(11):1326, 1998. 1.9, 5.2

[111] U. Kaufmann, P. Schlotter, H. Obloh, K. Köhler, and M. Maier. Hole conductivity and compensation in epitaxial GaN:Mg layers. *Physical Review B*, 62(16):10867–10872, 2000. 1.9, 2.1.7, 5.2, 5-2, 5.3.5, 5.3.6

[112] Hwa-Mok Kim, Yong-Hoon Cho, Hosang Lee, Suk Il Kim, Sung Ryong Ryu, Deuk Young Kim, Tae Won Kang, and Kwan Soo Chung. High-Brightness Light Emitting Diodes Using Dislocation-Free Indium Gallium Nitride/Gallium Nitride Multiquantum-Well Nanorod Arrays. *Nano Letters*, 4(6):1059–1062, jun 2004. 1.9

[113] P. Tchoulfian, F. Donatini, F. Levy, A. Dussaigne, P. Ferret, and J. Pernot. Direct Imaging of p-n Junction in Core-Shell GaN Wires. *Nano letters*, 14(6):3491–8, jun 2014. 1.9, 6.4.1

[114] M. Tchernycheva, V. Neplokh, H. Zhang, P. Lavenus, L. Rigutti, F. Bayle, F. H. Julien, A. Babichev, G. Jacopin, L. Largeau, R. Ciechonski, G. Vescovi, and O. Kryliouk. Core–shell InGaN/GaN nanowire light emitting diodes analyzed by electron beam induced current microscopy and cathodoluminescence mapping. *Nanoscale*, 7(27):11692–11701, 2015. 1.9, 1-16

[115] Katsumi Kishino, Kazuya Nagashima, and Kouji Yamano. Monolithic Integration of InGaN-Based Nanocolumn Light-Emitting Diodes with Different Emission Colors. *Applied Physics Express*, 6(1):012101, dec 2012. 1.9, 1-16

[116] A.-L. Bavencove, G. Tourbot, E. Pougeoise, J. Garcia, P. Gilet, F. Levy, B. André, G. Feuillet, B. Gayral, B. Daudin, and Le Si Dang. GaN-based nanowires: From

nanometric-scale characterization to light emitting diodes. *Physica Status Solidi (a)*, 207(6):1425–1427, May 2010. 1.9

[117] A. C. E. Chia and R. R. LaPierre. Contact planarization of ensemble nanowires. *Nanotechnology*, 22(24):245304, 2011. 1.9

[118] Yong-Ho Ra, R Navamathavan, Ji-Hyeon Park, and Cheul-Ro Lee. High-quality uniaxial In(x)Ga(1-x)N/GaN multiple quantum well (MQW) nanowires (NWs) on Si(111) grown by metal-organic chemical vapor deposition (MOCVD) and light-emitting diode (LED) fabrication. *ACS applied materials and interfaces*, 5(6):2111–7, 2013. 1.9

[119] Christopher Kölper, Matthias Sabathil, Friedhard Römer, Martin Mandl, Martin Strassburg, and Bernd Witzigmann. Core-shell InGaN nanorod light emitting diodes: Electronic and optical device properties. *Physica Status Solidi (a)*, 209(11):2304–2312, November 2012. 1.9

[120] Katsumi Kishino, Jumpei Kamimura, and Kouichi Kamiyama. Near-infrared InGaN nanocolumn light-emitting diodes operated at 1.46μm. *Applied Physics Express*, 5(3):5–8, 2012. 1.9

[121] Katherine E. Plass, Michael A. Filler, Joshua M. Spurgeon, Brendan M. Kayes, Stephen Maldonado, Bruce S. Brunschwig, Harry A. Atwater, and Nathan S. Lewis. Flexible Polymer-Embedded Si Wire Arrays. *Advanced Materials*, 21(3):325–328, January 2009. 1.9

[122] C. J. Lewins, E. D. Le Boulbar, S. M. Lis, P. R. Edwards, R. W. Martin, P. A. Shields, and D. W. E. Allsopp. Strong photonic crystal behavior in regular arrays of core-shell and quantum disc InGaN/GaN nanorod light-emitting diodes. *Journal of Applied Physics*, 116(4):044305, July 2014. 2

[123] K.A. Bertness, A. Roshko, L.M. Mansfield, T.E. Harvey, and N.A. Sanford. Mechanism for spontaneous growth of GaN nanowires with molecular beam epitaxy. *Journal of Crystal Growth*, 310(13):3154–3158, June 2008. 2

[124] Qixin Guo and Akira Yoshida. Temperature dependence of band gap change in InN and AlN. *Japanese Journal of Applied Physics, Part 1: Regular Papers and Short Notes and Review Papers*, 33(5 A):2453–2456, 1994. 2.1.1

[125] Philip A. Shields and Duncan W.E. Allsopp. Nanoimprint lithography resist profile inversion for lift-off applications. *Microelectronic Engineering*, 88(9):3011–3014, September 2011. 2.1.3, 2-6, 3.1

[126] A.E. Grigorescu, M.C. van der Krogt, C.W. Hagen, and P. Kruit. 10nm lines and spaces written in HSQ, using electron beam lithography. *Microelectronic Engineering*, 84(5-8):822–824, may 2007. 2.1.4, 3.7

[127] Marcus Rommel, Bengt Nilsson, Piotr Jedrasik, Valentina Bonanni, Alexandre Dmitriev, and Jürgen Weis. Sub-10nm resolution after lift-off using HSQ/PMMA double layer resist. *Microelectronic Engineering*, 110:123–125, oct 2013. 2.1.4

[128] P. R. Edwards, R. W. Martin, K. P. O'Donnell, and I. M. Watson. Simultaneous composition mapping and hyperspectral cathodoluminescence imaging of InGaN epilayers. *Physica Status Solidi C: Conferences*, 2477(7):2474–2477, 2003. 2.2.5

[129] H Harima. Properties of GaN and related compounds studied by means of Raman scattering. *Journal of Physics: Condensed Matter*, 14:R967–R993, 2002. 2.2, 2.2.6, 3.6, 3.6, 3.3, 5.1, 5.3.3, 5.3.6, 5.3.6, 5.3.6

[130] C. A. Arguello, D. L. Rousseau, and S. P. S. Porto. First-order Raman effect in wurtzite-type crystals. *Physical Review*, 181(3):1351–1363, 1969. 2.2.6, 3.6

[131] H. J. Leamy. Charge collection scanning electron microscopy. *Journal of Applied Physics*, 53(6), 1982. 2.2.7, 6.4.1, 6.4.1

[132] Emmanuel D. Le Boulbar, Paul R. Edwards, Shahrzad Hosseini Vajargah, Ian Griffiths, Ionut Gîrgel, Pierre-Marie Coulon, David Cherns, Robert W. Martin, Colin J. Humphreys, Chris R. Bowen, Duncan W. E. Allsopp, and Philip A. Shields. Structural and Optical Emission Uniformity of m -Plane InGaN Single Quantum Wells in Core–Shell Nanorods. *Crystal Growth & Design*, 16:1907 – 1916, 2016. 3.1, 6.1, 6.1, 7, 7

[133] I. Tiginyanu, A. Sarua, G. Irmer, J. Monecke, S. Hubbard, D. Pavlidis, and V. Valiaev. Fröhlich modes in GaN columnar nanostructures. *Physical Review B*, 64(23):233317, nov 2001. 3.6

[134] A. Sarua, J. Monecke, G. Irmer, I. M. Tiginyanu, G. Gartner, and H.L. Hartnagel. Frohlich modes in porous III – V semiconductors. *Journal of Physics: Condensed Matter*, 13:6687 – 6706, 2001. 3.6

[135] Prasana Sahoo, S. Dhara, S. Dash, A.K. Tyagi, Baldev Raj, C.R. Das, P. Chandramohan, and M.P. Srinivasan. Surface optical modes in GaN nanowires. *International Journal of Nanotechnology*, 7(9/10/11/12):823, 2010. 3.6

[136] R. Mata, A. Cros, K. Hestroffer, and B. Daudin. Surface optical phonon modes in GaN nanowire arrays: Dependence on nanowire density and diameter. *Physical Review B*, 85(3):1–5, jan 2012. 3.6

[137] Piotr Perlin, Claude Jauberthie-Carillon, Jean Paul Itic, Alfonso San Miguel, and Alain Polian. Raman-scattering and X-Ray absorption in gallium nitrider under high pressure. *Physical Review B*, 45(1), 1992. 3.3

[138] A. R. Goñi, H. Siegle, K. Syassen, C. Thomsen, and J.-M. Wagner. Effect of pressure on optical phonon modes and transverse effective charges in GaN and AlN. *Physical Review B*, 64:1–6, 2001. 3.3

[139] Xue Wang, Jana Hartmann, Martin Mandl, Matin Sadat Mohajerani, Hergo H. Wehmann, Martin Strassburg, and Andreas Waag. Growth kinetics and mass transport mechanisms of GaN columns by selective area metal organic vapor phase epitaxy. *Journal of Applied Physics*, 115(16), 2014. 3.7

[140] Benjamin Leung, Qian Sun, Christopher D Yerino, Jung Han, and Michael E Coltrin. Using the kinetic Wulff plot to design and control nonpolar and semipolar GaN heteroepitaxy. *Semiconductor Science and Technology*, 27(2):024005, feb 2012. 3.7, 4.2, 4.5.3

[141] Ionut Gîrgel, Paul R. Edwards, Emmanuel Le Boulbar, Pierre-Marie Coulon, Suman-Lata Sahonta, Duncan W. E. Allsopp, Robert W. Martin, Colin J. Humphreys, and Philip A. Shields. Investigation of indium gallium nitride facet-dependent nonpolar growth rates and composition for core–shell light-emitting diodes. *Journal of Nanophotonics*, 10(1):016010, 2016. 4, 4-6, 4-7, 4-8, 4.1, 4-10, 4.2, 6.1, 7

[142] Qiming Li and George T. Wang. Strain influenced indium composition distribution in GaN/InGaN core-shell nanowires. *Applied Physics Letters*, 97(18):181107, 2010. 4.1, 4.6

[143] C. A. Parker, J. C. Roberts, S. M. Bedair, M. J. Reed, S. X. Liu, and N. A. El-Masry. Determination of the critical layer thickness in the InGaN/GaN heterostructures. *Applied Physics Letters*, 75(18):2776, 1999. 4.1, 4-9

[144] M. Leyer, J. Stellmach, Ch. Meissner, M. Pristovsek, and M. Kneissl. The critical thickness of InGaN on (0001)GaN. *Journal of Crystal Growth*, 310(23):4913–4915, nov 2008. 4.1, 4.6

[145] M. Pristovsek, J. Stellmach, M. Leyer, and M. Kneissl. Growth mode of InGaN on GaN (0001) in MOVPE. *Physica Status Solidi (C)*, 6(S2):S565–S569, jun 2009. 4.1, 4.6

[146] S. Pereira, M. R. Correia, E. Pereira, K. P. O'Donnell, C. Trager-Cowan, F. Sweeney, and E. Alves. Compositional pulling effects in InGaN/GaN layers: A combined depth-resolved cathodoluminescence and Rutherford backscattering/channeling study. *Physical Review B*, 64(20):205311, 2001. 4.1, 4.6

[147] J Neugebauer. Ab initio Analysis of Surface Structure and Adatom Kinetics of Group-III Nitrides. *Physica Status Solidi (B)*, 227(1):93–114, 2001. 4.2, 4.5.3

[148] John E Northrup and J Neugebauer. Theory of GaN (10-10) and (11-20) surfaces. *Physical Review B*, 53(16):R10477 – R10480, 1996. 4.2

[149] J. Chen, S. M. Zhang, B. S. Zhang, J. J. Zhu, X. M. Shen, G. Feng, J. P. Liu, Y. T. Wang, H. Yang, and W. C. Zheng. Influences of reactor pressure of GaN buffer layers on morphological evolution of GaN grown by MOCVD. *Journal of Crystal Growth*, 256(3-4):248–253, 2003. 4.2

[150] Michael A. Reshchikov and Hadis Morkoç. Luminescence properties of defects in GaN. *Journal of Applied Physics*, 97(6):061301, 2005. 4.4, 5.3.3

[151] M. R. Correia, S. Pereira, E. Pereira, J. Frandon, and E. Alves. Raman study of the A[sub 1](LO) phonon in relaxed and pseudomorphic InGaN epilayers. *Applied Physics Letters*, 83(23):4761, 2003. 4.4

[152] H. P. D. Schenk, P. de Mierry, M. Laugt, F. Omnes, M. Leroux, B. Beaumont, and P. Gibart. Indium incorporation above 800 °C during metalorganic vapor phase epitaxy of InGaN. *Applied Physics Letters*, 75(17):2587, 1999. 4.5.1

[153] Nicholas A. Fichtenbaum, Carl J. Neufeld, Chris Schaake, Yuan Wu, Man Hoi Wong, Michael Grundmann, Stacia Keller, Steven P. DenBaars, James S. Speck, and Umesh K. Mishra. Metalorganic Chemical Vapor Deposition Regrowth of InGaN and GaN on N-polar Pillar and Stripe Nanostructures. *Japanese Journal of Applied Physics*, 46(No. 10):L230–L233, mar 2007. 4.5.3

[154] Chaowang Liu, Alexander Šatka, Lethy Krishnan Jagadamma, Paul R. Edwards, Duncan Allsopp, Robert W. Martin, Philip Shields, Jaroslav Kovac, Frantisek Uherek, and Wang Wang. Light Emission from InGaN Quantum Wells Grown on the Facets of Closely Spaced GaN Nano-Pyramids Formed by Nano-Imprinting. *Applied Physics Express*, 2(12):121002, dec 2009. 4.5.3

[155] Cao Miao, Yoshio Honda, Masahito Yamaguchi, and Hiroshi Amano. Growth of InGaN/GaN multiple quantum wells on size-controllable nanopyramid arrays. *Japanese Journal of Applied Physics*, 53(030306), 2014. 4.5.3

[156] S. Pereira, M. R. Correia, E. Pereira, C. Trager-Cowan, F. Sweeney, K. P. O'Donnell, E. Alves, N. Franco, and A. D. Sequeira. Structural and optical properties of InGaN/GaN layers close to the critical layer thickness. *Applied Physics Letters*, 81(7):1207, 2002. 4.5.3

[157] Hyung Koun Cho, Kyu Han Lee, Sun Woon Kim, Keun Seop Park, Yong-Hoon Cho, and Jun Hee Lee. Influence of growth temperature and reactor pressure on microstructural and optical properties of InAlGaN quaternary epilayers. *Journal of Crystal Growth*, 267(1-2):67–73, jun 2004. 4.5.3

[158] M. Moret, B. Gil, S. Ruffenach, O. Briot, Ch. Giesen, M. Heuken, S. Rushworth, T. Leese, and M. Succi. Optical, structural investigations and band-gap bowing parameter of GaInN alloys. *Journal of Crystal Growth*, 311(10):2795–2797, may 2009. 4.5.5, 4-9

[159] K. P. ODonnell, I Fernandez-Torrente, P.R Edwards, and R.W Martin. The composition dependence of the InGaN bandgap. *Journal of Crystal Growth*, 269(1):100–105, aug 2004. 4.5.5, *a*, 4.5.5

[160] J. Wu, W. Walukiewicz, K. M. Yu, J.W Ager, E. E. Haller, Hai Lu, and William J. Schaff. Small band gap bowing in InGaN alloys. *Applied Physics Letters*, 80(25):4741, 2002. 4-9

[161] F. A. Ponce, S. Srinivasan, A. Bell, L. Geng, R. Liu, M. Stevens, J. Cai, H. Omiya, H. Marui, and S. Tanaka. Microstructure and electronic properties of InGaN alloys. *Physica Status Solidi (B) Basic Research*, 240(2):273–284, 2003. 4-9

[162] M. Kurouchi, T. Araki, H. Naoi, T. Yamaguchi, A. Suzuki, and Y. Nanishi. Growth and properties of In-rich InGaN films grown on (0001) sapphire by RF-MBE. *Physica Status Solidi (B) Basic Research*, 241(12):2843–2848, 2004. 4-9

[163] Md Rafiqul Islam, Md Rejvi Kaysir, Md Jahirul Islam, A. Hashimoto, and A. Yamamoto. MOVPE Growth of InxGa1-xN (x ˜ 0.4) and Fabrication of Homojunction Solar Cells. *Journal of Materials Science and Technology*, 29(2):128–136, 2013. 4-9

[164] G. Orsal, Y. El Gmili, N. Fressengeas, J. Streque, R. Djerboub, T. Moudakir, S. Sundaram, A. Ougazzaden, and J.P. Salvestrini. Bandgap energy bowing para-

meter of strained and relaxed InGaN layers. *Optical Materials Express*, 4(5):1030, apr 2014. 4-9, 6.3

[165] Christopher Hahn, Amy A Cordones, Sean C Andrews, Hanwei Gao, Anthony Fu, Stephen R Leone, and Peidong Yang. Effect of Thermal Annealing in Ammonia on the Properties of InGaN Nanowires with Different Indium Concentrations. *The Journal of Physical Chemistry C*, 7(117):3627–3634, 2013. 4.5.5

[166] Torsten Langer, Andreas Kruse, Fedor Alexej Ketzer, Alexander Schwiegel, Lars Hoffmann, Holger Jönen, Heiko Bremers, Uwe Rossow, and Andreas Hangleiter. Origin of the "green gap": Increasing nonroadiative recombination in indium-rich GaInN/GaN quantum well structures. *Physica Status Solidi (C) 8*, 8(7-8):2170–2172, 2011. 4.5.5

[167] Dong-joon Kim, Yong-tae Moon, Keun-man Song, In-hwan Lee, and Seong-ju Park. Effect of Growth Pressure on Indium Incorporation During the Growth of InGaN by MOCVD. *Journal of Electronic Materials*, 30(2):99–102, 2001. 4.5.5

[168] Rachel A. Oliver, Menno J. Kappers, Colin J. Humphreys, and G. Andrew D. Briggs. The influence of ammonia on the growth mode in InGaN/GaN heteroepitaxy. *Journal of Crystal Growth*, 272(1-4):393–399, dec 2004. 4.5.5

[169] Keun-Man Song and Jinsub Park. Effects of the growth pressure of a -plane InGaN/GaN multi-quantum wells on the optical performance of light-emitting diodes. *Semiconductor Science and Technology*, 28(1):015010, jan 2013. 4.5.5

[170] Milton Ohring. *Materials Science of Thin Films Deposition and Structure*. Academic Press, London, 2nd ed. edition, 1992. 4.5.5

[171] S. Pereira, M. R. Correia, E. Pereira, K. P. O'Donnell, C. Trager-Cowan, F. Sweeney, E. Alves, A. D. Sequeira, N. Franco, and I. M. Watson. Depth resolved studies of indium content and strain in InGaN layers. *Physica Status Solidi (B) Basic Research*, 228(1):59–64, 2001. 4.6

[172] Hezhi Zhang, Gwénolé Jacopin, Vladimir Neplokh, Ludovic Largeau, François H Julien, Olga Kryliouk, and Maria Tchernycheva. Color control of nanowire InGaN/GaN light emitting diodes by post-growth treatment. *Nanotechnology*, 26(46):465203, 2015. 4.7, 6.2, 6.2.3

[173] N. Koide, H. Kato, M. Sassa, S. Yamasaki, K. Manabe, M. Hashimoto, H. Amano, K. Hiramatsu, and I. Akasaki. Doping of GaN with Si and properties of blue

m/i/n/n+ GaN LED with Si-doped n+-layer by MOVPE. *Journal of Crystal Growth*, 115(1-4):639–642, 1991. 5.1

[174] R. Dingle and M. Ilegems. Donor-acceptor pair recombination in GaN. *Solid State Communications*, 9(3):175–180, 1971. 5.2

[175] W. Götz, N. M. Johnson, J. Walker, D. P. Bour, and R. A. Street. Activation of acceptors in Mg-doped GaN grown by metalorganic chemical vapor deposition. *Applied Physics Letters*, 68(1996):667–669, 1996. 5.2, 5.2

[176] Chris G. Van de Walle. Interactions of hydrogen with native defects in GaN. *Physical Review B*, 56(16):R10020–R10023, 1997. 5.2, 5.2, 5.3.5

[177] B. Monemar, P. P. Paskov, G. Pozina, C. Hemmingsson, J. P. Bergman, T. Kawashima, H. Amano, I. Akasaki, T. Paskova, S. Figge, D. Hommel, and A. Usui. Evidence for Two Mg Related Acceptors in GaN. *Physical Review Letters*, 102(23):235501, June 2009. 5.2, 5.1, 5.3.3, 6.3

[178] Y. S. Park, T. W. Kang, H. Im, S.-K. Lee, Y.-H. Cho, C. M. Park, M.-S. Han, and R. A. Taylor. Effects of Surface Recombination on Exciton Dynamics in GaN Nanorods. *Journal of Nanoelectronics and Optoelectronics*, 4(2):307–311(5), 2009. 5.2, 5.1

[179] Bo Monemar, Plamen Paskov, Galia Pozina, Carl Hemmingsson, Peder Bergman, David Lindgren, Lars Samuelson, Xianfeng Ni, Hadis Morkoç, Tanya Paskova, Zhaoxia Bi, and Jonas Ohlsson. Photoluminescence of Mg-doped m-plane GaN grown by MOCVD on bulk GaN substrates. *Physica Status Solidi (A) Applications and Materials Science*, 208(7):1532–1534, 2011. 5.2, 5.3.5

[180] S. Khromov, C. G. Hemmingsson, H. Amano, B. Monemar, L. Hultman, and G. Pozina. Luminescence related to high density of Mg-induced stacking faults in homoepitaxially grown GaN. *Physical Review B*, 84(7):075324, August 2011. 5.2, 5.3.3

[181] Meng Zhang, Pallab Bhattacharya, Wei Guo, and Animesh Banerjee. Mg doping of GaN grown by plasma-assisted molecular beam epitaxy under nitrogen-rich conditions. *Applied Physics Letters*, 96(13):21–24, 2010. 5.1, 5.2, 5.2

[182] G. Callsen, M. R. Wagner, T. Kure, J. S. Reparaz, M. Bügler, J. Brunnmeier, C. Nenstiel, A. Hoffmann, M. Hoffmann, J. Tweedie, Z. Bryan, S. Aygun, R. Kirste, R. Collazo, and Z. Sitar. Optical signature of Mg-doped GaN: Transfer processes. *Physical Review B*, 86(7):075207, 2012. 5.1, 5.3.2, 5.3.3, 5.3.5, 6.4.1

[183] R. Juday, A. M. Fischer, Y. Huang, J. Y. Huang, H. J. Kim, J.-H. Ryou, R. D. Dupuis, D. P. Bour, and F. A. Ponce. Hydrogen-related, deeply bound excitons in Mg-doped GaN films. *Applied Physics Letters*, 103(8):082103, 2013. 5.1, 5.3.3

[184] Bo Monemar, Sergey Khromov, Galia Pozina, Plamen Paskov, Peder Bergman, and Carl Hemmingsson. Luminescence of Acceptors in Mg-Doped GaN. *Japanese Journal of Applied Physics*, 52:8–10, 2013. 5.1

[185] B. Monemar, P. P. Paskov, G. Pozina, C. Hemmingsson, J. P. Bergman, S. Khromov, V. N. Izyumskaya, V. Avrutin, X. Li, H. Morkoç, H. Amano, M. Iwaya, and I. Akasaki. Properties of the main Mg-related acceptors in GaN from optical and structural studies. *Journal of Applied Physics*, 115(5):053507, 2014. 5.1, 5.2, 5.3.2, 5.3.3

[186] O. Gelhausen, M. R. Phillips, E. M. Goldys, T. Paskova, B. Monemar, M. Strassburg, and A. Hoffmann. Dissociation of H-related defect complexes in Mg-doped GaN. *Physical Review B*, 69(12):125210, 2004. 5.2

[187] L. Eckey, U. von Gfug, J. Holst, A. Hoffmann, A. Kaschner, H. Siegle, C. Thomsen, B. Schineller, K. Heime, M. Heuken, O. Schon, and R. Beccard. Photoluminescence and Raman study of compensation effects in Mg-doped GaN epilayers. *Journal of Applied Physics*, 84(10):5828, 1998. 5.2, 5.3.2, 5.3.3, 5.3.4, 5.4

[188] John L. Lyons, Anderson Janotti, and Chris G. Van De Walle. Shallow versus deep nature of Mg acceptors in nitride semiconductors. *Physical Review Letters*, 108(15):1–5, 2012. 5.2

[189] F. Shahedipour and B. W. Wessels. Investigation of the formation of the 2.8 eV luminescence band in p-type GaN:Mg. *Applied Physics Letters*, 76(21):3011, 2000. 5.2, 5.3.5

[190] Q. Wang, X. Liu, M. G. Kibria, S. Zhao, H. P. T. Nguyen, K. H. Li, and Z. Mi. by micro-Raman scattering and X-ray. *Nanoscale*, 6(19):9970–9976, 2014. 5.2, 5.3.6

[191] B. Schineller, A. Guttzeit, P. H. Lim, M. Schwambera, K. Heime, and O. Scho. The influence of Mg-concentration and carrier gas on the electrical and optical properties of GaN : Mg grown by MOVPE. *Journal of Crystal Growth*, 195:274–279, 1998. 5.3, 5.3.1

[192] Ronny Kirste, Marc P. Hoffmann, James Tweedie, Zachary Bryan, Gordon Callsen, Thomas Kure, Christian Nenstiel, Markus R. Wagner, Ramon Collazo, Axel

Hoffmann, and Zlatko Sitar. Compensation effects in GaN:Mg probed by Raman spectroscopy and photoluminescence measurements. *Journal of Applied Physics*, 113(10):103504, 2013. 5.3.2, 5.3.6, 5.3.6, 5.4, 6.3

[193] Avinash Patsha, S. Amirthapandian, Ramanathaswarny Pandian, Santanu Bera, Anirban Bhattacharya, and Sandip Dhara. Direct Evidence of Mg Incorporation Pathway in Vapor-Liquid-Solid Grown p-type Nonpolar GaN Nanowires. *Journal of Physical Chemistry C*, 118(41):24165–24172, OCT 16 2014. 5.3.3, 5.3.3

[194] Christoph Böcklin, Ratko G. Veprek, Sebastian Steiger, and Bernd Witzigmann. Computational study of an InGaN/GaN nanocolumn light-emitting diode. *Physical Review B*, 81(15):155306, apr 2010. 5.3.3

[195] U. Kaufmann, M. Kunzer, H. Obloh, M. Maier, Ch. Manz, A. Ramakrishnan, and B. Santic. Origin of defect-related photoluminescence bands in doped and nominally undoped GaN. *Physical Review B*, 59(8):5561–5567, 1999. 5.3.3

[196] Qimin Yan, Anderson Janotti, Matthias Scheffler, and Chris G. Van De Walle. Role of nitrogen vacancies in the luminescence of Mg-doped GaN. *Applied Physics Letters*, 100(14):0–4, 2012. 5.3.3, 6.3

[197] G. Pozina, P. P. Paskov, J. P. Bergman, C. Hemmingsson, L. Hultman, B. Monemar, H. Amano, I. Akasaki, and A. Usui. Metastable behavior of the UV luminescence in Mg-doped GaN layers grown on quasibulk GaN templates. *Applied Physics Letters*, 91(22):89–92, 2007. 5.3.3

[198] Stephan Lany and Alex Zunger. Dual nature of acceptors in GaN and ZnO: The curious case of the shallow Mg[sub Ga] deep state. *Applied Physics Letters*, 96(14):142114, 2010. 5.3.3

[199] D. J. Dewsnip, A. V. Andrianov, I. Harrison, D. E. Lacklison, J. W. Orton, J. Morgan, G. B. Ren, T. S. Cheng, S. E. Hooper, and C. T. Foxon. Observation of resonant Raman lines during the photoluminescence of doped GaN. *Semiconductor Science and Technology*, 12(1):55–58, 1997. 5.3.3

[200] Y. S. Park, J. H. Na, R. A. Taylor, C. M. Park, K. H. Lee, and T. W. Kang. The recombination mechanism of Mg-doped GaN nanorods grown by plasma-assisted molecular-beam epitaxy. *Nanotechnology*, 17(3):913–916, 2006. 5.3.3

[201] A. M. Fischer, S. Srinivasan, F. A. Ponce, B. Monemar, F. Bertram, and J. Christen. Time-resolved cathodoluminescence of Mg-doped GaN. *Applied Physics Letters*, 93(15):151901, 2008. 5.3.3

[202] Toma Stoica and Raffaella Calarco. Doping of III-Nitride Nanowires Grown by Molecular Beam Epitaxy. *IEEE Journal of Selected Topics in Quantum Electronics*, 17(4):859–868, 2011. 5.3.5, 5.3.6, 5.3.6

[203] Damien Carter and Catherine Stampfl. Atomic and electronic structure of single and multiple vacancies in GaN nanowires from first-principles. *Physical Review B*, 79(19):1–14, 2009. 5.3.5

[204] S. Hautakangas, K. Saarinen, L. Liszkay, J. Freitas, and R. Henry. Role of open volume defects in Mg-doped GaN films studied by positron annihilation spectroscopy. *Physical Review B*, 72(16):165303, oct 2005. 5.3.5

[205] G. Martinez Criado, A. Cros, A. Cantarero, R. Dimitrov, O. Ambacher, and M. Stutzmann. Optical characterization of Mg-doped GaN films grown by metal-organic chemical vapor phase deposition. *Journal of Applied Physics*, 88(6):3470–3478, 2000. 5.3.5

[206] V. N. Bessolov, Yu. V. Zhilyaev, E. V. Konenkova, V. a. Fedirko, and D. R. T. Zahn. Raman and infrared spectroscopy of GaN nanocrystals grown by chloride-hydride vapor-phase epitaxy on oxidized silicon. *Semiconductors*, 37(8):940–943, 2003. 5.3.6

[207] H. Harima, T. Inoue, S. Nakashima, K. Furukawa, and M. Taneya. Electronic properties in p-type GaN studied by Raman scattering. *Applied Physics Letters*, 73(14):2000–2002, 1998. 5.3.6

[208] G. Popovici, G. Y. Xu, A. Botchkarev, W. Kim, H. Tang, A. Salvador, H. Morkoc, R. Strange, and J. O. White. Raman scattering and photoluminescence of Mg-doped GaN films grown by molecular beam epitaxy. *Journal of Applied Physics*, 82(8):4020, 1997. 5.3.6

[209] H. Harima, T. Inoue, S. Nakashima, M. Ishida, and M. Taneya. Local vibrational modes as a probe of activation process in p-type GaN. *Applied Physics Letters*, 75(10):1383, 1999. 5.3.6

[210] Markus Pristovsek. Wavelength limits for InGaN quantum wells on GaN. *Applied Physics Letters*, 102(24):242105, 2013. 6.1

[211] R. A. Oliver, F. C P Massabuau, M. J. Kappers, W. A. Phillips, E. J. Thrush, C. C. Tartan, W. E. Blenkhorn, T. J. Badcock, P. Dawson, M. A. Hopkins, D. W E Allsopp, and C. J. Humphreys. The impact of gross well width fluc-

tuations on the efficiency of GaN-based light emitting diodes. *Applied Physics Letters*, 103(14), 2013. 6.1, 7

[212] M. J. Wallace, P. R. Edwards, M. J. Kappers, M. A. Hopkins, F. Oehler, S. Sivaraya, R. A. Oliver, C. J. Humphreys, D. W E Allsopp, and R. W. Martin. Effect of the barrier growth mode on the luminescence and conductivity micron scale uniformity of InGaN light emitting diodes. *Journal of Applied Physics*, 117(11):1–6, 2015. 6.1

[213] Pierre-Marie Coulon, Shahrzad H.-V., An Bao, P. R. Edwards, E. Le Boulbar, I. Gîrgel, R. W. Martin, C. Humphreys, Rachel A. Oliver, D.W.E. Allsopp, and P.A. Shields. Evolution of the m-plane Quantum Well Morphology and Composition within a GaN/InGaN Core-Shell Structure. *Crystal Growth & Design*, 17(2):474–482, 2016. 6.1, 6.3, 7

[214] Yingda Chen, Hualong Wu, Guanglong Yue, Zimin Chen, Zhiyuan Zheng, Zhisheng Wu, Gang Wang, and Hao Jiang. Enhanced Mg doping efficiency in P-Type GaN by indium-surfactant-assisted delta doping method. *Applied Physics Express*, 6(4), 2013. 6.1

[215] S J Chung, M. Senthil Kumar, Y. S. Lee, E-K. Suh, and M. H. An. Characteristics of Mg-doped and In–Mg co-doped p-type GaN epitaxial layers grown by metal organic chemical vapour deposition. *Journal of Physics D: Applied Physics*, 43(18):185101, 2010. 6.1

[216] Binglei Fu, Zhe Liu, Naixin Liu, Zhi Li, Zhao Si, Xuecheng Wei, Baojuan Sun, Ping Ma, Tongbo Wei, Jinmin Li, and Junxi Wang. Elimination of defects in In–Mg codoped GaN layers probed by strain analysis. *Japanese Journal of Applied Physics*, 060301(53):060301, 2014. 6.1

[217] Charng-gan Tu, Che-hao Liao, Yu-feng Yao, Horng-shyang Chen, Chun-han Lin, Chia-ying Su, Pei-ying Shih, Wei-han Chen, Erwin Zhu, Yean-woei Kiang, and C C Yang. Regularly patterned non-polar InGaN / GaN quantum-well nanorod light-emitting diode array. *Optics express*, 22(December):A1799 – A1809, 2014. 6.2.2, 7

[218] John C. C. Fan, Frank J. Bachner, and George H. Foley. Effect of O2 pressure during deposition on properties of rf-sputtered Sn-doped In2O3 films. *Applied Physics Letters*, 31(11):773, 1977. 6.2.2

[219] A. Y. Polyakov, N. B. Smirnov, A. V. Govorkov, S. J. Pearton, and J. M. Zavada. Proton implantation effects on electrical and luminescent properties of p-GaN. *Journal of Applied Physics*, 94(5):3069–3074, 2003. 6.2.3

[220] David Massoubre, Enyuan Xie, Benoit Guilhabert, Johannes Herrnsdorf, Erdan Gu, Ian M Watson, and Martin D. Dawson. Micro-structured light emission from planar InGaN light-emitting diodes. *Semiconductor Science and Technology*, 29(1):015005, 2014. 6.2.3

[221] T. Mori, T. Kozawa, T. Ohwaki, Y. Taga, S. Nagai, S. Yamasaki, S. Asami, N. Shibata, and M. Koike. Schottky barriers and contact resistances on p-type GaN. *Applied Physics Letters*, 69(23):3537, 1996. 6.2.4

[222] Kirt R Williams, Student Member, Richard S Muller, and Life Fellow. Etch Rates for Micromachining Processing. *Journal of Microelectromechanical Systems*, 5(4):256 – 269, 1996. 6.2.4

[223] H. W. Seo, L. W. Tu, Y. T. Lin, C. Y. Ho, Q. Y. Chen, L. Yuan, D. P. Norman, and N. J. Ho. p-GaN/InGaN/n-GaN pedestal nanorods: Effect of postgrowth annealing on the electrical performance. *Applied Physics Letters*, 94(20):201907, 2009. 6.2.5

[224] George T. Wang, Qiming Li, Jonathan Wierer, Jeffrey Figiel, Jeremy B. Wright, Ting S. Luk, and Igal Brener. Top-down fabrication of GaN-based nanorod LEDs and lasers. *Proc. of SPIE*, 8278:827816–827816–6, 2012. 6.2.5

[225] R. Neumann, M. Al-Suleiman, M. Erenburg, J. Ledig, H.-H. Wehmann, and A. Waag. Contacts on high aspect ratio 3D structures. *Microelectronic Engineering*, 88(11):3224–3226, November 2011. 6.2.5

[226] Atsushi Tanaka, Hiroshi Amano, Yoshio Honda, Syuho Nitta, Maki Kushimoto, Manato Deki, Junya Matushita, Kentaro Nagamatsu, and Ousumane Barry. Facet Distribution of Leakage Current and Carrier Concentration in m-Plane GaN Schottky Barrier Diode Fabricated with MOVPE. In *IWN 2016 PS2.162*, 2016. 6.2.5

[227] In-Hwan Lee, In-Hoon Choi, Cheul-Ro Lee, Sung-Jin Son, Jae-Young Leem, and Sam Kyu Noh. Mobility enhancement and yellow luminescence in Si-doped GaN grown by metalorganic chemical vapor deposition technique. *Journal of Crystal Growth*, 182(3-4):314–320, 1997. 6.3

[228] Shigefusa F. Chichibu, T. Azuhata, T. Sota, and Shuji Nakamura. Spontaneous emission of localized excitons in InGaN single and multiquantum well structures. *Applied Physics Letters*, 69(December):4188–4190, 1996. 6.3

[229] Mathew C. Schmidt, Kwang Choong Kim, Hitoshi Sato, Natalie Fellows, Hisashi Masui, Shuji Nakamura, Steven P. DenBaars, and James S. Speck. High power and high external efficiency m-plane InGaN light emitting diodes. *Japanese Journal of Applied Physics, Part 2: Letters*, 46(4-7), 2007. 6.3

[230] Chi Feng Huang, Cheng Yen Chen, Chih Feng Lu, and C. C. Yang. Reduced injection current induced blueshift in an InGaNGaN quantum-well light-emitting diode of prestrained growth. *Applied Physics Letters*, 91(5):2005–2008, 2007. 6.3

[231] T. Wang, D. Nakagawa, M. Lachab, T. Sugahara, and S. Sakai. Optical investigation of InGaN/GaN multiple quantum wells. *Applied Physics Letters*, 74(21):3128, 1999. 6.3

[232] Guibao Xu, Guan Sun, Yujie J. Ding, Hongping Zhao, Guangyu Liu, Jing Zhang, and Nelson Tansu. Investigation of large Stark shifts in InGaN/GaN multiple quantum wells. *Journal of Applied Physics*, 113(3), 2013. 6.3

[233] Pierre-Marie Coulon, Maxime Hugues, Blandine Alloing, Emmanuel Beraudo, Mathieu Leroux, and Jesus Zuniga-Perez. GaN microwires as optical microcavities: whispering gallery modes Vs Fabry-Perot modes. *Optics Express*, 20(17):18707, 2012. 6.3

[234] Yu Jung Lu, Ming Yen Lu, Yu Chen Yang, Hung Ying Chen, Lih Juann Chen, and Shangjr Gwo. Dynamic visualization of axial p-n junctions in single gallium nitride nanorods under electrical bias. *ACS Nano*, 7(9):7640–7647, 2013. 6.4.1

[235] Baijun Zhang, Takashi Egawa, Hiroyasu Ishikawa, Yang Liu, and Takashi Jimbo. High-bright InGaN multiple-quantum-well blue light-emitting diodes on Si (111) using AlN/GaN multilayers with a thin AlN/AlGaN buffer layer. *Japanese Journal of Applied Physics, Part 2: Letters*, 42(3 A), 2003. 6.4.2

[236] Chunlan Mo, Wenqing Fang, Yong Pu, Hechu Liu, and Fengyi Jiang. Growth and characterization of InGaN blue LED structure on Si(1 1 1) by MOCVD. *Journal of Crystal Growth*, 285(3):312–317, 2005. 6.4.2

[237] Charng-gan Tu, Yu-feng Yao, Che-hao Liao, Chia-ying Su, Chieh Hsieh, Chun-han Lin, Hao-tsung Chen, Yean-woei Kiang, and C C Yang. well nanorod light-emitting diode array. *Optics express*, 23(17):21919–21930, 2015. 7, 7

[238] J. M. Calleja, S. Lazić, J. Sanchez-Páramo, F. Agulló-Rueda, L. Cerutti, J. Ristić, S. Fernández-Garrido, M. A. Sánchez-Garcia, J. Grandal, E. Calleja, A. Trampert, and U. Jahn. Inelastic light scattering spectroscopy of semiconductor nitride nanocolumns. *Physica Status Solidi (B)*, 244(8):2838–2846, aug 2007. 7

[239] Joachim Piprek and Z. M. Simon Li. Sensitivity analysis of electron leakage in III-nitride light-emitting diodes. *Applied Physics Letters*, 102(13):1–5, 2013. 7

[240] R. A. Oliver. Critical Assessment 23: Gallium nitride-based visible light-emitting diodes. *Materials Science and Technology*, 32(8):737–745, 2016. 7

[241] Jonathan J. Wierer, Aurelien David, and Mischa M. Megens. III-nitride photonic-crystal light-emitting diodes with high extraction efficiency. *Nature Photonics*, 3(3):163–169, 2009. 7

[242] Renjie Wang, Hieu P. T. Nguyen, Ashfiqua T. Connie, J. Lee, Ishiang Shih, and Zetian Mi. Color-tunable, phosphor-free InGaN nanowire light-emitting diode arrays monolithically integrated on silicon. *Optics Express*, 22(December):1768–1775, 2014. 7

[243] Renjie Wang, Yong-Ho Ra, Yuanpeng Wu, Songrui Zhao, Hieu P. T. Nguyen, Ishiang Shih, and Zetian Mi. Tunable, full-color nanowire light emitting diode arrays monolithically integrated on Si and sapphire. *Spie Opto*, 9748(February):97481S, 2016. 7